CTA Quantification and Multi-modal Visualization

for Assessing Coronary Artery Disease

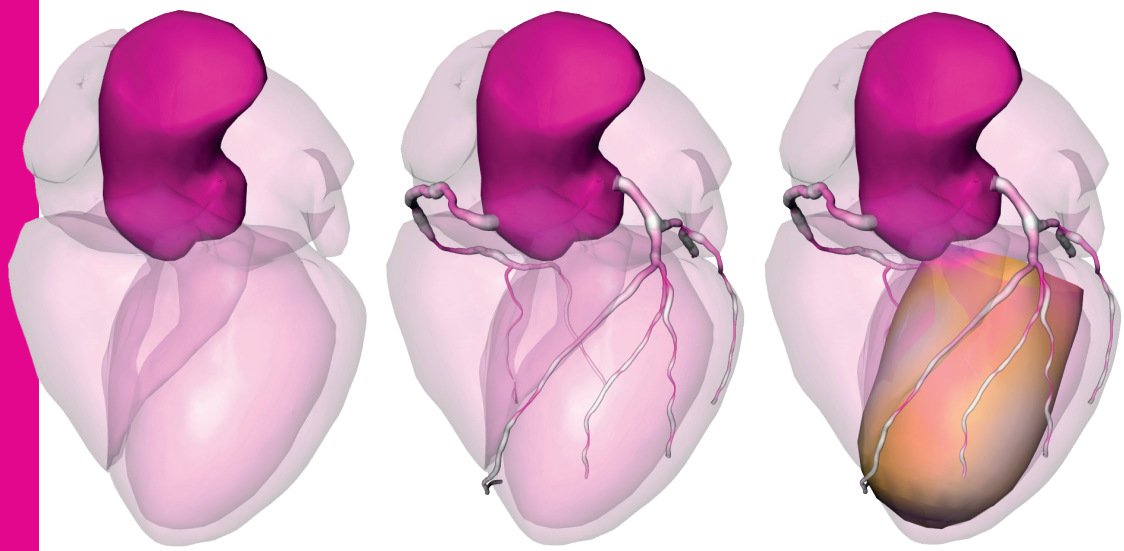

Hortense A. Kirişli

CTA Quantification and Multi-modal Visualization for Assessing Coronary Artery Disease

Hortense Ayla Kirişli

The work in this thesis was conducted at the Departments of Radiology and Medical Informatics of the Erasmus MC, University Medical Center, Rotterdam, The Netherlands and was financially supported by the Dutch Ministry of Economic Affairs (AgentschapNL) under the title "'Het Hart in Drie Dimensies'" (PID06003).

Financial support by

Cardialysis BV (Rotterdam, the Netherlands)
Medis medical imaging systems BV (Leiden, the Netherlands)
Ecole du Ski Français Chamonix (Chamonix-Mont-Blanc, France)

for the publication of this thesis is gratefully acknowledged.

Additional financial support for the publication of this thesis was generously provided by the Department of Radiology, Erasmus MC; Erasmus University Rotterdam and the ASCI graduate school.

This work was carried out in the ASCI and COEUR graduate schools.
ASCI dissertation series number 274.

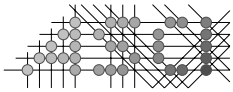

Layout and cover design by Hortense Kirişli.
Printed by GVO Drukkers en Vormgevers BV | Ponsen & Looijen.

ISBN 978-90-6464-661-4

CTA Quantification and Multi-modal Visualization for Assessing Coronary Artery Disease

CTA kwantificatie en multi-modale visualisatie
voor het beoordelen van kransslagaderziekte

PROEFSCHRIFT

ter verkrijging van de graad van doctor aan de
Erasmus Universiteit Rotterdam
op gezag van de rector magnificus

Prof.dr. H.G. Schmidt

en volgens besluit van het College voor Promoties.

De openbare verdediging zal plaatsvinden op
vrijdag 14 juni 2013 om 11.30 uur door

Hortense Ayla Kirişli

geboren te Bonneville, Frankrijk

Promotiecommissie

Promotoren:	Prof.dr. W.J. Niessen Prof.dr.ir. J.H.C. Reiber
Overige leden:	Dr. K. Nieman Prof.dr. P.J. de Feyter Prof.dr. B. van Ginneken
Copromotor:	Dr.ir. T. van Walsum

Contents

chapter 1

General Introduction

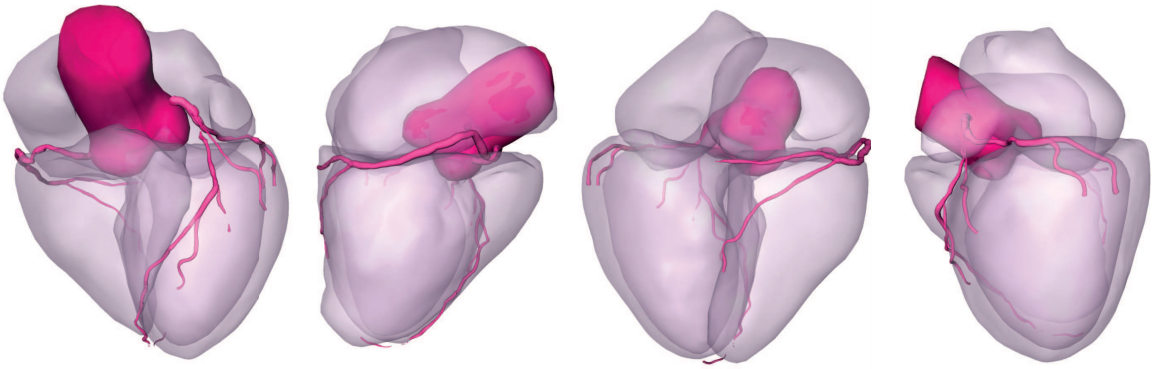

"Put your heart, mind, and soul into even your smallest acts.
This is the secret of success."
Swami Sivananda

In cardiovascular disease, relating a coronary stenosis to a cardiac perfusion defect is of importance for selecting and planning the proper treatment. However, this is challenging owing to the high anatomical variability of the coronary arteries between patients. Anatomical and functional imaging is routinely obtained from multiple imaging modalities. The goal of the work described in this thesis is to develop and evaluate techniques to quantify cardiac and coronary geometry from computed tomography angiography (CTA), and to combine this anatomical information with functional information extracted from either perfusion magnetic resonance imaging (MRI) or single-photon emission computed tomography myocardial perfusion imaging (SPECT-MPI) to support diagnosis and therapy planning in coronary artery disease (CAD).

In the remainder of this chapter, the cardiac anatomy and pathologies will be introduced (Section 1.1 and 1.2), and the imaging techniques currently used to assess coronary artery disease will be presented in Section 1.3, with a highlight on hybrid imaging. Following the introduction, an outline of this thesis is proposed in Section 1.4

1.1 The Cardiovascular System

1.1.1 Cardiac Anatomy

The *heart* is a muscular organ which pumps blood to the entire body; it is at the center of our circulatory system. It consists of two *atria*, two *ventricles* and four *valves*.

The atria are the chambers receiving blood and the ventricles are the ejecting chambers. The deoxygenated blood enters into the right atrium (RA) through the superior vena cava (SVC). It is subsequently pumped into the right ventricle (RV) through the *tricuspid* valve before being ejected through the *pulmonary* valve to the pulmonary arteries into the lungs. There, the blood is oxygenated. Oxygenated blood returns from the lungs to the left atrium (LA) through the pulmonary veins, and is then pumped into the left ventricle (LV) through the *mitral* valve, before being ejected through the *aortic* valve to the aorta (Ao), and distributed to the entire body through the vascular system.

The cardiac muscle consists of 3 layers. The most internal layer, i.e. the one in contact with the blood, is called the *endocardium*. The most outer layer, i.e. the one which envelopes the heart, is called the *epicardium*. Between the endocardium and the epicardium lays the *myocardium*: the muscular tissue responsible for the contraction of the heart. Figure 1.1 provides an overview of the cardiac anatomy.

1.1.2 Cardiac Physiology

The cardiac cycle is divided into two phases: *systole* and *diastole*.

During *systole*, the oxygenated blood is ejected from the left ventricle through the aortic valve to the aorta, and the deoxygenated blood is ejected from the right ventricle to the pulmonary arteries through the pulmonary valve. The mitral and triscupid valves are closed to avoid any blood reflux in the atria.

During *diastole*, oxygenated blood is filling the left ventricle and desoxygenated blood is filling the right ventricle. Diastole consists of two phases: the passive filling, i.e. filling induced by the opening of the ventricular valves, and the active filling, i.e. filling resulting from the contraction of the atria. The aortic and pulmonary valves are closed.

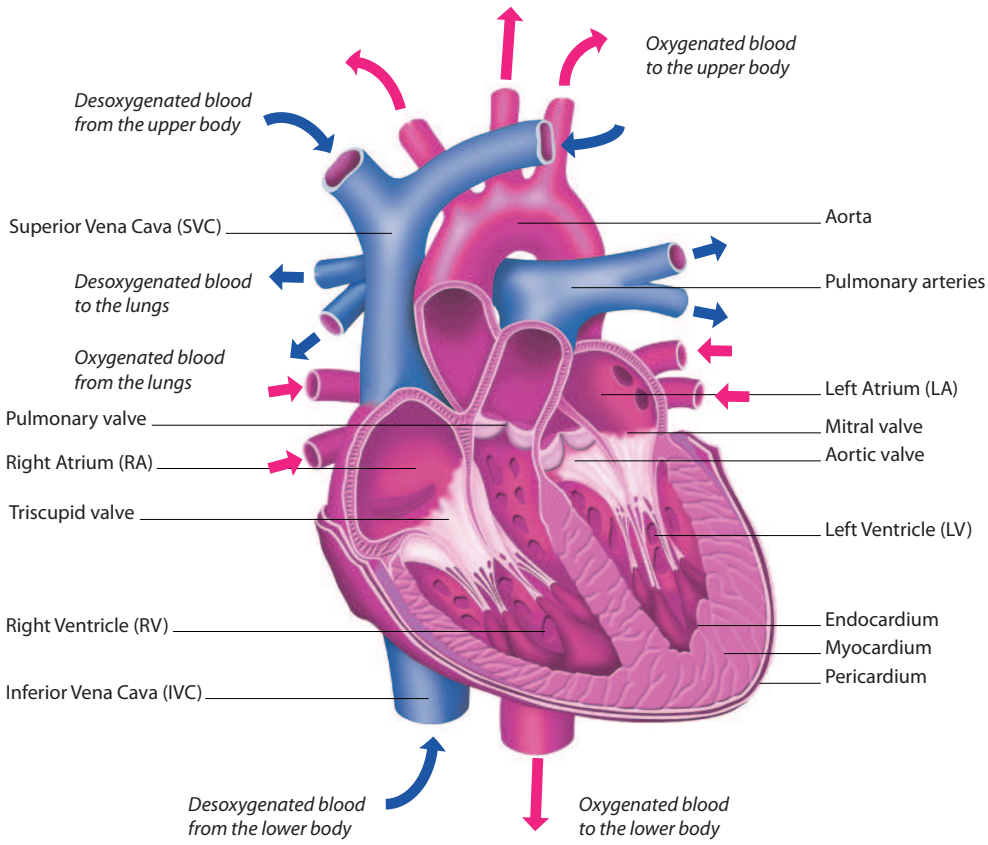

Figure 1.1: Cardiac anatomy. Figure adapted from *http://www.howitworksdaily.com*

1.1.3 Coronary Arteries Anatomy

The arteries supplying oxygenated blood to the myocardium are called the *coronary arteries*. The *coronary arteries* originates from the aorta and are divided into two parts: the left and the right coronary artery tree. The right coronary artery tree (RCA) supplies oxygenated blood to the right ventricle and, generally, to the inferior and infero-septal part of the left ventricle. The left coronary artery tree consists of a common artery trunk, called left main (LM) coronary artery, which divides into two branches: the left anterior descending artery (LAD) and the left circumflex artery (LCX). The LAD, together with its diagonal and septal branches, supplies blood to the anterior region of the left ventricle; the LCX, together with its marginal branches, provides blood to the lateral and infero-lateral region of the left ventricle. Figure 1.2 provides an overview of the coronary arteries anatomy. Additionally, the coronary artery tree is commonly divided into 17 segments, as presented in Figure 1.4.

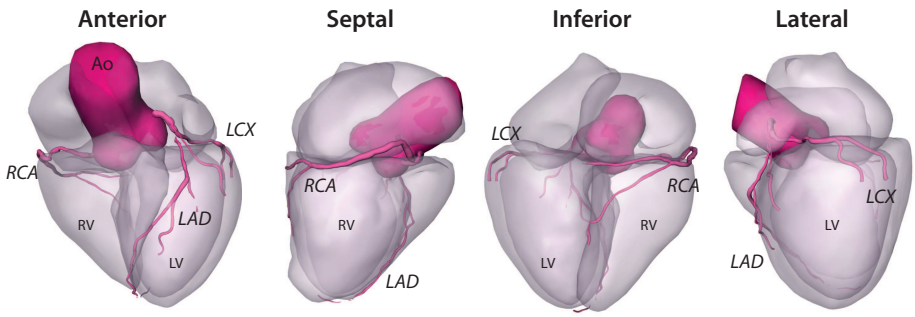

Figure 1.2: Vascular anatomy. Anterior, septal, inferior and lateral view of the heart. Right coronary artery (RCA), left anterior descending artery (LAD), left circumflex artery (LCX), right ventricle (RV), left ventricle (LV).

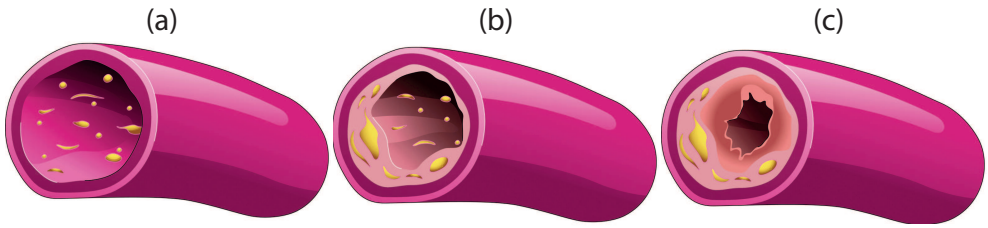

Figure 1.3: Process of atherosclerosis. (a) Healthy coronary artery. (b) Some fat, cholesterol, and other substances are building up in the arterial wall. (c) The narrowing may compromise the blood flow. *Stock photo*

1.2 Cardiac Pathologies

1.2.1 Heart Failure

Heart failure (HF) occurs when the heart is unable to provide sufficient pump action to distribute blood flow to meet the needs of the body. This cardiac pathology may be caused by either a systolic dysfunction, i.e. reduction of the amount of blood ejected by the ventricles, or a diastolic dysfunction, i.e. troubles with the filling of the ventricles. To compensate, the cardiac rhythm of the patient may increase, or hypertrophy/dilation of the ventricles may occur to increase the blood filling and/or ejection. With time, such compensatory mechanisms may become harmful (tachycardia, dilation too important,...).

1.2.2 Coronary Artery Disease

Oxygen and nutrients, which are required for normal heart function, are supplied to the myocardium by the blood traveling through the coronary arteries. If a coronary artery becomes narrowed or occluded owing to the build-up of plaque (e.g. fat, cholesterol, calcium), the amount of blood flowing to the myocardium is reduced and, thus, less oxygen

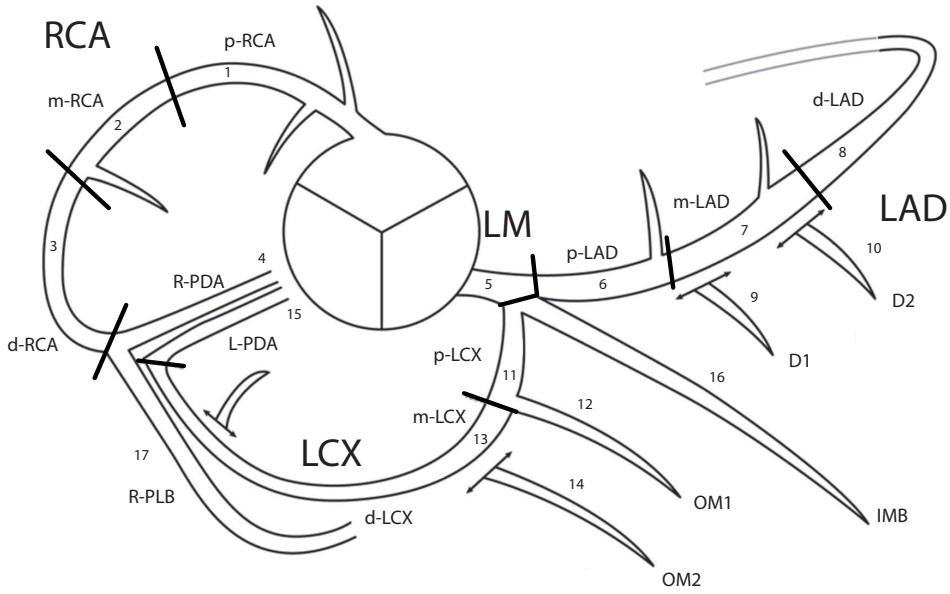

Figure 1.4: 17-segments coronary artery nomenclature, derived, adopted, and adjusted from Austen et al. (1975). Left main (LM), left anterior descending artery (LAD), right coronary artery (RCA), left circumflex artery (LCX), diagonal branch (D), obtuse marginal branch (OM), posterior descending artery (PDA), posterior lateral artery (PL) and intermediate branch (IMB). Proximal (p), middle (m), distal (d). 1: p-RCA, 2: m-RCA, 3: d-RCA, 4: PDA, 5: LM, 6: p-LAD, 7: m-LAD, 8:d-LAD, 9: D1, 10: D2, 11: p-LCX, 12: OM1, 13: m-LCX, 14: OM2, 15: d-LCX, 16: IMB, 17: PL.

and nutrients are delivered to these myocardial regions. The restriction in blood and oxygen is called *ischemia* and the narrowing of vessel is referred to as *stenosis* (Figure 1.3). Coronary artery stenoses can either cause temporary changes to ischemic myocardial regions or, if the myocardium is not supplied with sufficient blood for more than six hours, can induce an irreversible defect of the myocardium, and result in *myocardial infarction*. It is thus crucial to detect coronary artery stenoses in an early stage.

1.3 Diagnosis of Coronary Artery Disease: Imaging Techniques

Various cardiovascular imaging techniques are used to diagnose coronary artery disease. The selection of which (combination of) cardiovascular imaging is to be performed is determined by the patient's history and current symptoms.

1.3.1 Conventional Coronary Angiography

Conventional Coronary Angiography (CCA) is a procedure to visualize the coronary arteries. Contrast agent is injected into the coronary arteries to allow the cardiologist to visualize the coronary arteries by X-ray imaging and detect possible narrowing (i.e. stenoses). Generally, access to the coronary artery is performed through the femoral artery (groin area) or the hand artery (wrist). A small tube is placed in the artery of interest to introduce different devices that may be needed. Examples of coronary angiograms can be found in Figure 1.5.

Quantitative coronary angiography Given multiple 2D X-rays angiograms, coronary segments (Figure 1.4) can visually be classified as normal (smooth parallel or tapering borders, visually $\leq$20% narrowing) or as having non-significant or significant coronary obstruction (visually $\geq$20% narrowing). Stenoses in segments visually scored as having $\geq$20% narrowing can be quantified by a quantitative coronary angiography (QCA) algorithm (Reiber et al., 1985). Stenoses are evaluated in the worst (available) angiographic view and classified as significant if the lumen diameter reduction exceeds 50%. The location, number and severity of the stenoses can be assessed. In current clinical practice, CCA is the gold standard imaging technique to diagnose CAD.

Fractional flow reserve In addition, a wire, with a miniature pressure probe at the tip, may be introduced to determine whether the coronary artery narrowing is compromising blood flow. The pressure before and after the coronary artery stenosis is measured to assess the pressure drop caused by the stenosis. The pressure drop is called *fractional flow reserve* index (FFR). If the FFR across the narrowing is greater than 20%, the narrowing is compromising the blood flow.

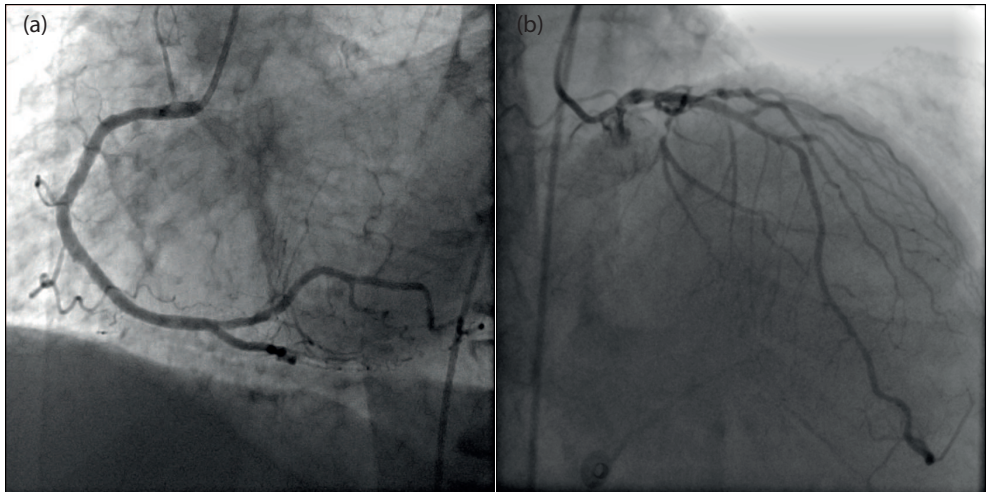

Figure 1.5: Conventional Coronary Angiography (CCA) (a) Right coronary artery tree. (b) Left coronary artery tree.

1.3.2 Computed Tomography Coronary Angiography

Computed Tomography Coronary Angiography (CTA) is an imaging technique which can be used to detect and assess coronary artery stenoses. During a CTA examination, X-rays pass through the body and are picked up by detectors in the scanner. The attenuation of the tissue at different orientations around the patient is measured. Patients undergoing a coronary CTA scan receive an iodine-containing contrast material (i.e. dye) as an intravenous injection to increase attenuation of the coronary arteries, and hence increase contrast in the image. Beta-blocker medication may be given to the patient reduce his heart rate for improved image quality. Computational techniques are used to create three-dimensional images and images in various planes (i.e. curved planar reformatted images) to fully evaluate the heart and coronary arteries. Figure 1.6 presents an example of a CT scanner (Somatom Definition, Siemens, Forchheim, Germany).

CTA is gaining popularity (Weustink and de Feyter, 2011) in assessing coronary artery disease: it is non-invasive, provides high-resolution three-dimensional (3D) images of the cardiac and coronary artery anatomy, and allows the interpreter to assess the presence, extent and type (calcified, mixed or non-calcified) of coronary plaques. Figure 1.6 shows examples of curved planar reformatted CTA image in which a calcified stenosis located in the left circumflex coronary artery is visualized.

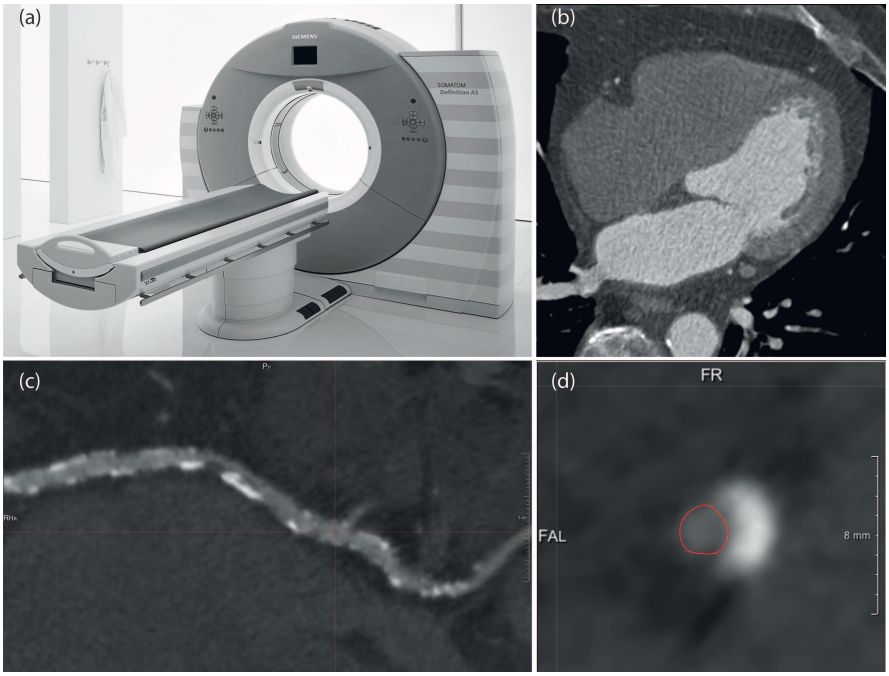

Figure 1.6: Computed Tomography Coronary Angiography. (a) CT scanner (Somatom Definition, Siemens, Forchheim, Germany). (b) Example of axial image. (c) Longitudinal view of a curved planar reformatted image of a left circumflex coronary artery. (d) Cross-sectional view of a curved planar reformatted image of a left circumflex coronary artery, presenting a calcified plaque.

1.3.3 Magnetic Resonance Imaging

Cardiac Magnetic Resonance Imaging (MRI) is a non-invasive imaging technique that can provide detailed anatomical and functional information of the heart. Images are created using a strong magnetic field, radio frequency pulses, and computational techniques. Unlike other imaging tests, MRI does not use ionizing radiation (X-rays). Coils, placed around the chest of the patient, send and receive radio waves, producing signals that are detected by the scanner. Then, a computer processes the signals and generates a series of images, each of which shows a thin slice of the body. During cardiac MRI, a contrast agent (saline solution such as gadolinium) may be injected into a vein in the hand or arm via an intravenous catheter, to change the magnetic properties of the blood, increasing the contrast in cardiac imaging.

Cardiac perfusion imaging is used to determine the extent of myocardial damage and to assess its effect on heart function, such as limited blood flow to the myocardium and scarring within the heart muscle after a heart attack. Cardiac perfusion MRI consist of two imaging phases: imaging at rest and imaging at stress. The stress response is induced by exercise or drug stimulation. The blood circulation of patient under stress is compared to the blood circulation at rest, to detect any abnormal blood flow to the myocardium. An example of MRI scanner and cardiac coil, as well as a number of images from a stress imaging sequence, are shown on Figure 1.7.

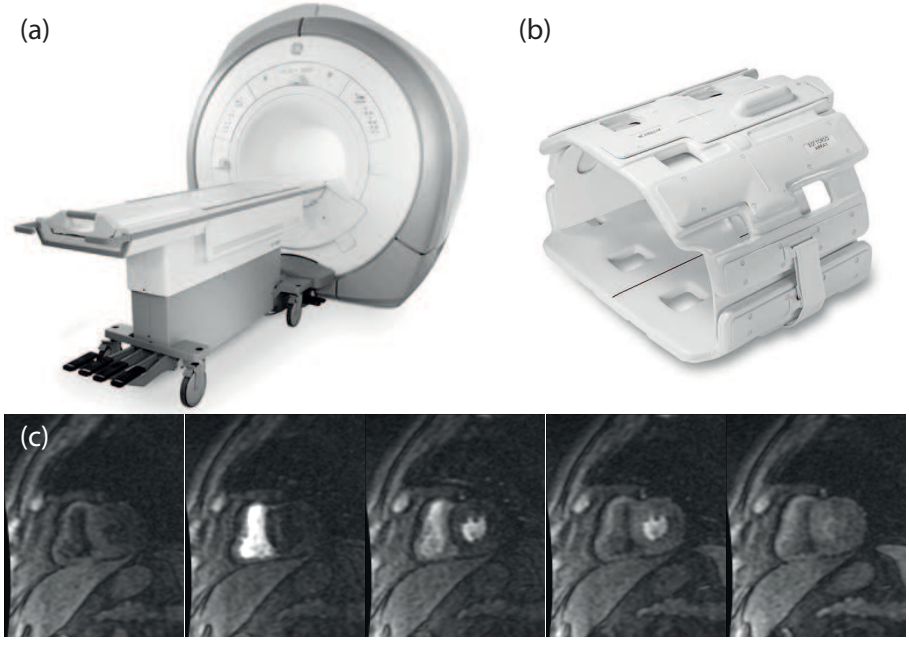

Figure 1.7: Cardiac magnetic resonance imaging (MRI). Signa HDxt 1.5T scanner (a) and an eight-element phased-array receiver coil (b) (GE Medical systems, Milwaukee, Wisconsin USA). (c) Example of stress perfusion MRI sequence.

1.3.4 Single-Photon Emission Computed Tomography

Nuclear imaging techniques use small amounts of radionuclides (i.e. radioactive material) to detect and determine the severity of a variety of diseases, including coronary artery disease. Radionuclides accumulate in the heart and emit a small amount of energy owing to radioactive decay. In Single-Photon Emission Computed Tomography (SPECT), a single gamma ray is emitted which can be detected by a gamma camera(s) slowly rotating around the patient's torso. From these measurements, an image showing the uptake of the radionuclide in time (perfusion) can be reconstructed. In combined SPECT-CT systems, SPECT reconstruction is improved by using CT-derived information, e.g. for attenuation correction. Also, the functional information derived from SPECT can then more easily be combined with anatomical information provided by CT. As for cardiac MRI, the SPECT exam consists of a rest and stress test. Figure 1.8 presents an example of a combined SPECT/CT scanner and generated images.

1.3.5 Cardiac Hybrid Imaging

When diagnosing CAD using both CTA and myocardial perfusion (MRI or SPECT) images, the expert needs to *mentally* integrate anatomical and functional information. Each myocardial perfusion defect should be related to a culprit coronary artery, in order to determine whether a coronary artery stenoses is inducing a hemodynamically significant perfusion defect.

The American Heart Association (AHA) has published some recommendations concerning coronary artery perfusion territories, with respect to their standardized 17-segment bull's eye plot (BEP) model (Cerqueira et al., 2002). However, because variability in coronary anatomy between patients can be high, the use of a standard model may not be optimal. For instance, in a study of 50 patients, Pereztol-Valdés et al. (2005) demonstrated that only nine of the 17 AHA-segments are fed by a single coronary artery, while the other eight segments may be fed by more than one coronary artery (Figure 1.9). Integrating information in a patient-specific way may improve the diagnosis and treatment planning of patients for whom ambiguous assignment of perfusion defects and culprit coronary arteries is present.

The additional value of integrating information from multi-modal cardiac imaging techniques resides in the accurate patient-specific spatial correspondence of coronary stenoses and myocardial perfusion defects (Gaemperli et al., 2012). The potential improvement of decision-making in the management of patients is one of the most important reasons for use of integrated cardiac imaging. Integration of data derived from these complementary imaging techniques may thus offer valuable advantages in diagnosis, staging and treatment of CAD.

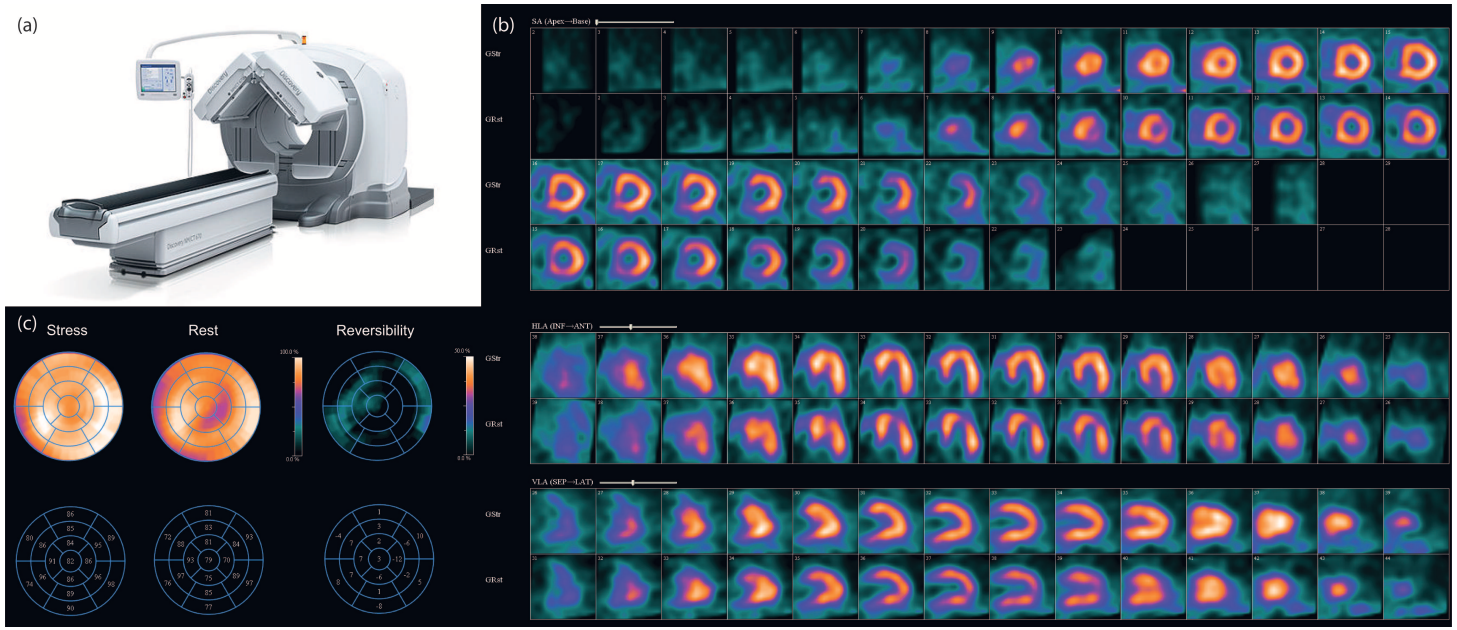

Figure 1.8: Single-Photon Emission Computed Tomography (SPECT). (a) X-ray CT scanner combined with a dual head SPECT gamma camera (Discovery NM/CT 670, GE Healthcare). (b) Example of images generated by SPECT exam. (c) Example of stress, rest and reversibility polar maps used for interpretation.

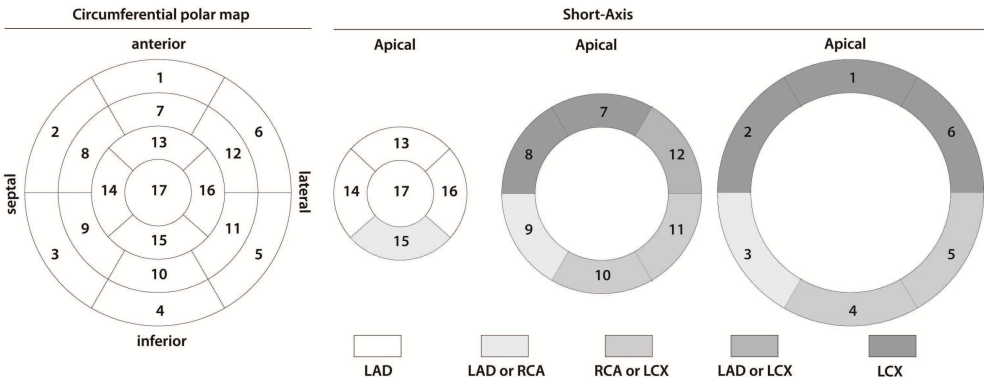

Figure 1.9: 17-segments representation of the left ventricle. This representation is called a *Bull's Eye Plot* (BEP) or polar map. Pereztol-Valdés et al. (2005) demonstrated that only 9 of the 17 AHA-segments are fed by a single coronary artery, while the other eight segments may be fed by more than one coronary artery.

1.4 This Thesis

The work presented in this thesis was carried out in the context of the "Heart in 3D" project. The "Heart in 3D" project was a collaboration of four biomedical imaging research groups at three universities in the Netherlands (Biomedical Imaging Group Rotterdam, Erasmus MC, Rotterdam; Division of Image Processing, LUMC, Leiden; Quantitative Imaging Group, Imaging Science and Technology, Faculty of Applied Sciences, Delft University of Technology, Delft; Vision lab, Delft University of Technology, Delft) and involved a consortium of four companies (Medis Medical Imaging Systems BV, Leiden, the Netherlands; Cardialysis BV, Rotterdam, the Netherlands; BioClinica, Leiden, the Netherlands; Oldelft Ultrasound, Delft, the Netherlands). Three PhD students were involved in the project (Hortense A. Kirişli, Vikas Gupta and Rahil Shahzad).

The goal of the "Heart in 3D" project is to develop algorithms and software to integrate complementary diagnostic information on cardiac anatomy, function and pathology (the status of the coronary arteries, myocardial perfusion and ventricular function) from multi-modality imaging studies. Novel algorithms and quantitative analysis tools were to be developed, to support diagnosis and disease staging in cardiovascular disease.

The goal of the work described in this thesis is to develop and evaluate techniques to quantify cardiovascular disease from CTA, and to combine anatomical information extracted from CTA with functional information extracted from either cardiac perfusion MRI or SPECT myocardial perfusion imaging (SPECT-MPI). To this end, cardiac and coronary artery tree models are created from CTA, and integrated with functional quantification of the myocardium. This is achieved within a patient-specific comprehensive visualization system. The contributions of this thesis are:

(i) **3D segmentation of the cardiac chambers from CTA images.** In Chapter 2, a fully automatic method to delineate the cardiac chambers is developed and evaluated quantitatively and qualitatively using 60 and 1420 multi-center/multi-vendor CTA data respectively.

(ii) **Coronary artery stenosis detection and quantification from CTA images.** In Chapter 3, an automatic method is developed for coronary artery stenosis detection and quantification, and evaluated against CTA consensus and quantitative coronary angiography. The initially extracted centerlines are subsequently used for lumen segmentation, which is performed using graph cuts and robust kernel regression. The expected diameter of the healthy lumen is estimated by applying robust kernel regression on the coronary artery lumen diameter profile; stenoses are subsequently detected and quantified. In Chapter 4, we introduce a standardized evaluation framework to reliably evaluate and compare the performance of the algorithms devised to detect and quantify coronary artery stenoses, and to segment the coronary artery lumen in CTA data. The algorithms from 11 research groups were quantitatively evaluated and compared.

(iii) **Multi-modal cardiovascular image fusion.** In Chapter 5, we introduce a patient-specific visualization system, called Synchronized Multimodal heART Visualization (SMARTVis), for relating coronary stenoses and perfusion deficits derived from CTA and perfusion MRI respectively. We present the result of a first clinical evaluation, involving two experts and four patients having suspected double-vessel disease. In Chapter 6, we extended the SMARTVis system to integrate perfusion information from SPECT-MPI. We investigated the additional diagnostic value of fused CTA/SPECT-MPI analysis compared with side-by-side analysis, in patients with suspected coronary artery disease (CAD). We present the result of a multi-center evaluation, involving four experts and 17 patients suspected of having single-, double- or triple-vessel disease. The SMARTVis comprehensive visualization system can be effectively used to assess disease status in multi-vessel CAD patients, offering valuable new options for the diagnosis and management of these patients.

The thesis concludes with a discussion on the results and future research directions (Chapter 7).

chapter 2

Evaluation of a multi-atlas based method for segmentation of cardiac CTA data: a large-scale, multicenter and multi-vendor study

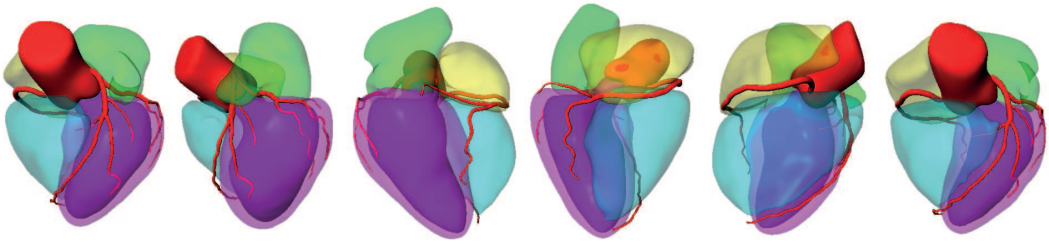

This chapter is based on the manuscript:
Evaluation of a multi-atlas based method for segmentation of cardiac CTA data:
a large-scale, multi-center and multi-vendor study,
H.A. Kirişli, M. Schaap, S. Klein, S.L. Papadopoulou, M. Bonardi, C.H. Chen, A.C. Weustink,
N.R.A. Mollet, E.P.A. Vonken, R.J. van der Geest, T. van Walsum and W.J. Niessen,
Medical Physics, 37(12):6279–6292, 2010.

Abstract

Purpose Computed tomography angiography (CTA) is increasingly used for the diagnosis of coronary artery disease (CAD). However, CTA is not commonly used for the assessment of ventricular and atrial function, although functional information extracted from CTA data is expected to improve the diagnostic value of the examination. In clinical practice, the extraction of ventricular and atrial functional information, such as stroke volume and ejection fraction, requires accurate delineation of cardiac chambers. In this chapter, we investigated the accuracy and robustness of cardiac chamber delineation using a multi-atlas based segmentation method on multicenter and multivendor CTA data.

Methods A fully automatic multi-atlas based method for segmenting the whole heart (i.e. the outer surface of the pericardium) and cardiac chambers from CTA data is presented and evaluated. In the segmentation approach, eight atlas images are registered to a new patient's CTA scan. The eight corresponding manually labeled images are then propagated and combined using a per voxel majority voting procedure, to obtain a cardiac segmentation.

Results The method was evaluated on a multicenter/multivendor database, consisting of 1) a set of 1380 Siemens scans from 795 patients, and 2) a set of 60 multivendor scans (Siemens, Philips and GE) from different patients, acquired in six different institutions worldwide. A leave-one-out 3D quantitative validation was carried out on the eight atlas images; we obtained a mean surface-to-surface error of 0.94 ± 1.12 mm and an average Dice coefficient of 0.93 was achieved. A 2D quantitative evaluation was performed on the 60 multivendor data sets. Here, we observed a mean surface-to-surface error of 1.26 ± 1.25 mm and an average Dice coefficient of 0.91 was achieved. In addition to this quantitative evaluation, a large-scale 2D and 3D qualitative evaluation was performed on 1380 and 140 images, respectively. Experts evaluated that 49% of the 1380 images were very accurately segmented (below 1 mm error) and that 29% were accurately segmented (error between 1 and 3 mm), which demonstrates the robustness of the presented method.

Conclusions A fully automatic method for whole heart and cardiac chamber segmentation was presented and evaluated using multicenter/multivendor CTA data. The accuracy and robustness of the method was demonstrated by successfully applying the method to 1420 multicenter/multivendor data sets.

2.1 Introduction

Computed tomography angiography (CTA) is a non-invasive imaging technique that is an increasingly popular alternative to conventional and invasive 2D X-ray angiography for cardiac examination (Schlosser et al., 2007; Türkvatan et al., 2008), particularly for the diagnosis of coronary artery disease (CAD). However, CTA is not commonly used for the assessment of ventricular and atrial function, although functional information extracted from CTA data is expected to improve the diagnostic value of the examination (Abadi et al., 2009).

Segmentation of the four cardiac chambers enables comprehensive assessment of disease in chambers other than the left ventricle (LV), such as right ventricle overload. Accurate assessment of ventricular and atrial functional measures (e.g. myocardial mass, stroke volume and ejection fraction) requires segmentation of the complete cardiac anatomy. It has been shown that, if a robust cardiac segmentation method is provided, chamber and myocardial volumes derived from the segmentation results provide reliable functional measurements, and that fully automatic analysis of four-chamber cardiac function can be achieved (Abadi et al., 2009). Whole-heart isolation (Funka-Lea et al., 2006) (i.e. the outer surface of the pericardium) is especially useful for visualization of the coronary arteries and for obtaining a region of interest for subsequent segmentation of the coronaries, ventricles and atria.

As manual delineation of cardiac chambers is a tedious and time consuming task, various automatic cardiac image segmentation methods have been developed for 2D, 3D and 4D images. Most of these studies focused on the LV, because functional parameters derived from the diastolic and systolic LV volume are important predictors for heart disease (Abadi et al., 2009). Recently, automatic segmentation of all cardiac chambers has been addressed for CTA (Lorenz and von Berg, 2006; Ecabert et al., 2008; Zheng et al., 2008; Peters et al., 2010). These segmentation algorithms use, for instance, machine learning (Zheng et al., 2008), model-based approaches (Frangi et al., 2001; Ecabert et al., 2008), and atlas-based approaches (Kirişli et al., 2010a).

In this work, we present a fully automatic multi atlas-based method for segmenting the whole heart and cardiac chambers from 3D CTA data. In our approach, eight atlas images are registered to a new patient's CTA scan; the eight corresponding manually labeled images are then propagated and combined using a per voxel majority voting procedure, to obtain a cardiac segmentation of the new patient. Both the implementation of our segmentation technique and the atlases are publicly available.

Our main contribution is a thorough evaluation of our automatic segmentation technique. We quantitatively and qualitatively evaluate the accuracy of the method using a large multi-center/multi-vendor set of representative clinical data (1420 images from 835 patients). Quantitative evaluation is performed on eight cardiac 3D CTA images and on random 2D slices extracted from 60 multi-center/multi-vendor scans of different patients. Qualitative evaluation based on grade classification is performed on 140 cardiac 3D CTA images and on three randomly selected 2D slices from each of the 1380 data sets. This evaluation enables us to investigate the accuracy and robustness of our automatic segmentation approach.

The chapter is organized as follows. Our definition of the cardiac anatomy is specified in Section 2.2. Information on the CTA data used is given in Section 2.3. Section 2.4 describes evaluation of the segmentation method and Section 2.5 describes our experiments. Finally, our results are presented in Section 2.6 and are discussed in Section 2.7.

2.2 Four-chamber heart model

The following definitions of the cardiac chambers to be delineated were used in our approach, and they are based on those described in Boxt (2005).

The whole-heart (Heart) is delimited by the parietal pericardium. The parietal pericardium may be identified as a paper-thin high signal intensity surface surrounding the heart and great arteries. Direct visualization of the parietal pericardium depends upon the presence and extent of low-density fatty deposition in the pericardial fat pad and middle mediastinum.
The aorta (Ao) includes a part of the ascending aorta trunk, the right, left and posterior aortic sinus and stops at the aortic valve.
The left ventricle (LV) starts at the mitral valve, goes to the main LV cavity, then to the left ventricle outflow track, and stops at the aortic valve. The contours of the endocardium LV (endoLV) match the inner surface of the LV, while the contours of the epicardium LV (epiLV) match the outer part of the LV. The papillary muscles are included in the LV cavity.
The right ventricle (RV) starts at the tricuspid valve, then goes to the RV main cavity, to the right ventricle outflow track, and stops at the pulmonary valve, excluding the pulmonary trunk.
The left atrium (LA) starts at the pulmonary veins, excluding the branches (high inter-patient location variability) so that a contour is drawn through the veins. It includes the main LA cavity, and stops at the mitral valve. The left atrium appendage is part of the segmentation.
The right atrium (RA) includes the right atrium appendage and the main RA cavity. The inferior and superior vena cava and the coronary sinus are excluded.

2.3 Materials

A total of 1420 CTA images was used in the experiments. Table 2.1 presents an overview of the data. For each subgroup, the vendor, institution, and the number of subjects and images are shown. Image acquisition was carried out at multiple sites and CT scanners from different vendors were used (Somatom Definition, Siemens Medical Solutions, Forchheim, Germany; Brillance 64 or iCT 256, Philips Medical Systems, Best, The Netherlands; LightSpeed VCT, GE, Buckinghamshire, United Kingdom). Our database includes three different CT scanner technologies: 64-multidetector CT, 256-multidetector CT and dual-source CT.

Most of the CTA data were acquired in the Erasmus MC (University Medical Center, Rotterdam, The Netherlands) with a dual-source CT scanner (Somatom Definition,

Table 2.1: multi-center/multi-vendor database used in the current evaluation study

Vendor	Scanner	Type	Institution	N_P (patients)	N_I (images)
SIEMENS	Somatom Definition	Dual-source	Erasmus MC, Rotterdam, The Netherlands	**795**	**1380**
PHILIPS			UMC Utrecht, Utrecht, The Netherlands	**20**	**20**
	Brillance iCT 256	256-slices		18	18
	Brillance 64	64-slices		2	2
GE	LightSpeed VCT	64-slices		**20**	**20**
			Centre Cardiologique du Nord, Paris, France	11	11
			Atlantic Medical Imaging, Galloway, NJ, USA	4	4
			Froedtert Hospital, Milwaukee, WI, USA	2	2
			Hong-Kong Sanatorium Hospital, Hong-Kong, China	2	2
			Keio University Hospital, Tokyo, Japan	1	1

Table 2.2: Information on the Siemens data used in our large-scale evaluation. Distribution of the 1380 images (selected from 795 patients) over the diastolic and systolic phase, and kernel (b26f smooth/b46f sharp)

		Systole		
		Yes	**No**	**Total**
Diastole	**Yes**	585	150	735
	No	60	-	
	Total	645		

	Kernel	
	b26f	b46f
Diastole	651	84
Systole	594	51
Total	1245	135

Siemens Medical Solutions, Forchheim, Germany). We retrospectively obtained CTA data of 795 patients, aged 12 to 88 (59.5 ± 12) years, who underwent a cardiac CTA examination between April 2004 and January 2009. These images were acquired for clinical diagnosis and follow-up of patients with (suspected) cardiac problems. Therefore, the images exhibit different types of pathology, and also include stents and pacemakers. This dataset (including patients of different age, gender, and ethnicity) is also representative for the typical variability in cardiac anatomy, image quality, patient position and orientation. For each patient, we selected images reconstructed at the diastolic and/or systolic phase, depending on the availability of the data (Table 2.2). Images were reconstructed using either a smooth (b26f) or a sharp (b46f) kernel; the mean voxel size of this dataset is $0.33 \times 0.33 \times 0.4$ mm. A total of 1380 images were selected for our evaluation study.

Twenty Philips data sets (4 women, 16 men, aged 33-79 years) were acquired at the University Medical Center Utrecht (Utrecht, The Netherlands) with a Philips 64-slice (Brillance 64, Philips, Best, The Netherlands) or a 256-detector (iCT 256, Philips, Best, The Netherlands) CT scanner, between October 2009 and February 2010. Two patients had a pace-maker, five an artificial aortic valve and two an artificial mitral valve. The mean voxel size of the Philips data is 0.44x0.44x0.45 mm.

Twenty GE data sets were acquired at five different institutions: 1) Centre Cardiologie du Nord, Paris, France (12 images), 2) Atlantic Medical Imaging, Galloway, New Jersey, USA (4 images), 3) Froedtert Hospital, Milwaukee, Wisconsin, USA (2 images), 4) Sanatorium Hospital, Hong Kong, Hong Kong (2 images), and 5) Keio University Hospital, Tokyo, Japan (1 image). The data were all acquired with a 64-slice CT scanner (LightSpeed VCT, GE Healthcare, Buckinghamshire, UK) in 2005; age and gender information was not available. The mean voxel size of the GE data is $0.42 \times 0.42 \times 0.75$ mm.

In addition, as our method requires training images, in the present study, the eight training Siemens CTA data sets of the Rotterdam Coronary Artery Algorithm Evaluation Framework (Schaap et al., 2009a) were used. They are publicly available on *http://coronary.bigr.nl*. Five data sets were acquired with a 64-slice CT scanner and three data sets with a dual-source CT scanner (Sensation 64 and Somatom Definition, Siemens Medical Solutions, Forchheim, Germany). Diastolic reconstructions were used. Three data sets were reconstructed using a sharp (b46f) kernel; all others were reconstructed using a medium-to-smooth (b30f) kernel. The mean voxel size of the data sets is $0.32 \times 0.32 \times 0.4$ mm.

2.4 Method

Our method is a multi-atlas based segmentation approach: the following sections describe the atlas building, the multi-atlas segmentation, the underlying registration method and the optimization of the method parameters.

2.4.1 Atlas building

For each of the eight atlas images, manual segmentation of the seven cardiac structures was performed by a medical student (Observer 1), and was followed by a correction step performed by a radiologist. Using the same segmentation guidelines (cardiac anatomical definition), a second radiologist (Observer 2) annotated both the heart and the LV. The segmentations of the second radiologist were used to determine the inter-observer variability.

The structures were labeled according to the guidelines provided in Section 2.2. Contours were manually annotated on the three standard orthogonal views (axial, coronal and sagittal). The contour points were interpolated by computing a 3D implicit function (Turk and O'Brien, 1999) that describes a surface. The 3D implicit function was then converted into a binary mask.

The manual annotation was very time consuming, taking about 6 hours per dataset.

2.4.2 Multi-Atlas Segmentation

The patient's image to be segmented is denoted by $P(\mathbf{x})$. The method creates a labeled image $L(\mathbf{x})$ which defines the cardiac chambers of the patient.

The presented method follows the scheme of multi-atlas based segmentation methods (Rohlfing et al., 2004). Multi-atlas based segmentation requires a set of N atlas images $A_i(\mathbf{x})$, and their N corresponding labeled images $L_i(\mathbf{x})$, which are created by a human expert ($i \in [1,N]$). The segmentation of an image $P(\mathbf{x})$ is performed in three stages. Firstly, the patient image $P(\mathbf{x})$ is registered to all the images $A_i(\mathbf{x})$, using a non-rigid registration algorithm. This results in N transformations $\widehat{T}_{1,\ldots,N}$. The transformation $\widehat{T}_i$ is then applied to the label image $L_i(\mathbf{x})$. Finally, in the label fusion stage, the deformed labeled images $L_i(\widehat{T}_i(\mathbf{x}))$ are combined into a single segmentation L of the patient image. In this study, majority voting is used as label image fusion method.

2.4.3 Registration framework

Registration is used to spatially align an atlas image A_i and a patient's image P. This is achieved by applying a transformation T to A_i. The registration process is commonly expressed as an optimization problem:

$$\widehat{T} = \arg\max_{T} \mathscr{C}(P, A_i \circ T_i) \tag{2.1}$$

where $\mathscr{C}$ is a cost function that measures the similarity between the two images, and $\widehat{T}$ is the transformation that maximizes the similarity $\mathscr{C}$ of P and the deformed atlas $A_i \circ T_i$. Registration thus requires a similarity metric $\mathscr{C}$, a transformation model for T

and an optimization algorithm. Extensive reviews on the subject of image registration have been published (Brown, 1992; Maintz and Viergever, 1998; Lester and Arridge, 1999; Hill et al., 2001).

In this work, we apply a two-stage registration approach. First, the CTA images are registered using an affine transformation, to roughly align the two images. The affine registration result is then used as an initialization for a non-rigid registration using a B-spline transformation model. In both stages, a multi-resolution approach is adopted, in which the registration process starts with images that have lower complexity (smoothed and down-sampled). After aligning these images, the registration process continues with a higher resolution version. This is repeated up to the original image resolution. Two parameters have to be set to define this multi-resolution strategy: the number of resolutions and the image pyramid schedule, which defines the amount of blurring and down-sampling for each resolution level. A powers-of-2 pyramid schedule is used, and the optimal number of resolutions is determined experimentally (see following section). A similar multi-resolution approach is used for the B-spline control point grid, in which the grid resolution is doubled with every image resolution level. The B-spline control point spacing in the final resolution is a user-specified parameter; its optimal value is also experimentally determined.

For the cost function ($C(.)$ in Equation 2.1), we evaluated five intensity-based similarity metrics: sum of squared differences (SSD) (Thévenaz et al., 1998; Kybic and Unser, 2003), normalized cross correlation (NCC) (Studholme et al., 1996; Penney et al., 1998), mutual information (MI) Thévenaz and Unser (2000); Pluim et al. (2003), normalized mutual information (NMI) (Rohlfing et al., 2004) and localized mutual information (LMI) (Klein et al., 2008).

Minimization of the dissimilarity using a specific metric is performed using an iterative stochastic gradient descent optimizer Klein et al. (2009). This optimizer reduces computation time by computing the cost function on a randomly sampled subset of image voxels, newly selected in each iteration. The number of voxels sampled in each iteration is a user-specified parameter, and is set to 2048 as suggested in Klein et al. (2007) and Klein et al. (2009). The samples are not limited to voxel positions, which results in smoother cost functions Klein et al. (2010)Thévenaz and Unser (2008). A cubic B-spline interpolator is used to evaluate the image at non-voxel locations. Samples are selected from the entire image domain, except for the LMI cost function where all samples are selected from a small neighborhood, around a location that is randomly chosen in each iteration; see Klein et al. (2008) for details. The size of the (cubical) neighborhood is a user-specified parameter; its influence is investigated in the following section. The number of iterations performed by the stochastic gradient descent optimizer is set to 512 for the affine registration and 2048 for the B-spline registration.

The registration method is based on the Insight Segmentation Toolkit ITK (*http://www.itk.org*) and implemented using Elastix (Klein et al., 2010), a package for medical image registration publicly available on *http://elastix.isi.uu.nl*. All the segmentations were processed on the Dutch national computer cluster LISA (*http://www.sara.nl/*).

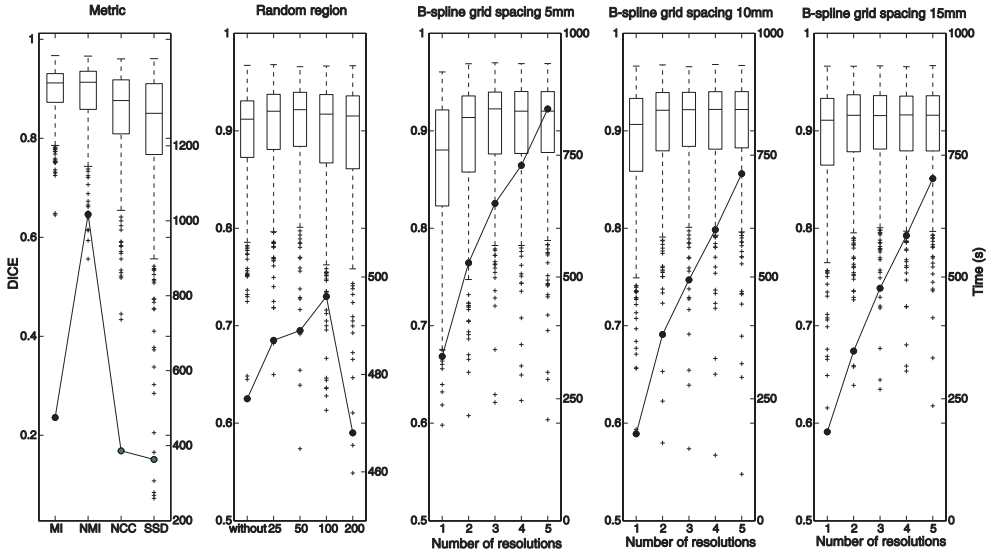

Figure 2.1: Optimization of registration parameters. Similarity measure and random sampling neighborhood size (left), number of resolutions / B-spline grid spacing (right). The line with dots represents the average time for one registration.

2.4.4 Parameter optimization

This section describes the optimization procedure for several important registration parameters.

First, all eight atlas images were registered to each other, which resulting in $8 \times 7 = 56$ registrations. Thus, for an image pair (A, B), both the forward $A \rightarrow B$ and inverse $B \rightarrow A$ registration were performed. The Dice coefficients (see Section 2.5.4 for a definition) of each pair of chamber segmentation after registration were computed, and the computation times were measured. The mean Dice coefficient of all 56 registrations, averaged over all 7 cardiac structures, was used as an optimization criterion to select proper values for the user-configurable registration parameters. Here, three parameters were optimized: 1) *the similarity measure* (MSD, NC, NMI, MI or LMI, where the size of the cubical neighborhood in LMI was chosen to be 25^3, 50^3, 100^3 or 200^3 mm; the localized sampling strategy was only applied in the non-rigid registration stage), 2) *the B-spline control point spacing in the final resolution* (5, 10 or 15 mm), and 3) *the number of resolutions* (1, 2, 3, 4, or 5). Finally, the performance of the method when varying the number of atlases was evaluated.

Similarity measure: To determine the best performing similarity measure, the other user-configurable parameters were fixed. A three-level multi-resolution strategy with a powers-of-2 pyramid schedule and a B-spline control point spacing of 10 mm in the final resolution level was used. The results of the similarity measure optimization are presented in Figure 2.1 (left box plot). For our application, even if both the patient and

atlas images were from the same modality, SSD achieved poor results, mainly because of the non-equal intensity distribution due to difference in contrast enhancement over the data. NCC, which assumes a linear relation between the intensity values of the image, improved the results. However, MI and NMI, which only assume a relation between the probability distributions of the intensities of the images, outperformed the previous metrics. Comparison of MI with LMI demonstrated that the LMI similarity measure gives better registration results, with an optimal neighborhood size of 50^3 mm.

B-spline control point spacing and number of resolutions: For the last 15 pilot experiments, the similarity measure was fixed to LMI with a neighborhood size of 50^3 mm, and both the B-spline control point spacing and the number of resolutions were tuned simultaneously, as they might be related. Figure 2.1 (three right-hand box plots) shows the results obtained when using one to five resolutions, and different B-spline control point spacings. It shows that a three-level multi-resolution strategy, with a B-spline control point spacing of $10 \times 4 = 40$ mm at the lowest resolution , 20 mm at the next resolution, and 10 mm in the final resolution level, gives the best results.
It should be noted that we cannot claim to have found the optimum parameter settings, since we did not perform a complete, exhaustive search on the parameter space (evaluating all possible combinations of similarity metric, multi-resolution strategy, and B-spline control point spacing). The results in Figure 2.1 suggest that the parameters are near optimal for our set of data. Optimizing the registration parameters using another set of atlas images (e.g. different modality or different anatomical region) may lead to different results.

Number of atlases: Figure 2.2 presents a plot of the method performance (in terms of overlap) as a function of the number of atlases: results of all unique atlas combinations, using voting strategy, are presented in the left box plot and results using combined ranked atlases are presented in the right one. For the right figure, the atlases were ranked based on their overlap value with the reference standard (i.e. the manual segmentation), which we use as a measure for the registration success. The plots clearly suggest that the segmentation accuracy improves very little after using, in both cases, approximately five atlases, all structures taken together. In general, when using suitable atlas selection criteria, a lower optimal number of atlases is achieved, compared to random atlas selection. However, in our experiment, the advantage of using an atlas selection criterion does not show clearly: the optimal number of atlases determined using a selection criterion is equal to the optimal number obtained using random atlas selection. This might be explained by the limited number of atlases available. Recently, Aljabar et al. (2009) investigated the effect of atlas selection on brain structure segmentation accuracy. Using an image-based similarity criterion as well as an age-based atlas selection criterion, they demonstrated that atlas selection can be beneficial, if a large number of atlases is available. Thus, using a larger set of atlases and an appropriate selection criterion might help to get a lower optimal number of atlases. In the remaining experiments, we will use the eight atlases available.

A package for cardiac segmentation using our method is publicly available and can be downloaded on *http://www.bigr.nl/heartin3d*. It contains the executable to run atlas registration on a Linux 64 bit, a Windows 32 bit or a Windows 64 bit machine, the Elastix parameter files, the atlas images and their labeled images.

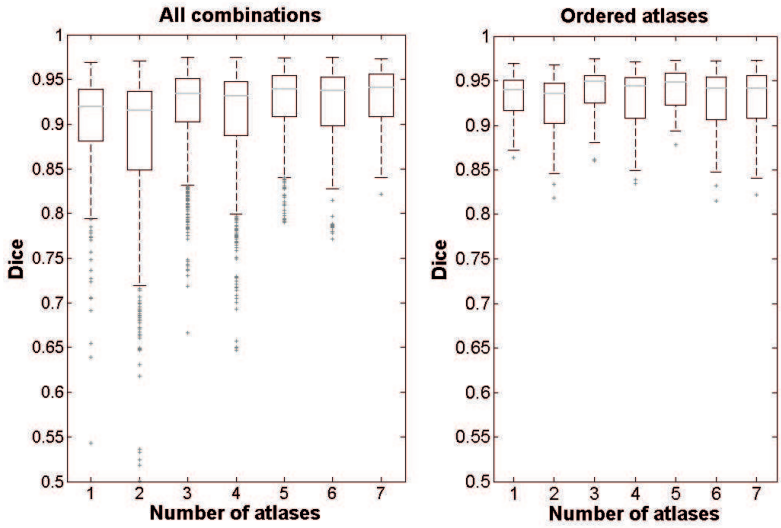

Figure 2.2: Cardiac segmentation method performance (in terms of overlap averaged over all cardiac structures) as a function of the number of atlases. All unique combinations of atlases (left); combination of ranked atlases (right). Majority voting was used as a combination strategy.

2.5 Experiments: multi-center / multi-vendor evaluation

Both quantitative and qualitative evaluations were conducted to assess the performance of the method. The quantitative evaluation provides an objective evaluation of the method and enables comparison with previously published methods. However, comparison with results in literature should always be done with care, as results have been obtained on different data sets. A limitation of quantitative evaluation is that it requires a set of manually annotated structures, which is time consuming and not feasible for large numbers of 3D data. Therefore, we also conducted qualitative evaluations, as they can be performed in less time and hence on a larger number of data. The quantitative and qualitative evaluation measures used in this work are introduced in Section 2.5.4.

2.5.1 Experiment I: Eight cases leave-one-out study

The first experiment was a leave-one-out test, using the eight atlas data sets. For each patient, the atlas set thus consisted of the seven remaining atlases. Since the manual segmentations of the chambers are available in this experiment, a 3D quantitative analysis was performed and the metrics defined in Section 2.5.4 were computed. As second-observer manual annotations were available for the heart, epicardium and endocardium, inter-observer variability was computed for these three structures. Note that, in the previous section, the same images were used to tune the registration method. However, in that section, the label fusion step was omitted and only the average quality of all pair-wise registrations was measured.

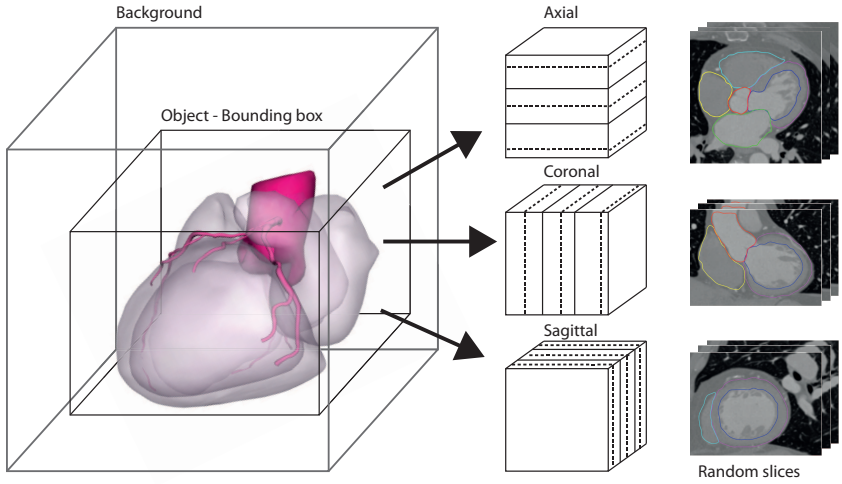

Figure 2.3: 2D quantitative evaluation. Random slice selection. A bounding box containing the object is calculated. This box is then divided into three sub-regions, in one direction (axial, sagittal or coronal), and one slice is randomly selected in each sub-region. This process is repeated for each of the three directions.

2.5.2 Experiment II: multi-center/multi-vendor study

In the second experiment, we investigated the accuracy of the method when applied to images acquired with scanners from different vendors and at different centers. Twenty images from Siemens, GE and Philips scanners were used. Since no manual segmentations were available for these data sets, a 2D quantitative evaluation was performed. For each dataset, contours were drawn by an expert on 9 randomly selected slices (Figure 2.3), on the 3 orthogonal directions (axial, sagittal, coronal). The quality of the segmentation was also assessed qualitatively by inspecting the 3D volumes and assigning a grade (Table 2.3).

2.5.3 Experiment III: large-scale study

In the third experiment, we investigate the robustness of our method against variations in heart anatomy (size, shape, and orientation), pathology, and scan parameters (diastolic/systolic phase, reconstruction kernel). The performance of our method was evaluated on a large, clinically representative set of CTA images: 1380 Siemens images were segmented with our multi-atlas based approach. First, a subset of 100 data sets was selected: 50 scans of the diastolic (respectively, systolic) phase, reconstructed with a smooth kernel (25 scans) and with a sharp kernel (25 scans) were randomly selected from our database. A double reader 2D and 3D qualitative evaluation was performed to assess the inter-observer variability in the grade classification. The 2D qualitative evaluation consisted of visually checking three 2D slices for each orthogonal direction (axial, coronal, sagittal), for each of the 7 segmented structures. The slices were selected

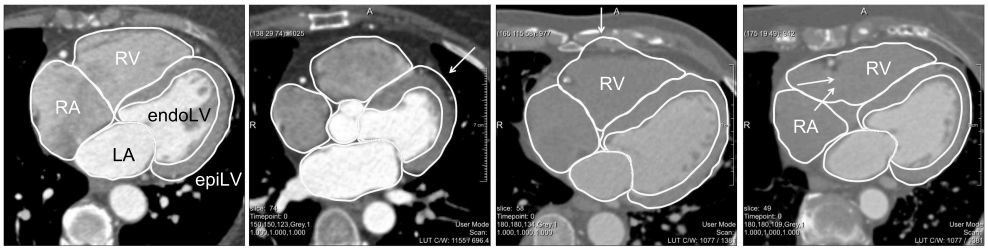

Figure 2.4: Cardiac segmentation grade classification. Examples: From left to right: grade 1 (deviation up to 1 mm), grade 2 (one region deviates up to 3 mm), grade 3 (one region deviates up to 1 cm), grade 4 (up to 50% has been incorrectly segmented).

randomly from the bounding-box containing the segmented object (as explained in Figure 2.3). Then, the same 2D qualitative evaluation was conducted on the entire set of 1380 images.

2.5.4 Evaluation measures

For the quantitative evaluation, a number of commonly applied evaluation metrics were used. The automatic segmentations S were compared to the reference standard M by computing:

- the Dice similarity coefficient $DSC = \frac{2|M \cap S|}{|M|+|S|}$
- the mean surface-to-surface distance between segmented surface S and reference standard M, and the standard deviation.
- the lower quartile (Q1), median and upper quartile (Q3) of the shortest surface-to-surface distance.
- the directed Hausdorff distance, from surface S to surface M.

In this work, we used the term *qualitative* evaluation to refer to the visual grade classification, in which the *quality* of the segmentation is ranked. We used a segmentation quality grade classification based on regional segmentation accuracy, as proposed by Abadi et al. (2009). The grades are listed in Table 2.3, and examples are shown in Figure 2.4. Table 2.4 gives an overview of the evaluations performed.

2.6 Results

2.6.1 Experiment I: Eight cases leave-one-out study

Tables 2.5 presents results of the fully-automatic cardiac 3D quantitative evaluation of the segmentation on the atlas images. A mean segmentation error of 0.94 ± 1.12 mm and an average Dice coefficient of 0.93 were obtained. Furthermore, Table 2.6 shows the mean and standard deviation of the shortest distance between the automatic segmentation

Table 2.3: Qualitative evaluation. Segmentation quality grade classification, published in Abadi et al. (2009). For each cardiac structure a separate grade is assigned. The term 'region' employed here refers to a certain part of a cardiac structure.

Grade	Description
1	Very accurate: Deviation up to 1mm
2	Most regions accurate: 1 or 2 regions may deviate up to 3mm
3	Most regions accurate: 1 region may deviate up to 1cm or more than 2 regions may deviate up to 3mm
4	A significant region (up to 50%) has not been segmented or has been incorrectly segmented
5	Segmentation failed

Table 2.4: Overview of the quantitative and qualitative evaluation. [a] see Section 2.6.1, [b] see Section 2.6.2 and [c] see Section 2.6.3 for more details.

		Quantitative		**Qualitative**	
Vendor	N	2D	3D	2D	3D
SIEMENS	8	-	Obs 1&2[a]	-	-
	20	Obs1[b]	-	Obs 1&2[c]	Obs 1&2[b,c]
	80	-	-	Obs 1&2[c]	Obs 1&2[c]
	1280	-	-	Obs2[c]	-
PHILIPS	20	Obs1[b]	-	-	Obs1[b]
GE	20	Obs1[b]	-	-	Obs1[b]

and reference standard (Automatic vs. Observer 1), between the automatically obtained and radiologist segmentations (Automatic vs. Observer 2), and also the inter-observer variability (Observer 1 vs. Observer 2). It shows that the error between the automatic and the reference standard is either close to (heart) or smaller than (endoLV) the inter-observer variability. Visual inspection revealed that most segmentation errors occurred at the valves and near the apex.

2.6.2 Experiment II: multi-center/multi-vendor study

Table 2.7 gives the results of the 2D quantitative evaluation and Figure 2.5 presents the results of the 3D qualitative evaluation. In general, the method performs better on Siemens data, followed by Philips data, and GE data. This may be explained by differences in scanner hardware or acquisition protocol. Also, the atlas images were acquired on a Siemens scanner, which may explain the slightly better results obtained on the Siemens data. Segmentations of the Philips data obtained a similar qualitative grade classification as the Siemens data, but the quantitative results were somewhat lower (1.30±1.32 mm for Philips data, 1.00±1.06 mm for Siemens data).

Table 2.5: Experiment I : 8 cases leave-one-out study. Dice coefficient, mean surface-to-surface distance ± standard deviation, median, first quartile (Q1), third quartile (Q3), maximum distance (max). Distances are in millimeters (mm).

Structure	Dice	Mean ± stdev	Median	Q1	Q3	Max
Heart	0.96	0.99±1.25	0.72	0.30	1.69	9.20
epiLV	0.95	1.04±1.15	0.87	0.37	1.75	7.55
endoLV	0.95	0.62±0.63	0.60	0.35	1.08	4.92
RV	0.90	1.40±1.47	1.18	0.54	2.26	9.94
LA	0.94	0.66±0.84	0.53	0.29	1.06	6.77
RA	0.89	1.44±1.88	1.03	0.44	2.21	12.13
Ao	0.94	0.44±0.56	0.41	0.03	0.77	4.10

Table 2.6: Experiment I : 8 cases leave-one-out study. Distances in millimeters (mm). Mean surface-to-surface distance ± standard deviation between automatic segmentation and reference standard (Auto/Obs1), between automatic segmentation and the second observer annotations (Auto/Obs2). For the inter-observer variability (Obs1/Obs2), the mean surface-to-surface distance ± standard deviation, the median, first quartile (Q1), third quartile (Q3) and maximum distance (max) are provided. The atlas images were manually segmented by Observer 1.

	Auto/Obs1	Auto/Obs2	Obs1/Obs2				
Structure	**mean ± stdev**	**mean ± stdev**	**mean ± stdev**	**median**	**Q1**	**Q3**	**max**
Heart	0.99±1.25	1.08±1.34	0.80±1.24	0.84	0.46	1.65	12.43
epiLV	1.04±1.15	0.98±1.12	0.75±0.90	0.82	0.57	1.58	7.68
endoLV	0.62±0.63	0.66±0.84	0.89±0.86	0.91	0.33	1.14	4.74

2.6.3 Experiment III: large-scale study

Table 2.8 & 2.9 present the results of the 2D and 3D qualitative evaluation performed on a subset of 100 from the 1380 data sets, in the form of confusion matrices. The observers agreed on the grade in 77% (2D) and 65% (3D) of the cases, and when observers disagreed, the difference in grading was never superior to one. From these results, we conclude that the grade classification is sufficiently objective and not affected by observer bias. It can be seen that raters had more trouble distinguishing between grade 1 and 2.

The results per structure are presented in Figure 2.6 and compared with the evaluation by Abadi et al. (2009). There, the authors performed segmentation of the cardiac structures using the model-based algorithm developed by Ecabert et al. (2008). Using our method, the quality of the segmentation was in most cases highly accurate (grade 1 and 2). While there were only two complete segmentation failures (grade 5), we did observe that errors occurred at the apex (where the contrast with surrounding tissues is poor), at the valves and near the pulmonary artery bifurcations (where shape and position vary significantly between patients). Overestimates were mainly due to inclusion of

Table 2.7: Experiment II: multi-center/multi-vendor study. 2D quantitative evaluation. For each image, cardiac contours are drawn by an expert on 5 randomly selected 2D slices (See Figure 2.3)), on axial, sagittal and coronal view. Comparison with the automatic segmentation: Dice coefficient, mean surface-to-surface distance ś standard deviation (in millimeters).

		N	Heart	epiLV	endoLV	RV	LA	RA	Ao	Mean
Dice	**SIEMENS**	20	0.93	0.94	0.94	0.89	0.94	0.89	0.92	0.92
	PHILIPS	20	0.91	0.91	0.92	0.90	0.91	0.88	0.91	0.90
	GE	20	0.89	0.91	0.92	0.87	0.88	0.86	0.89	0.89
Distance	**SIEMENS**	20	0.83±0.85	1.02±0.97	0.89±0.95	1.28±1.17	0.93±0.91	1.23±1.20	0.83±1.35	1.00±1.06
	PHILIPS	20	1.23±1.19	1.28±1.48	1.21±1.10	1.43±1.46	1.09±1.05	1.70±1.58	1.22±1.19	1.30±1.32
	GE	20	1.39±1.25	1.57±1.46	1.31±1.06	1.51±1.49	1.54±1.35	1.69±1.61	1.49±1.35	1.50±1.37

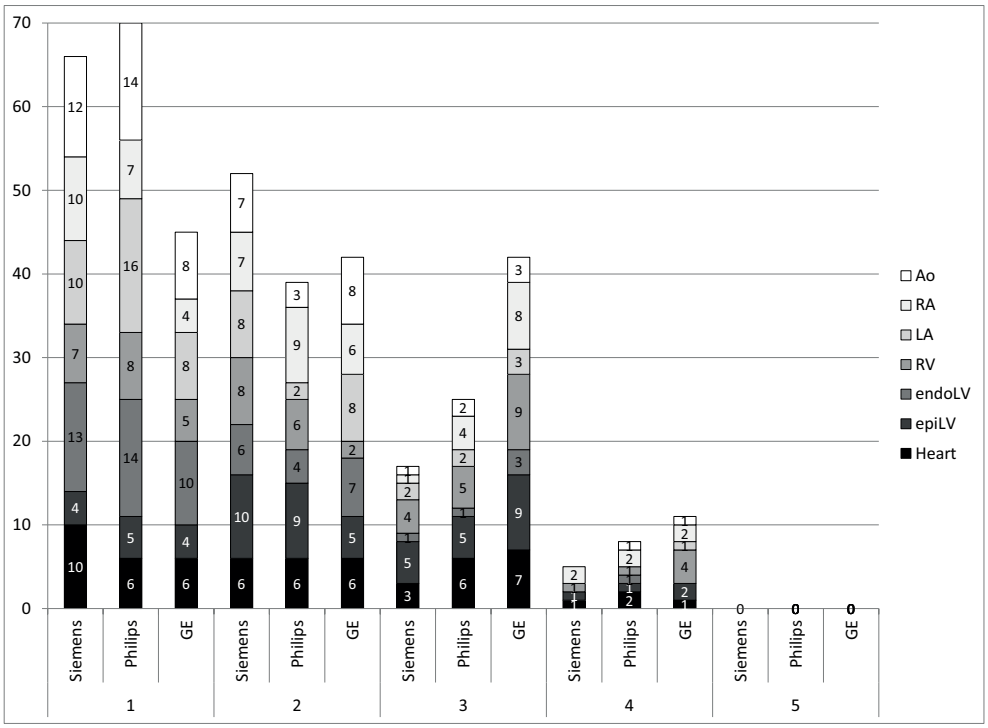

Figure 2.5: Experiment II: multi-center/multi-vendor study. 3D qualitative evaluation. Segmentations of the seven structures were visually checked by Obs1 and a grade was assigned (Table 2.3). Twenty patients were included per vendor. The numbers indicated in the bars correspond to the number of patient for who the segmentation of the structure has been assigned the grade.

Table 2.8: Experiment III: large-scale study. 2D qualitative evaluation on 100 CTA data sets. Segmentations of the seven structures were visually checked in the three orthogonal views (axial, sagittal & coronal) by two observers (Obs1 & Obs2), and a grade was assigned (Table 2.3).

		Obs2				
	Grade	**1**	**2**	**3**	**4**	**5**
Obs1	**1**	48.6%	4.3%	0%	0%	0%
	2	9.9%	16.7%	4.0%	0%	0%
	3	0%	3.0%	7.6%	0.8%	0%
	4	0%	0%	0.2%	4.3%	0%
	5	0%	0%	0%	0%	0.6%

pericardial fat as a part of the myocardium. Figure 2.10 shows examples of automatic cardiac segmentations.

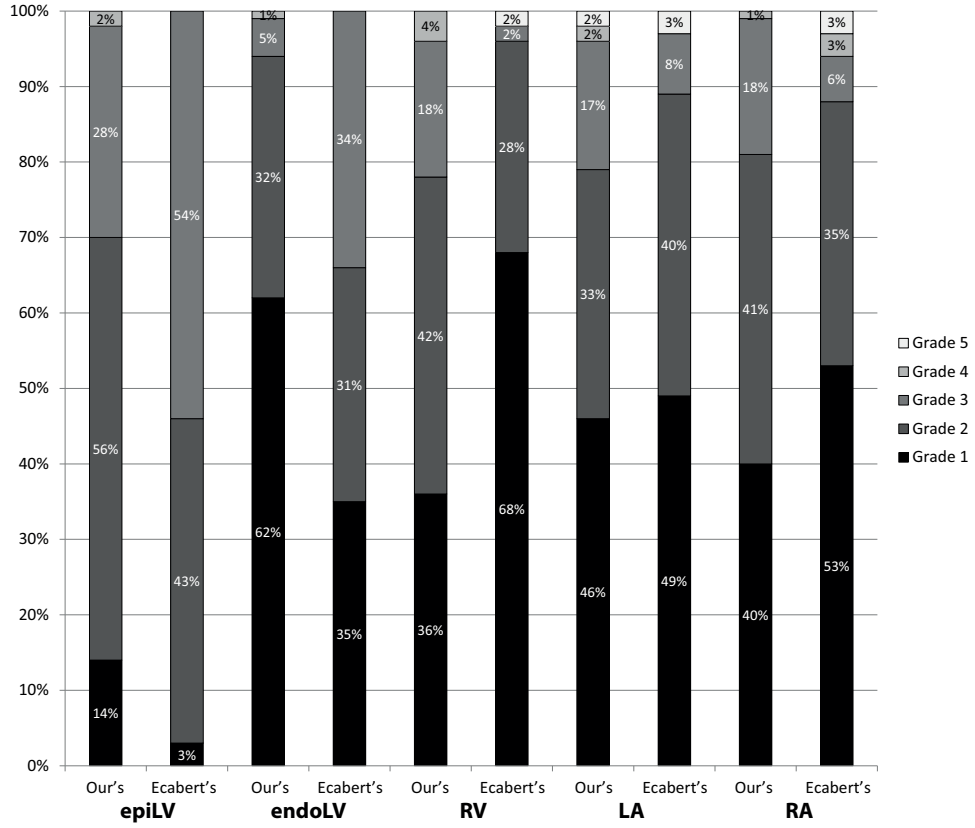

Figure 2.6: Experiment III: large-scale study. 3D qualitative evaluation, based on the grade classification outlined in Table 2.3. Both our method (left) and the method of Ecabert *et al.* (right) were evaluated on a set of 100 images. Results obtained with the segmentation technique of Ecabert et al. (2008) were taken from the work of Abadi et al. (2009). Care should be taken when comparing the results, as the two studies were performed using different data sets.

Figure 2.7 presents the results of the 2D qualitative evaluation for the complete set of 1380 images. It shows that 49% of the segmentations were very accurate (grade 1, error below < 1 mm) and that 29% were considered accurate (grade 2, error between 1 and 3 mm). The failure rate was 1%. Segmentation failures occurred when the cardiac morphology in the target image differed significantly from the atlas images. This happened, for instance, when the patient had congenital heart disease (transposition of great vessel), left pneumonectomy (unusual location and shape of the heart), or an aortic aneurysm (see Figure 2.9). In the latter case, the aorta was as large as the atria. As our method utilizes prior knowledge of cardiac anatomy and searches for a structure that is similar in shape, size, and appearance, it is not possible to segment such images correctly.

Additionally, a comparison of the method's performance as a function of reconstruction time point (diastole or systole) was performed; results are presented in Figure 2.8.

Table 2.9: Experiment III: large-scale study. 3D qualitative evaluation on 100 CTA data sets. Segmentations of the seven structures were visually checked by two observers (Obs1 & Obs2), and a grade was assigned (Table 2.3).

		Obs2				
	Grade	**1**	**2**	**3**	**4**	**5**
	1	30.0%	12.5%	0%	0%	0%
	2	9.0%	22.6%	7.0%	0%	0%
Obs1	**3**	0%	3.1%	8.8%	1.7%	0%
	4	0%	0%	1.5%	3.4%	0.1%
	5	0%	0%	0%	0%	0.3%

Generally, the method performs better on diastolic images, which can be explained by the fact that the atlas images were also diastolic reconstructions. By comparing diastolic and systolic results, it appears that the percentage of segmentations classified as grade 1 decreases (except for the aorta) while the percentage of cases graded in class 3 and 4 increases. The percentage of segmentations classified as grade 2 depends on the structure, and the percentage of segmentations classified as grade 5 is equal in both cases.

2.7 Discussion

2.7.1 Previous work

Table 2.10 lists our results and the results of the model-based approach of Ecabert et al. (2008) and of the machine learning approach of Zheng et al. (2008). It should be noted that all evaluations were performed on different data sets, thus care should be taking when comparing these studies directly, due to potential differences in manual segmentations and datasets (acquisition protocols, scanner). Also, both contrast and resolution vary with the acquisition protocol and scanner hard- and software. Only a comparative study using the same set of training and testing data would allow an objective evaluation of different cardiac segmentation methods. Our evaluation was performed with images from eight patients, acquired with either a 64-slice or a dual-source CT scanner (Sensation 64 and Somatom Definition, Siemens Medical Solutions, Forchheim, Germany). The results of Zheng *et al.* were obtained using images of 186 patients, acquired with the same two Siemens scanners, at different institutions; the results of Ecabert *et al.* were obtained using images from 13 patients, acquired with a 16, a 40 or a 64-slice CT scanner (Brillance CT, Philips Medical Systems, Cleveland, OH). The main conclusion that can be derived from Table 2.10 is that our level of accuracy is in the same order of magnitude as that of previously published methods. In general, our method achieves better results for the aorta, left atria and ventricle. It is indeed more challenging to delineate the right cardiac chambers. In fact, the visibility of the edges, for instance at the ventricular septal wall and at the valves planes (tricuspid and pulmonary), considerably varies depending on the amount of contrast enhancement in the chambers.

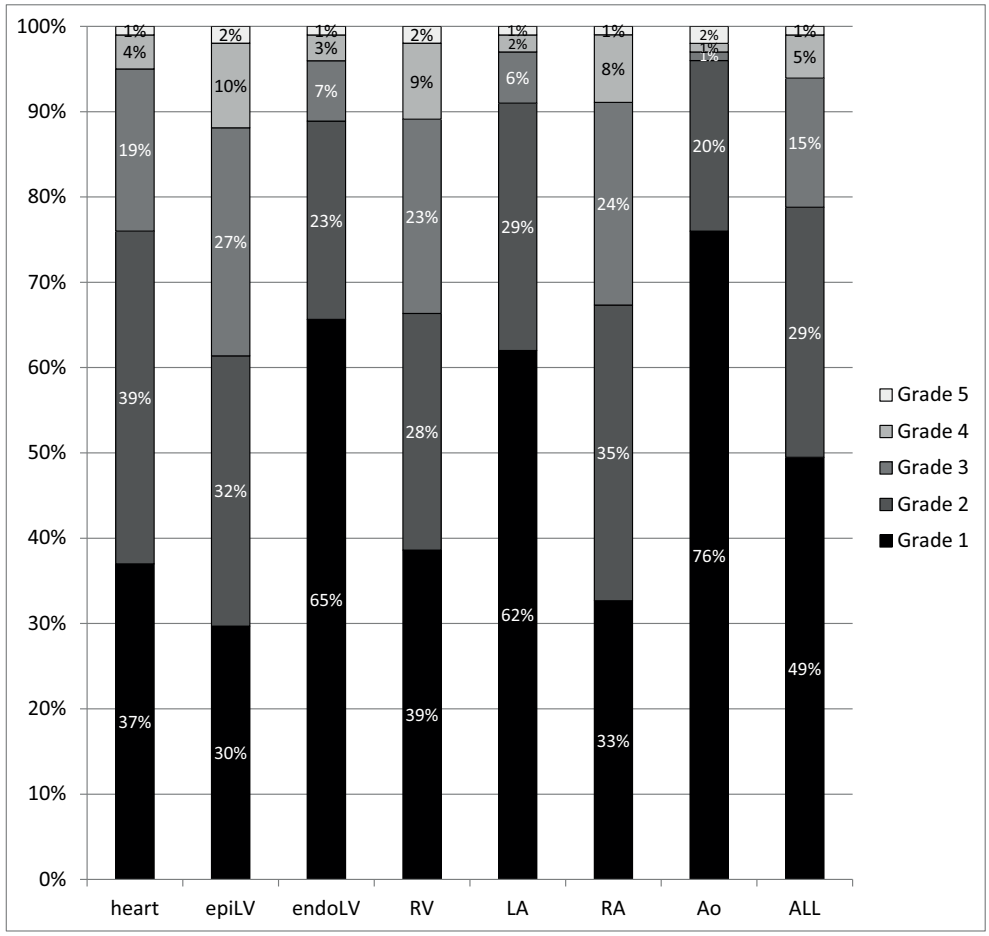

Figure 2.7: Experiment III: large-scale evaluation study. 2D qualitative evaluation on 1380 CTA data sets. Segmentations of the seven structures were visually checked in three orthogonal views (axial, coronal and sagittal), and a grade was assigned (Table 2.3).

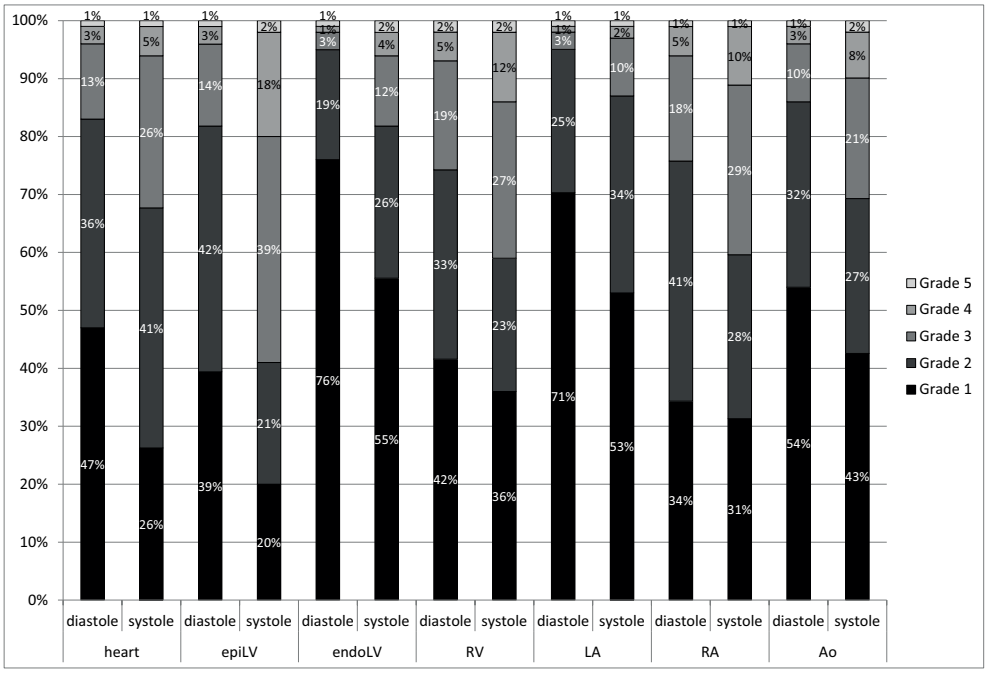

Figure 2.8: Experiment III: large-scale evaluation study. 2D qualitative evaluation on 1380 CTA data sets. Comparison of the grade classification evaluation for diastolic and systolic images.

Figure 2.9: Experiment III: large-scale evaluation study. Examples of abnormal hearts. From left to right: left pneumonectomy, aortic aneurysm and congenital heart disease (transposition of great vessels).

2.7.2 Computation time

For clinical application, computation time is an important issue that has to be taken into account. Multi-atlas based segmentation can be time consuming, especially when using a large number of atlases. In our work, five segmentations could run simultaneously on a node of the LISA computing cluster. Each of these nodes is composed of 8 CPU cores (2 quad-core processors Intel® Xeon™ 3.4 GHz, EM64T, 800 MHz FSB, 4GB memory), with a total of 24GB of memory. The complete processing of these five scans (eight registrations, eight labeled image propagations and one fusion per segmentation) took around 100 minutes. Therefore, the segmentation of one image can effectively be done in 20 minutes on a single 8-core machine. Computational time could be reduced by implementing (part of) the registration algorithm on a GPU.

2.7.3 Atlas selection and combination

Our method uses all eight atlases which were available to us, and the deformed segmentations are combined using a straightforward majority voting rule. Several novel atlas selection and atlas combination rules have recently been proposed (Isğum et al., 2009; Aljabar et al., 2009; van Rikxoort et al., 2010; Sabuncu et al., 2010; Sdika, 2010). However, there is no ideal combination strategy; for each particular application, the best combination strategy has to be determined and a trade-off needs to be made between accuracy and computational costs.

In general, atlas selection can be helpful when a large number of atlases is available, to reduce the computational cost while maintaining accuracy. For brain image segmentation, Aljabar et al. (2009) demonstrated that, using suitable atlas selection criteria (e.g. image-based and age-based), a lower optimal number of atlases was achieved compared to random atlas selection. In our case, only eight atlases were available. We presented in Section 2.4.4 plots showing the accuracy (in terms of overlap) as a function of the number of atlases used, for both random selection and ranked selection cases. The results suggested that the segmentation accuracy improves very little after using approximately five atlases. Atlas selection did not improve the results consistently, even though we used a near-optimal atlas selection criterion based on overlap with the reference standard manual segmentation (which would in practice of course not be possible).

Although the majority voting procedure achieves good results for cardiac segmentation, several novel combination rules may be used to further improve our segmentation results. Whereas Artaechevarria et al. (2009) demonstrated that no combination algorithm is consistently better than the others for all images and all regions within the images, local weighting generally improved their segmentation results (except in low contrast regions). Recently, Sabuncu et al. (2010) compared different label fusion algorithms. Their results demonstrated that local weighted fusion algorithms yield better segmentations than global ones, and that weighted label fusion methods perform significantly better than majority voting. Also, Sdika (2010) recently proposed a new framework in which atlas accuracy maps are generated by combining, using a nearest neighbor transform, atlas-based segmented images and intensity classification images. The accuracy maps reflect the performances of the atlases. Accuracy map values were

then used as weights in the voting procedure, giving a higher weight to atlases that (locally) perform better. However, it should be noted that all these novel combinations rules were evaluated for a different problem than ours, namely brain segmentation, and that segmentation results were enhanced mainly in regions with complex shapes such as the cortex. In future work, it would be interesting to investigate whether or not these new voting procedures improve CTA cardiac segmentation.

For a related problem to ours, namely chest CT heart segmentation, an atlas selection and combination rule, called adaptive (local) multi-atlas segmentation (AMAS/ALMAS), was proposed by van Rikxoort et al. (2010). In their work, atlas selection is based on the difference image after affine registration: 1) an affine registration is performed with each atlas available and the target image, 2) the similarity between the deformed atlas image and the target image is subsequently computed, by calculating the absolute voxel-wise difference image, and 3) the atlases with the highest similarity are selected for further non-rigid registration, up to the point that the disagreement between the propagated labels gets above a certain user-defined threshold. The same majority voting combination strategy as ours was used to combine the automatically selected atlases. When applied to chest CT heart segmentation, ALMAS achieved the same performance as a conventional multi-atlas method, but with a lower computational cost. The approach could be of interest to our application, in order to reduce computation time, but since our method is fully automatic and already relatively fast, we did not further investigate this.

An interesting idea to improve segmentation accuracy was recently presented by Wolz et al. (2010). They proposed to automatically propagate a relatively small set of manually labeled atlases to a larger set of unlabeled images, through a succession of multi-atlas segmentations of similarly looking images. Thus, the problem of registering images that are very dissimilar is broken down into a problem of registering a series of images that are similar. The disadvantage of the approach is the introduction of user-configurable parameters, such as the number of closest unlabeled images used for propagation and the number of closest labeled images used for each application of multi-atlas segmentation. Nevertheless, it would be interesting to apply the proposed method for our particular application, given our eight available atlases and our large database of CTA scans.

2.7.4 Extraction of functional information and other possible application

Our evaluation study focused on the accuracy and robustness of atlas-based cardiac chambers segmentation, which is a prerequisite for targeted visualization and analysis of functional information. We did not explicitly evaluate whether our segmentation method allows accurate extraction of functional information from dynamic CTA data. However, Abadi et al. (2009) showed that, if a robust cardiac segmentation method is provided, chamber and myocardial volumes derived from the segmentation results give reliable functional measurements. Thus, based on our results and the work of Abadi et al. (2009), we conclude that derivation of functional parameters should be possible using our segmentation method.

In future work, we will investigate possible relations between cardiac chamber characteristics (e.g. morphology and dynamics) and metadata (e.g. sex, age, risk factors and clinical outcomes).

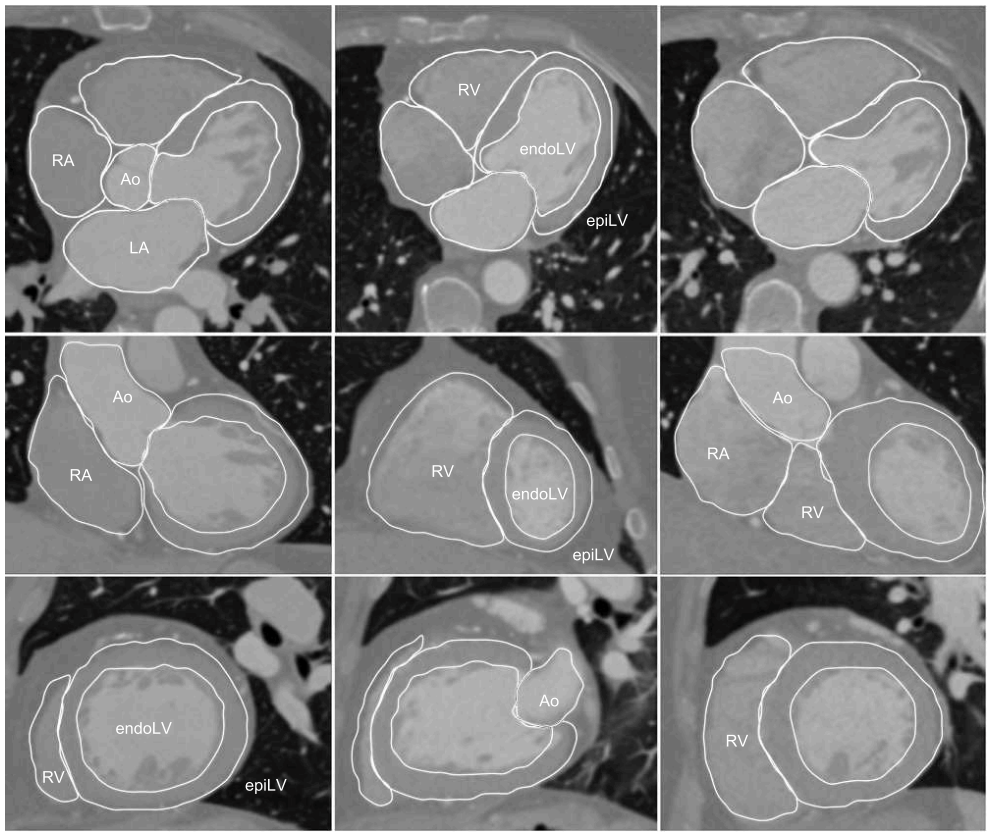

Figure 2.10: Fully automatic cardiac segmentation results from three patients out of the 1380 CTA data sets. Axial view (top), coronal view (middle) and sagittal view (bottom).

2.8 Conclusion

We have presented and evaluated a fully automatic multi-atlas based method for whole heart and cardiac chamber segmentation on CTA data routinely acquired for clinical diagnosis and follow-up of patients with (suspected) cardiac problems. Through quantitative and qualitative evaluations on multi-vendor/multi-center data sets, we demonstrated that robust and accurate automatic cardiac segmentation can be achieved. Since the accuracy is close to the inter-observer variability and the success rate is high, the automatic cardiac segmentation method might be used to extract functional information from CTA data. The complete segmentation pipeline, including the labeled atlas images, is publicly available and can thus be utilized by other researchers.

Table 2.10: CTA cardiac segmentation error measures reported in different papers. Mean surface-to-surface distance ± standard deviation. Distances are in millimeters (mm). Note: all studies were performed using different data sets; thus, it is not possible to compare the results directly due to potential differences in manual segmentations, acquisition protocols, and scanner hard- and software.

	Patients	Heart	EpiLV	EndoLV	RV	LA	RA	Ao
Our method	8	0.99±1.25	1.04±1.15	0.62±0.63	1.40±1.47	0.66±0.84	1.44±1.88	0.44±0.56
Ecabert et al. (2008)	13	0.82±1.00	0.82±1.07	0.98±1.32	0.84±0.94	0.71±0.88	0.89±0.96	0.74±0.89
Zheng et al. (2008)	186	-	1.21±0.41	1.13±0.55	1.55±0.38s	1.32±0.42	1.57±0.48	-

chapter 3

Automatic coronary artery stenoses detection and quantification in Computed Tomography Angiography

This chapter is based on the manuscript:
Automatic Detection and Quantification of Coronary Artery Stenoses using Contrast Enhanced Cardiac CT Scans,
R. Shahzad*, **H.A. Kirişli***, C. Metz, H. Tang, M. Schaap, W.J. Niessen, L. van Vliet and T. van Walsum
** both authors contributed equally to this research*,
Submitted, 2013.

Abstract

Purpose Accurate detection and quantification of coronary artery stenoses are essential requirements for treatment planning of patients with suspected coronary artery diseases. In this chapter, we developed and evaluated a method to automatically detect and quantify coronary artery stenoses in CTA images.
Methods First, centerlines are extracted using a two-point minimum cost path approach and subsequently refined, to avoid crossing calcified plaques. The extracted coronary tree is then splitted into individual segment, and the resulting centerlines are used as an initialization for the lumen segmentation, performed using graph cuts and robust kernel regression. Finally, the expected diameter of the healthy lumen is estimated by applying robust kernel regression on the coronary artery lumen diameter profile. Stenoses are subsequently detected and quantified by computing the difference between estimated and expected diameter profiles.
Results We evaluated our method using the data provided in the Rotterdam Coronary Artery Algorithm Evaluation Framework (*http://coronary.bigr.nl/stenoses*). The evaluation on 30 datasets showed, for the detection, a sensitivity of 29% and a PPV of 24% as compared to QCA, and a sensitivity of 21% and a PPV of 23% as compared to manual assessment on CTA. The stenosis degree was estimated with an absolute average difference of 31% when compared to QCA, and a weighted κ value of 0.29 when compared to CTA. A Dice of 68% and 65% was reported for lumen segmentation of healthy and diseased vessel segments respectively. According to the ranking of the evaluation framework, our method finished fifth for detection, second for quantification and second for segmentation.
Conclusions Coronary artery lumen can be automatically segmented with a precision similar to the expert's one, but detection and quantification of coronary artery stenosis is still a unsolved problem; discrimination between significant and non-significant lesions remains a challenge.

3.1 Introduction

Coronary artery disease (CAD) is a major cause of death worldwide (Roger et al., 2012). CAD induces plaque build up in the coronary arteries, which may cause luminal narrowing, also known as *stenosis*. As stenoses may induce myocardial infarction, it is crucial to detect CAD at an early stage.

Many tests are available to detect CAD (Fayad and Fuster, 2001). At present, invasive coronary angiography (ICA) is the gold standard imaging technique for diagnosing CAD and quantitative coronary angiography (QCA) is used to quantify the degree of stenosis. However, ICA is an invasive procedure and is of projective nature. Computed tomography coronary angiography (CTA), on the other hand, is increasingly used to access CAD and has the advantage over ICA of being less invasive and of providing high resolution 3-dimentional (3D) images of the coronary arteries. In addition to the detection and quantification of coronary stenoses, CTA also provides information regarding the type of plaque (calcified, mixed or soft). However, interpreting CTA images for the purpose of stenoses detection requires considerable experience (Pugliese et al., 2009), and is a tedious task.

Consequently, since few years, the number of publications presenting and/or evaluating (semi-) automatic coronary artery stenosis detection and quantification techniques in cardiac CTA datasets is growing, and an evaluation framework dedicated to this problem has been introduced in 2012 (Chapter 4 of this thesis).

In this study, we present an automatic method for coronary artery stenoses detection, quantification and lumen segmentation, aiming at facilitating and supporting the interpretation of CTA by the radiologists. The method has been evaluated using the publicly available datasets provided by the Rotterdam Coronary Artery Algorithm Evaluation Framework (*http://coronary.bigr.nl/stenoses*).

3.2 Materials

Forty-eight multi-center multi-vendor datasets were used for this study. The datasets were obtained from the publicly available Rotterdam Coronary Artery Algorithm Evaluation Framework (*http://coronary.bigr.nl/stenoses/*). Datasets are distributed over five calcium score categories such that the distribution is representative of the population undergoing CTA examination in clinical practice (Nieman et al., 2009): no calcium (11 patients), between 0.1 and 10 (6 patients), between 11 and 100 (14 patients), between 101 and 400 (11 patients), and above 400 Agatston score (6 patients). The population contains 30 males (63%), and the patients age $58.76 \pm 8.71[41;80]$ years. Both CTA and ICA examinations were performed, thus, two reference standards are available: CTA consensus reading and QCA analysis of the angiograms. Eighteen of the 48 CTA images, together with the CTA and QCA reference standards, are made available for training; the remaining thirty datasets are used for testing the algorithms; for those, only the CTA images are made available.

For additional information about the image acquisition, data selection and reference standards, the reader may refer to Chapter 4 of this thesis, or to the framework website.

3.3 Method

3.3.1 Centerline Extraction

First, for each branch of the coronary artery tree, an initial centerline is obtained, by adaptation of the minimum cost path extraction method presented in Metz et al. (2009). A 3D path with minimum cost is found between two manually placed seed points, located at the ostium and at the distal end of each coronary artery. The cost image is based on the multi-scale vesselness measure $V(x)$ (Frangi et al., 1998) and a sigmoid like threshold function $T(x)$ (Metz et al., 2009), defined as:

$$C_v(x) = \frac{1}{V(x)T(x) + \epsilon} \tag{3.1}$$

where ϵ is a small positive value introduced to avoid singularities (see Section 3.3.5).

However, the obtained centerlines are inaccurate, both at calcified locations (the minimum cost path runs through calcified plaque) and at bifurcations (the minimum cost path runs close to the border of the lumen rather than in the middle of the vessel). Therefore, the centerlines are refined.

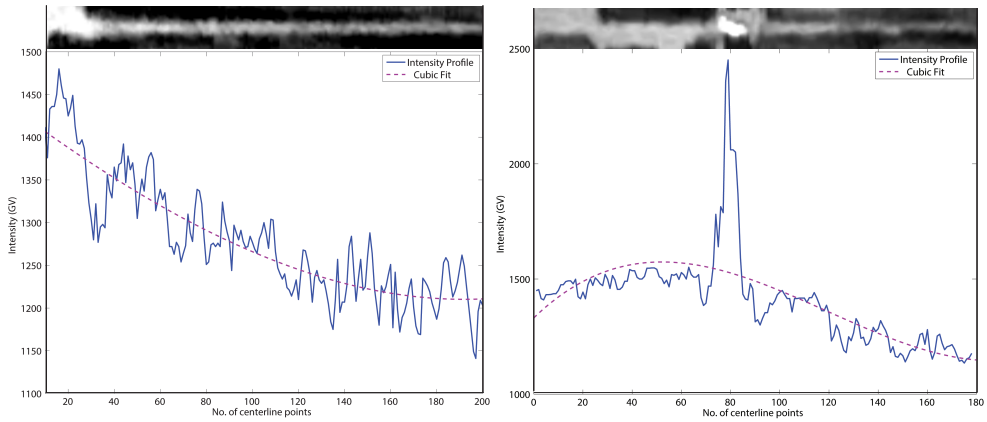

Figure 3.1: Intensity profiles through two coronary arteries, presenting (a) no calcium objects (b) a high density calcium object.

Calcium lesions within the artery are suppressed in the initial cost image by using the intensity profile of the contrast material along the initially extracted centerline. In the case of a healthy vessel presenting no calcified plaque (Figure 3.1(a)), the intensity profile is a smooth curve with progressive intensity decrease from the proximal to distal part of the vessel, due to the decrease of contrast agent concentration in the artery. In the case of a diseased vessel presenting calcified plaque (Figure 3.1(b)), the intensity profile may present spike(s), indicating that the initially extracted centerline is running through high intensity object(s). When the contrast material is not evenly distributed within the artery, spikes not corresponding to calcified plaques may appear in the intensity profile. In order to 1) differentiate true calcium objects from noise, and 2) estimate the intensity

value of the lumen of the coronary artery, we apply a regression fit to the intensity profile of the initially extracted centerline. Given an intensity profile, centerline points $x \in X$ running through calcified region(s) are detected if the following condition is verified:

$$I(x) - F(x)|_{x \in X} \geq T_{ca} \tag{3.2}$$

where $I(x)$ and $F(x)$ are the CTA image and the regression fit intensity value, respectively, at the position x along the centerline, and T_{ca} is a predefined intensity threshold value (see Section 3.3.5).
Each centerline position x verifying Eq.3.2 is subsequently considered as a seed-point, and a 3D-6-connected neighborhood region-growing segmentation algorithm is applied. If the connected voxel has an intensity value superior or equal to the maximum value of the intensity fitting curve F, it is classified as belonging to the calcified plaque. Last, the intensity value of each voxel belonging to the segmented calcified region is set to $0HU$ in the original CTA image (Figures 3.2(a)(b)).

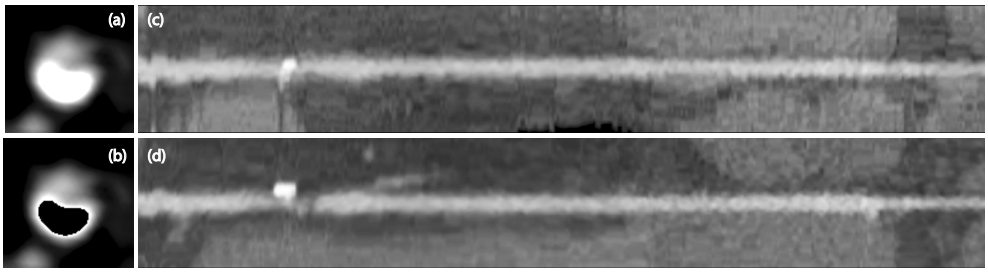

Figure 3.2: A random cross-sectional image slice through a calcium lesion (a) before and (b) after calcium suppression. CMPR image (c) before and (d) after refinement.

Finally, in order to refine the centerline runing close to the border of the lumen rather than in the middle of the vessel, we generate a stack of curved multi-planar reformatted (cMPR) images, i.e. stack of images perpendicular to the initial centerline, and apply a minimum cost path approach to this image stack, as proposed by Tang et al. (2012), using a modified cost image $C_{mv}(x)$, based on both $V(x)$ and a medialness measure $M(x)$ (Gülsün and Tek, 2008), defined as follows:

$$C_{mv}(x) = \frac{1}{M(x)V(x) + \epsilon} \tag{3.3}$$

Figures 3.2(c)(d) show an example of cMPR before and after the refinement step.

3.3.2 Bifurcation detection

As the extraction of the centerlines uses one start point and multiple end points, some part of the coronary artery tree may present multiple centerlines overlapping. This information is used to divide the coronary artery tree into individual segments, using Mean Shift filtering (van Walsum et al., 2008).

Given a set of spatial points $\{\{x_{11}\dots x_{N_1 1}\}\dots\{x_{1S_N}\dots x_{N_{S_N}S_N}\}\}$ belonging to $S = \{S_1\dots S_N\}$ centerlines having N_{S_i}, $i \in [1,N]$, points respectively, we apply the Mean Shift filter (Comaniciu and Meer, 2002) to obtain an average centerline that represent these N centerlines.
The Mean Shift algorithm is expressed as:

$$x_{kl}^{\tau+1} = \frac{\sum_{i,j} c_{kl,ij}\phi_{kl,ij} G\left(x_{kl}^{\tau}|x_{ij},\sigma\right) x_{ij}}{\sum_{i'j'} c_{kl,i'j'}\phi_{kl,i'j'} G\left(x_{kl}^{\tau}|x_{i'j'},\sigma\right)} \tag{3.4}$$

where x_{kl}, representing the k^{th} data point of centerline S_l, is the point being shifted, G a Gaussian distribution with standard deviation σ, and $(c_{kl,ij},\phi_{kl,ij})$ weighting factors for the x_{ij} data point (i^{th} data point of centerline S_j). Convergence is reached if the distance between x_{kl}^{τ} and $x_{kl}^{\tau+1}$ is smaller than some small threshold ϵ, determined during parameter optimization (Section 3.3.5). The correspondence weighting factor $c_{kl,ij}$ specifies to what extend the point x_{kl} being shifted corresponds to the data point x_{ij}. The orientation dependent weighting factor $\phi_{kl,ij}$ is introduced as it does not make sense to include centerlines that are close together but have a different orientation in the averaging procedure.

Application of Eq. 3.4 to all points x_{kl} of all centerlines S_i yields shifted centerlines S_i'. The shifting process is followed by another process of combining these shifted curves into a directed graph representation. For each centerline to be added, the parts overlapping with the existing graph are determined and merged in the graph data structure. For each of the non-overlapping parts, new edges are created in the graph. Subsequently, the coronary artery tree is divided into segments and bifurcations are detected.

3.3.3 Coronary artery lumen segmentation

Given the refined centerlines, the coronary artery lumen is segmented using the method introduced by Schaap et al. (2009b), following a two step approach. First, an optimal labeling of lumen and background is found, by using graph-cuts technique with edge-weights depending on the intensity of the centerline. Second, the falsely segmented regions not belonging to the vessel of interest are suppressed, using prior knowledge on the vessel shape (no holes, smooth surface, no inclusion of side branches). This is performed using robust kernel regression on a cylindrical parameterization of the lumen boundary.

Figure 3.3 shows the different steps of the segmentation process, and Figure 3.4 shows the contours of the entire vascular tree after the segmentation step.

3.3.4 Coronary artery stenosis detection and quantification

Given the coronary artery lumen segmentation (per segment of the coronary artery tree), the cross-sectional area A_x of the vessel is computed at every position x along the coronary artery segment, $x \in [1,N]$ with N being the number of positions along the centerline. The radius is then derived as $r_x = \sqrt{A_x/\pi}$.

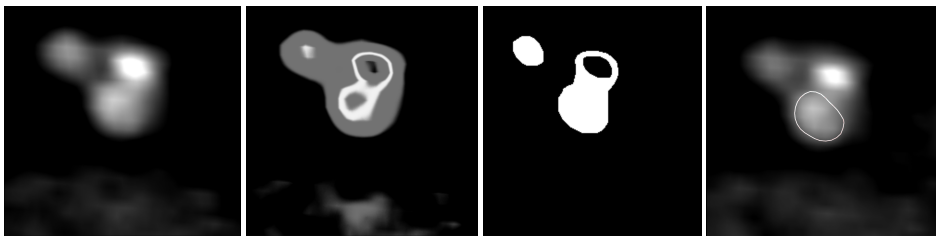

Figure 3.3: A MPR image of a vessel, with visible calcium lesion and side branch (a) Original image (b) Resulting image after segmentation (c) Binarized segmented image after graph-cuts (lumen bright, background black) (d) Resulting lumen segmentation after robust kernel regression.

To compute the degree of stenosis, the radius of a healthy vessel is needed, as a reference. We estimated the radius $\hat{r}_x$ of the healthy vessel by applying a robust weighted Gaussian kernel regression (Debruyne et al., 2008) to the 1D function describing the vessel radius r_x along the centerline, as follows:

$$\hat{r}_x = \frac{\sum_{x'=1}^{N} G(x'|x,\sigma_x) w_{x'} r_{x'}}{\sum_{x'=1}^{N} G(x'|x,\sigma_x) w_{x'}} \qquad (3.5)$$

$$\begin{cases} w_x = G(r_x | r_x^{max}, \sigma_r) \\ r_x^{max} = \dfrac{\sum_{x'=1}^{N} G(x'|x,\sigma_{max}) r_{x'}}{\sum_{x'=1}^{N} G(x'|x,\sigma_{max})} \\ G(x'|x,\sigma) = \frac{1}{\sigma\sqrt{2\pi}} e^{-\frac{(x'-x)^2}{2\sigma^2}} \end{cases} \qquad (3.6)$$

Figure 3.4 shows a 3D model of a segmented coronary artery tree, color-coded with the degree of stenosis. The radius profile of the LAD is shown and two stenoses are detected.

3.3.5 Parameter optimization

The optimal parameters were selected based on the results obtained on the 18 training datasets. The lower and upper scales for the multi-scale vesselness measure (V_x) used in Eq. 3.1 and in Eq 3.3 were set to 0.8 mm and 3 mm. The other parameters used in Eq. 3.1 were taken from Metz et al. (2009). The minimum and maximum scales for the medialness measure ($M(x)$) used in Eq. 3.3 were set to 0.5 mm and 2 mm, the number of intermediate scale steps to 8, and the number of angles to 24. The ϵ used to compute the cost images was set to 0.0001. The value of T_{ca} in Eq. 3.2 was set to 200HU. The cMPR images were generated at 0.5 mm distance perpendicular to the centerline having a cross-sectional region of 10 mm, and corresponding to a voxel size of $0.1 \times 0.1 \times 0.5\ mm^3$. The parameters used for lumen segmentation in Section 3.3.3 were obtained from Schaap et al. (2009b). In the Eq. 3.4 of the Mean Shift algorithm, σ and ϵ were set to 0.5 and 0.01 respectively. In the equations Eq. 3.5 and 3.6 of the stenoses detection/quantification, the parameter σ_x (corresponding to the longitudinal distance) was set to 8, σ_r (corresponding to the radius) to 0.25, and σ_{max} (corresponding to the maximum radius, estimated by Gaussian average) to 200.

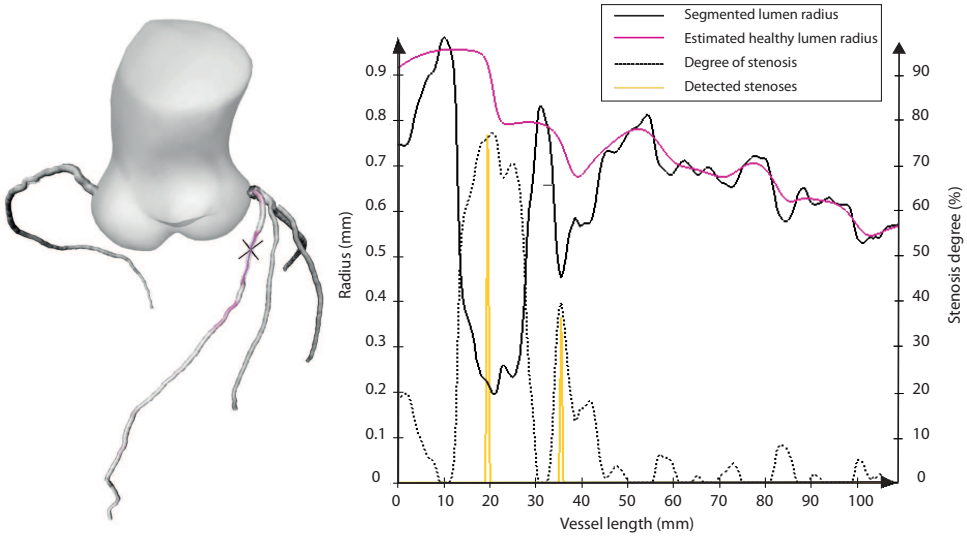

Figure 3.4: Automatic stenosis detection and quantification. (a) Coronary artery tree of patient#14, color-coded with degree of stenosis. The patient present a moderate stenosis in the proximal LAD (b) The radius of a healthy vessel segment (black line) is estimated by applying a robust weighted Gaussian kernel regression to the actual vessel radius (pink line). The degree of stenosis can then be derived (dashed black line) and significant stenoses are automatically detected (yellow picks).

It was observed from the training experiments that the reference QCA stenoses quantification is usually lower than the reference CTA degree of stenosis in the mild stenotic regions, and that our method overestimates the degree of stenosis in case of highly calcified lesions (blooming effect). Therefore, we first applied an off-set value of -20% to the QCA quantifications to all lesions detected on CTA with a degree between 20% and 49%, and refined the CTA quantification, to cope for the blooming artifact, as follows:

$$\begin{cases} G'_{CTA} = G_{CTA} - 10\%, & \text{if } T_{ca} \geq 500 \text{ and } G_{CTA} \geq 70\% \\ G'_{CTA} = G_{CTA}, & \text{otherwise} \end{cases}$$

where G'_{CTA} is the refined CTA degree of stenosis, G_{CTA} the initial one, T_{ca} a predefined intensity threshold value.

Using the above parameters, 90% of the training lesions detected by our method on CTA images were estimated without or with one grade error in quantification (Figure3.5).

3.4 Results

Table. 3.1, 3.2 and 3.3 present the training and testing results using our method with respect to the three observers' performance. The training set consists of 18 data and the testing set of 30 data.

Table 3.1 shows the average results of our method and 3 observers for stenosis detection measures: sensitivity and positive predictive value. In general, our results are

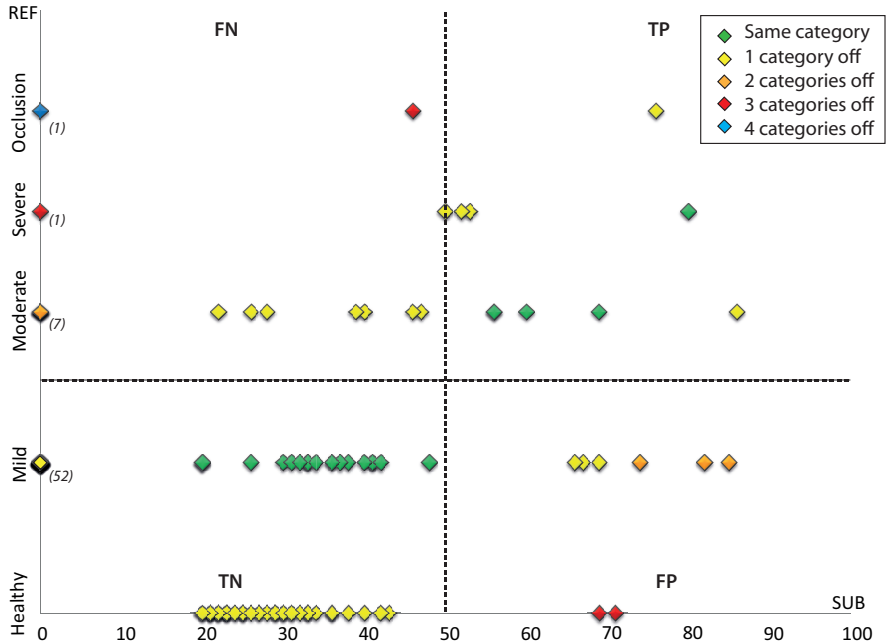

Figure 3.5: Stenoses detection and quantification - Results obtained on the 18 training datasets after optimization of the parameters: 90% of the stenoses detected with our new method are quantified with an error of one grade or less (yellow and green detections).

Table 3.1: Detection - Our method's performances are compared with the observers' ones.

(%)	Training				Testing			
Method	**QCA**		**CTA**		**QCA**		**CTA**	
	Sens.	*PPV*	*Sens.*	*PPV*	*Sens.*	*PPV*	*Sens.*	*PPV*
Observer 1	72	49	92	57	86	40	83	61
Observer 2	76	66	82	73	75	51	70	81
Observer 3	52	68	63	74	64	43	66	60
Our method	48	63	37	56	29	24	21	23

worse than the average observers' performance (sensitivity of 75%, PPV of 45% on QCA; sensitivity of 73%, PPV of 67% on CTA). Therefore, the ability of our method to discriminate significant stenoses from non-significant ones remains very limited (hard threshold at 50%). Nevertheless, as compared to the current state-of-the art algorithms evaluated, our method ranks fifth out of 11 submissions, over the testing set.

Table 3.2 shows the average results of our method and 3 observers for stenosis quantification measures. Despite our limited performance to discriminate non-significant stenoses from significant ones, our method is able to quantify the degree of stenosis as compared to the QCA with an accuracy comparable to the experts (averaged absolute difference of 31%, a RMS difference of 36%). Though the quantification agreement obtained with the proposed approach as compared to the CTA reference was fair, it should

Table 3.2: Quantification - Our method's performances are compared with the observers' ones.

	Training			Testing		
Method	**QCA**		**CTA**	**QCA**		**CTA**
	Abs Diff (%)	*RMS diff (%)*	*Weighted* κ	*Abs Diff (%)*	*RMS diff (%)*	*Weighted* κ
Observer 1	29.7	35.1	0.71	30.1	35.2	0.74
Observer 2	25.5	31.8	0.84	31.1	36.5	0.77
Observer 3	29.1	35.1	0.73	30.6	36.9	0.73
Our method	26.3	34.8	0.37	31.0	39.3	0.29

Table 3.3: Segmentation - Our method's performances are compared with the observers' ones. Diseased (D) / Healthy (H) segments.

	Training						Testing					
Method	**Dice** (%)		**MSD** (mm)		**MAXSD** (mm)		**Dice** (%)		**MSD** (mm)		**MAXSD** (mm)	
	D	*H*	*D*	*H*	*D*	*H*	*D*	*H*	*D*	*H*	*D*	*H*
Observer 1	74	79	0.26	0.26	3.29	3.61	76	77	0.24	0.24	2.87	3.47
Observer 2	66	73	0.31	0.25	2.70	3.00	64	72	0.34	0.27	2.82	3.26
Observer 3	76	80	0.24	0.19	3.07	3.25	79	81	0.23	0.21	3.00	3.45
Our method	66	70	0.37	0.32	2.49	3.04	65	68	0.39	0.41	2.73	3.20

be pointed out that, on training test ($\kappa = 0.37$), 90% of the lesions were estimated in the correct or adjacent class (Figure 3.5). Our method ranks second out of 9 submissions, over the testing set.

Table 3.3 shows the average results of our submission and 3 observers for coronary artery lumen segmentation measures: Dice, root mean squared distance (RMSD) and maximum distance (MAXD). Overall, the Dice and RMSD values obtained on healthy vessel segments are better than the one obtained on diseased ones. The Dice and RMSD were worse than than the average observers' performance, but the MAXD is better. Fig 3.6 presents few examples of coronary artery lumen segmentations, in comparison to the one obtained by 1) one of the three manual observers and 2) using our previous approach Shahzad et al. (2012a) (i.e. without the calcium suppression step). Our method ranks second out of 6 submissions.

3.5 Discussion

Though the coronary artery lumen can be automatically segmented with a precision similar to the experts, there is still room for improvement of our stenoses detection/quantification approach. In the current approach, the stenoses are quantified solely based on the diameter profile of the segmented lumen. Therefore, in case of diffuse disease or long stenoses, the degree of luminal narrowing is generally underestimated. As the method does not detect a lot of false positives (41 FP's over 48 datasets), it could be used in clinical practice for triage or as a second reader to assist the radiologist, without presenting too many false detections.

The relatively low value of the Kappa statistic in the CTA stenoses quantification measure may either be caused by a high number of FPs and FNs, by a high number of lesions reported with more than one grade difference as compared to the CTA reference, or by the linear weights which heavily penalize misclassifications. On the training set, a weighted Kappa value of 0.37 was obtained, and only 10% of the stenoses had a quantification error of more than one grade (Figure 3.5). This highlights that the linearly weighted Kappa is very sensitive to misclassification.

The majority of the stenoses detected with our approach were quantified with an error of only one grade, and most of the misclassifications occured between the mild ($20\% - 50\%$) and moderate ($50\% - 70\%$) grades. As 50% is the hard threshold used to discriminate between significant and non-significant lesions, accurate detection of significant stenoses remains a challenge. Considering that our method maybe used for triage of patients or as a second reader, the use of a third group "maybe significant", in addition to the significant and non-significant group maybe considered, to which all the borderline ($40\% - 60\%$ for instance) detected stenoses are assigned. The radiologist's would then have to inspect in more details those stenoses to make a final decision.

The results show that the additional centerline refinement step consisting of calcium suppression from the cost image improves the segmentations, compared to our previous approach (Shahzad et al., 2012a). Previously, the centerline was attracted to the calcified plaque and therefore, the plaque rather than the vessel was segmented. The segmentation of the current approach are better in agreement with the observer's ones. Nonetheless, the issue with calcified plaques is not completely solved, as it persists for highly calcified regions (Fig 3.6(d)(e), the red segmentations appear isolated due to the fact that we try to represent a 3D segmentation in a 2D longitudinal representation). In such cases, our refined centerline tends to run at the very outer border of the lumen, and the derived segmentation is of minimal radius size. However, in such extreme cases, it is not always clear how to manually segment the lumen either, and the inter-observer variability is therefore also high.

Given similarly accurate lumen segmentations, our approach outperforms the algorithms proposed by Broersen et al. (2012) and Wang et al. (2012) at the quantification stage, and achieves the best (though fair) quantification agreement as compared to the CTA reference standard. The results thus suggest that robust regression seems to be a good approach to quantify lesions from accurate lumen segmentation. However, there is still room for improvement. Refinement of the stenosis grades using additionally morphological and intensity features may benefit both the detection and quantification.

3.6 Conclusions

We presented a method to automatically detect and quantify coronary arteries stenoses, and to perform coronary lumen segmentation. The current results highlight that coronary artery lumen can be automatically segmented with a precision similar to the expert's one, but that detection and quantification of coronary artery stenosis is still a unsolved problem; discrimination between significant and non-significant lesions remains a challenge.

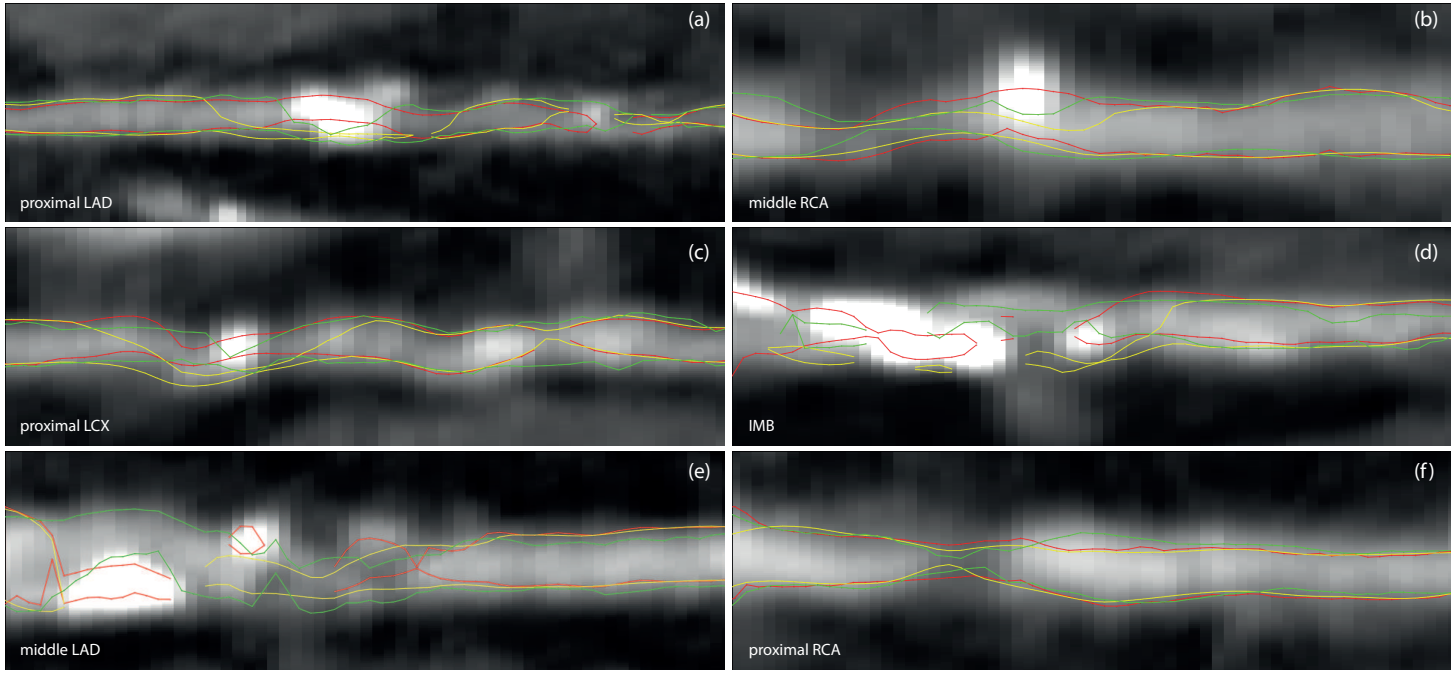

Figure 3.6: Coronary artery lumen segmentation examples. Our previous method (method without the calcium suppression step in the centerline refinement) (red), our method (yellow), one of the observer (green). (a)(b)(c) Cases where our method (with the calcium suppression step in the centerline refinement) achieves segmentation similar to the observer. (d) Case where the method avoid the calcified plaque; however, the observer segmented the other side of the plaque. (e) Case where issue with large calcified plaque remains. (f) Example of segmentation of a coronary segment presenting a soft plaque.

chapter 4

Standardized evaluation framework for evaluating coronary artery stenoses detection & quantification and lumen segmentation algorithms in Computed Tomography Angiography

This chapter is based on the manuscript:
Standardized evaluation framework for evaluating coronary artery stenoses detection, stenoses quantification and lumen segmentation algorithms in Computed Tomography Angiography, **H.A. Kirişli**, M. Schaap, C. Metz, A.S. Dharampal, W.B. Meijboom, S.L. Papadopoulou, A. Dedic, K. Nieman, M.A. de Graaf, M.F.L. Meijs, M.J. Cramer, A. Broersen, S. Cetin, A. Eslami, L. Flórez-Valencia, K.L. Lor, B. Matuszewski, I. Melki, B. Mohr, I. Öksüz, R. Shahzad, C. Wang, P.H. Kitslaar, G. Unal, A. Katouzian, M. Orkisz, C.M. Chen, F. Precioso, L. Najman, S. Masood, D. Ünay, L. van Vliet, R. Moreno, R. Goldenberg, E. Vuçini, G.P. Krestin, W.J. Niessen, T. van Walsum, *Submitted*, 2013.

Abstract

Purpose Though conventional coronary angiography (CCA) has been the standard of reference for diagnosing coronary artery disease in the past decades, computed tomography angiography (CTA) has rapidly emerged, and is nowadays widely used in clinical practice. Here, we introduce a standardized evaluation framework to reliably evaluate and compare the performance of the algorithms devised to detect and quantify the coronary artery stenoses, and to segment the coronary artery lumen in CTA data. The objective of this evaluation framework is to demonstrate the feasibility of dedicated algorithms to: 1) (semi-)automatically detect and quantify stenosis on CTA, in comparison with quantitative coronary angiography (QCA) and CTA consensus reading, and 2) (semi-)automatically segment the coronary lumen on CTA, in comparison with expert's manual annotation.
Methods A database consisting of 48 multicenter multivendor cardiac CTA datasets with corresponding reference standards are described and made available. The algorithms from 11 research groups were quantitatively evaluated and compared.
Results The results show that 1) some of the current stenosis detection/quantification algorithms may be used for triage or as a second-reader in clinical practice, and that 2) automatic lumen segmentation is possible with a precision similar to that obtained by experts.
Conclusions The framework is open for new submissions through the website *http://coronary.bigr.nl/stenoses/*.

4.1 Introduction

Coronary artery disease (CAD) is a major cause of death worldwide (Roger et al., 2012). Plaque build-up in the coronary artery vessel wall may cause luminal narrowing, called *stenosis*, and induce *ischemia* in myocardial tissue (i.e. the heart muscle). Prolonged periods of ischemia may lead to myocardial death. It is thus crucial to detect coronary artery disease in an early stage.

Various cardiovascular imaging techniques are used to assess and quantify the presence and state of coronary artery stenoses. The choice of which cardiovascular imaging techniques to perform is determined by the patient's history and current symptoms. In current clinical practice, conventional coronary angiography (CCA) is the gold standard imaging technique to diagnose CAD. With CCA, the location, number and severity of the stenoses can be assessed. Computed tomography coronary angiography (CTA) is gaining popularity (Weustink and de Feyter, 2011); it is less invasive than CCA, provides high-resolution three-dimensional (3D) images of the cardiac and coronary artery anatomy, and allows the interpreter to assess the presence, extent and type (calcified or non-calcified) of coronary plaques. CTA has evolved as a reliable gatekeeper of CCA in patients with low to intermediate pre-test probability of CAD[1] (Achenbach et al., 2012).

CTA images are currently interpreted using several visualization techniques (Raff et al., 2009). Transaxial image stacks are the basic visualization mode, and consist of a series of 2-dimensional (2D) axial images stacked in the longitudinal (i.e. cranio-caudal) direction. Such a visualization is characterized by minimal distortion and maximum resolution; however, 3-dimensional (3D) anatomical information, such as the coronary artery lumen morphology, is to be "mentally" reconstructed by the interpreter. As a complement, (curved) multi-planar reformatted (MPR/cMPR) images permit to visualize the coronary artery in orthogonal and oblique planes; such visualizations are especially recommended to delineate the morphology of the lumen (Figure 4.1). Maximum intensity projection (MIP) images may also be used to visualize vessels that run out of a given plane; MIP images are obtained by projecting the voxels with maximum intensity within a slab volume onto a plane.

The CTA interpretation is then summarized into a report(Raff et al., 2009), which contains, beside patient's clinical data, technical procedure information (i.e. image acquisition, image quality), clinical scan findings and interpretation. For each coronary artery lesion present in one of the modified 17-AHA-segments (American Heart Association, Fig. 4.2), the interpreter reports: 1) the stenosis location (origin, proximal, mid, distal, end) 2) the stenosis severity (mild, moderate, severe, occluded), 3) the stenosis plaque type (non-calcified, mixed, calcified), 4) the overall image quality / artifacts, and 5) the confidence in the interpretation. The final clinical decision making is based on these reported coronary findings; it is thus crucial to accurately detect or rule out significant CAD on CTA. Various studies investigated the diagnostic accuracy of CTA as compared to CCA (Meijboom, W.B. and Meijs, M.F L. et al., 2008; den Dekker et al., 2012). It has been demonstrated that CTA is 1) highly sensitive for detecting and ruling out significant CAD, and 2) moderately specific, even with severe coronary calcification (64-slices scanners and above).

[1] Pre-test probability of obstructive CAD are estimated using the Duke risk score (Pryor et al., 1993)

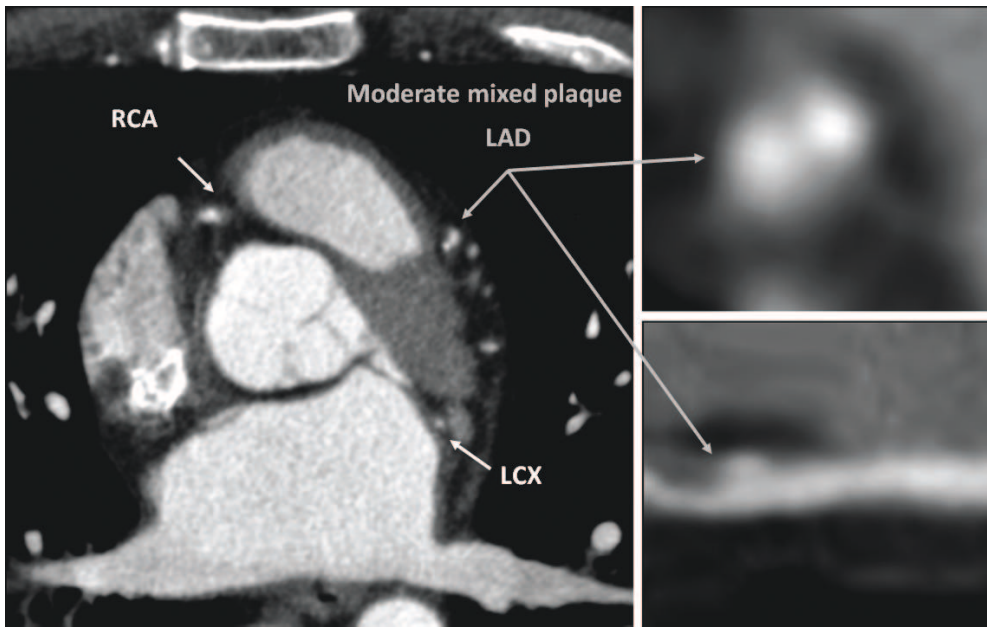

Figure 4.1: Visualization techniques used to interpret CTA images: transaxial (left) and multi-planar images (cross-sectional view at the upper-right, longitudinal view at the bottom right). Left anterior descending artery (LAD), right coronary artery (RCA) and left circumflex artery (LCX). This patient (training dataset #05) presents a moderate mixed plaque in segment #8 of the LAD.

The purpose of our work is to investigate to what extent automated approaches can be used to interpret cardiac CTA data for the presence of CAD. This paper has two main contributions: first, we introduce a framework to evaluate (semi-)automatic methods for coronary artery stenosis detection and quantification, and lumen segmentation, and second, we report on the results of this evaluation framework, comparing several state-of-the art coronary artery stenosis detection, quantification and segmentation algorithms.

In Section 4.2, we discuss previous work on detection and quantification of stenoses in CTA images. The evaluation framework is presented in Section 4.3. It includes a publicly available multicenter multivendor database of CTA data (Section 4.3.2), two reference standards derived from CCA and CTA (Section 4.3.5 and 4.3.4), a set of well-defined evaluation measures (Section 4.3.6), and an on-line tool to compare methods' performances (4.3.10). Section 4.4 gives a description of the first use of the framework during a MICCAI workshop, and includes a short description of the methods that were tested. The results of these methods as produced by the framework are presented in Section 4.5 and discussed in Section 4.6. Concluding remarks are made in Section 4.7.

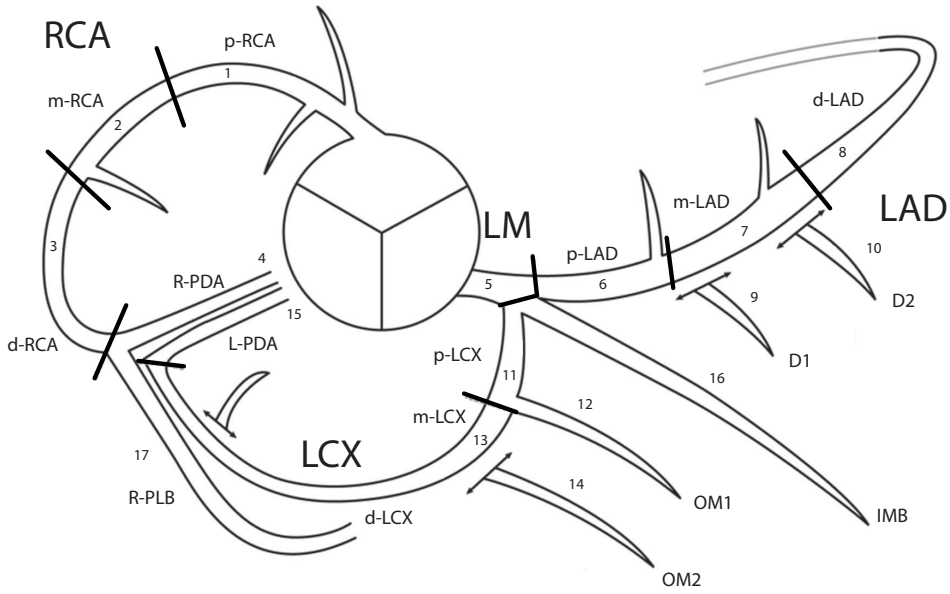

Figure 4.2: Coronary segmentation diagram - Axial coronary anatomy definitions derived, adopted, and adjusted from Austen et al. (1975)

Table 4.1: Quantitative stenosis grading and stenosis types

Grade		Description
0	Normal	Absence of plaque and no luminal stenosis
1	Mild	Plaque with 20% - 49% stenosis
2	Moderate	Plaque with 50% - 69% stenosis
3	Severe	Plaque with 70% - 99% stenosis
4	Occluded	Complete occlusion of the lumen

Type	Description
Non-calcified	Plaque without calcium
Calcified	Plaque with $\geq$ 50% calcium
Mixed	Plaque with $\leq$ 50% calcium

4.2 Previous work

Here, we give an overview of the previously published stenosis detection, quantification and grading methods, and report how they were evaluated; we refer readers to Lesage et al. (2009) for an extensive review on vessel lumen segmentation methods.

Recently, the number of publications presenting and/or evaluating coronary artery stenosis detection and quantification techniques in cardiac CTA datasets is growing, thus increasing the need for a standardized evaluation framework.

Table 4.2 gives an overview of the previously published methods, evaluated against CTA and/or QCA. As presented in Figure 4.3, these methods can be categorized into two groups: 1) the ones that use accurate lumen segmentation together with either an intensity threshold or an estimation of the healthy vessel diameter to detect stenoses (Wesarg et al., 2006; Khan et al., 2006; Saur et al., 2008; Zhou et al., 2010; Kelm et al., 2011; Arnoldi et al., 2010; Halpern and Halpern, 2011; Xu et al., 2012) , and 2) the ones that use feature extraction computed along a centerline to directly detect plaque (Teßmann et al., 2009; Mittal et al., 2010; Zuluaga et al., 2011). Note that the latter methods focus on *plaque* detection rather than *stenosis* detection. In their evaluation stage, binary (healthy or diseased) labels were assigned to each cross-section by the observers, based on the presence of *plaque* rather than based on the presence/severity of lumen narrowing. Most algorithms were quantitatively evaluated mainly on their detection rate (i.e. how accurately can a significant stenosis be detected by the algorithm); two articles (Halpern and Halpern, 2011; Xu et al., 2012) introduced more granularity in the stenosis quantification (i.e. more grades). Moreover, solely three algorithms (Khan et al., 2006; Boogers et al., 2010; Halpern and Halpern, 2011) were compared to QCA.

To the best of our knowledge, the only commercially available system that automatically detects significant coronary artery stenosis in CTA is the COR Analyzer (Rcadia Medical Imaging Ltd., Haifa, Israel). The summary of 14 clinical trials evaluating the system is available in Goldenberg and Peled (2011). The system reports location and type (calcified, soft, mixed) of significant coronary lesions ($\geq$ 50% stenosis). It is positioned as a computer-aided simple triage (CAST) system (Goldenberg et al., 2012) to rule out significant coronary artery disease. It may also serve as a second opinion diagnostic aid and as a prioritization tool for high volume practices. The QAngio CT RE system (Medis Specials, Medis Medical Imaging bv, Leiden, the Netherlands; *www.medisspecials.com*) is commercially available, but is used for research purpose. This system has been evaluated in Boogers et al. (2010, 2012); it addresses the three tasks (detection, quantification, lumen segmentation) in a fully automatic fashion, but is intended to be used with minimal user interaction.

Since a few years, the number of initiatives that set up a publicly available evaluation framework in the medical image analysis community is growing (*http://www.grand-challenge.org/*). For instance, in the cardiovascular domain, Schaap et al. (2009a) and Hameeteman et al. (2011) successfully compared algorithms for coronary artery centerline extraction (*http://coronary.bigr.nl/centerlines*) and for carotid artery lumen segmentation and stenosis grading (*http://cls2009.bigr.nl/*) in CTA datasets. Up to now, no standardized evaluation methodology has been published to reliably evaluate and compare the performance of existing or newly developed stenosis detection/quantification

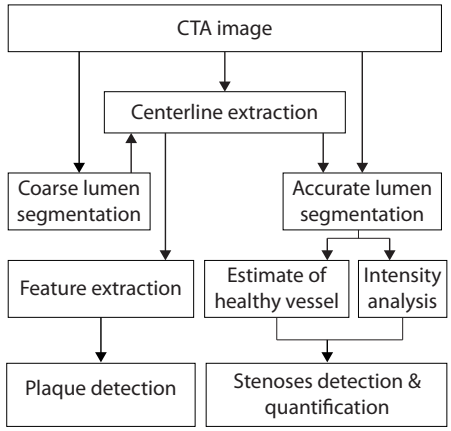

Figure 4.3: Overview of the building blocks and workflow of the previously published algorithms for coronary artery plaque detection and stenosis detection & quantification in CTA images.

and lumen segmentation algorithms. The proposed evaluation framework will provide such a large-scale standardized evaluation methodology and reference database.

4.3 Evaluation framework

In this section, we describe the datasets, the reference standards, the evaluation measures, as well as the ranking, used in our evaluation framework.

4.3.1 Cardiac CTA data

Study design The study was designed to include image data of symptomatic patients who presented either stable or unstable anginal syndromes, and who underwent both CTA and CCA examinations. Datasets were retrospectively acquired in three university hospitals, and evaluated anonymously. Thus, no IRB approval was required, according to the ethics committee guidelines of the medical centers, i.e. the Erasmus University Medical Center (ErasmusMC, Rotterdam, the Netherlands), the University Medical Center Utrecht (UMCU, Utrecht, the Netherlands) and the Leiden University Medical Center (LUMC, Leiden, the Netherlands).

Patient selection Patients were selected such that they are representative of the population undergoing CTA examination for the assessment of obstructive CAD. According to the AHA guidelines (Budoff et al., 2006) and to the alternative diagnostic algorithm of Weustink and de Feyter (2011), patients with a low to intermediate pre-test probability of disease and an Agatston coronary calcium score (CCS) between 0 and 400 are, in current clinical practice, likely to undergo a CTA test. Therefore, patients were selected based on their CCS, and distributed over five CCS risk categories (Table 4.3); the number of patients included in each category was derived from the work of Nieman et al. (2009).

Table 4.2: Overview of the previously published stenoses detection, quantification and grading methods. The analyses were performed in at least the 4 main arteries (left main, LAD, LCX, RCA), and possibly in the first-order arterial branches (diagonal, ramus, obtuse marginal, or posterior descending artery). The reported evaluation measures were computed *stenosis-based*. TP, FP, FN, TN are the true positive, the false positive, the false negative and the true negative detections; PPV and NPV are the true positive value and false positive value; sens. and spec. refer to sensitivity and specificity and acc. to the accuracy.

Article	Patients/ Observers	Reference	Quantification?	Type	Used evaluation measures
Wesarg et al. (2006)	10/1	CTA	-	Calcified	TP, FP, FN
Khan et al. (2006)	50/1	CTA/QCA	$\geq 50\%$	All	sens., spec.
Saur et al. (2008)	127/1	CT/CTA	-	Calcified & mixed	TP, FP, PPV
Teßmann et al. (2009)	45/1	CTA	-	All	TP, FP, FN, PPV
Mittal et al. (2010)	165/1	CTA	-	Calcified	PPV
Arnoldi et al. (2010)	59/2	QCA	$\geq 50\%$	All	sens., spec., acc., PPV, NPV
Zhou et al. (2010)	20/2	CTA	$\geq 50\%$	All	FP, FN
Halpern and Halpern (2011)	207/1	CTA	3 grades	All	TP, FP
Kelm et al. (2011)	229/3	CTA	$\geq 50\%$	Non-calcified	sens., FP
Boogers et al. (2010)	100/1	CTA/QCA	All	All	Bland-Altman (% stenosis)
Zuluaga et al. (2011)	9/2	CTA	-	All	sens., spec., acc., Kappa
Xu et al. (2012)	13/3	CTA	4 grades	All	Kappa

Table 4.3: Distribution of patients (percentage of males) per coronary calcium score (CCS) category and per vendor. CCS refers to the Agatston score. The distribution of patients over the CCS categories was deduced from the work of Nieman et al. (2009), who reported on incidence of the different groups.

Center	Vendor	Scanner	CCS					Total N (% males)
			0 *Low*	0.1-10 *Minimal*	11-100 *Mild*	101-400 *Moderate*	+400 *High*	
EMC	**SIEMENS**	Somatom Definition	6 (100%)	1 (100%)	3 (80%)	4 (50%)	2 (50%)	16 (75%)
UMCU	**PHILIPS**	Brillance 64	3 (33%)	3 (66%)	5 (80%)	3 (33%)	2 (50%)	16 (56%)
LUMC	**TOSHIBA**	Aquilion ONE 320	2 (50%)	2 (0%)	6 (80%)	4 (75%)	2 (50%)	16 (68%)
		All	11 (72%)	6 (50%)	14 (78%)	11 (55%)	6 (50%)	48 (67%)

Table 4.4: Patient's information

	All	EMC	UMCU	LUMC
Scan date				
min	06/2005	08/2006	06/2005	06/2008
max	06/2011	12/2008	06/2006	06/2011
Age				
mean ± std	58.76 ± 8.71	58.81 ± 11.05	57.31 ± 7.25	60.17 ± 7.05
[min, max]	[41, 80]	[43, 80]	[41, 69]	[52, 74]
Gender				
males (%)	32(67%)	12(75%)	11(69%)	10(63%)
CV risk factors				
Obesity	6 (13%)	0 (0%)	3 (19%)	3 (19%)
Smoking	20 (42%)	3 (18%)	8 (50%)	9 (56%)
Hypertension	21 (44%)	7 (44%)	6 (38%)	8 (50%)
Diabetes	5 (10%)	0 (0%)	1 (6%)	4 (25%)
Fam. Hist.	23 (48%)	9 (56%)	6 (38%)	8 (50%)

Our study population consists of 48 symptomatic patients, aged between 41 and 80 years old (58.76 ± 8.71 y.o.), enrolled in three university hospitals between June 2005 and June 2011; patients' characteristics are listed in Table 4.4. Patients with a previous history of percutaneous coronary stent placement, coronary artery bypass surgery, pacemaker, an impaired renal function (serum creatinine $\geq$120 μmol/l), persistent arrhythmias, an inability to perform a breath hold of 15 s, a known allergy to iodinated contrast material, or a CTA of non-diagnostic image quality (motion artifacts) were excluded from our study.

Scan protocol The CTA data was acquired on : 1) a dual-source CT scanner (Somatom Definition, Siemens, Forchheim, Germany) at the ErasmusMC, 2) a 64-slice CT scanner (Brillance 64, Philips Medical Systems, Best, the Netherlands) at the UMCU, and 3) a 320-slice CT scanner (Aquilion ONE 320, Toshiba Medical Systems, Tokyo, Japan) at the LUMC. A non-enhanced CT scan was performed before the CTA; the total calcium scores of all patients were calculated using dedicated software in each center. A bolus-tracking technique was used to synchronize the start of image acquisition with the arrival of contrast agent in the coronary arteries.

Image reconstruction A single image per patient was used, reconstructed at the mid-to-end diastolic phase (350 ms before the next R-wave or at 65% to 70% of the R-R interval), with either retrospective (Siemens and Philips data) or prospective (Toshiba data) electrocardiographic gating.

4.3.2 Training and testing datasets

Eighteen of the 48 CTA images, together with the CTA and QCA reference standards, were made available for training; the remaining thirty datasets were used for testing

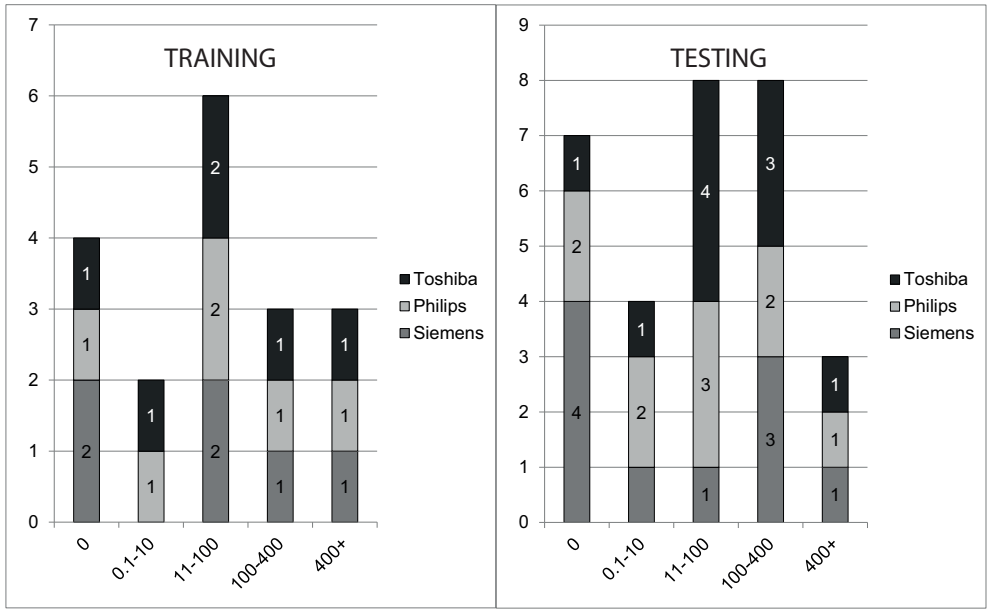

Figure 4.4: Distribution of 18 training and 30 testing datasets with respect to the different CCS categories and vendors.

Table 4.5: Distribution of the coronary artery lesions ($\geq 20\%$) for the training and testing datasets. A lesion is considered as being significant if the luminal narrowing is $\geq 50\%$.

	Artery				
	RCA	LAD	LCX	IMB	**All**
Training					
CTA					
$\geq 20\%$	36	51	12	4	103
$\geq 50\%$	12	10	5	0	27
Testing					
CTA					
$\geq 20\%$	50	73	18	2	143
$\geq 50\%$	18	22	7	0	47

the algorithms; for those, only the CTA images were made available. The training and testing datasets were selected with respect to the different vendors, the CCS categories, and the disease prevalence, i.e. distribution of stenoses over the different degrees and coronary arteries; the distribution is shown in Figure4.4 and Table 4.5. The 26% and 32% of the lesions are significant ($\geq$ 50% luminal narrowing) for training and test datasets respectively.

4.3.3 Sub-challenges

In our framework, three sub-challenges are defined: 1) coronary artery stenosis detection, 2) coronary artery stenosis detection & quantification, and 3) coronary artery stenosis detection & quantification and coronary artery lumen segmentation. Coronary artery stenosis detection is a mandatory task, as it is the focus of the evaluation framework. As some of the methods can also output, next to the stenosis detection, the stenosis grade and/or the lumen segmentation, we additionally provide the possibility to evaluate those two outputs.

Generally, semi-automatic algorithms may be used as aids for visual inspection of studies by clinicians; therefore, mainly accurate stenosis quantification is important. Fully automatic systems, on the other hand, may be used for triage, and therefore, should be able to identify patients without CAD with high specificity (usually above 60%, to not overwhelm the expert with a considerable amount of false positive detections and speed-up the diagnostic process), while maintaining very high sensitivity. Every miss would then result, in the best case, in a delayed treatment for the patient.

4.3.4 Reference standard from CTA

The multicenter multivendor CTA scans were analyzed at the Erasmus MC, University Medical Center Rotterdam (Rotterdam, the Netherlands).

Stenoses detection/quantification Three independent experienced observers (A.S.D., W.B.M., S.L.P.), unaware of the results of the CCA, graded the CTA datasets; a unique reference standard was then derived from the three observers' grades following the protocol outlined in Figure 4.5. A dedicated tool implemented in MeVisLab was used (*http://www.mevislab.de*) by the observers for the annotations. The axial source images, as well as MPR and cMPR views, were used to evaluate the CTA datasets for the presence of coronary obstructions (i.e. lesions with $\geq$ 20% luminal narrowing). For each lesion with visually $\geq$ 20% luminal narrowing, the observers had to report the location, the plaque type (non-calcified, calcified, mixed), and the degree, according to the categories of Table 4.1. All segments from the 17 modified AHA segment model (Figure 4.2), which are present and have a diameter greater than 1.5 mm, were included in the analysis. Finally, each segment was scored as having significant CAD if at least one stenosis with $\geq$ 50% luminal narrowing was reported during the visual assessment.

Lumen segmentation Three independent experienced observers (A.S.D., W.B.M., A.D.), unaware of the results of the CCA, segmented a set of selected vessel segments in CTA images. All segments presenting a significant stenosis ($\geq$ 50% luminal narrowing), as well as three additional segments (one in each of the main vessels) were randomly selected to be segmented; segments with a complete occlusion in the CTA stenoses detection/quantification reference standard were excluded. Figure 4.6 gives the details per vendor and per vessel of the number of segments being considered in the lumen segmentation evaluation. For the annotation process, we followed the same procedure as was used in the cls2009 challenge presented in Hameeteman et al. (2011). First,

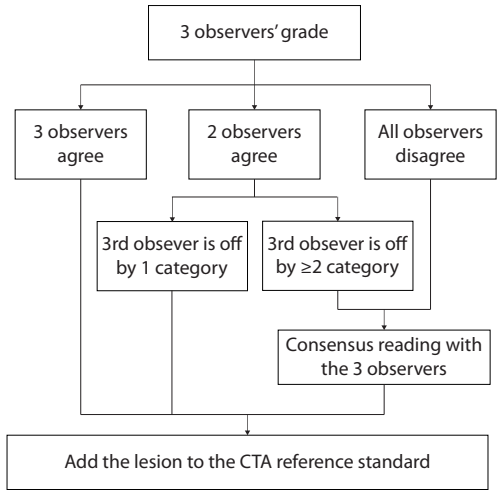

Figure 4.5: CTA stenoses detection/quantification reference standard protocol. Consensus reading with the 3 observers was necessary in 3% of the cases.

one observer annotated the centerline of each of the 17-segments of the modified AHA model (Figure 4.2) by clicking points in axial, sagittal and coronal views, followed by a centerline refinement step in cross-sectional views and cMPR images. Subsequently, using this centerline, three observers independently drew lumen contours in six cMPRs. These longitudinal contours were then used to construct cross-sectional contours on cross-sectional images sampled along the centerline. As a final refinement step, these cross-sectional contours could be manually edited. This procedure resulted in a set of cross-sectional contours along the vessel centerline, for each vessel segment selected and for each observer. These contours determine the reference standard for the evaluation of the lumen segmentations. An example of the CTA reference standard is presented in Figure 4.7.

4.3.5 Reference standard from CCA

The reference standard from CCA for the detection and quantification of stenoses was obtained with quantitative coronary angiography (QCA). One experienced cardiologist (K.N.), unaware of the results of the CTA scoring results, identified and analyzed all coronary segments using the modified 17-segment AHA classification (Figure 4.2) on a separate workstation. Segments were visually classified as normal (smooth parallel or tapering borders, visually $\leq$ 20% narrowing) or as having coronary obstruction (visually $\geq$ 20% narrowing). The stenoses in segments visually scored as having $\geq$ 20% narrowing were quantified using the validated QCA algorithm (Cardiovascular Angiography Analysis System II, CAASII, Pie Medical Imaging Maastricht, the Netherlands) (Haase et al., 1993). Stenoses were evaluated in the worst (available) angiographic view (Figure 4.8) and classified as significant if the lumen diameter reduction exceeded 50%.

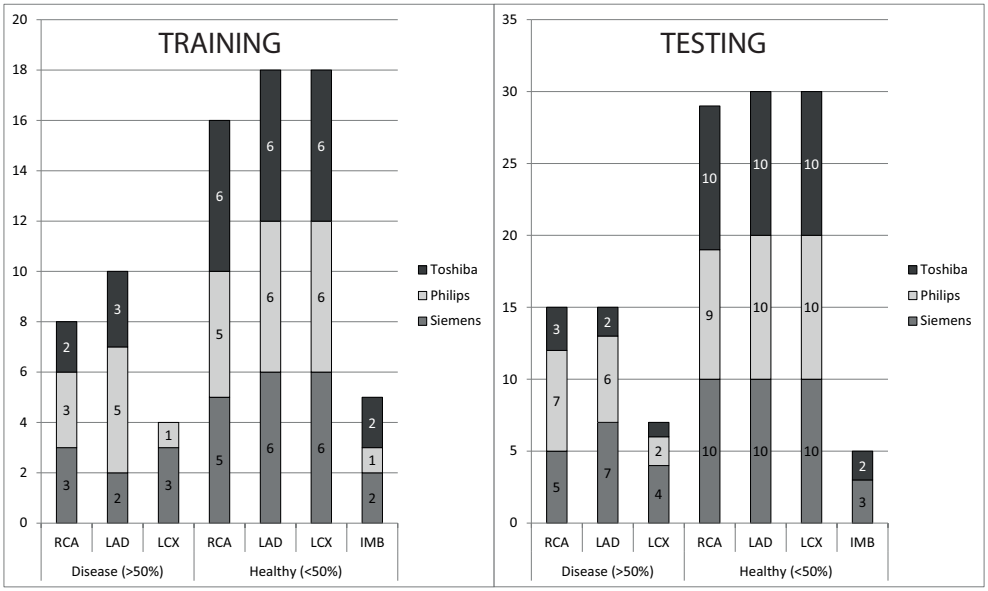

Figure 4.6: Overview of the segments considered for the lumen segmentation evaluation. *Diseased* segments are segments presenting in CTA consensus with at least one significant stenosis (≥50%). *Healthy* segments are segments presenting in CTA consensus with no significant stenosis (≤50%). Occluded segments were excluded from the lumen segmentation evaluation. The training set consists of 18 datasets and the testing set of 30 datasets.

4.3.6 Evaluation measures

The evaluation measures for the coronary artery stenosis detection and quantification are reported per coronary calcium category (Figure 4.4) and over all patients, as providing the errors per dataset may reveal information about the reference stenosis grades. The final evaluation measure (as reported in Table 4.8 and 4.10) is obtained over all patients. The evaluation measures for the lumen segmentation are communicated per patient, and the number and identity of evaluated segments remains hidden.

Stenosis detection

Two metrics are used to evaluate the performance of the coronary artery stenosis detection algorithms: the sensitivity (Eq.(4.1)) and the positive predictive value (Eq.(4.2)).

$$S = \frac{TP}{TP + FN} \tag{4.1}$$

$$PPV = \frac{TP}{TP + FP} \tag{4.2}$$

where TP, FN, FP are the true positive, false negative and false positive detections, respectively. Table 4.6 defines the TP, FN, FP and TN.

Table 4.6: Stenosis detection, as compared to CTA and CCA reference standard. Descriptions of true-positive (TP), false-negative (FP), false-positive (FP) and true-negative (TN) detection.

Detection	**Description** for *segment-based* and *lesion-based* analysis
TP	Both the reference standard and the algorithm stenosis/segment have a grade $\geq 50\%$.
FN	The reference standard stenosis/segment has a grade $\geq 50\%$ while the algorithm stenosis/segment has a grade $< 50\%$.
FP	The reference standard stenosis/segment has a grade $< 50\%$ while the algorithm stenosis/segment has a grade $\geq 50\%$.
TN	Both the reference standard and the algorithm stenosis/segment have a grade $< 50\%$.
	Description for *patient-based* analysis
TP	At least 1 significant stenosis in a patient detected by both the reference standard and the algorithm, regardless of location of stenosis
FN	No significant stenosis detected by the algorithm and at least 1 significant stenosis detected by the reference standard.
FP	Significant stenosis detected by the algorithm and no significant stenosis detected by the reference standard.
TN	No significant stenosis in a patient detected either by the reference standard and the algorithm.

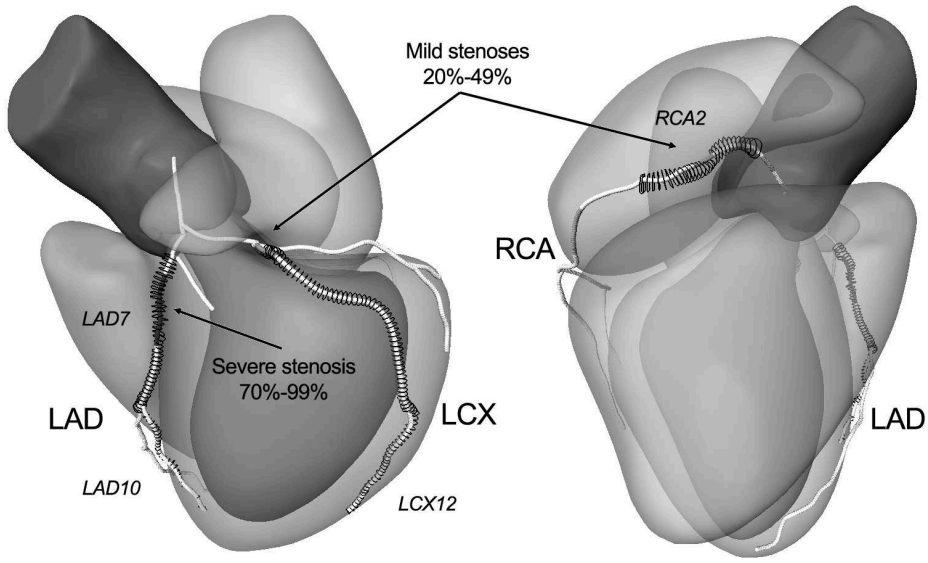

Figure 4.7: Example of CTA reference standard. Training dataset 08 presents five mild stenoses (one in RCA1, two in RCA2, one in RCA3, one in LCX12) and one severe stenosis (LAD7). Thus, segment LAD7 is selected to be segmented, as well as three other random segments in each of the main arteries, i.e. segments RCA2, LAD10 and LCX12.

The evaluation as compared to the CTA reference standard is *lesion-based*. The stenoses considered here are the union of the stenoses in the reference standard and in those detected by the algorithm. An example of stenosis detection is presented in Figure 4.9 for training dataset#10 and results of observer#1, and more details about the matching procedure can be found in the todo.

The evaluation as compared to the QCA reference standard is *segment-based*. The segments considered here are all anatomically present segments from the modified 17-AHA-segments model (Fig. 4.2), with a minimal lumen diameter greater than 1.5 mm.

Stenosis quantification

As compared to the reference standard derived from CCA, two metrics are used to evaluate the performance of the coronary artery stenosis quantification algorithms, per segment: the absolute average difference (AAD, Eq.(4.3)) and the root mean squared difference (RMSD, Eq.(4.4)).

$$AAD = \frac{\sum_{i=1}^{S} \left| g^i - g^i_{ref} \right|}{S} \tag{4.3}$$

$$RMSD = \sqrt{\frac{\sum_{i=1}^{S} \left(g^i - g^i_{ref} \right)^2}{S}} \tag{4.4}$$

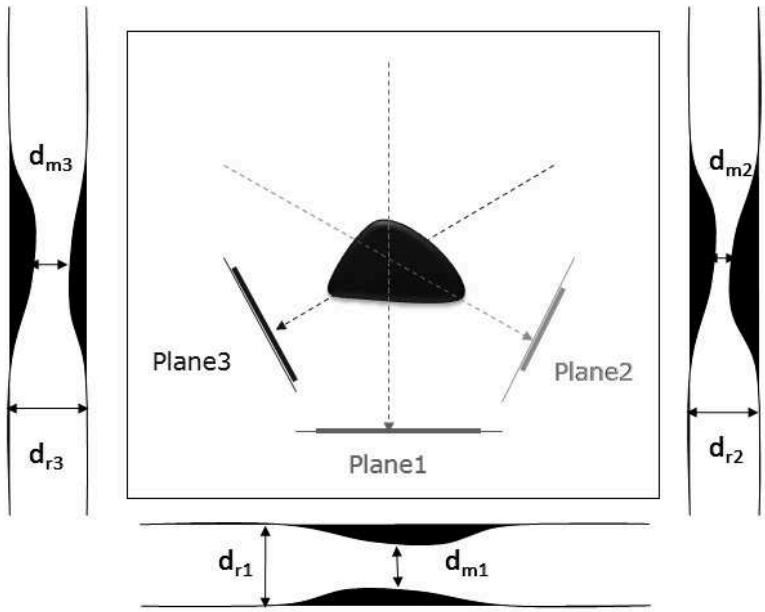

Figure 4.8: Quantitative coronary angiography (QCA). For each acquired X-ray imaging plane, the minimal luminal diameters (d_m) are measured and compared to the reference diameter (d_r) of the vessel immediately adjacent. Given the minimal (projected) diameter, the percentage of stenosis can be calculated, i.e. in plane 2 in the given example.

with g_{ref} the reference standard stenosis grade, g the estimated stenosis grade, and S the number of considered segments in the evaluation.

When evaluating the performance of the coronary artery stenosis quantification algorithms per lesion as compared to the CTA reference standard, close misses (e.g. grading a stenosis as being mild while the reference standard indicates it is moderate) should be less heavily penalized than misses that are further apart (e.g. grading a stenosis as being severe or occluded while the reference standard indicates it is mild). Therefore, we use the linearly weighted Cohen's Kappa metric (Cohen, 1968). It measures how much different the observed agreement is from the expected agreement, and is standardized to take values between -1 and 1, where 1 is perfect agreement, 0 is exactly what would be expected by chance, and negative values indicate agreement less than chance, i.e. potential systematic disagreement between the reference standard and the algorithm.

To fairly compare the Kappa values of different algorithms, the Kappa must be computed using the same number of stenoses. However, in the CTA reference standard, true negative (TN) detections are not reported, while required to compute the Kappa value. We accommodate this issue by estimating an average TN per dataset as follows: given the 48 datasets, we measured a total arterial segments length of 22080 *mm*, among which 2120 *mm* are diseased sections (i.e. presenting lesions with $\geq$ 20% obstruction). As there are 246 lesions, the average length of a lesion is of 8.6 *mm*. At the end, the 19960 *mm* of healthy vessel can be interpreted as 2321 TN, and thus, as 48 (TN+FP) per dataset.

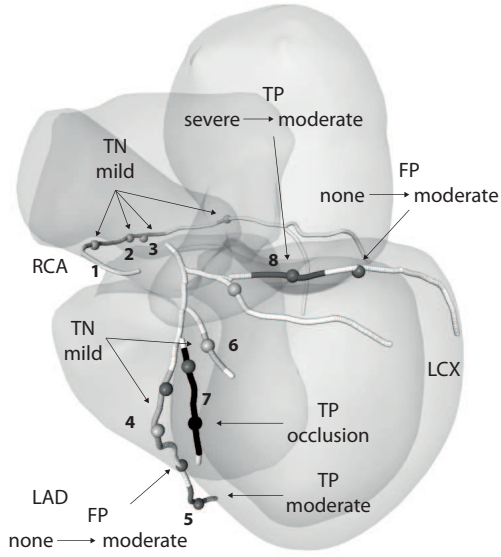

Figure 4.9: Detection example for training dataset10 and results of observer#1. The patient presents 8 stenoses (grey-scale segments) and the observer#1 detected 14 stenoses (grey-scale spheres). Reference stenoses #1, #2, #3, #4 and #6 are TN detections, i.e. the observer assigned a *mild* grade ($\leq 50\%$). Reference stenoses #5 (severe) and #8 (moderate) are TP detections, i.e. the observer assigned a *moderate* grade ($\geq 50\%$). Reference stenosis #7 (occlusion) is also a TP because the observer's average grade (*severe* + *occluded*) is $\geq 50\%$. The observer detected two FP *moderate* lesions in LAD and LCX. For more details about the grades, see Table 4.1; grey-scale from white to black correspond to *healthy*, *mild*, *moderate*, *severe* and *occlusion*.

In the case that an algorithm would report (on average) more than 48 (TN+FP) lesions per dataset, its Kappa value would be set to -1 (less than chance agreement), as exceeding this limit does not make sense. More details about the computation of the Kappa statistics are provided in Section 4.3.7.

Lumen segmentation

The segmentation is evaluated by comparing the result with the lumen contours that were manually drawn by three observers (see Section 4.3.4). The segmentations are compared to the reference standard using three measures: the Dice similarity index (Dice), the mean distance (MSD), and the Hausdorff distance (MaxD). Each metric is determined for each cross-sectional contour of the observer annotations, thus in 2D, and the results of all contours of a vessel segment are combined, yielding three scores per vessel segment per observer. To perform the 2D metric calculation, for each observer contour, the segmentation was intersected with the corresponding cross-sectional contour plane. From the intersection result (i.e. a set of segmentation contours), the

segmentation contour closest to the observer contour and not too far away from it, is assumed to be the valid segmentation contour. If a valid segmentation contour is found, it is linearly resampled to ensure that the points along the contour are sufficiently close. Subsequently, the true positive area (overlap area), the false negative area (missed lumen) and the false positive area (segmentation outside lumen) are determined for this contour, by applying a 2D scan conversion algorithm to both contours. Also, the distances from each observer contour point to the segmentation contour, and vice versa, are determined and integrated over the contours, and also the maximum distance is determined. True positive area, false negative area and false positive area are summed over all contours of the vessel segment, after which the Dice index is determined. Similarly, the mean squared distance is the average of all contours' mean squared distance of the vessel segment, and the Hausdorff distance is the maximum of the contours' Hausdorff distance. If no segmentation contour is sufficiently close to the observer contour, it is assumed that the segmentation does not contain this part of the vessel segment. In that case, the complete lumen area is counted as false negative area, the mean distance is equal to the mean radius of the manual contour, and the Hausdorff distance is equal to the maximum distance between the manual contour and its center.

4.3.7 Ranking the algorithms

In order to rank the different algorithms for coronary artery stenosis detection, stenosis quantification and lumen segmentation, the evaluation metrics presented in the previous section have to be combined. This is achieved by first assigning to each algorithm a rank for each evaluation metric. The rank is between 1 (best) and N (worst), N being the number of observers and algorithms to be compared. The final rank is then obtained by averaging the ranks over the evaluation metrics.

It should be noted that it is possible for method A to have better average measures than method B, while still having a worse average rank.

Stenosis detection

The detection algorithms are ranked based on the overall sensitivity and positive predictive value achieved as compared to the CTA and CCA reference standards, as follows:

$$R_D = \frac{1}{4} \cdot \left(\text{rank}_{Sens}^{CCA} + \text{rank}_{PPV}^{CCA} + \text{rank}_{Sens}^{CTA} + \text{rank}_{PPV}^{CTA} \right)$$

with rank_{Sens}^{CCA} and rank_{PPV}^{CCA} respectively the sensitivity and PPV ranks achieved over all data as compared to the CCA reference standard, and rank_{Sens}^{CTA} and rank_{PPV}^{CTA} respectively the sensitivity and PPV ranks achieved overall data as compared to CTA reference standard.

Stenosis quantification

The quantification algorithms are ranked based on their AAD and RMSD of the degree of stenosis as compared to the CCA reference standard (segment-based), and on

their weighted Cohen's Kappa coefficient as compared to CTA reference standard (lesion-based), as follows:

$$R_Q = \frac{1}{4} \cdot \left(\text{rank}_{AAD}^{CCA} + \text{rank}_{RMSD}^{CCA} + 2 \cdot \text{rank}_{Kappa}^{CTA} \right)$$

with rank_{AAD}^{CCA} and rank_{RMSD}^{CCA} respectively the AAD and RMSD ranks achieved over all data as compared to the CCA reference standard, and $\text{rank}_{Kappa}^{CTA}$ the linearly weighted Kappa rank achieved over all data as compared to the CTA reference standard. We added a weight of 2 to the $\text{rank}_{Kappa}^{CTA}$ to make the total weight for the CTA rank equal to the total weight for the CCA ranks.

Lumen segmentation

The segmentation algorithms are ranked based on the overlap, the mean distance, and the Hausdorff distance (average over the 3 observers' reference annotations), while making distinction between segments having non-significant and significant stenoses, as follows:

$$R_S = \frac{1}{N} \cdot \sum_{p=1}^{N} \left(\frac{\sum_{h=1}^{3} \text{rank}_h^p}{3} + \omega^p \cdot \frac{\sum_{d=1}^{3} \text{rank}_d^p}{3} \right)$$

where $\omega^p = 1$ if patient p has evaluation metrics computed for diseased segments (i.e. segments with significant stenoses), and $\omega^p = 0$ otherwise, N being the number of patients.

First, for each algorithm, a rank rank_m^p is computed per patient p and evaluation metric m. Then, an average rank rank^p is obtained by averaging the three (if the patient does not present any significant stenosis) or six (if the patient presents at least one significant stenosis) rank_m^p ranks; this leads to N ranks. The final rank is obtained by averaging of the N rank^p patient ranks.

4.3.8 Algorithm categories

Depending on the amount of user-interaction, we distinguish two different categories of algorithms:

Fully automatic Fully automatic methods detect and quantify coronary artery stenosis and segment the lumen without user-interaction. The CTA image is the only input used by the method.

Minimal user-interaction Methods with minimal-user interaction are allowed to use two additional points per vessel: 1) one point S at the ostium, i.e. start of the vessel, and 2) one point E at the end of each vessel. Points S and E are provided with the data.

4.3.9 Provided centerlines

Coronary analysis methods often start with detecting a coronary centerline (see Section 4.2). To facilitate those methods that can do coronary analysis, but do not have a centerline extraction available, three teams of the centerline extraction challenge (Schaap et al., 2009a) were asked to provide centerline extraction results to the participants of this challenge: 1) automatic and manually corrected from the LKEB group (Leiden, the Netherlands) based on Yang et al. (2011, 2012), 2) automatic from Rcadia (Haifa, Israel) based on Goldenberg et al. (2012), and 3) automatic from VRVis (Vienna, Austria) based on Zambal et al. (2008). The participants can then use one of these set of centerlines as input for their method (as long as they use the same centerline extraction algorithm for all datasets) and submit the combined method to a category, depending on the automation of the used centerline extraction algorithm.

4.3.10 Web-based evaluation framework

The proposed framework for coronary artery stenosis detection & quantification and lumen segmentation in CTA images is made publicly available through a web-based interface (*http://coronary.bigr.nl/stenoses/*). The 48 cardiac CTA datasets, as well as the corresponding stenosis detection, quantification and lumen segmentation reference standard of the training datasets, are available for download for anyone who wishes to validate their algorithm. Furthermore, the website provide several tools to inspect and compare the algorithms.

4.4 MICCAI 2012 workshop

The evaluation framework was launched during the "3D Cardiovascular Imaging: a MICCAI segmentation challenge" workshop that was organized in conjonction with the 15th International Conference on Medical Image Computing and Computer Assisted Intervention (MICCAI), and was held on October 1st, 2012 in Nice Sophia Antipolis, Côte d'Azur, France. Around 200 groups from academia and industry were invited by e-mail to participate in the challenge. Seventy-five teams created an account on our website, fifty of which sent the data confidentiality form, which was required to download the datasets. Forty-four teams downloaded the training set and twenty-nine teams downloaded additionally the testing set. Eleven teams submitted results: eight of them participated in the quantification sub-challenge and five of them participated in the lumen segmentation sub-challenge. The 11 evaluated algorithms are described below and more details can be found in the full paper version that all authors submitted for the workshop, available on our website (*http://coronary.bigr.nl/stenoses/*).

4.4.1 Broersen et al.

The algorithm by Broersen et al. (2012) has four stages. First, an automatic tree extraction (Yang et al., 2012) and segment labeling step is performed (Yang et al., 2011). Second, lumen and vessel wall contours are detected in each vessel (running from the

ostia to the most distal point)(Boogers et al., 2012). Next, regions with potential lesions are automatically determined for each segment based on deviations from a regression on the lumen areas in the vessel representing normal vessel tapering. Additional lesions are detected in calcified regions as well as in regions with significant lumen intensity drops. Finally, the lesion information from all vessels is combined into a unique list of lesions.

4.4.2 Cetin et al.

The algorithm by Cetin and Unal (2012) has four stages. First, the coronary vessels are extracted around the provided centerline coordinates (manually refined, based on Yang et al. (2011)) by the "vessel tractography" method presented in Cetin et al. (2013). Second, longitudinal vessel volumes are generated for each branch to provide rotation invariance. Third, the following features along the centerline of the vessel are extracted: intensity features based on a cylindrical sampling pattern with varying radii, length and position; and a geometric feature based on the energy of the vessel radius profile. Finally, a random forest based classifier is utilized to detect the stenosis coordinates along the vessel.

4.4.3 Duval et al.

The algorithm by Duval et al. (2012) has three stages. Firstly, five circular Regions-of-Interest (RoI) are extracted around each centerline point (automatic, based on (Goldenberg et al., 2012)). Secondly, for each extracted RoIs, thirteen features are calculated based on intensity and Haar-like features using suitably partitioned RoIs. To combat the inherent centerline detection error the same calculations are repeated on four neighbors of each centerline point. Thirdly, five independent random forests are used corresponding to the centerline point and its neighbors. The stenosis is deemed present if all the random forests are in agreement.

4.4.4 Eslami et al.

The algorithm by Eslami et al. (2012) has three stages. First, the CTA is resampled with multiple cross sectional planes, employing the provided centerlines (manually refined, based on Yang et al. (2011)) to construct a cylindrical representation of the underlying vessel. Secondly, segmentation is performed using an inflating tube technique, starting from vessel centerline. Finally, stenoses are detected and quantified by comparing the extracted lumen area with the second order regression of the lumen area over the vessel length. Furthermore, the intensity of boundary voxels is contrasted against the intensity of left ventricle cavity and myocardium to take into account the partial volume effect.

4.4.5 Flórez-Valencia et al.

The algorithm by Flórez Valencia et al. (2012) has three stages. First, an axis is extracted using Dijkstra's algorithm with costs calculated as in Gülsün and Tek (2008). Second, a tracking algorithm is used along this axis, smoothed by a Bezier curve, to construct a generalized cylindrical model of the artery from cross-sectional contours segmented

using Fast-Marching (Baltaxe Milwer et al., 2007). The parameters of the model are deduced from these contours and corrected by a Kalman state estimator. Finally, stenoses are detected and quantified assuming that diameters of healthy arteries should decrease linearly from the ostium. Hence, the estimated diameters are compared to theoretical ones.

4.4.6 Lor et al.

The algorithm by Lor and Chen (2012) has three stages. First, a Gaussian distribution is utilized to adaptively locate the center of cross-sectional plaque with the variance of the posterior density as the plausible size. Such a concentric model is also applied to segment the vessel lumen. Second, the quantitative evaluation of diameter stenosis is determined using Kalman filtering. Finally, the stenosis degree is given using a Bayes classifier based on the posterior probability of severity conditioned on stenosis percentage and plaque type of the training data. The method was evaluated based on the centerline extracted by the vascular segmentation developed by Yang et al. (2012).

4.4.7 Melki et al.

The algorithm by Melki et al. (2012) has three main stages. First, the coronary arteries tree is constructed using the provided centerlines (automatic, based on (Goldenberg et al., 2012)). Common parts of the centerlines are merged in order to organize the whole tree in a set of disjoint segments. Second, a first step of stenosis candidate detection is applied using the vessel cross section area profile. Regions showing a deviation higher than 50% of a synthetic lumen area profile are flagged. Finally, they apply a false positive removal step in order to eliminate the erroneous candidates. This step is performed by inspecting the appearance properties of each flagged region.

4.4.8 Mohr et al.

The algorithm by Mohr et al. (2012) has four stages. First, initialization steps are performed including generating an orthogonal image stack from the provided centerlines (automatic, based on Goldenberg et al. (2012)) and estimating the lumen and wall segmentation. Second, calcium is identified using Bayes Information Criterion, and lumen and wall tissue is classified by Expectation-Maximization assuming Gaussian distributions in segments along the vessel. Third, the lumen segmentation is refined using a level-set driven by a speed function including the a posteriori probabilities obtained from the classification. Finally, stenoses are identified and quantified by estimating the expected vessel profile using line fitting.

4.4.9 Öksüz et al.

The algorithm by Öksüz et al. (2012) consists of five stages. First pulmonary vessels are removed with thresholding and morphological operations. Afterwards, Frangi et al. (1998) vesselness filter is applied on the processed data. Vessel segmentation is realized by 3D region growing and fast marching, respectively. Plane fitting is performed on

every centerline point (manually refined centerline, Yang et al. (2011)), where the corresponding vessel diameter is computed. Finally, a running window based median filtering followed by smoothing is applied, and nominal vessel diameter is estimated by linear regression. A positive difference between computed and estimated diameter values is defined as stenosis at that location.

4.4.10 Shahzad et al.

The algorithm by Shahzad et al. (2012b) has three stages. First, centerlines are extracted using a two point minimum cost path approach (Metz et al., 2009) and are subsequently refined, after which bifurcations are detected. The resulting centerlines represent the vessel segments, and are used as an initialization for the lumen segmentation, performed using graph cuts and robust kernel regression (Schaap et al., 2009b). Finally, the expected diameter of the healthy lumen is estimated by applying robust kernel regression on the coronary artery lumen diameter profile; stenoses are subsequently detected and quantified by computing the difference between estimated and expected diameter profiles.

4.4.11 Wang et al.

The algorithm by Wang et al. (2012) has four stages. It uses an implicit model-guided level set method. First, a 3D vessel model from a set of initial centerlines (automatic, based on Goldenberg et al. (2012)) is generated. Second, this model is incorporated in the level set propagation to regulate the growth of the vessel contour. Third, new centerlines are extracted after evolving the level set and the diameter of vessels is re-estimated in order to generate a new vessel model. Finally, the propagation and remodeling steps are repeated until convergence. For detecting and quantifying stenoses, the proposed method was run twice with different parameter settings to segment the outer wall and the lumen.

4.5 Results

The results presented in this section are based on the algorithms presented at the MICCAI'12 workshop (*http://coronary.bigr.nl/stenoses/*). Since the MICCAI'12 workshop, the ranking strategy has been modified. As a consequence, for each team that participated to the MICCAI'12 workshop, the public results available on our website are different from the one reported in their workshop paper.

Space limitations prevent us from incorporating more statistics here, but the on-line evaluation framework provides the possibilities to rank the methods on different measures or scores, and create statistics on a subset of the data (per vendor). The website also contains the most recent version of the results. The on-line results can be different from the results reported in this paper, as new submissions or method improvements may have occurred.

In this Section, result tables also contain the results of the observers, which have been scored in the same ways as the other evaluated methods. It should be noted that,

Table 4.7: Performance of the 11 evaluated methods, 3 observers and their consensus for the detection of coronary artery stenoses (≥ 50% diameter reduction) on the 30 testing datasets. True positive (TP), false positive (FP), false negative (FN), true negative (TN), average false positive detection per patient (FP/pat). QCA analysis is *segment-based*; 394 segments evaluated, prevalence of disease is 7%. CTA analysis is *lesion-based*. The values in bold correspond to the best performance for each measure. Methods are listed by alphabetic order.

Method	QCA				CTA			
	TP	FP	FN	TN	TP	FP	FN	FP/pat
CTA consensus	*23*	*21*	*5*	*345*	*47*	*0*	*0*	*0*
Observer 1	*24*	*36*	*4*	*330*	*39*	*25*	*8*	*0.8*
Observer 2	*21*	*20*	*7*	*346*	*33*	*8*	*14*	*0.3*
Observer 3	*18*	*24*	*10*	*342*	*31*	*21*	*16*	*0.7*
Broersen et al.	7	30	21	336	13	29	34	1.0
Cetin and Unal	15	63	13	303	25	71	22	2.4
Duval et al.	16	115	12	251	20	243	27	8.1
Eslami et al.	**19**	183	**9**	183	24	570	23	19
Flórez Valencia et al.	5	54	23	312	7	140	40	4.4
Lor and Chen	14	87	14	279	15	484	32	16.1
Melki et al.	13	94	15	272	20	196	27	6.5
Mohr et al.	16	95	12	271	24	129	23	4.2
Öksüz et al.	6	21	22	345	8	23	39	0.8
Shahzad et al.	1	**7**	27	**359**	**26**	71	**21**	2.4
Wang et al.	7	**7**	21	**359**	5	**10**	42	0.3

as the CTA reference standard was derived from a consensus reading of the same 3 observers, the observers' performance for coronary stenoses detection and quantification as compared to CTA reference standard may be biased at their advantage.

4.5.1 Detection of stenosis

The ability of a method to discriminate significant stenoses from non-significant ones is evaluated. Table 4.8 shows the average results and ranking of the 11 submissions (5 fully automatic, 6 semi-automatic) and 3 observers for stenosis detection measures: sensitivity and PPV. In the overall ranking, the algorithms of Cetin and Unal (2012) and Mohr et al. (2012) rank the first, in the semi-automatic and automatic category respectively.

As compared to QCA (*segment-based* analysis), the best sensitivity (68%) was achieved by the method proposed by Eslami et al. and the best PPV (50%) was obtained with the algorithm of Wang et al..

As compared to CTA (*lesion-based* analysis), the best sensitivity (55%) was achieved by the method proposed by Shahzad et al. and the best PPV (33%) was obtained with the algorithm of Wang et al.. Here, the results were worse than the average observers' performance (sensitivity of 73%, PPV of 67%). With respect to the CTA reference standard and over all calcium categories, the approach of Mohr et al. tends to over-estimate the degree of mild stenoses, thus increasing the number of FP detections, and under-estimate the degree of significant stenoses (especially moderate ones), thus increasing

Table 4.8: Performance of the 11 evaluated methods, 3 observers and their consensus for the detection of coronary artery stenoses (≥ 50% diameter reduction) on the 30 testing datasets. The values in bold correspond to the best performance for each measure. QCA analysis is *segment-based*; CTA analysis is *lesion-based*.

Method	Cat.	QCA				CTA				Avg. rank
		Sensitivity		PPV		Sensitivity		PPV		
		%	Rank	%	Rank	%	Rank	%	Rank	
CTA consensus	*Manual*	*82*	*1.0*	*52*	*1.0*	*100*	*1.0*	*100*	*1.0*	*1.2*
Observer 2	*Manual*	*75*	*3.0*	*51*	*2.0*	*70*	*3.0*	*81*	*2.0*	*2.5*
Observer 1	*Manual*	*86*	*1.0*	*40*	*5.0*	*83*	*2.0*	*61*	*3.0*	*2.8*
Observer 3	*Manual*	*64*	*5.0*	*43*	*4.0*	*66*	*4.0*	*60*	*4.0*	*4.2*
Cetin and Unal	Min. user	54	8.0	19	7.0	53	6.0	26	8.0	7.2
Mohr et al.	Auto.	57	6.0	14	9.0	51	7.0	16	10.0	8.0
Wang et al.	Auto.	25	11.0	**50**	3.0	11	15.0	**33**	5.0	8.5
Broersen et al.	Auto.	25	11.0	18.9	8.0	27.7	12.0	31	6.0	9.2
Shahzad et al.	Min. user	4	15.0	13	11.0	**55**	5.0	27	7.0	9.5
Eslami et al.	Min. user	**68**	4.0	9	14.0	51	7.0	4	14.0	9.8
Duval et al.	Auto.	57	6.0	12	12.0	43	9.0	8	12.0	9.8
Öksüz et al.	Min. user	21	13.0	22	6.0	17	13.0	26	9.0	10.2
Melki et al.	Auto.	46	10.0	12	13.0	43	9.0	9	11.0	10.8
Lor and Chen	Min. user	50	9.0	14	10.0	32	11.0	3	15.0	11.2
Flórez Valencia et al.	Min. user	18	14.0	9	15.0	15	14.0	5	13.0	14.0

Table 4.9: Performance of the 11 evaluated methods, 3 observers and their consensus for the *per-patient* detection of coronary artery stenoses ($\geq$ 50% diameter reduction) on the 30 testing datasets. Prevalence of disease: 60%. The values in bold correspond to the best performance for each measure (sensitivity, specificity, positive predictive value, negative predictive value). Methods are listed by alphabetic order. Results in percentage. **NA* in case (TN + FN) is null.

Method	Cat.	QCA				CTA			
		Sens.	**Spec.**	**PPV**	**NPV**	**Sens.**	**Spec.**	**PPV**	**NPV**
CTA consensus	*Manual*	*94*	*67*	*81*	*89*	*100*	*100*	*100*	*100*
Observer 2	*Manual*	*100*	*58*	*78*	*100*	*95*	*78*	*91*	*88*
Observer 1	*Manual*	*94*	*50*	*74*	*86*	*95*	*67*	*87*	*86*
Observer 3	*Manual*	*94*	*75*	*85*	*90*	*86*	*75*	*90*	*67*
Broersen et al.	Auto.	72	42	65	50	71	44	75	40
Cetin and Unal	Min. user	94	50	74	86	90	33	75	60
Duval et al.	Auto.	94	33	68	80	86	25	76	40
Eslami et al.	Min. user	**100**	0	57	NA	**100**	0	70	NA
Flórez Valencia et al.	Min. user	**100**	8	62	**100**	**100**	0	63	NA
Lor and Chen	Min. user	**100**	7	55	**100**	**100**	0	70	NA
Melki et al.	Auto.	**100**	8	62	**100**	95	0	69	0
Mohr et al.	Auto.	**100**	0	63	NA	**100**	0	70	NA
Öksüz et al.	Min. user	74	73	82	62	76	67	**84**	55
Shahzad et al.	Min. user	28	**92**	**83**	46	100	44	81	**100**
Wang et al.	Auto.	39	83	78	48	33	**78**	78	33

Table 4.10: Performance of the 8 evaluated methods, 3 observers and their consensus for the quantification of coronary artery stenoses on the 30 testing datasets. The quantification measures are computed using the union of the submitted lesions and the reference ones, thus including not only the TP, but also the FP and FN, to assess the whole system accuracy. The values in bold correspond to the best performance for each measure.

Method	**Cat.**	**QCA**				**CTA**		**Avg. rank**
		Avg. Abs. Diff.		**R.M.S. Diff.**		**Weighted Kappa**		
		%	Rank	%	Rank	κ	Rank	
CTA consensus	*Manual*	*28.8*	*3.0*	*34.4*	*3.0*	*1.00*	*1.0*	*2.0*
Shahzad et al.	Min. user	**21.1**	1.0	**29.1**	1.0	**0.28**	5.0	3.0
Observer 1	*Manual*	*30.1*	*4.0*	*35.2*	*4.0*	*0.74*	*3.0*	*3.5*
Observer 2	*Manual*	*31.1*	*6.0*	*36.5*	*5.0*	*0.77*	*2.0*	*3.8*
Observer 3	*Manual*	*30.6*	*5.0*	*36.9*	*6.0*	*0.73*	*4.0*	*4.8*
Wang et al.	Auto.	28.8	2.0	33.7	2.0	0.18	8.0	5.0
Broersen et al.	Auto.	32.5	7.0	39.3	7.0	0.27	6.0	6.5
Öksüz et al.	Min. user	47.0	9.0	53.1	9.0	0.21	7.0	8.0
Lor and Chen	Min. user	38.6	8.0	42.7	8.0	-0.03	12.0	10.0
Mohr et al.	Auto.	49.6	10.0	56.0	12.0	0.15	9.0	10.0
Flórez Valencia et al.	Min. user	51.6	12.0	55.6	11.0	0.01	10.0	10.8
Eslami et al.	Min. user	50.9	11.0	55.0	10.0	-0.02	11.0	10.8

Table 4.11: Performance of the 5 evaluated methods for coronary artery lumen segmentation on the 30 testing datasets. The values in bold correspond to the best performance for each measure.

Method	Cat.	DICE				MSD				MaxD				Avg. rank
		Diseased		Healthy		Diseased		Healthy		Diseased		Healthy		
		%	Rank	%	Rank	mm	Rank	mm	Rank	mm	Rank	mm	Rank	
Observer 3	*Manual*	*79*	*1.6*	*81*	*1.3*	*0.23*	*2.0*	*0.21*	*1.5*	*3.00*	*5.1*	*3.45*	*4.9*	*2.7*
Mohr et al.	Auto.	**70**	3.6	**73**	3.4	**0.40**	4.2	**0.39**	3.8	**2.68**	2.9	**2.75**	2.2	3.3
Observer 1	*Manual*	*76*	*2.3*	*77*	*3.2*	*0.24*	*2.6*	*0.24*	*2.8*	*2.87*	*4.3*	*3.47*	*4.8*	*3.4*
Observer 2	*Manual*	*65*	*5.0*	*72*	*4.9*	*0.34*	*4.7*	*0.27*	*3.7*	*2.82*	*4.5*	*3.26*	*4.3*	*4.5*
Shahzad et al.	Min. user	58	6.3	66	5.8	0.49	6.5	0.43	5.3	2.81	5.0	3.05	3.0	5.2
Wang et al.	Auto.	69	4.5	69	4.6	0.45	5.4	0.5	5.9	3.94	5.7	6.48	5.9	5.4
Broersen et al.	Auto.	67	4.5	69	4.9	0.50	5.8	0.70	5.9	3.89	5.4	5.86	5.7	5.4
Flórez Valencia et al.	Min. user	42	7.8	38	7.7	0.83	7.2	1.13	7.7	3.81	4.4	6.96	5.6	6.8

the number of FN detections and, consequently, penalizing the sensitivity. Their QCA sensitivity (57%) was less affected, probably because the degree of stenosis is generally over-estimated in CTA as compared to QCA (calcified lesions, due to blooming artifact), which compensates for under-estimation on CTA.

In addition, Table 4.7 presents the performance of the methods in terms of TP, FP and FN detections, with respect to QCA and CTA reference standard. Overall, a good TP detection rate was achieved at the expense of FP and/or FN rates, and vice-versa. Note that for many of the methods, the number of reported FP was very large; these methods are therefore not yet suitable for implementation in clinical practice (i.e. risk of overwhelming the clinician). The current results highlight that discrimination between significant and non-significant lesions remains a challenge and that a trade-off between the ability to detect significant lesions and the ability of ruling out disease needs to be made.

Last, Table 4.9 presents the diagnostic performance of the methods, observers and consensus for the detection of significant stenosis on QCA and CTA in a *per-patient* analysis. The sensitivity, specificity, PPV and NPV, with respect to CCA and CTA reference standard are reported. The results indicate that half of the methods (Eslami et al.; Flórez Valencia et al.; Lor and Chen; Melki et al.; Mohr et al.) are not yet able to perform triage of the patients to rule out significant coronary artery disease, as they achieve very low specificity. Three methods (Broersen et al.; Duval et al.; Wang et al.) perform relatively good as compared to the observers. The last three methods (Cetin and Unal; Öksüz et al.; Shahzad et al.) have a diagnostic performance close to the observer's one, and thus may be considered to be used as computer-aided triage systems, or as a second reader, where a high sensitivity is required and false positives are *reasonably* acceptable.

4.5.2 Quantification of stenoses

Less-obstructive plaques outnumber severely obstructive plaques (Falk et al., 1995), and most occlusions result from progression of the former plaques. It is thus as crucial to detect mildly to moderately obstructive lesions (20% to 70%) as to detect severely obstructive plaque ($\geq 70\%$). We therefore investigated the ability of a method to correctly estimate the degree of obstruction.

Table 4.10 shows the average results and ranking of 8 submissions (3 fully automatic, 5 semi-automatic) and 3 observers for stenosis quantification measures. Here, the quantification measures are computed using the union of the submitted lesions and the reference ones (i.e. including not only the TP, but also the FP and FN) to assess the whole system accuracy. For the Kappa statistic, a fixed number of negative detection TN is used, and is determined as follows:

$$\mathrm{TN} = \mathrm{N} \times 48 = \mathrm{TN}_{\mathrm{algorithm}} + \mathrm{FP}_{\mathrm{algorithm}} \tag{4.5}$$

with N the number of datasets, and $\mathrm{TN}_{\mathrm{algorithm}}$ and $\mathrm{FP}_{\mathrm{algorithm}}$ the true negative and false positive detections of the algorithm respectively.

First, as the observers quantified the coronary stenoses using semi-quantitative grades (see Section 4.3.4 and Table 4.1), their grades were converted to quantitative values (i.e. number between 0 and 100) for the comparison with QCA: a stenosis reported as being

mild on CTA was assigned to be 35% on QCA, moderate to be 60%, severe to be 80% and occluded to be 100%. This explains the relatively large observers' errors with respect to QCA. Second, some methods detect a large number of FP stenoses in CTA (Table 4.7); this is consequently expressed by negative or nul Kappa values (algorithms of Eslami et al., Lor and Chen and Flórez Valencia et al.). Identically, detecting too many FP in QCA would penalize the algorithm, by increasing their average absolute and root mean square differences.

The method proposed by Shahzad et al. achieves the best quantification results as compared to QCA, with an averaged absolute difference of 21% and a RMS difference of 29%. This method outperforms the observers and all the other methods. This is due to their low number of FP detections. The method of Shahzad et al. also achieves the best performance with regard to the Kappa value ($\kappa = 0.28$). Though their Kappa value is positive, it remains relatively low. This may either be caused by a high number of FP or FN, or by a high number of lesions reported with more than one grade difference as compared to the CTA reference.

The quantification results show that current stenosis quantification algorithms are not sufficiently reliable to be used stand-alone in clinical practice, but could be used as a second-reader.

4.5.3 Lumen segmentation

Table 4.11 shows the average results and ranking of 5 submissions (3 fully automatic, 2 semi-automatic) and 3 observers for coronary artery lumen segmentation. The method proposed by Mohr et al. outperforms all the other methods, as well as two of the observers.

Overall, though the Dice value obtained on healthy vessel segments is higher than the one obtained on diseased ones, the mean square distance and maximum distance obtained on healthy segments is higher than the ones obtained on diseased ones, which may be caused by the smaller scale of the diseased vessel.

Figure 4.10 provides a visual impression for segment LAD7 of dataset#08 of the reference standard of observer#1 (top) and evaluated algorithms of respectively Broersen et al., Flórez Valencia et al., Mohr et al., Shahzad et al., and Wang et al.. Dataset #08 presents a severe mixed plaque in segment LAD7. While the algorithms of Mohr et al., Broersen et al. and Wang et al. successfully segment the diseased vessel segment as compared to the reference from the observer #1, the last two algorithms tend to undersegment the soft plaque. In this case, both the algorithm of Flórez Valencia et al. and Shahzad et al. fail to segment the mixed plaque: the first include the calcified part of the lesion within the segmentation, while the second is attracted towards the calcium spot. Note for this particular view of the vessel, the method of Shahzad et al. and Broersen et al. fail to display segmentation at some vessel position; in fact, their segmentation lies in another plane, and thus, no intersection was available.

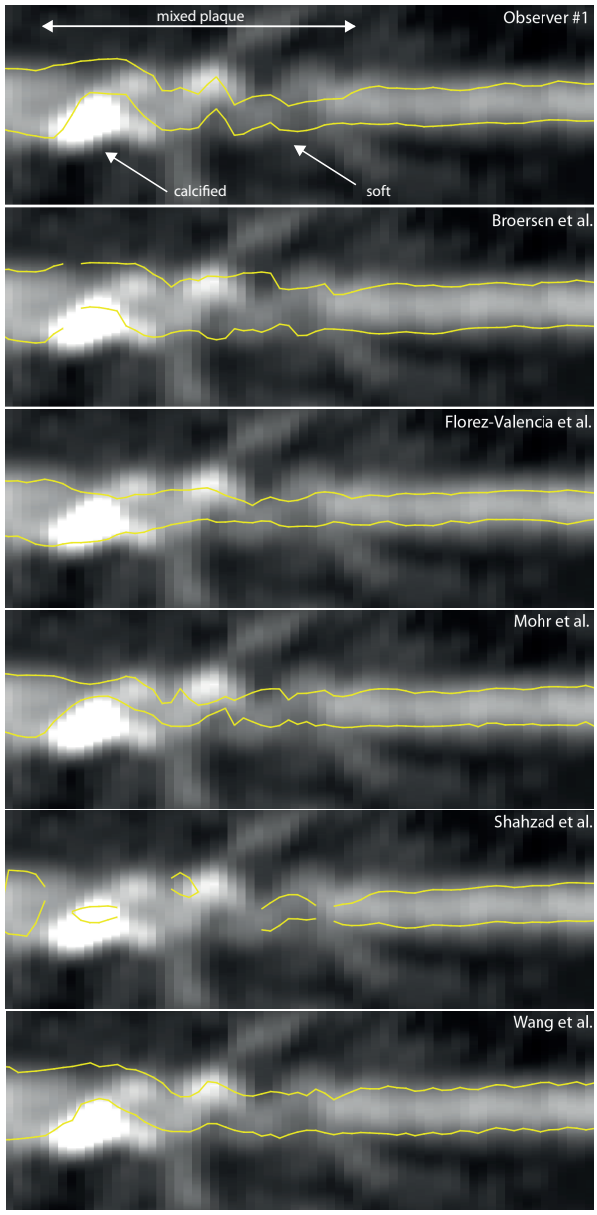

Figure 4.10: Lumen segmentation example for training dataset #08. Visual impression of the reference standard of observer#1 and evaluated algorithms of Broersen et al., Flórez Valencia et al., Mohr et al., Shahzad et al., and Wang et al.. Dataset #08 presents a severe mixed plaque in segment LAD7. Note that for this particular view of the vessel, the method of Shahzad et al. and Broersen et al. fail to display segmentation at some vessel position; in fact, their segmentation lies in another plane, and thus, no intersection was available.

4.6 Discussion

We presented a standardized evaluation framework allowing the effective comparison of coronary artery stenosis detection and quantification methods, and coronary lumen segmentation algorithms, on CTA images. The framework has been used to compare 11 algorithms as part of the "3D Cardiovascular Imaging: a MICCAI segmentation challenge" workshop at MICCAI'12, and remains publicly available via the website *http://coronary.bigr.nl/stenoses/*.

4.6.1 Evaluation framework

The quality of an evaluation framework critically relies on the datasets that are made available for training and testing, and the quality of the reference standard. In our framework, currently, 48 cardiac CTA datasets with corresponding reference standard are available. Datasets were acquired at three different Dutch medical centers, with CT scanners from three different vendors (Siemens Healthcare, Philips Healthcare and Toshiba Medical Systems), ensuring that algorithms would not be biased toward a specific scanner or acquisition protocol. The datasets were carefully selected in order to be representative of the types of pathologies which occur in clinical practice. Unfortunately, we were not able to include datasets from one of the remaining main CT scanner vendors (GE Healthcare) in the current framework. Also, it may be interesting to include CTA images acquired with 1) various acquisition protocols (retro/prospective ECG gating, flash mode, low-dose), 2) different reconstruction modes (different kernels), and 3) with different scanner models from a single vendor. Thus, the variety of CTA datasets provided in our framework could still be improved.

In our framework, we utilized two reference standards: the performance of (semi-) automatic algorithms designed to detect and quantify stenoses was evaluated using both CTA consensus reading and QCA analysis.

Creating a reference standard with multiple observers is a tedious and complex task. To build the CTA reference standard, multiple observers annotated the datasets, which annotations were then combined. Even though the same guidelines were given to all the observers, their annotations were not always consistent, thus making a merging step necessary. For instance, defining the start and end of a lesion can be challenging, especially in case of diffuse disease. One observer may indicate that a whole segment is diseased (leading to a single stenosis which extends over the whole segment), while another may indicate multiple smaller stenoses with varying degrees. Such disagreements between observers were solved during the consensus reading.

Another challenge is to build references from CTA and QCA which are consistent. As two different modalities are used, one providing 3D images and one providing 2D images, the observers' interpretation may considerably differ. Though the same coronary tree nomenclature was provided to CTA and QCA observers, mismatches between segments may occur: a stenosis detected at the end of the proximal LAD segment (LAD6) on the CTA image may be visualized as being in the proximal part of the mid LAD segment (LAD7) on QCA. To avoid such mismatch, the QCA reference has been corrected to match the CTA reference. Second, there can be detection/quantification mismatch: a significant

stenosis may be reported in a certain segment on CTA, while no stenosis is reported on QCA, and vice-versa. Segments presenting mild stenoses on the CTA images usually do not present any obstruction on the CCA. Also, it may occur that, due to blooming artifacts caused by calcified plaque, motion artifacts or reduced image quality, a stenosis is overestimated on CTA, and is thus not present on the CCA image. Reversely, a stenosis detected on the CCA and not visible in CTA may be caused by an erroneous computation of the QCA, for instance by using wrong landmarks to estimate the "normal" vessel diameter immediately adjacent to the stenosis.

A limitation of the current evaluation framework is the point-based definition of stenosis location. Participants should provide a *single* point per stenosis, which is generally the central point. This may result in mismatches between the stenoses detected by the methods and the reference standard. If the method returns a series of smaller stenoses while the reference indicates a larger one, there is no mismatch: the large reference stenosis is detected, and will be assigned the average of the grades of the short stenoses. However, in the opposite case there will be mismatch: in the best case, only one of the reference stenoses will be correctly matched (i.e. if the provided point lies within the range of one of the small reference stenoses). Potentially, a better matching procedure could be implemented, which would take the *start* and *end* points of the stenoses as input. However, we believe that this situation occurs relatively infrequently. In addition, if a series of small stenoses has been reached by concensus, it could be argued that a method should detect this in a similar manner.

A second limitation is the use of hard classification into categories by the observers. For example, for a specific plaque, a method may yield a stenosis degree of 49%, while an observer grades the lesion as being moderate and the QCA reveals a 52% stenosis. Although the methods' stenosis degree estimation is close to the observers' one, the hard detection threshold at 50% would penalize the method, classifying its result as a FN. A potential solution would be to add a *borderline* category, so that the algorithm would not be punished neither for reporting nor for missing *borderline* stenoses. Another solution would be to use ROC curves for evaluating the algorithm performance. However, we believe that this limitation has had little impact in the overall evaluation, as in the current 48 datasets consisting of 637 coronary artery segments, only 15 of them had a QCA between 45% and 55%.

Last, as indicated in Section 5, the three observers' performance for coronary stenoses detection and quantification as compared to CTA reference standard may be biased at their advantage, as the CTA reference standard was derived from a consensus reading of the same three observers. To allow a fair comparison of the observers' performance with both the CTA reference standard and other evaluated methods, coronary artery detection and quantification in CTA should be obtained from different observers than the ones involved in the consensus reading.

4.6.2 Evaluated algorithms

The aim of our standardized evaluation framework is to provide an objective methodology to compare the performance of different algorithms for certain clinical tasks. It is hence important, that the framework is adopted by all state-of-the-art algorithms. In

the MICCAI challenge, 11 algorithms have been evaluated using the proposed framework, showing the potential of the framework to achieve this. However, not all recently published methods have yet been evaluated with our framework.

The authors of previously published stenosis detection algorithms, i.e. the ones presented in Table 4.2 were all invited by e-mail to participate in our MICCAI challenge, but none of them did and we did not further investigate why these groups did not participate.

Since the evaluation framework remains accessible, we hope and expect that an increasing number of algorithms will be evaluated. From the previous challenges we organized (Schaap et al., 2009a; Hameeteman et al., 2011), we know that this indeed happens. Also, for newly published methods, reviewers of journals typically require a method to be evaluated using such standardized frameworks.

4.6.3 Evaluation results

Nine of the eleven evaluated algorithms are developed following the work-flow of Figure 4.3, consisting of 1) the computation of an accurate lumen segmentation, either directly from the input CTA image or using previously extracted centerlines, and 2) the subsequent detection (and quantification) of coronary artery stenoses by estimate of the healthy vessel (Broersen et al., 2012; Eslami et al., 2012; Flórez Valencia et al., 2012; Mohr et al., 2012; Öksüz et al., 2012; Shahzad et al., 2012b; Wang et al., 2012), or by analysis of intensity and geometry features (Lor and Chen, 2012; Melki et al., 2012). Though the nine methods actually segment the lumen, only five of them participated in the segmentation sub-challenge (exceptions are Eslami et al. (2012), Lor and Chen (2012), Melki et al. (2012) and Öksüz et al. (2012)). The lumen segmentation results show that the moderate detection and quantification performances of the algorithm proposed by Flórez Valencia et al. (2012) stem directly from the poor lumen segmentation results. To detect and quantify lesions, six of the algorithms estimated a "healthy" lumen radius using various regression approaches on the segmented lumen radius profile (linear for the approaches of Broersen et al. (2012), Flórez Valencia et al. (2012), Mohr et al. (2012) and Öksüz et al. (2012), second-order for the approach of Eslami et al. (2012), robust for the approach of Shahzad et al. (2012b)). In the algorithm proposed by Wang et al. (2012) only, the outer vessel wall was segmented from the CTA image. Given similarly accurate lumen segmentation, the algorithm proposed by Shahzad et al. (2012b) outperforms the approaches proposed by Broersen et al. (2012) and Wang et al. (2012) at the quantification stage. The results thus suggest that robust regression seems to be a good approach to quantify lesions from accurate lumen segmentation. Last, the algorithm proposed by Mohr et al. (2012) outperforms the three others at the segmentation stage, which suggests that tissue classification and calcium segmentation performed prior to lumen segmentation is a very promising approach.

Only one of the evaluated algorithms is not involving accurate lumen segmentation, but is using features information extracted from the CTA image to detect plaques (Duval et al., 2012). Though reasonable sensitivity is achieved, the methods' performance is penalized by the important amount of reported FPs detections, and is therefore ranked just after the algorithms cited in previous paragraph (which make use of accurate lumen segmentation and regression) for detection.

The algorithm proposed by Cetin and Unal (2012), which makes use of both accurate lumen segmentation and feature extraction to detect lesions, seems very promising as it ranks first for detection.

Last, though the vessel lumen can be automatically segmented with a precision similar to the expert's one, detection and quantification of coronary artery stenosis is still not a solved problem; performance of the quantification is in general much worse than the observers.

The evaluation of the 11 different algorithms with the standardized evaluation framework provides useful directions for further investigations. First, it may be interesting to investigate the robustness of the segmentation methods with regard to the initial centerline used. Also, it would be interesting to combine the best segmentation method with the best detection and quantification method, and to combine the results of several algorithms and investigate whether a combination of algorithms outperforms the best single algorithm (Niemeijer et al., 2011).

To conclude, a clear limitation of our challenge remains that the evaluated algorithms are not available. In the future, the concept of a challenge would benefit from a framework where the evaluated algorithms become publicly available, such that it becomes possible to run the submitted algorithms on other datasets, without having to re-implement the complete pipeline, which is often tedious, if not possible at all, given that in literature often all information and/or data required to reproduce an algorithm is not available.

4.7 Conclusion

A publicly available evaluation framework to compare coronary artery stenosis detection and quantification methods, as well as lumen segmentation algorithms was presented in this article. The results showed that current stenosis detection/quantification algorithms are not sufficiently reliable to be used stand-alone in clinical practice, but that some could be used for triage or as a second-reader, and that automatic lumen segmentation is possible with a precision similar to the expert's one. The evaluation framework remains open for new submissions at *http://coronary.bigr.nl/stenoses/*.

chapter 5

Comprehensive visualization of multimodal cardiac imaging data for assessment of coronary artery disease: first clinical results of the SMARTVis tool

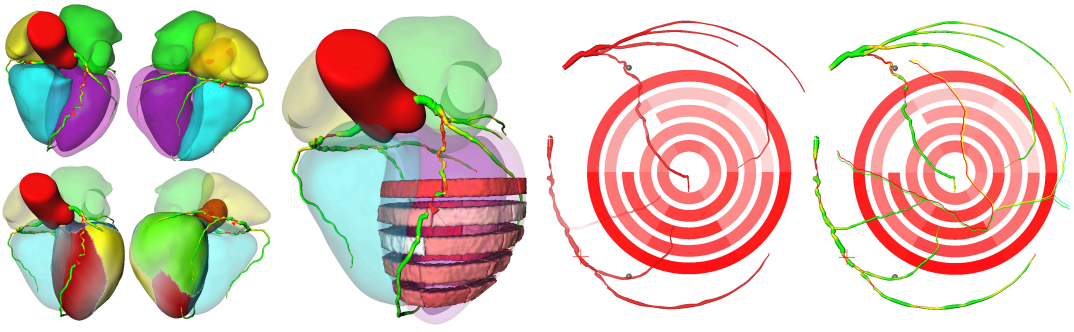

This chapter is based on the manuscript:
Comprehensive visualization of multimodal cardiac imaging data
for assessment of coronary artery disease: first clinical results of the SMARTVis tool,
H.A. Kirişli, V. Gupta, S. Kirschbaum, A. Rossi, C.T. Metz, M. Schaap, R.J. van Geuns,
N.R.A. Mollet, B.P.F. Lelieveldt, J.H.C. Reiber, T. van Walsum and W.J. Niessen,
International Journal of Computer Assisted Radiology and Surgery, 7(4):557–571, 2012.

Abstract

Purpose In clinical practice, both coronary anatomy and myocardial perfusion information are needed to assess coronary artery disease (CAD). The extent and severity of coronary stenoses can be determined using computed tomography coronary angiography (CTCA); the presence and amount of ischemia can be identified using myocardial perfusion imaging, such as perfusion magnetic resonance imaging (PMR). To determine which specific stenosis is associated with which ischemic region, experts use assumptions on coronary perfusion territories. Due to the high variability between patient's coronary artery anatomies, as well as the uncertain relation between perfusion territories and supplying coronary arteries, patient-specific systems are needed.
Methods We present a patient-specific visualization system, called Synchronized Multimodal heART Visualization (SMARTVis), for relating coronary stenoses and perfusion deficits derived from CTCA and PMR respectively. The system consists of the following comprehensive components: 1) two or three dimensional fusion of anatomical and functional information, 2) automatic detection and ranking of coronary stenoses, 3) estimation of patient-specific coronary perfusion territories.
Results The potential benefits of the SMARTVis tool in assessing CAD were investigated through a case-study evaluation (conventional vs. SMARTVis tool): two experts analyzed four cases of patients with suspected multivessel coronary artery disease. When using the SMARTVis tool, a more reliable estimation of the relation between perfusion deficits and stenoses led to a more accurate diagnosis, as well as a better interobserver diagnosis agreement.
Conclusions The SMARTVis comprehensive visualization system can be effectively used to assess disease status in multivessel CAD patients, offering valuable new options for the diagnosis and management of these patients.

5.1 Introduction

Coronary artery disease (CAD) is a major cause of death worldwide (Roger et al., 2012). Oxygen and nutrients, which are required for normal heart function, are supplied to the myocardium (i.e. the heart muscle) by the blood traveling through the coronary arteries. If a coronary artery becomes narrowed or occluded with build-up of plaque (e.g. cell, fat and cholesterol), the amount of blood flowing to the myocardium is reduced and, thus, less oxygen and nutrients are delivered to these myocardial regions. The restriction in blood and oxygen is called *ischemia* and the narrowing of vessel is called *stenosis*. Coronary artery stenoses can either cause temporary changes to these ischemic myocardial regions or, if the myocardium is not supplied with sufficient blood during a too long period, can cause death of the myocardial tissue, which can lead to myocardial infarction.

Many tests are available for detecting and diagnosing CAD, such as electrocardiograms, exercise stress tests, echocardiograms, nuclear scan tests, stress thallium tests and angiography. Each of these tests has unique advantages, the choice of which (and how many) tests to perform is determined by the patient's history and current symptoms. In current clinical practice, angiography is the gold standard imaging technique for diagnosing CAD; the location, the number and the severity of the vessel stenoses can be determined. Nevertheless, computed tomography coronary angiography (CTA) imaging technique is gaining popularity (Weustink and de Feyter, 2011); it (non-invasively) provides high-resolution images of the cardiac and coronary artery anatomy, which allow assessment of the presence, extent and type (calcified or non-calcified) of coronary plaques (i.e. stenoses). Depending on the location and information regarding the severity of the stenoses, an ischemic test may be required to evaluate if, and to what extent, the obstruction is causing a perfusion defect. Cardiac perfusion magnetic resonance imaging (PMR) is one of the possible ischemic tests; PMR can be used to measure the global and regional myocardial perfusion of the heart (Kirschbaum and van Geuns, 2009; Kirschbaum et al., 2011), and thus provides information on myocardial perfusion abnormalities (i.e. presence of ischemia).

CTA images are analyzed using different visualization techniques, such as multiplanar reformatted (MPR) and curved-planar reformatted (CPR) images; MPR and CPR images are oblique views obtained from axial sections of the CTA images (see Figure 5.1). Conventionally, the interpretation of left ventricular function is performed by visually checking the cardiac PMR images (under rest and stress) and by looking at time-intensity curves (TIC) and perfusion-linked parameters on a bull's eye plot (BEP). Figure 5.2 presents an example of these representations. A BEP is a two dimensional (2D) representation of the three dimensional (3D) myocardium; the left ventricle, which has an ellipsoid shape, is unfolded to a disc. The short-axis left ventricle sections are displayed with rings on the 2D BEP: the most apical slice is plotted at the center, while the most basal slice forms the outermost ring of the BEP.

After independently viewing the CTA and PMR images, the expert needs to *mentally* integrate anatomical and functional information: each myocardial defect has to be assigned to a culprit coronary artery, in order to determine which coronary artery stenoses are in fact hemodynamically significant (i.e. induce a perfusion defect). The potential

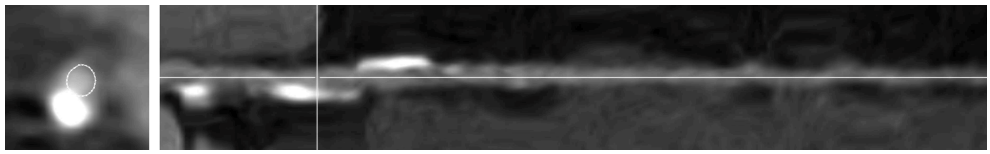

Figure 5.1: Multiplanar reformatted view of a vessel in a computed tomography coronary angiography image. The white cross on the long-axis view (right) shows the position of a calcified plaque. It is synchronized with the short-axis view (left), on which the vessel segmentation (white contour) is overlaid.

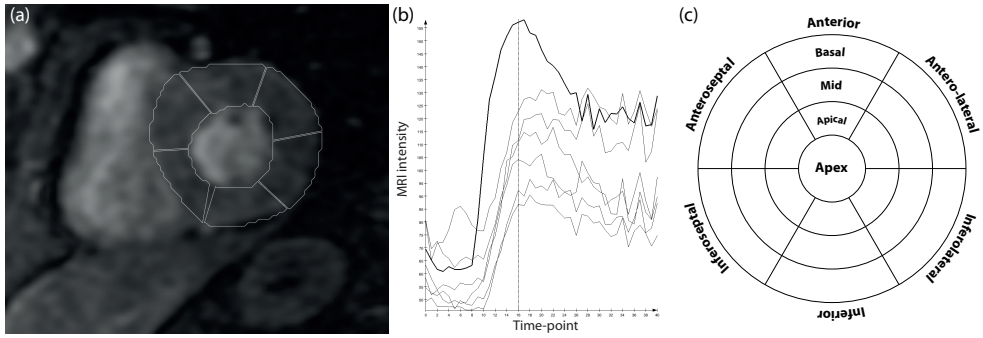

Figure 5.2: (a) Example of a mid-ventricular stress perfusion magnetic resonance slice (b) Corresponding signal-intensity versus time curves for 6 left ventricular segments (black curves) and blood pool (thick black curve), derived from a motion-compensated PMR image sequence (c) Nomenclature of the Bull's Eye Plot

improvement of decision-making in the management of patients is one of the most important reasons for use of integrated imaging; integration of data derived from these complementary (i.e. CTA and PMR) techniques may offer valuable advantages in diagnosis, staging and treatment of CAD. Therefore, there is a need for visualization methods that integrate multimodal cardiac data.

The American Heart Association (AHA) has published some recommendations concerning coronary artery perfusion territories, with respect to their standardized 17-segment BEP model (Cerqueira et al., 2002). However, because variability in coronary anatomy between patients can be high, the use of a standard model may not be optimal. For instance, Pereztol-Valdés et al. (2005) demonstrated that only nine of the 17 AHA-segments are fed by a single coronary artery, while the other eight segments may be fed by more than one coronary artery (Figure 5.3). If the patient only has a single obstructive lesion (i.e. single vessel disease, low-risk patient[1]), it is clear which coronary is causing the perfusion defect, and, thus, integrating information in a patient-specific way would lead to the same diagnosis. Also, symptomatic CAD patients at very-high-risk (i.e. with significant stenoses in the 3 main coronary arteries) would not benefit from such a combined approach, as they are usually immediately referred for revascularization. Consequently, integrating information in a patient-specific way is mainly beneficial

[1] the *risk* refers to the pre-test probability of having CAD.

in the diagnosis of *intermediate-risk patients*, who have suspected stenoses in 2 of the 3 main coronary arteries, as there may be ambiguous assignment of perfusion defects and culprit coronary arteries.

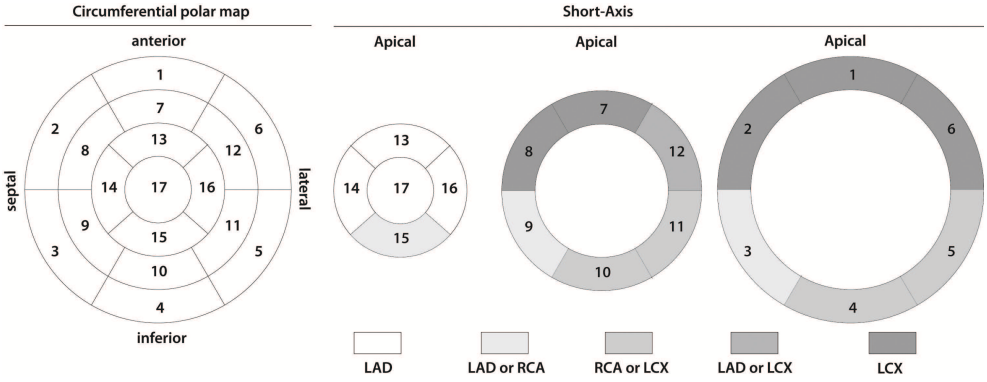

Figure 5.3: Correspondence between the 17 left ventricular myocardial segments and each coronary artery, according to results from Pereztol-Valdés et al. (2005).

In this work, we present several visualization methods, implemented in the Synchronized Multimodal heART Visualization (SMARTVis) tool, that allow a comprehensive analysis of cardiac multimodal imaging data, for assessment of CAD. Our contribution is threefold.

First, we present an innovative integration of image processing methods to (semi)-automatically analyze cardiac multimodal imaging data (e.g. heart segmentation, coronary centerline tracking and lumen segmentation from CTA; registration and segmentation of PMR images).

Second, using the results from the image processing stage, we present comprehensive visualizations for relating coronary stenoses and perfusion defect regions: 1) projection of the coronary artery tree onto a 2D BEP, 2) integration of the perfusion information into a 3D model of the heart, 3) automatic detection and ranking of coronary stenoses, 4) estimation (distance-based) of the patient-specific coronary perfusion territories, and 5) synchronization of the 2D and 3D viewers with CTA and PMR images. To our knowledge, an integration of all of these elements into a single coordinated visual analysis tool is novel, maximizing the diagnostic complementarities of the imaging modalities.

Third, we investigated the benefits of the SMARTVis tool in assessing CAD by performing both a comparative study and a case-study evaluation. Here, two experts analyzed four patients with suspected multivessel disease, using conventional tools and the SMARTVis tool.

Related work is discussed in the following section. In Section 5.3, we describe how information is extracted from multimodal imaging data and comprehensively visualized. Section 5.4 is dedicated to the evaluation of the SMARTVis tool. In Section 5.5, we discuss feedback from the expert clinicians and the limitations of our approach. Finally, Section 5.6 presents the conclusions and possibilities for future studies.

5.2 Related work

Currently, various methods exist to combine multimodal data and they can be divided in two groups: methods that are based on image fusion and ones that use models to integrate multimodal information.

Image fusion, which results in hybrid images, can be used to combine anatomic and functional data: Faber et al. (2004) proposed a method to integrate the information from SPECT myocardial perfusion imaging (SPECT-MPI) with biplane X-ray angiograms, and Gaemperli et al. (2007a) suggested fusing SPECT-MPI with CTA. van Werkhoven et al. (2009) demonstrated that CTA has an incremental prognostic value over SPECT-MPI in patients with suspected CAD. More recently, the feasibility and potential value of the combined analysis of integrated anatomical and functional data have been discussed by Scholte et al. (2010); they concluded that SPECT-MPI/CTA image fusion provides additional clinical value compared to the analysis of either technique alone or side-by-side. Nowadays, the introduction of SPECT-CT and PET-CT systems enables data to be acquired from both modalities in a single session, making hybrid image acquisition even easier.

Model-based visualization techniques can also be used to combine multimodal imaging data Termeer et al. (2007) proposed a comprehensive visualization framework, called CoViCAD, to combine multiple MR images. Here, coronary centerlines were extracted from a whole-heart MR scan and scar tissue was visualized in late-enhancement MR images. At that time, whole-heart MR technology did not provide enough spatial resolution to extract absolute diameter information for the coronary arteries. The coronary artery tree was therefore represented by constant radius tubes around the centerlines; thus, no indication about possible stenosis was provided. In the present work, two novel visualizations are provided: 1) the introduction of a 3D volumetric BEP, which preserves the volumetric nature of the left ventricular wall and thus allows better appreciation of transmurality information, and 2) the overlay of coronary arteries on the epicardial surface of the 3D volumetric BEP, providing additional contextual information.

Termeer et al. (2008) also proposed visualization techniques to study the effect of coronary artery stenosis on myocardial perfusion, using a simulation approach. Here, a coronary tree, with absolute radius, was extracted from a single CTA image. After simulating the blood flow in the coronary arteries with a numerical model, the simulated left ventricle perfusion was visualized on a 2D BEP; under-perfused regions and coronary artery blood supply territories were enhanced. However, such a model can only be used to observe the effect of stenoses. In fact, the presented computational simulation of perfusion has not been validated (i.e. compared with true perfusion values extracted from perfusion imaging such as PMR or SPECT) and, therefore, there is no guarantee that the presented perfusion values correspond closely to the reality.

This limitation has been addressed by Kühnel et al. (Kühnel et al., 2008a,b). They combined anatomical information derived from CTA with scar tissue information extracted from LE-MRI images and perfusion information from PMR images. Various 2D and 3D visualizations were proposed to emphasize suspicious myocardial regions: 1) overlaying of the coronary tree mask and scar tissue directly on the 2D LE-MRI images, 2) integration of functional information with a 3D model of the coronary artery tree, 3)

incorporation of a selected 2D LE-MRI slice into the 3D model, 4) interaction with the 2D BEP, and 5) detection of findings. However, neither a mapping of the coronary arteries on top of the 2D BEP nor a 3D model of the heart was provided.

The present work is an extension of our earlier work (Kirişli et al., 2011); here, we focus on model-based visualization techniques to combine CTA and PMR imaging data. Within this context, we have implemented a number of existing comprehensive visualization techniques within the SMARTVis tool (Termeer et al., 2008; Kühnel et al., 2008a,b): projection of the coronary artery tree onto the 2D BEP, integration of the functional information into a 3D model, a coronary perfusion territory map, multiple linked views (2D, 3D and MPR viewers) and animation (automatic camera position). However, we also overcome the limitation encountered by Termeer *et al.* (Termeer et al., 2007, 2008), as we are able to: 1) reconstruct and project the coronary artery tree with absolute diameter, and 2) analyze the impact of coronary artery stenoses on myocardial perfusion derived directly from PMR instead of a simulated model. The main novelty of the presented work compared to Kirişli et al. (2011) is the case-study clinical evaluation, in which we investigated whether integration of coronary anatomy and myocardial perfusion data can improve risk assessment, diagnosis and management of patients with CAD. In addition, the computation of patient-specific perfusion territories (Section 5.3.5), as well as the automatic detection and stenosis quantification (Section 5.3.5), constitute the technical innovation compared to our previous work (Kirişli et al., 2011).

5.3 Method

An overview of the multimodal image analysis and fusion is presented in Figure 5.4. First, CTA and PMR images were analyzed separately. Then, anatomical information extracted from CTA was combined with functional information derived from PMR images. Finally, comprehensive visualization techniques were used to facilitate the joint analysis of coronary stenoses and myocardial perfusion defect.

5.3.1 CTA image analysis

In daily clinical practice, CTA images are analyzed using different visualization techniques, such as MPR and CPR (Figure 5.1), in order to detect vessel stenoses. MPR and CPR images are oblique views obtained from axial sections of the CTA images and, thus, their generation requires vessel centerlines.

In our work, the semi-automatic method proposed by Metz et al. (2009) was used to extract vessel centerlines: a minimum cost path approach was applied, in which the user interaction was minimized to two mouse clicks in the coronary arteries. First, a vesselness/intensity cost function was computed. Then, a point in the aorta close to the coronary ostia was user-defined to derive a cumulative cost-image; a point was also defined by the user distally, at the end of the coronary artery. The centerline was determined by following the path of steepest descent in the cumulative cost image to the end point of the artery. The technique has been evaluated on images with a wide range of image qualities: good, adequate (i.e. presence of artifacts but evaluation possible with moderate confidence, poor (i.e. presence of image degrading artifacts and evaluation

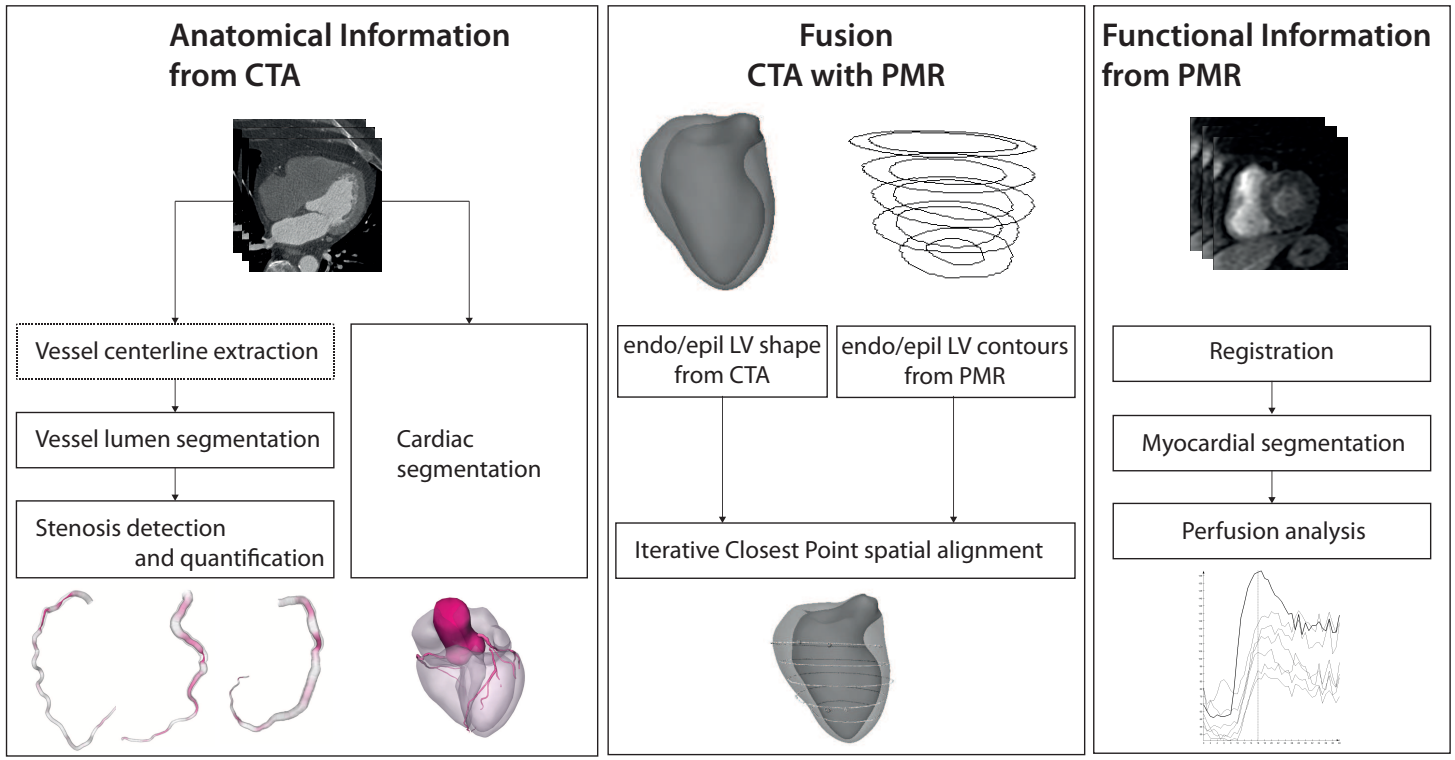

Figure 5.4: Overview of the multi-modal image analysis and fusion. The dashed box corresponds to semi-automatic process, while the solid boxes correspond to fully automatic processes. Anatomical information is extracted from computed tomography coronary angiography (CTA); functional information is extracted from perfusion magnetic resonance (PMR) imaging.

possible with low confidence). Also, the amount of pathology (i.e. calcification) present was considered in the evaluation. Results show that the method is able to cross regions suffering from bad image quality and pathological regions. The computation time for the centerline extraction was around 3 min for each of the three main arteries (LAD, RCA, LCX) and around 1.5 min for each side branch.

The resulting centerlines were used as an initialization for the segmentation of the coronary artery tree. Here, a recently introduced supervised shape-based segmentation method proposed by Schaap et al. (2011) was used; the geometry and the appearance of the vessels were learned from annotated data. First, the vessels were segmented with multivariate linear regression, using image intensities sampled in a region of interest around the initial centerlines. Then, the position of the vessel boundaries was refined with a robust non-linear regression technique, using image intensities sampled on the boundary of the rough segmentations. The computation time for the lumen segmentation required 10-15 min per dataset, depending on the number of vessels to segment. This step was followed by a visual inspection and manual refinement of the lumen segmentation where needed.

Additionally, a 3D model of the heart, which includes ventricles, atria and aorta, was derived automatically from CTA data, using the multi-atlas based segmentation approach presented in Kirişli et al. (2010b).

The cardiac segmentation method has been evaluated on a multicenter/multivendor database of 855 patients (1420 diastolic/systolic images), including patients of different age, gender, and ethnicity; the population is also representative for the typical variability in cardiac anatomy, image quality, patient position, and orientation. Experts evaluated that 49% of the images were very accurately segmented (less than 1 mm error) and that 29% were accurately segmented (error between 1 and 3 mm), which demonstrates the robustness of the presented method. The authors reported 1% failure, due to significant differences in cardiac morphology, such as left pneumonectomy, aortic aneurysm, and congenital heart disease. The cardiac segmentation was on average performed within 20 min.

Finally, as the centerline tracking and lumen segmentation can be run concurrently with the cardiac segmentation, the entire CTA processing can be performed within 20-30 min, depending on the number of coronary arteries processed.

5.3.2 Cardiac perfusion MR image analysis

Cardiac PMR provides information about myocardial perfusion. In clinical practice, physiologically relevant features, together with their time-intensity behavior, are extracted from the PMR images, which require tracking of regional myocardial intensity in all the frames of a perfusion sequence as a function of time.

In this work, the fully automatic framework was used to analyze the PMR images. First, because the intensity signal must be derived from the same myocardial region in successive frames, the PMR images were compensated for respiratory motion using a registration method based on independent component analysis (Milles et al., 2008). Subsequently, the registered data were used to automatically segment the myocardium with active appearance models (Gupta et al., 2010). Registration failures may occur

when images of poor quality or presenting large breathing motion are processed. When registration failures occurred, the commercial QMass MR software (Medis Medical Imaging Systems B.V., Leiden, The Netherlands) was used to segment the myocardium. This happened during the analysis of the stress PMR sequence of one patient presenting large breathing motion.

Finally, given the myocardium segmentation, time-intensity curves (TIC) and perfusion parameters were computed (with QMass MR): baseline signal intensity (signal intensity value before the first-pass of the contrast agent), peak enhancement (PE) or amplitude (maximal signal intensity value normalized by the baseline value), mean intensity (mean intensity during the first-pass of contrast-agent), time to (50%) of PE (time between the start of the first-pass and the time at which (50% of) PE is achieved), upslope (maximum steepness during the first-pass of contrast-agent).

The upslope of the myocardial TIC was normalized with the upslope of the left ventricular blood pool signal, and is referred to as the *relative upslope*. The myocardial perfusion reserve index (MPRI) was calculated by dividing the segment's relative upslope of the stress TIC by the corresponding segment's relative upslope of the rest TIC. For each slice consisting of 50 frames, the process of registering all the frames, obtaining the myocardial contours, and deriving the perfusion parameters takes (on average) 1.5 min. For datasets with 4-6 slices, the entire PMR processing thus requires 6-9 min.

5.3.3 Data fusion and integration

Because CTA and PMR images were acquired at different imaging devices and at different times, some spatial registration is needed in order to combine the complementary information of coronary anatomy and myocardial perfusion imaging.

In this work, we used an iterative closest point (ICP) approach, in which an affine transformation is determined. The ICP algorithm requires a set of moving points $m \in M$, points from PMR epicardial contours, and a set of target points $t \in T$, points from the 3D CTA epicardium model. The transformation is initialized by aligning the centers of gravity of both point sets; this results in two new sets of points M_0 and T_0. Given a user-defined maximum number of iterations ($N = 100$) and/or a maximum distance ($\epsilon = 1.10^{-5}$) as stopping criterion, the iterative procedure will search for the affine transformation that minimizes the distance between each $m \in M_i$ and $T \in T_0$, M_i being the set of moving points after the i^{th} iteration. The ICP alignment of the CTA and PMR data is performed within a minute.

5.3.4 Coordinated and multiple views

A common frame of reference, adapted from Termeer et al. (2007) (Figure 5.5) and based on the segmentation of the left ventricle, was used to combine the information extracted from the CTA and PMR data. Each point of the CTA image, particularly those on the myocardium and vessels, can be parameterized using cylindrical coordinates (ρ,θ,z), where **z** represents the left ventricle long-axis, θ represents the angle with the short-axis and ρ represents the distance to the long-axis. This 3D model is then unfolded along the left ventricle long-axis, to fit the 2D model of a BEP. Here, the radius of the disc

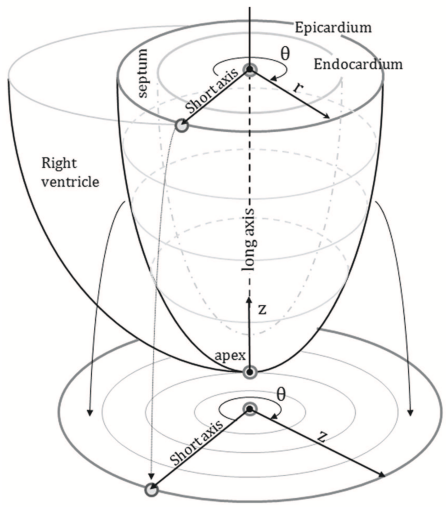

Figure 5.5: Common frame of reference - A bull's eye plot is a 2D representation of the myocardium; it is constructed by unfolding and reformatting the 3D elipsoid myocardium to a 2D circle. Adapted from Termeer*et al.* Termeer et al. (2007).

corresponds to the z value and the angle to the θ values. The third dimension, ρ, is encoded in the rendering: the more transparent the artery is, the further it is from the left ventricle epicardial surface.

Upon establishing 2D-3D correspondence, an interesting position such as a stenosis located on the 3D (resp. 2D) model can be simultaneously located on the 2D (resp. 3D) model. Additionally, the MPR view of the vessel is interactive: by moving the cursor along the MPR images, the actual position along the vessel is simultaneously indicated on both the 2D and 3D models. Moreover, to facilitate the 3D navigation by the expert, the optimal camera position in the 3D model is automatically updated, given the MPR cursor position. Finally, the integration of a selected 2D CTA slice in the 3D model is possible.

5.3.5 Visualizations for comprehensive analysis

An overview of the proposed comprehensive visualizations is presented in Figure 5.6.

Automatic detection of stenosis

Given the vessel segmentation obtained from the CTA data, the coronary artery stenoses were detected and quantified accordingly to the method presented in Chapter 3 (Shahzad et al., 2012a). The cross-sectional area A_z of the vessel was computed at every position z along the vessel centerline, $z \in [1, L]$ and L being the number of positions along the centerline. Given the assumption that a vessel is a tubular structure, the radius was then derived as follows: for all z between 1 and L, $r_z = \sqrt{A_z/\pi}$.

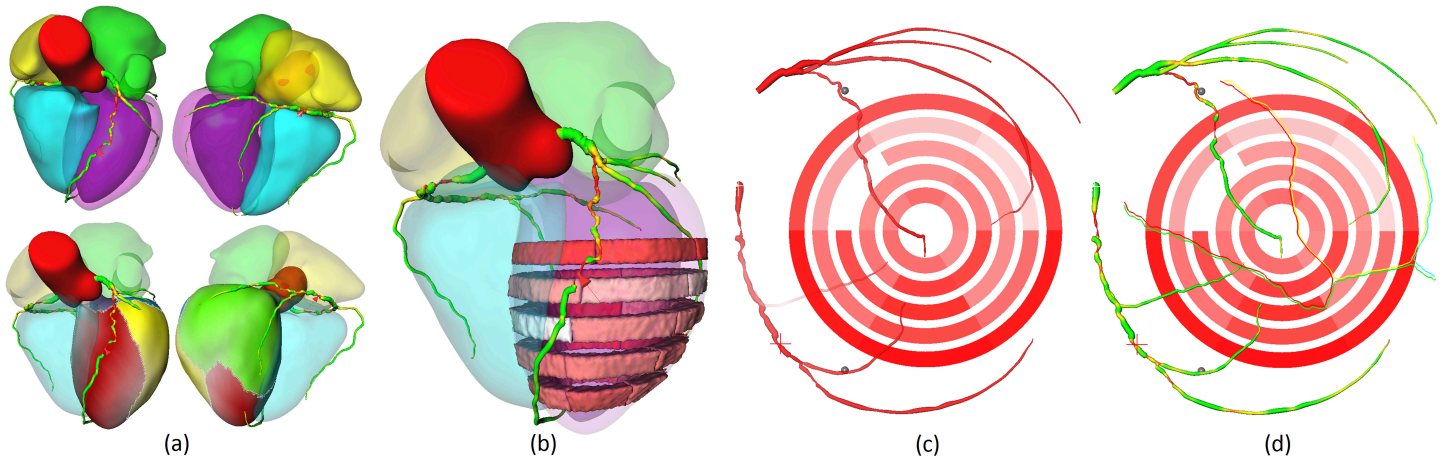

Figure 5.6: Comprehensive visualizations proposed in the SMARTVis tool - (a) 3D model of the heart and coronary artery tree extracted from CTA, arteries are color coded with the degree of stenosis. Also, patient-specific perfusion territories are shown on the left ventricle (LAD in red, LCX in blue, MO in yellow and RCA in green). (b) 3D model of the heart with perfusion information integrated. (c) 2D perfusion bull's eye plot (BEP) with coronary tree projected on top; the more transparent the artery, the further it is from the epicardium. (d) 2D perfusion BEP with coronary tree and coronary perfusion territories projected on top; arteries are color coded with the degree of stenosis. The spheres next to the 2D BEP indicate the position of connection with the right-ventricle

To compute the degree of stenosis, the radius of a healthy vessel is needed, as a reference. Here, we estimated the radius of the healthy vessel by applying a robust weighted Gaussian kernel regression (Debruyne et al., 2008) to the 1D function describing the vessel radius r_z along the centerline, given a set of weights w_z.

For each patient of our study, all the coronary arteries were analyzed and the estimated significant stenoses were listed and ranked. Visually, the degree of stenosis can be color coded, which allows the expert to obtain a rapid first impression of the patient's degree of disease.

Patient-specific coronary territory map

In our work, we applied the method presented in Beliveau et al. (2007) to compute patient-specific coronary perfusion territories from CTA.

From our left ventricular epicardial segmentation derived from CTA, a 3D triangulated left ventricle shape S was created, with a maximum edge length of $2mm$. Then, all the coronary artery centerlines were projected onto S using the closest point method, except centerline points from the right coronary artery (RCA) that are more than $2cm$ from the myocardium. Subsequently, the shortest path (the geodesic distance over the surface) to each of the projected coronary arteries was computed for each node of S, using Dijkstra's algorithm; each node was then associated with the closest projected coronary. Examples of 3D coronary perfusion territories are shown on Figure 5.6 (two models at the bottom left): the red area is perfused by the left anterior descending (LAD) coronary artery , the yellow area by the marginal branch (MO), the blue area by the left circumflex artery (LCX) and the green area by the RCA. The purple region corresponds to the uncertain area (i.e. the left main branch, common to LAD, MO and LCX). The boundary between territories is represented by white dots. The nodes of the boundary can be expressed in cylindrical coordinates (ρ,θ,z) and can be projected onto the 2D BEP; Figure 5.6d shows an example.

Comprehensive 2D model

As in the comprehensive visualization proposed in Termeer et al. (2007), the coronary arteries are projected onto the conventional 2D perfusion BEP, giving additional context information. Each point of the vessel centerlines c_i, $i \in [1, L]$, is parameterized to (ρ_i,θ_i,z_i) using the coordinate system presented in Section 5.3.4 and the radius r_i is stored. Using the same unfolding, the points c_i are projected to c_i' onto the 2D BEP. The coronary arteries are then reconstructed by creating tubes with center c_i' and radius r_i. In Figure 5.6c, the distance to the myocardium is encoded into the rendering: the more transparent the artery is, the further it is from the left ventricle epicardium surface. Here, the right artery is more transparent compared to other branches; in fact, the right artery runs through the right atrioventricular groove before approaching the left ventricle and, usually, only the distal branches of the RCA are actually close to the left ventricle. However, as a stenosis may occur in any position in the RCA, it is important to show the complete artery on the 2D model, and not only the distal part of the RCA. In Figure 5.6d, the coronary arteries are color-coded with their estimated degree of stenosis, and the patient-specific coronary perfusion territories can be overlaid too.

Comprehensive 3D model

Figure 5.6a presents examples of a 3D model of the heart with the coronary artery tree and the (optional) coronary perfusion territories mapped onto the LV. The coronary artery tree is color coded with the estimated degree of stenosis. Figure 5.6b shows a 3D model of the heart with integrated perfusion information derived from PMR. Such an integrated visualization provides a direct 3D correspondence between the vessel and the myocardial region supplied by the vessel.

5.3.6 Implementation

The development of the SMARTVis visualization and analysis tool was done using MeVisLab (*http://www.mevislab.de*), a rapid prototyping platform designed for (medical) image processing and visualization. The automatic detection of stenoses and computation of patient-specific coronary perfusion territory maps, as well as the cylindrical parameterization, were developed in C++. Additional dynamic functionalities were added to our graphical user interface using Python or JavaScript.

5.4 Evaluation

5.4.1 Data

Our patient population is a subset of the 50 patients included in the study of Kirschbaum et al. (2011), in which they compared adenosine PMR imaging with invasive fractional flow reserve (FFR). Fifty symptomatic patients with suspected CAD and normal left ventricular ejection fraction who were referred for invasive coronary angiography (ICA) were asked to participate in the study. All of them underwent adenosine cardiac PMR imaging and ICA within 4 weeks. ICA was part of the routine clinical management, and functional assessment (FFR) was performed for vessel(s) which had a stenosis estimated as being larger than 30% as visualized on ICA. FFR assessment is an invasive accurate diagnostic tool to determine the physiological significance of a coronary lesion and distinguishes ischemia-producing lesions from those that do not; a significant reduction in FFR was defined as less than 0.80. The conclusion of the study was that an MPRI (cf. Section 5.3.2) value of 1.9 was the best threshold for the prediction of an FFR of 0.80. From these 50 patients, only 35 also underwent CTA before PMR, with an interval of 41 ± 37 days between CTA and PMR examinations. All the images were acquired at Erasmus MC, University Medical Center Rotterdam (Rotterdam, the Netherlands) between October 2007 and April 2008.

For evaluation of the SMARTVis tool, we included patients who match the following inclusion criteria. First, there should be a correlation between the true-positive and true-negative MPRI and FFR measurement. Also, there should be suspected stenoses in at least 2 of the 3 main coronary arteries using ICA, and a minimum of 1 significant stenosis and a maximum of 2 significant stenoses using FFR. Following these criteria, six patients that had false-positive or false-negative correlation between MPRI and FFR measurement, five who had no significant stenosis (i.e. the FFR was > 0.8 for the suspected lesions), 19 who had suspected stenoses in only one vessel using ICA and one that had

Table 5.1: Patients selected for the evaluation of the SMARTVis tool. Hemodynamically significant stenosis are indicated in bold (FFR < 0.8).

Patient	Sex	Age	ICA suspected stenosis	FFR
patient02	M	78	LAD	0.82
			LCX	**0.57**
patient10	M	63	**LAD**	**0.73**
			LCX	1.0
patient25	M	53	**LAD**	**0.75**
			LCX	0.94
			RCA	**0.73**
patient37	M	74	**LAD**	**0.74**
			RCA	**0.74**

triple-vessel disease using FFR were excluded. Finally, this resulted in a selection of 4 patients for the evaluation of our integrated visualization tool (Table 5.1).

CTA images were acquired with a dual-source CT scanner (Somatom Definition, Siemens Medical Solutions, Forchheim, Germany). A tube voltage of 120 kV was used. All datasets were acquired with ECG-pulsing. Diastolic reconstructions were used, with reconstruction intervals ranging from 250 to 400 ms before the R-peak. The data were reconstructed using a smooth (B26f) kernel. The mean voxel size of the datasets is $0.32 \times 0.32 \times 0.4mm^3$.

PMR images were acquired using a 1.5 Tesla MRI scanner (Signa CV/i, GE Medical Systems, Milwaukee, Wisconsin), with a cardiac eight-element phased-array receiver coil placed over the thorax (Signa CV/i, GE Medical systems, Milwaukee, Wisconsin USA). Cine cardiac PMR imaging was performed with a steady-state free precession technique (FIESTA). A first bolus of contrast media (Gadolinium diethyltriaminepentaacetic acid, Magnevist, Schering, Germany) was injected and rest first pass perfusion images were acquired. The temporal resolution per slice of 120 ms allowed imaging of 3-5 slices per R-R interval. Fifteen minutes after rest perfusion imaging, vasodilatation was induced by adenosine and a second bolus of contrast media was injected; stress first pass perfusion images were acquired, using the same pulse sequence and the same orientations used for rest perfusion.

5.4.2 Case-study design

To investigate the benefits of the proposed comprehensive visualization tool for assessing CAD, we performed a case-study evaluation on the four selected patient datasets, according to the guidelines presented by Yin (2009). First, we describe the case-study setup, then the patient analysis is described (i.e. the observers' diagnosis) and discussed.

Our main study question was defined as: "How can the comprehensive visualizations proposed in the SMARTVis tool assist radiologists/cardiologists in analyzing multimodal

imaging data in the assessment of coronary artery disease?", and the case was defined as: "Use of the SMARTVis tool by two domain scientists referred to as RJvG, an expert cardiologist in MR imaging with over 10 years experience, and AR, a fellow student in radiology, expert in CTA imaging with 3 years experience". The different functionalities of the SMARTVis tool were explained by the first author to the experts in a training session, using images of one of the excluded patient datasets; the tool was operated by the clinical expert during the evaluation. Both RJvG and AR are co-authors of this paper; they contributed to this work by providing feedback on our prototypes and clinical inputs, but did not work on the implementation itself. Thus, their role as case-study subjects was not compromised.

Our evaluation was divided into two parts: 1) conventional analysis, and 2) analysis using the SMARTVis tool. The comparative diagnostic study was performed on two different days, with a one-day interval, to limit the influence of the previous session. The patient's data were also analyzed in a different order: patient02, patient10, patient25, patient37 during the conventional analysis, and patient10, patient02, patient37, patient25 during the analysis using the SMARTVis tool. Beforehand, a number of case-study propositions were defined to answer the main study question. During the evaluation sessions, we collected feedback on the usability of the tool, according to the study propositions. In Section 5.4.3, each proposition is stated, together with the expert's feedback, and discussed.

On the first day, together with each expert, in two separate sessions, we analyzed the four selected patient's multimodal imaging data using conventional tools. For each patient, the CTA image was first inspected using an axial view and the MPR views of the annotated vessels. The expert was asked to list the positions and degree ($< 50\%$, $50\% - 70\%$ or $> 70\%$) of all visually significant stenoses detected on CTA. Then, the rest/stress perfusion sequences were visually analyzed and the expert's decision was also supported by the TICs and perfusion BEP. Here, the expert was asked to list all the suspected ischemic regions. Finally, by mentally combining information from CTA and PMR data, the expert assigned each of the listed suspected ischemic regions to a specific coronary artery lesion and made a decision concerning which coronary artery(ies) should undergo ICA and possible revascularization. On the consecutive day, the experts analyzed the patient's multimodal imaging data using our SMARTVis tool. Using the automatic stenosis detection and quantification, as well as the color-coded vessel model, in addition to the MPR view of the vessels, the significant stenoses were again listed by the expert. The suspected ischemic regions detected previously were reported and, using our 2D and 3D comprehensive model as well as the coronary perfusion territories, the expert again assigned each of the listed suspected ischemic region to a specific coronary artery lesion and made a new decision concerning which coronary artery(ies) should undergo ICA and possible revascularization.

The 2D and 3D comprehensive visualization models are shown in Figures 5.7-5.10 and the results of the comparative diagnostic study are presented in Table 5.2.

During the analysis of patient02, RJvG assigned an apical inferoseptal and inferior perfusion defect to a stenosis in the RCA using the conventional tool. However, with ICA and FFR, no significant stenosis was detected in the RCA; using the SMARTVis tool, the same perfusion defect was assigned to a stenosis in the LAD (Figure 5.7). An obstruction in the LAD was indeed suspected using ICA, but the FFR indicated that it was not

Table 5.2: Comparative diagnostic study made using the conventional tools or the SMARTVis tool. List of the vessels which were referred for ICA. Only vessels with an FFR < 0.8 are listed.

Patient	Side-by-side		Fused with SMARTVis		FFR
	RJvG	AR	RJvG	AR	
patient02	-	LAD	LAD	LAD	-
	LCX	LCX	LCX	LCX	LCX
	RCA	-	-	-	-
patient10	LAD	LAD	LAD	LAD	LAD
	-	-	-	-	-
	RCA	-	-	-	-
patient25	-	-	LAD	LAD	LAD
	LCX	-	-	-	-
	RCA	RCA	RCA	RCA	RCA
patient37	LAD	LAD	LAD	LAD	LAD
	LCX	-	-	-	-
	RCA	RCA	RCA	RCA	RCA

hemodynamically significant (FFR = 0.8). However, as RJvG considered the stenosis in LAD significant based on CTA data; he thus decided to assign this apical inferoseptal and inferior perfusion defect to this LAD lesion. It should be noted that the lesion in LAD was calcified and the one in the LCX was not. The stenosis degree of calcified lesions in CTA can be over-estimated due to imaging artifacts, while the non-calcified plaques are usually less easily detected and assessed. AR detected many more ischemic regions than RJvG for this patient, in the anterior and anterolateral wall; thus, AR referred ICA of the LAD, in both analyses. Nevertheless, it should be noted that the FFR value of the LAD (FFR = 0.82) is close to the cut-off value (FFR = 0.8) used to discriminate hemodynamically significant and non-significant lesions.

During the analysis of patient10, RJvG assigned an inferoseptal perfusion defect to a borderline stenosis in the RCA when using conventional tools, while, when using the coronary perfusion territories provided by the SMARTVis tool (Figure 5.8), the same perfusion defect was linked to the LAD; the LAD is indeed the coronary which is feeding the inferoseptal myocardium region of this patient and actually causing the perfusion defect ($FFR_{LAD} = 0.73$). The diagnosis of AR was correct in both analyses.

During the analysis of patient25, RJvG assigned a perfusion defect in apical inferior and inferoseptal wall to the RCA (resp. LAD) and in the inferolateral wall to the LCX (resp. RCA) using the conventional (resp. SMARTVis) tool; this patient has a right-dominant system, thus the RCA is feeding a larger area. In that case also, the coronary overlay and perfusion territory map helped him to correct his diagnosis. Similarly, AR misclassified the perfusion defect in the inferoseptal wall to the RCA, missing the significant stenosis in the LAD with the conventional tool, but reaching a correct diagnosis using the SMARTVis tool.

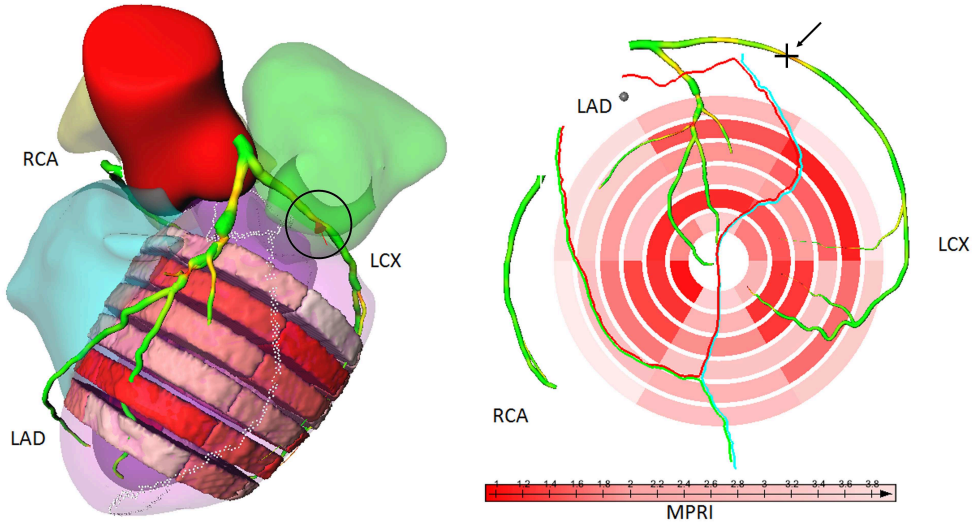

Figure 5.7: Patient02 - On ICA, suspected stenoses (30%) were visually detected in both LAD and LCX. Based on the FFR measurement, only the stenosis in the LCX was significant ($FFR_{LCX} = 0.57$) while the stenosis in the LAD was not considered to be significant ($FFR_{LAD} = 0.82$).

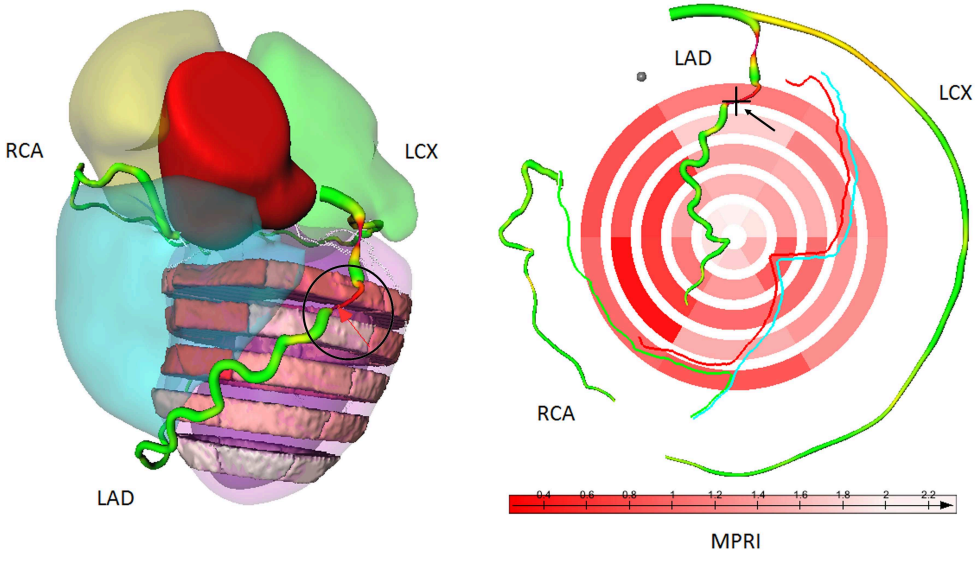

Figure 5.8: Patient10 - On ICA, suspected stenoses (30%) were visually detected in both LAD and LCX. Based on the FFR measurement, only the stenosis in the LAD was significant ($FFR_{LAD} = 0.73$) while the stenosis in the LCX was not considered to be significant ($FFR_{LCX} = 1.0$).

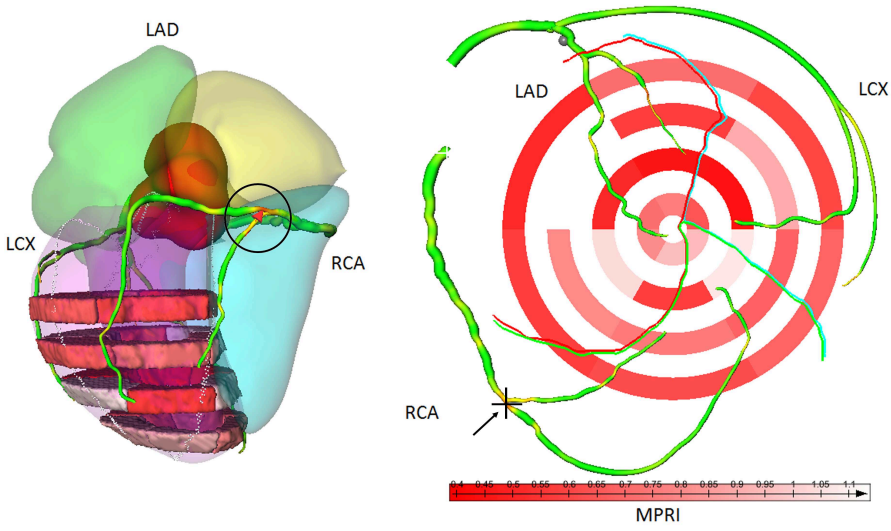

Figure 5.9: Patient25 - On ICA, suspected stenoses (30%) were visually detected in the three main arteries (LAD, LCX and RCA). Based on the FFR measurement, only the stenoses in the LAD and RCA were significant ($FFR_{LAD} = 0.75$, $FFR_{RCA} = 0.73$) while the stenosis in the LCX was not considered to be significant ($FFR_{LCX} = 0.94$).

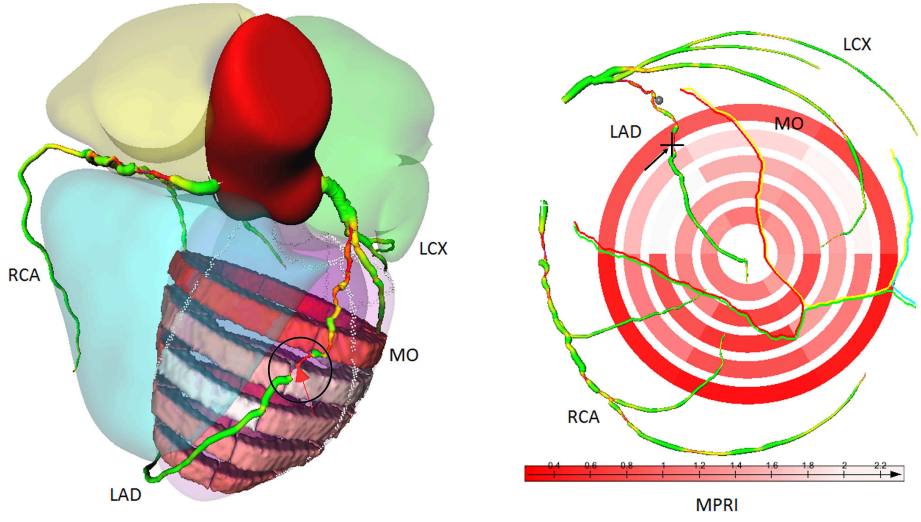

Figure 5.10: Patient37 - On ICA, suspected stenoses (30%) were visually detected in LAD and RCA. Based on the FFR measurement, both stenoses were indeed significant ($FFR_{LAD} = 0.74$, $FFR_{RCA} = 0.74$).

During the analysis of patient37, RJvG assigned a perfusion defect in the apical slice to the RCA instead of the LAD and a mid-anterior defect to the LCX instead of the LAD, using the conventional tool. These errors were corrected with the SMARTVis tool. AR made the same diagnosis using both tools.

In general, RJvG changed his diagnosis in all four cases and AR in one; the diagnosis of RJvG improved in three of the four cases and AR in one. Table 5.2 shows that there is no variability between the diagnosis of both observers with the SMARTVis tool, whereas, during the conventional evaluation, the observers had disagreement on one or two vessel(s) per patient. All the diagnoses were correct after using the SMARTVis tool, except for one case. The diagnosis of *patient02* remained incorrect, owing to overestimation of the degree of stenosis or overestimation of the number of abnormal perfusion regions during the analysis by the observers.

To conclude, when using the SMARTVis tool, a more reliable estimation of the correlation between perfusion deficits and stenoses led to a more accurate diagnosis, as well as a better inter-observer diagnosis agreement, which demonstrates the reproducibility of the results obtained with the SMARTVis tool. Thus, systems that integrate coronary anatomy and myocardial perfusion information may provide new opportunities for the risk assessment, diagnosis and management of patients with CAD.

5.4.3 Expert feedback

The comparative diagnostic study demonstrated the clinical added value of the SMARTVis tool. Nevertheless, the experts' feedback is useful to understand *why* and *how* the SMARTVis tool performs better than the side-by-side analysis; this feedback complements the experiments. It should be noted that the experts' feedback is influenced by their personal preferences, based on years of experience and domain of expertise, which provide little basis for generalization.

Below, each case-study proposition is stated, together with the experts feedback, and then discussed.

The projection of the coronary artery tree on top of the 2D BEP facilitates the correlation between stenosis and ischemic myocardial region.
Both RJvG and AR agreed. RJvG emphasized that the anatomy varies greatly between individual and, thus, no standard correlation can be used. It also helped AR to better understand which myocardial territory belongs to an obstructive coronary stenosis.

The integrated visualization of the perfusion information in the 3D model of the heart facilitates the correlation between stenosis and ischemic myocardial region.
RJvG considered this to be an important part of the tool. Having an anatomical context (particularly for the right ventricle) to understand the location of the perfusion sectors and the position of the arteries with respect to the cardiac anatomy was appreciated. Such an anatomical context is not available in the 2D representation. RJvG did make the suggestion to extend the tool with the option to hide selective perfusion BEP sectors in order to look more closely at a region of interest. Although AR agreed, she did not use the 3D model during her analysis.

The color-coding of the degree of vessel stenosis facilitates the localization of interesting areas in terms of coronary disease, and the automatic stenosis ranking helps to further refine the location and quantification.
Although both of them agreed, RJvG explained that, with regard to the current resolution of CTA technology, he would interpret the results derived from automatic vessel segmentation with caution. With improvement in CTA resolution, he might have more confidence in the automatic stenosis grading. Similarly, AR used it mainly as verification: first, she analyzed and detected/quantified stenoses using the MPR vessel view; then, she compared her position/ quantification with the estimations provided by the tool. However, they both agreed that the color coding is useful to obtain a first impression about the extent of the disease.

Automatic position synchronization between MPR vessel viewer and the 2D and 3D models facilitates analysis of the data.
Both RJvG and AR agreed; for instance, when they wanted to refine their analysis to relate a perfusion defect with a particular artery, they visualized the suspected vessel on the MPR viewer while moving the cursor to see the corresponding location with respect to the cardiac anatomy and perfusion sectors.

The 3D model of the heart primarily helps in the interpretation of the coronary tree projection on the 2D model.
RJvG agreed, the 2D projection of the coronary tree seems to him to be too much distorted and the interpretation is difficult; he had a problem in to recognizing the different arteries. Thus, the 3D model, synchronized with the 2D model and the MPR view, supported his interpretation. AR also agreed, but did not really need the 3D model to interpret the 2D representation. After one patient analysis, she stated that she was used to this model and was able to perform visual analysis using the 2D model only.

The coronary perfusion territory map and boundaries help in a patient-specific way to relate an ischemic segment to a particular vessel stenosis.
RJvG confirmed that, in general, it is very difficult to make a decision concerning which coronary artery is actually supplying the septal wall. Moreover, due to contrast limitations, the septal arteries are difficult to segment. Thus, experts usually have to rely on models, which generate considerable error, as in the case of patient 10 and 25 where septal perfusion defects were assigned to the RCA instead of the LAD. Therefore, this functionality was important to him. AR agreed with the proposition; however, the 2D projection of the arteries onto the 2D BEP already gave her an indication about perfusion territories.

The 2D representation is your preferred view for investigating relations between stenoses and ischemic myocardial regions.
RJvG disagreed; the 2D model is too distorted, making his interpretation really difficult. In contrast, AR agreed; currently, she is used to work with 2D maps of the LV. Especially for relating a certain perfusion defect to a particular artery, AR used mainly the 2D viewer.

The 3D representation is your preferred view for investigating relations between stenoses and ischemic myocardial regions.
RJvG agreed; he likes having anatomical information, such as the heart model. During the analysis, RJvG first navigated within the 3D model of the heart (with the color coded vessel model), to get an idea of the patient-specific anatomy and the position of the coronaries with respect to the left and right ventricles. Then, he incorporated the perfusion information into the 3D model and related perfusion defects with obstructive disease. AR used the 3D viewer only to see the position of suspicious stenoses detected on MPR images; she did not use it to relate anatomical and functional data.

To conclude, concerning the most informative visualization, RJvG preferred the integrated 3D model whereas AR chose the 2D projection model. Regarding the coronary perfusion territories, although both observers could mentally determine which region is supplied by which artery, they both found the automatic boundary delineation very useful in making a decision for borderline cases. The color-coding of the degree of stenosis was primarily appreciated to obtain a quick overview of the patient's disease state. Finally, the automatic stenosis detection/quantification strengthened the observer CTA analysis.

5.5 Discussion, limitations and future work

We have proposed and evaluated a tool for comprehensive visualization of cardiac multimodal data. The results of a case-study with two experts in four patients demonstrated that integration of multimodal data in a common reference space supports the expert's diagnosis, by providing a more reliable estimation of the relation between perfusion deficits and stenoses, which led to a more accurate diagnosis as well as to a better inter-observer diagnosis agreement. However, some aspects can be improved.

In the fusion step of our processing pipeline, we used a registration approach (i.e. ICP) to spatially align CTA with PMR data. The alignment of the data for each patient was visually verified, but small registration errors could still be present. One source of error arises from the left ventricle segmentation errors in CTA and PMR. Another source of registration error originates from integrating different cardiac phases as obtained by CTA and PMR images: PMR images are generally acquired during systole, whereas CTA images are typically acquired at mid-diastole. During the fusion process, we did not compensate for the fact that the images were acquired during different time points in the cardiac cycle. The accuracy of the registration, and the impact of registration errors on the diagnosis, remains to be investigated.

The visualization of coronary perfusion information, as proposed in this work, supported the expert diagnosis during the evaluation. Regarding the experts' feedback, it was shown that the coronary artery tree projection on top of the 2D perfusion BEP, or the integration of the perfusion into the 3D model, already significantly supported the expert while making the diagnosis. However, there is room to improve the estimation of the perfusion territories, as our estimation is now solely based on distances to segmented coronary arteries. Studies on blood flow simulation in coronary arteries have shown that the radius of the vessel also influences the amount of blood flowing through the artery. Computing the perfusion coronary territories using a *validated* perfusion simulation model would therefore be preferred.

In the CT imaging technique, calcifications in the vessel wall can appear significantly larger than they actually are, due to their high density and the relatively limited intrinsic resolution of the CT acquisition. This is known as the blooming effect and it hampers the assessment of stenoses, especially in small arteries. Because calcifications appear larger than they actually are, this artifact can result in an over-estimation of the degree of stenosis. The effect of this, and other CT imaging artifacts on our automatic stenosis detection and quantification method remains to be investigated.

Nevertheless, our preliminary clinical validation study demonstrates that the errors induced by the different processing step of our pipeline affect the final diagnosis accuracy to a lesser extent than the error in assuming a standard physiological model. During the side-by-side analysis of CTA and PMR data, the diagnosis derived by assuming a standard physiological model leads to errors in the assignment of a perfusion defect to a culprit artery; these errors can be prevented when using the SMARTVis tool.

Our study also demonstrates that the SMARTVis tool offers an added diagnostic value when assessing CAD in intermediate risk patients (i.e. with suspected stenoses in at least two of the main arteries). As stated in the Introduction, such a tool is not expected to improve the diagnosis in low-risk patients (i.e. single-vessel disease patients) as only

one culprit artery can be assigned to the perfusion defect; moreover, it is unlikely to be used for triple-vessel disease patients (i.e. very-high-risk patients), as they are generally directly referred for revascularization. However, the SMARTVis tool is suitable for visual analysis of patients with all disease state. The same visualization technique can be used to interpret anatomical and functional information of single and triple-vessel disease patients in an integrated display. To what extent this would facilitate the diagnosis for these cases remains to be investigated; nevertheless, visualizations derived from the SMARTVis tool can be included in the patient report, to provide a quick overview of the patient's disease state.

Concerning our case-study evaluation, although the expert feedback was positive and the results were consistent, we need to conduct a larger study, also involving multicenter expert clinicians, in order to draw stronger conclusions. This will be considered for future work.

The time required to diagnose a patient has not yet been recorded; thus, we cannot state whether the SMARTVis tool allows a more efficient process of diagnosis. However, investigating whether making a diagnosis using the SMARTVis tool would be faster than it is nowadays using conventional tools should be part of a larger evaluation study.

After the evaluation, both experts were enthusiastic about the presented integrated visualization tool and were eager to use the SMARTVis tool in clinical practice. In our implementation, we use a generic data representation, and were able to import data from various research-oriented packages. Deployment of our tool for daily clinical use would therefore require only a further automation of the various processing steps. Additionally, the output of other software used in clinical practice can easily be integrated in the SMARTVis framework, provided that a conversion to our data representation can be performed. At present, most of the steps are performed using individual research oriented software packages. Nevertheless, a generic data representation was used when implementing the user interface. Therefore, the anatomical and functional information can be computed using any software used in daily clinical practice; a conversion to our representation would allow the information to be imported in the SMARTVis framework.

5.6 Conclusions

The SMARTVis tool allows to efficiently establish a spatial correspondence between obstructive coronary artery lesions and myocardial regions with perfusion defect, in a patient-specific way. The location of coronary stenoses and perfusion abnormalities can be visualized jointly in 2D and 3D, thereby facilitating study of the relationship between the anatomic causes of an occluded artery and the physiological effects on the myocardial perfusion.

In addition, we investigated the benefits of the comprehensive visualizations in assessing CAD through a comparative diagnostic study and a case-study research evaluation, conducted together with two clinical experts. It has been confirmed that such comprehensive visualizations allow to effectively relate perfusion defects and coronary lesions. Moreover, it has been demonstrated that the analysis leads to a more accurate diagnosis.

For future work, we plan to extend our tool in two directions. First, we would like to integrate more functional information, such as scar tissue extracted from late enhancement MRI data, wall motion abnormalities detected on short-axis MRI data, and calcium scoring extracted from CT data. Then, the generic setup of the SMARTVis concept enables extension to other perfusion modalities, such as SPECT and CT perfusion imaging. Altogether, this would enable a 'one-stop-shop' visual exploration of functional, anatomical and perfusion data of the heart, which would maximally exploit the complementarities of all available data.

chapter 6

Additional diagnostic value of integrated analysis of cardiac CTA and SPECT-MPI using the SMARTVis system in patients with suspected coronary artery disease

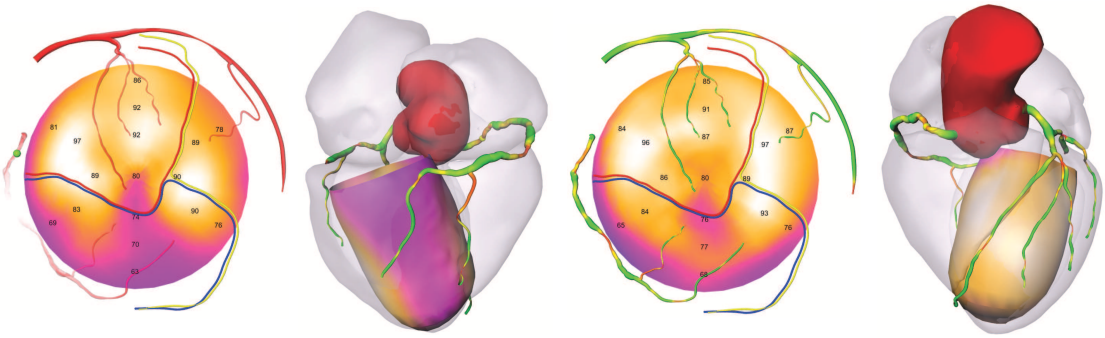

This chapter is based on the manuscript:
Additional diagnostic value of integrated analysis of cardiac CTA and SPECT-MPI using the SMARTVis system in patients with suspected coronary artery disease,
H.A. Kirişli*, V. Gupta*, R. Shahzad* *(* shared first authorship)*
I. Al Younis, A. Dharampal, R.-J. van Geuns, A.J. Scholte,
M.A. de Graaf, R.M.S. Joemai, K. Nieman,
L. van Vliet, T. van Walsum, B.P.F. Lelieveldt and W.J. Niessen,
Submitted, 2013.

Abstract

Purpose CT angiography (CTA) and SPECT myocardial perfusion imaging (SPECT-MPI) are complementary imaging techniques to assess coronary artery disease (CAD). Spatial integration and combined visualization of SPECT-MPI and CTA data may facilitate correlation of myocardial perfusion defects and subtending coronary arteries, and thus offer additional diagnostic value over either stand-alone or side-by-side interpretation of the respective data sets from the two modalities. In this study, we investigate the additional diagnostic value of a software-based CTA/SPECT-MPI image fusion system, over conventional side-by-side analysis, in patients with suspected CAD.
Methods Seventeen symptomatic patients who underwent both CTA and SPECT examination within a 90-day period were included in our study; seven of them also underwent an invasive coronary angiography. The potential benefits of the Synchronized Multimodal heART Visualization (SMARTVis) system in assessing CAD were investigated through a multi-center case-study: four experts from two medical centers performed 1) a side-by-side analysis, using structured CTA and SPECT reports, and 2) an integrated analysis, using the SMARTVis system in addition to the reports.
Results The fused interpretation led to 1) a more accurate diagnosis, reflected in an increase of the individual observers' sensitivity and specificity to correctly refer for invasive angiography eventually followed by revascularization, and 2) a better inter-observer diagnosis agreement (increase from 74% to 84%). The improvement was primarily found in patients presenting coronary artery disease in more vessels than the number of reported perfusion defects.
Conclusions Integrated analysis of cardiac CTA and SPECT-MPI using the SMARTVis system results in an improved diagnostic performance.

6.1 Introduction

Coronary artery disease (CAD) is a major cause of death worldwide (Roger et al., 2012). Plaque build-up in the coronary artery vessel wall may cause luminal narrowing and induce myocardial ischemia, potentially leading to myocardial death. It is thus crucial to detect CAD in an early stage. In current clinical practice, invasive coronary angiography (ICA) is the reference standard imaging technique for diagnosing CAD (Levine et al., 2011). It enables determining the location, the number and the severity of the vessel stenoses. Computed tomography coronary angiography (CTA) imaging is rapidly gaining clinical acceptance (Weustink and de Feyter, 2011) as it non-invasively provides high-resolution 3D images of the cardiac and coronary artery anatomy, which allow assessment of the presence, extent and type (calcified or non-calcified) of coronary stenoses. Depending on the location and information regarding the severity of the stenoses, a functional test may be required to evaluate presence and extent of myocardial ischemia. Single photon emission computed tomography myocardial perfusion imaging (SPECT-MPI) is widely used to non-invasively assess reversible myocardial ischemia.

In conventional side-by-side analysis, integration of CTA and SPECT-MPI findings is mentally performed by using a standardized myocardial segmentation model that allocates each myocardial segment to one of the three main coronary arteries (Cerqueira et al., 2002). However, individual coronary anatomy does not always correspond with the standardized this myocardial distribution (Pereztol-Valdés et al., 2005). Spatial integration and combined visualization of CTA and SPECT-MPI data may facilitate correlation of myocardial perfusion defects and subtending coronary arteries, and thus offer additional diagnostic value over either stand-alone or side-by-side interpretation of the respective data sets (Nakaura et al., 2005; Bax et al., 2007; Gaemperli et al., 2007b,a; Gaemperli and Kaufmann, 2008; Gaemperli et al., 2009; Slomka et al., 2009; Kaufmann, 2009; Santana et al., 2009; Sato et al., 2010).

Hybrid cardiac imaging systems, physically combining the CT and SPECT/PET acquisition, and software allowing fusion of images obtained separately, are promising non-invasive techniques to assess CAD. It is expected that such systems will gain in popularity in the future, to reduce the number of patients unnecessarily referred for ICA examination. Here, we present the software-based Synchronized Multimodal heART Visualization (SMARTVis) fusion system, which allows comprehensive analysis of cardiac multimodal imaging data for assessment of CAD. The aim of the present study is to investigate whether integrated analysis of cardiac CTA and SPECT-MPI with the SMARTVis system improves diagnostic performance, compared to conventional side-by-side interpretation.

6.2 Materials and Methods

6.2.1 Study population

Seventy-one patients who underwent cardiac CTA and SPECT-MPI at the Leiden University Medical Center (Leiden, The Netherlands) were randomly selected. After applying exclusion criteria (Figure 6.1), seventeen patients were included in our study; images

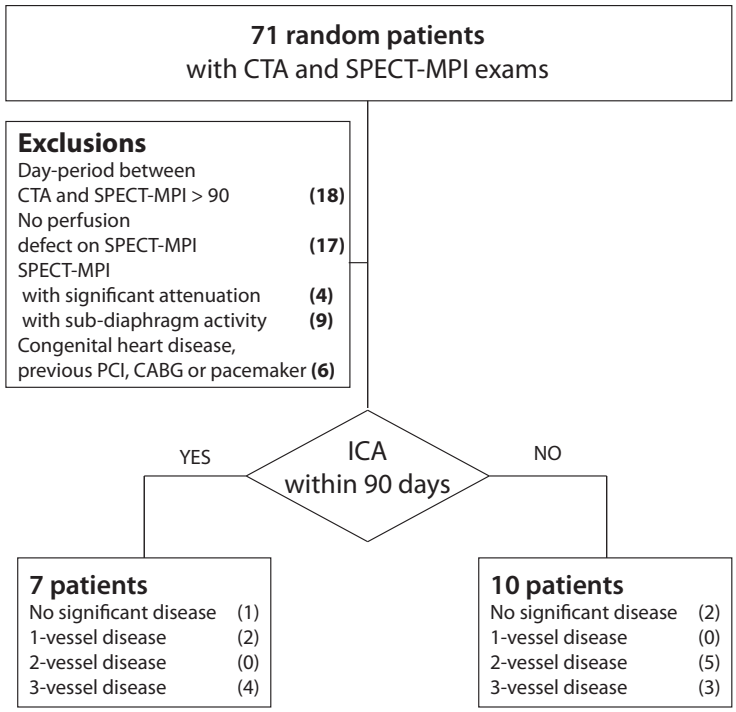

Figure 6.1: Patient's selection and exclusion criteria.

from an invasive coronary angiography (ICA) procedure performed within a 90-day period were available for seven of them. Patient characteristics are presented in Table 6.1. For retrospective study of anonymized data, institutional review board approval was waived by both institutes.

6.2.2 SPECT-MPI

Image acquisition SPECT-MPI were performed using a two-day protocol starting with the stress-test imaging. The patients underwent bicycle ergometry or, when contraindications were present, adenosine or dobutamine infusion to induce stress. The radioisotope, 500 MBq Tc-99m tetrofosmin, was injected either at peak exercise, 3 minutes after starting adenosine perfusion or at peak heart rate during dobutamine infusion. For both stress and rest scan, the images were acquired one hour after radioisotope injection. A triple-headed camera system (Toshiba CGA 9300, Tokyo, Japan) and a low-energy-high-resolution collimator were used. ECG gating was performed at 16 frames per cardiac cycle, with a tolerance window of 50%. The data were pre-filtered with a low-pass Butterworth filter (8th order, cutoff frequency 0.26 cycles/pixel) and reconstructed using filtered back-projection to yield short-axis images. No attenuation or scatter correction was applied.

Table 6.1: Patient characteristics (N=17)

Characteristics	
Age (y)	61 ± 9
Males (N)	15 (90%)
Body Mass Index ($kg \times m^{-2}$)	22.8 ± 4.4
Calcium score (Agatston)	$494(IQR85 - 1319; range0 - 4797)$
Medical history *based on CTA*	**N (%)**
No significant disease	3(17)
1-vessel disease	2(12)
2-vessel disease	5 (29)
3-vessel disease	7 (42)
Cardiovascular risk factors	**N (%)**
Current smoker	7(42)
Hypertension	11(65)
Diabetes mellitus	14(82)
Hypercholesterolemia	12(70)
Family history of CVD	4(24)
Imaging	**mean $\pm$ std [min,max]**
Day-period between CTA and SPECT-MPI	$31 \pm 31[1, 79]$
Day-period between CTA and ICA (N=7)	$45 \pm 30[8, 85]$

Image interpretation An experienced nuclear physicist, blinded to both CTA and ICA results, analyzed the scans using the Corridor4DM software package (Version 6.1, INVIA Solutions, Ann Arbor, MI, USA) (Ficaro et al., 2007). SPECT-MPI images were interpreted using oblique slices, polar maps and quantitative/functional values. The SPECT-MPI interpretation was summarized into a report, accordingly to the guidelines of Folks (2002): the observer graded each of the 19 myocardial segments (Figure 6.2) as being normal (no perfusion defect) or abnormal (stress perfusion or fixed defects), and indicated the presence/absence of myocardial infarction or ischemia.

6.2.3 Computed Tomography Angiography

Image acquisition Five patients were scanned using a 64-slice CT scanner (Aquilion 64, Toshiba Medical Systems Corporation, Otawara, Japan) and the remaining twelve patients were scanned using a 320-slice CT scanner (Aquilion ONE, Toshiba Medical Systems Corporation, Otawara, Japan). In case the heart rate was higher than 65 beats/min, additional oral Îš-blockers (metoprolol 50 mg, single dose, one hour before scan) were provided when tolerated. A prospectively triggered coronary calcium scan (non-contrast CT scan) was performed before CTA acquisition. CTA images were acquired with a collimation of $64 \times 0.5mm$ (resp. $320 \times 0.5mm$), a tube rotation time of 400 ms, and tube current of 300 mA at 120 kV for patients with normal posture ($BMI \leq 30kg.m^{-2}$). If a patient had a higher body mass index, tube current was increased to 350 or 400 mA

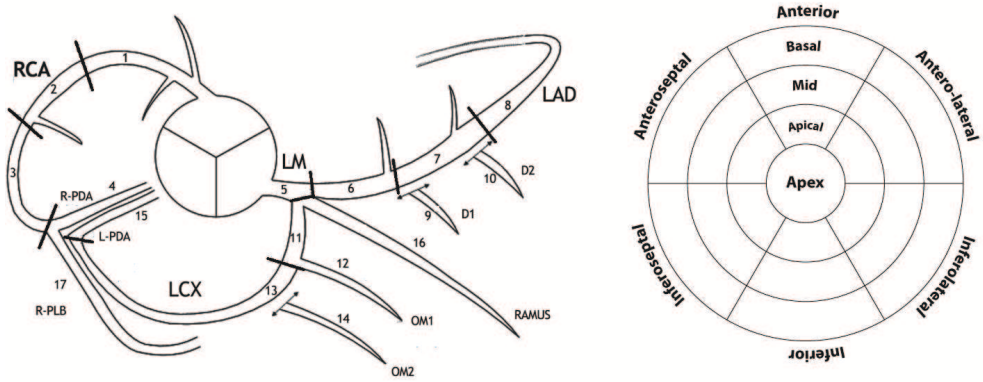

Figure 6.2: **(a)** Coronary segmentation diagram. Axial coronary anatomy definitions derived, adopted, and adjusted from Austen et al. (1975). Left main (LM), left anterior descending artery (LAD), right coronary artery (RCA), left circumflex artery (LCX), diagonal branch (D), obtuse marginal branch (OM), posterior descending artery (PDA), posterior lateral artery (PL) and intermediate branch (IMB). Proximal (p), middle (m), distal (d). 1: p-RCA, 2: m-RCA, 3: d-RCA, 4: PDA, 5: LM, 6: p-LAD, 7: m-LAD, 8:d-LAD, 9: D1, 10: D2, 11: p-LCX, 12: OM1, 13: m-LCX, 14: OM2, 15: d-LCX, 16: IMB, 17: PL. **(b)** 19 myocardial segments model used to interpret the SPECT-MPI.

at 135 kV. The acquisition of imaging was prospectively triggered at 75% of the R-to-R interval. Between 80 and 110 ml non-ionic contrast material (Iomeron 400H, Bracco Atlanta Pharma, Konstanz, Germany) was administered with a flow rate of 5 ml/sec depending on the total scan time. The timing of the scan was determined using automated detection of peak enhancement in the aortic root. Acquisition was conducted during an inspiratory breath hold of approximately 10 s.

Image interpretation A single experienced reader, blinded to both SPECT-MPI and ICA results, analyzed the scans using the Syngo.Via workstation (Siemens Healthcare, Erlangen, Germany). CTA images were interpreted using trans-axial image stacks and (curved) multi-planar reformatted images (MPR/cMPR). The CTA interpretation per coronary segment (AHA Model, Austen et al. (1975))was then summarized into a report, accordingly to the guidelines of Raff et al. (2009): for each coronary artery lesion present in one of the modified 17-AHA-segments (American Heart Association, Figure 1), the observer reported the stenosis location (origin, proximal, mid, distal, end), the stenosis severity (mild, moderate, severe, occluded), and the stenosis plaque type (non-calcified, mixed, calcified).

6.2.4 Quantitative Coronary Angiography

ICA was performed accordingly to standard medical practice. One experienced cardiologist, unaware of the CTA and SPECT-MPI scoring results, performed quantitative coronary angiography (QCA) on the seven available angiograms. All coronary segments were

identified and analyzed using the modified 17-segment AHA classification (Figure 1). Segments were visually classified as normal (smooth parallel or tapering borders, visually $\leq$ 20% narrowing) or as having coronary obstruction (visually $\geq$ 20% narrowing); the stenoses in these last segments were quantified by a validated QCA algorithm [21] (CAAS, Pie Medical, Maastricht, The Netherlands). Stenoses were evaluated in the worst (available) angiographic view and classified as significant if the lumen diameter reduction exceeded 50%.

6.2.5 SMARTVis : a software-based CTA/SPECT-MPI fusion system

In this work, we extend the **S**ynchronized **M**ultimodal he**ART Vis**ualization (SMARTVis) system introduced in Chapter 5 (Kirişli et al., 2012) to fuse CTA with SPECT-MPI nuclear myocardial perfusion imaging. An overview of the CTA and SPECT-MPI processing and fusion is given on Figure 6.3. The SMARTVis system provides comprehensive 2D and 3D fused visualizations of the anatomical and functional information for relating coronary stenoses and perfusion defect regions (Figure 6.4). The coronary artery tree extracted from CTA can be projected onto the 2D stress/rest polar map (PMAP), and, similarly, the perfusion information visualized on a 3D stress/rest PMAP can be fused with a 3D model of the heart and its coronary artery tree. Furthermore, the SMARTVis system provides a list of automatically detected and quantified coronary artery stenoses (Shahzad et al., 2012a). To further assist the user in assigning a culprit lesion to a specific perfusion defect, a (distance-based) estimation of the patient-specific coronary perfusion territories is provided. Last, the 2D and 3D PMAP viewers are synchronized with the CTA stenosis findings and images.

Beside the fused visualization, the SMARTVis system provides the opportunity to inspect 1) the non-contrast CT image and its automatically calculated per-vessel calcium scores (Shahzad et al., 2012b), 2) the CTA images and its automatically detected stenoses, and 3) the SPECT-MPI polar maps and left ventricular function curves. During the evaluation, only the fused visualizations were used by the observers.

6.2.6 Study design

The additional diagnostic value of the SMARTVis system to assess CAD was investigated through a case-study evaluation. An overview of the study design is presented in Figure 6.5.

First, structured reports were created for CTA and SPECT-MPI, conform the guidelines presented in Sections 6.2.3 and 6.2.2. Also, QCA analysis was performed for 7 patients. A treatment strategy (i.e. medical treatment or revascularization of specific coronary segment(s)) was further derived from QCA and SPECT-MPI findings and served as reference standard. As the guidelines recommend proof of ischemia prior to revascularization of coronary stenoses (Levine et al., 2011), the expert considered medical therapy indicated for significant lesions detected on QCA which resulted in infarction and no further complaints.

Subsequently, four experts from two medical centers (Erasmus Medical Center, Rotterdam, The Netherlands; Leiden University Medical Center, Leiden, The Netherlands)

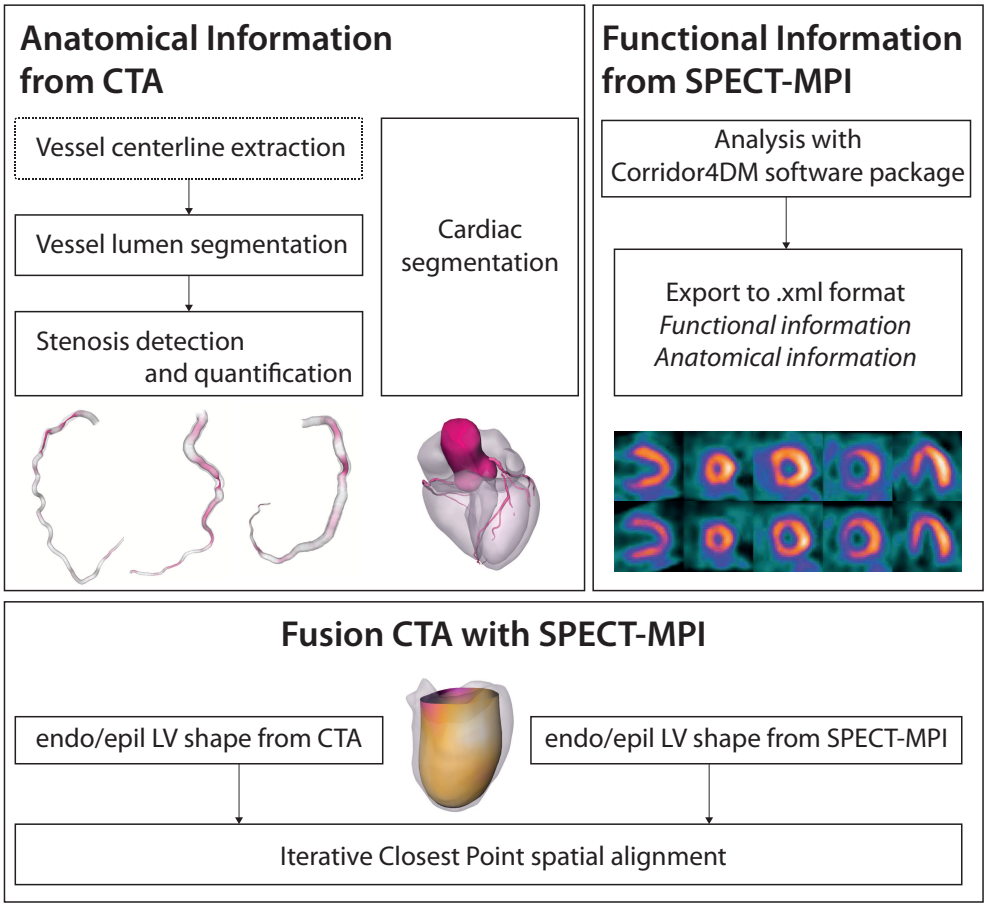

Figure 6.3: Overview of image processing performed on CTA and fusion of CTA/SPECT-MPI. The dashed box corresponds to semi-automatic process, while the solid boxes correspond to fully automatic processes. Coronary artery stenoses were detected and quantified on CTA using the method presented in Shahzad et al. (2012a); cardiac chamber shapes were obtained from CTA by applying method presented in Kirişli et al. (2010b). The SPECT-MPI left ventricle shape was automatically provided by the Corridor4DM software, as well as landmark points indicating the septal and apical positions. LV shapes and landmark points were subsequently used to align CTA and SPECT-MPI data by applying iterative closest point algorithm.

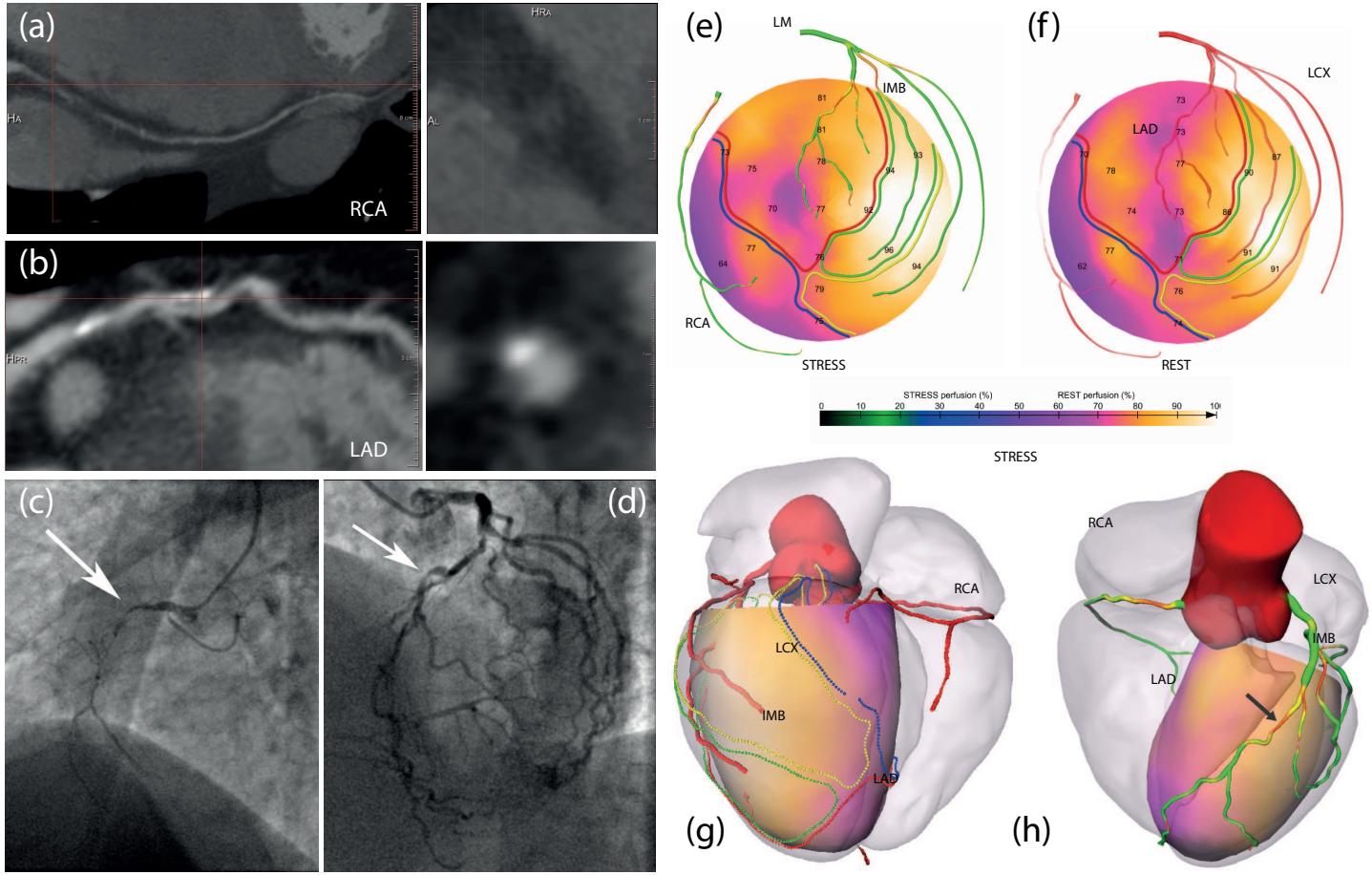

Figure 6.4: Example of patient 14 (male, 59 y.o.), who presents fixed perfusion defects in the inferior and anterior wall on SPECT-MPI and suspected triple-vessel disease on CTA. A complete occlusion was detected in the proximal RCA **(a)** and a moderate mixed plaque was detected in the middle LAD **(b)**. The QCA reveals a complete occlusion in proximal RCA **(c)** and a 50% stenosis in the middle LAD **(d)**. Comprehensive visualizations proposed in the SMARTVis system âĂŞ **(e)(f)** 2D stress and rest polar maps (PMAP) fused with projection of the coronary tree extracted from CTA. On the stress PMAP **(e)**, coronary arteries are color coded with the degree of stenosis; on the rest PMAP **(f)**, coronary arteries are coded with the distance to the epicardium: the more transparent the artery, the further it is from the epicardium. Patient-specific perfusion territories are also projected: LAD in red, LCX in yellow, MO in green and RCA in blue. **(g)(h)** 3D model of the heart and coronary artery tree extracted from CTA fused with 3D stress PMAP.

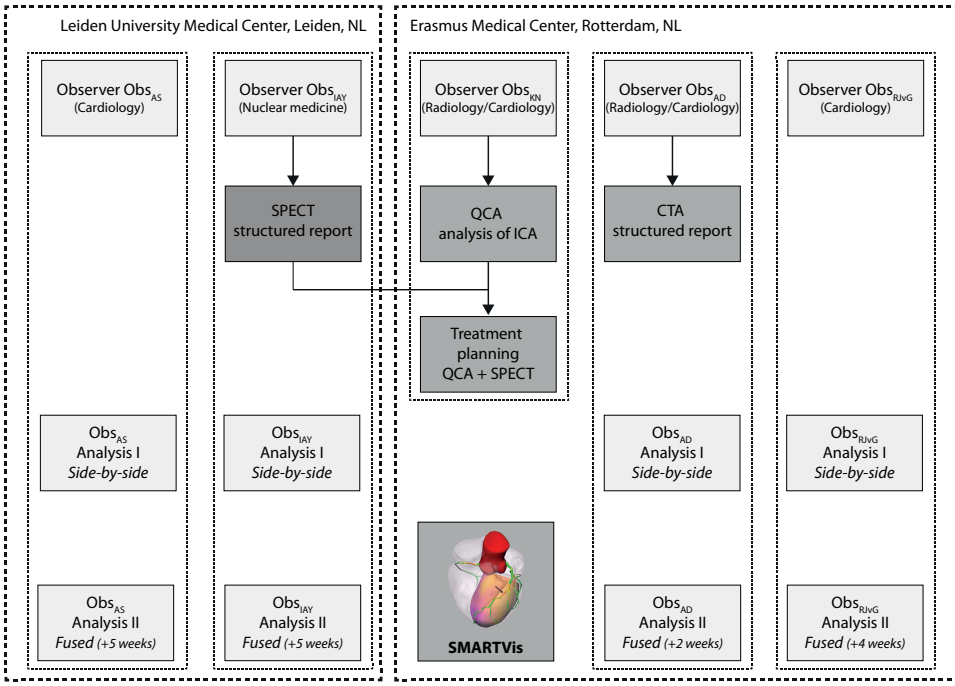

Figure 6.5: Overview of the evaluation study design. First, structured reports were created from CTA (ObsAD) and SPECT-MPI (ObsIAY), and QCA analysis was performed on the 7 available ICA. Treatment planning was performed for those 7 patients, based on QCA and SPECT-MPI findings. Second, four experts from two medical centers examined 17 patients with suspected CAD and performed 1) a side-by-side analysis, using structured CTA and SPECT-MPI reports, and 2) an integrated analysis, using the SMARTVis system in addition to the CTA and SPECT-MPI reports. Both analyses were performed with an interval of 2 to 5 weeks.

took part in the study. All observers were experienced with bot CTA and SPECT-MPI. During individual sessions, they examined the 17 selected patients and performed 1) a side-by-side analysis, using structured CTA and SPECT-MPI reports, and 2) an integrated analysis, using the SMARTVis system in addition to the CTA and SPECT-MPI reports. The side-by-side analysis was performed 2 to 5 weeks prior to the integrated analysis, and the patients were analyzed in a different order, to minimize the chance of recalling patient cases. The SMARTVis system was introduced by the first author to the observers during individual training sessions, using images of one of the excluded patient datasets. The tool was then operated by the clinical expert during the evaluation, under the supervision of the first author.

For each of the 17 coronary artery segments that presented at least one $\geq 20\%$ stenosis on CTA, the observer had first to indicate the correlation between stenoses and perfusion defects. The stenoses present in the considered coronary segment could either be related to a myocardial region presenting a perfusion defect on SPECT-MPI, or be considered as hemodynamically not significant (i.e. not inducing a perfusion defect).

Subsequently, the observer had to indicate the most appropriate therapeutic decision: medical therapy or revascularization of specific coronary segment(s).

6.2.7 Analysis

The revascularization decision strategy and target vessel selection of each observer were compared with both the other observer's decisions and the reference decision, derived from interpretation of QCA and SPECT-MPI. The diagnostic performance of CTA, SPECT-MPI and their fusion were compared on a per-vessel basis to determine the therapeutic decision agreements, as well as the sensitivity and specificity.

For all 17 patients, an inter-observer therapeutic decision agreement percentage was computed per patient p as follows:

$$Agreement^{p}_{inter-observer} = \frac{1}{4} \times \sum_{v=1}^{4} \omega_v \text{ and } \omega_v = \begin{cases} 100 & \text{if all observers agree} \\ 50 & \text{if 3 observers agree} \\ 0 & \text{otherwise} \end{cases}$$

with v the main arteries (RCA, LAD, LCX, IMB) and ω_v the observer therapeutic agreement for vessel v.

For the subset of 7 patients who underwent ICA, a therapeutic decision agreement percentage with respect to the QCA/SPECT-MPI decision was computed per patient p as follows:

$$Agreement^{p}_{QCA} = \frac{1}{4} \times \sum_{v=1}^{4} \omega_v \text{ and } \omega_v = \begin{cases} 100 & \text{if all observers agree} \\ 50 & \text{if 3 observers agree} \\ 0 & \text{otherwise} \end{cases}$$

with the QCA/SPECT-MPI decision.
Also, the sensitivity and specificity for revascularization of a coronary artery were computed.

6.3 Results

First, the results of the mono-modality analyses are reported (Sections 6.3.1 to 6.3.3). Subsequently, we report on inter-observer agreement and agreement with the reference standard (combined QCA/SPECT-MPI) for the conventional side-by-side analysis (Section 6.3.4), and the integrated analysis (Section 6.3.5), respectively. Finally, we compare the performance of integrated analysis of fused CTA/SPECT-MPIwith the side-by-side analysis (Section 6.3.6).

6.3.1 SPECT-MPI findings

Ten of the patients showed a reversible perfusion defect (58%), twelve had a fixed perfusion defect (70%), and five patients (30%) revealed a mixed perfusion defect. Eight patients (47%) showed a perfusion defect in a single coronary territory, seven (41%) in two of them, and two (12%) in all three of territories. The exact locations of the perfusion defects are listed in Table 6.3.

Table 6.2: Findings from CTA, SPECT-MPI and ICA for the 17 patients.

Patient	Sex	Age	CTA findings		SPECT-MPI findings		QCA findings	CTA	SPECT-MPI
			Agatston	≥ 50% stenosis	Reversible	Fixed	≥ 20% stenosis	suspected	suspected
1	M	61	819.6	11	Anterior basal-mid Inferior mid-apical		5(38%), 6(46%) 11(63%)	single	double
2	M	73	2840.5	1,2,3,7,8,9,10,11,12		Inferior mid-apical	NA	triple	single
3	M	55	9.9	-	Anterior-Anteroseptal mid	Inferior-Inferolateral mid-apical	-	no	double
4	M	56	4797.4	3,4,8,9,11,12,13	Anterolateral basal	Inferior	3 (53%) 12(51%), 13(70%)	triple	double
5	M	65	315.4	6,13,16	Anterior basal-mid Antero/Infero-lateral apical Antero/Infero-septal basal	Inferior	NA	double	triple
6	F	49	109.3	4,7,8,9,13	Anterior apical	NA	triple	single	
7	M	60	493.8	4,12,13,16	Antero/Infero-lateral apical		NA	double	single
8	F	81	NA	2,4,16,17		Anterior + Anteroseptal	NA	double	single
9	M	46	60.6	-		Inferior	NA	no	single
10	M	68	962.3	1,6,8,9	Anterolateral mid		NA	double	single
11	M	53	0	6,14	Anteroseptal mid Inferolateral basal-mid		NA	double	double
12	M	58	727.8	4,7,8,9,11,13,16	Antero/Infero-lateral basal-mid	Inferior + Inferoseptal	1(40%), 2(76%) 7(46%) 13(70%), 16(58%)	triple	double
13	M	60	373.8	1,2,6,7,14		Inferior	1(52%) 5(26%), 7(41%) 12(38%), 14(58%)	triple	single
14	M	59	NA	1,2,6,7,9,12,16		Inferior + Inferoseptal Anterior + Anteroseptal	1(100%) 6(50%)	triple	double
15	M	63	15.6	-		Anterior + Anterolateral + Apex Inferior + Inferoseptal	-	no	double
16	M	70	1932.5	8	Inferior + Inferolateral apical	8(100%)	single	single	
17	M	59	1676.9	3,10,12,13,14	Anterior Antero/Infero-lateral	Inferior + Inferoseptal	NA	triple	triple

6.3.2 CTA findings

Image quality was excellent in 12 patients (70%) and moderate in 5 patients (30%). The median Agatston score was 494 (IQR 85-1319; range 0-4797); 4 patients (24%) had a calcium score above 1000. In total, 263 segments were evaluated and significant stenoses were present in 66 of them (25%). The remaining 197 segments (75%) were normal or contained only non-significant stenoses ($\leq 50\%$). Among all segments, eighteen coronary segments (7%) were qualified as blurred and six segments (2%) were severely calcified. Three patients did not show any signs of CAD. In two patients single-vessel disease was suspected, in five double-vessel disease and in seven triple-vessel disease. The calcium scores and significant stenosis locations are listed in Table 6.3.

6.3.3 QCA findings

In seven of the seventeen patients (41%), a conventional ICA was performed within 45 ± 30 days after the CTA study. In these 7 patients, 15 (resp. 26) of the 100 vessel segments had a stenosis of more than 50% (resp. 20%) on ICA. One patient did not show any CAD, one patient had single-vessel disease, three double-vessel disease and two triple-vessel disease. The artery segment presenting $\geq 20\%$ stenosis and the QCA values are listed in Table 6.3. Based on the QCA and SPECT-MPI findings, revascularization was advised in segment(s) of ten coronary arteries.

6.3.4 Findings of side-by-side analysis

Detection of coronary lesions requiring revascularization For the seven patients in whom QCA was available, there was on average 81% agreement with regard to the therapeutic decision between the observers and the QCA/SPECT-MPI reference standard. Over the 4 (vessels) x 7 (patients) = 28 therapeutic decisions, the four observers agreed in fourteen cases (50%) with the QCA/SPECT-MPI therapeutic decision and three observer agreed in nine cases (32%). For the remaining five cases (18%), there was no consensus. The vessel-based sensitivities of the four observers to correctly refer for revascularization were 80%, 80%, 50% and 60% respectively; the vessel-based specificities were 83%, 83%, 100% and 84% respectively.

Inter-observer agreement Over all patients, the averaged inter-observer therapeutic decision agreement was 74%. Over the 4 (vessels) x 17 (patients) = 68 therapeutic decisions, the four observers agreed in 41 cases (60%) and one observer disagreed in 19 cases (28%). For the remaining 8 cases (12%), no consensus was reached.

6.3.5 Findings of fused analysis

Detection of coronary lesions requiring revascularization For the seven patients in whom QCA was available, there was on average 91% agreement with regard to the therapeutic decision between the observers and the QCA/SPECT-MPI reference standard. Over the 4 (vessels) x 7 (patients) = 28 therapeutic decisions, the four observers agreed in 20 cases (72%) with the QCA/SPECT-MPI therapeutic decision and three observers

agreed in 6 cases (21%). For the remaining 2 cases (7%), there was no consensus. The vessel-based sensitivities of the four observers to correctly refer for revascularization were 100%, 90%, 70% and 80% respectively; the vessel-based specificities were 94%, 83%, 100% and 100% respectively.

Inter-observer agreement Over all patients, the averaged inter-observer therapeutic decision agreement was 84%. Over the 4 (vessels) x 17 (patients) = 68 therapeutic decisions, the four observers agreed in 53 cases (78%) and one of the observer disagreed in 8 cases (12%). For the remaining 7 cases (10%), no consensus could be reached.

6.3.6 Comparison of fused and side-by-side analysis

Table 6.3: Diagnostic performance for the side-by-side and fused CTA/SPECT-MPI analysis.

	Side-by-Side				**Fused CTA/SPECT-MPI**			
Patients with ICA (N=7)								
QCA/SPECT-MPI agreement	81%				91%			
Inter-observer agreement	66%				82%			
Sensitivity (4 observers)	80%	50%	60%	80%	100%	70%	80%	90%
Specificity (4 observers)	83%	100%	94%	83%	94%	100%	100%	83%
All patients (N=17)								
Inter-observer agreement	74%				84%			

Detection of coronary lesions requiring revascularization By analyzing the integrated SPECT-MPI/CTA information using the SMARTVis system, the averaged therapeutic decision agreement improved in 4 cases (patients 01,04,13,14) and remained the same in the remaining 3 cases (patients 03,12,16). For all observers, it resulted in an increase of their sensitivity and specificity to correctly refer for revascularization.

For example, the QCA analysis of patient 01 (61 y.o. male) revealed a borderline stenosis in the mid-LAD coronary segment (46%) and a significant stenosis in the proximal LCX segment (63%). The SPECT-MPI reports indicated two reversible perfusion defects located in the anterior basal-mid and inferior mid-apical walls (suspected double-vessel disease). Consequently, the expert cardiologist recommended revascularizing both coronary artery segments. Also, the CTA report indicated one significant stenosis in p-LCX segment, and only mild (20-50%) stenoses in the LAD (suspected single-vessel disease). During the side-by-side analysis, only one observer conceded that a lesion in the mid-LAD was causing the hemodynamically significant perfusion defect in the anterior basal-mid wall, and two observers judged that the proximal LCX lesion was significant and that it required revascularization. During the integrated analysis, all four observers agreed that the perfusion defect in the anterior basal-mid wall was caused by a lesion requiring revascularization in mid-LAD, and three observers conceded that the lesion in

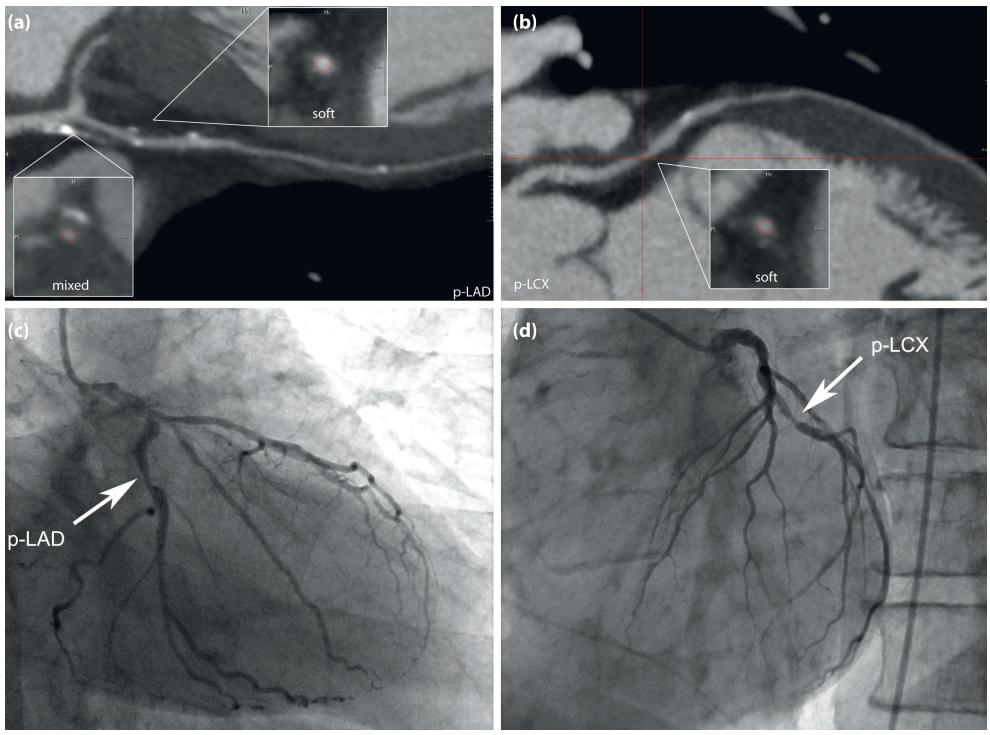

Figure 6.6: Example of patient 01 (61 y.o. male). The CTA report indicates only mild (20-50%) stenoses in the LAD **(a)** and one significant stenosis in p-LCX segment (suspected single-vessel disease) **(b)**. The QCA analysis reveals a 46% stenosis in the proximal LAD coronary segment **(c)** and a 63% stenosis in the proximal LCX segment **(d)**.

proximal LCX was inducing a hemodynamically significant perfusion defect in the inferior mid-apical wall. This perfusion defect was first incorrectly assigned by one observer to a mild lesions in RCA during the side-by-side analysis. Here, the SMARTVis system primarily assisted the observers in their interpretation by indicating the presence of a 52% stenosis in the mid-LAD segment and by showing the patient-specific coronary territories. Figure 6.6 shows the stenoses detected on CTA and QCA, and Figure 6.7 presents some visualization of the SMARTVis system.

Inter-observer agreement The inter-observer therapeutic decision agreement increased in eight of the cases (patients 01, 04, 05, 08, 10, 11, 13, 14), remained the same in seven of the cases (patients 02, 03, 07, 09, 12, 15, 16), and decreased in two cases (patients 06, 17). Over all patients, the inter-observer agreement rose from 74% during the side-by-side analysis to 84% during the integrated analysis using the SMARTVis system; over the 7 patients who underwent ICA, it increased from 66% to 82%, suggesting that increased observer agreement is also towards more correct therapeutic decisions using the SMARTVis system.

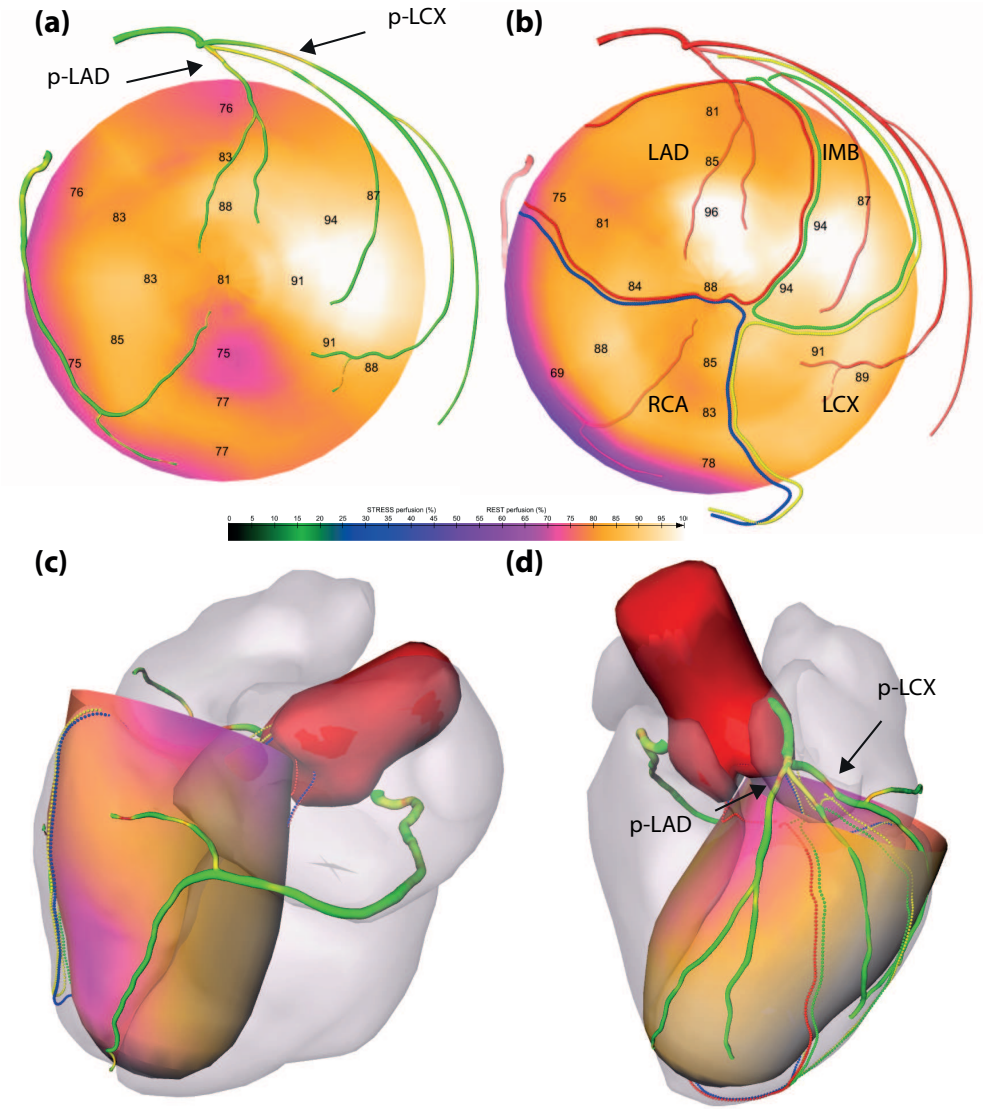

Figure 6.7: Example of patient 01 (61 y.o. male). **(a)** Stress polar map: the coronary vessel tree is color-coded with the automatically estimated degree of stenosis. **(b)** Rest polar map: the coronary arteries are coded with the distance to the epicardium: the more transparent the artery, the further it is from the epicardium. Patient-specific perfusion territories are also projected: LAD in red, LCX in yellow, MO in green and RCA in blue. **(c)(d)** 3D model of the heart and coronary artery tree extracted from CTA fused with 3D stress polar map.

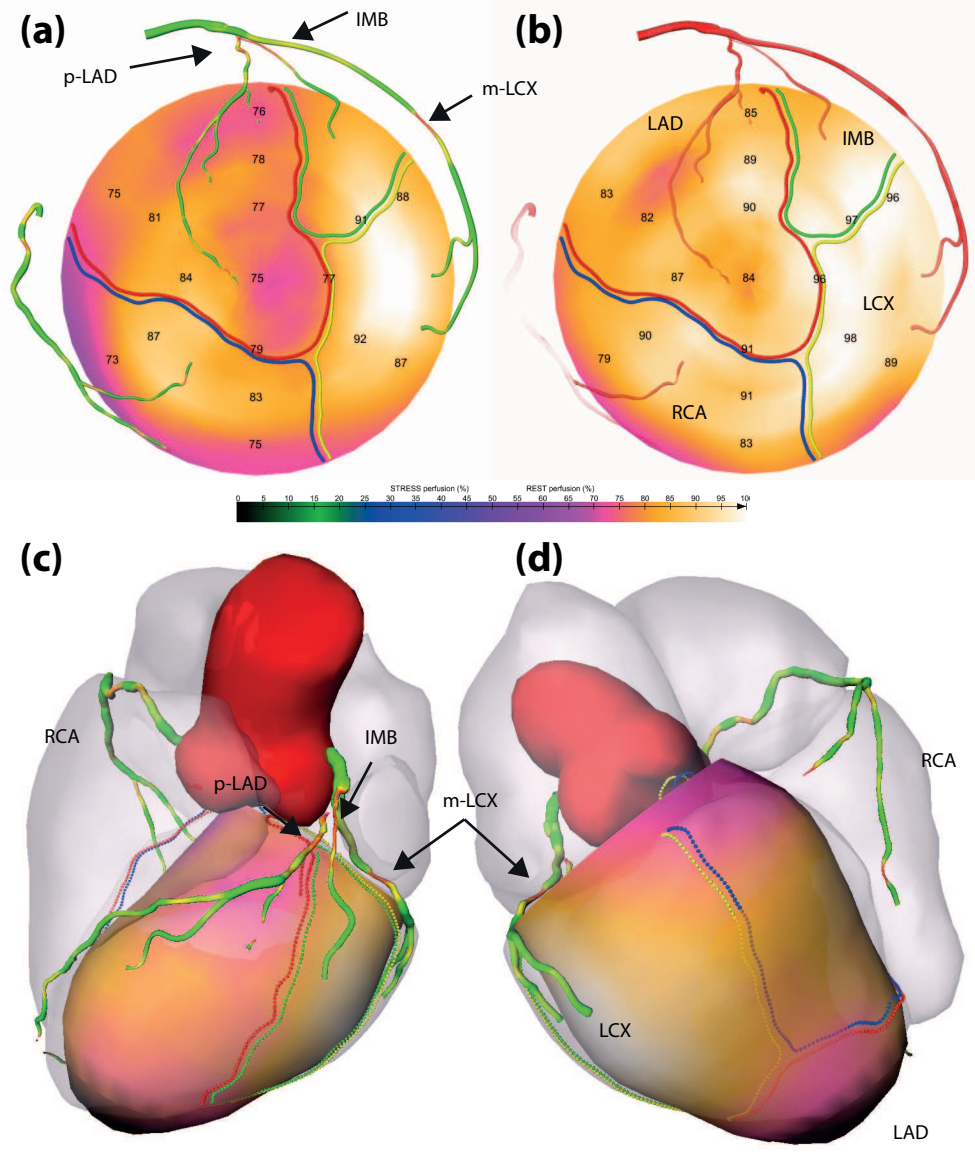

Figure 6.8: Example of patient 05 (65 y.o. male). **(a)** Stress polar map: the coronary vessel tree is color-coded with the automatically estimated degree of stenosis. **(b)** Rest polar map: the coronary arteries are coded with the distance to the epicardium: the more transparent the artery, the further it is from the epicardium. Patient-specific perfusion territories are also projected: LAD in red, LCX in yellow, MO in green and RCA in blue. **(c)(d)** 3D model of the heart and coronary artery tree extracted from CTA fused with 3D stress polar map.

For example, for patient 05 (65 y.o. male), the CTA report indicated the presence of a severe mixed stenosis in the p-LAD segment, a moderate mixed stenoses in the m-LCX segments, and multiple mild stenoses in the three main vessels (suspected double-vessel disease). The SPECT-MPI report indicated three reversible perfusion defects located in the anterior basal-mid, antero/infero-lateral apical and antero/infero-septal basal walls, as well as a fixed perfusion defect in the inferior wall (suspected triple-vessel disease). During the side-by-side analysis, all four observers agreed on the necessity to revascularize the stenosis in LAD, which causes the reversible anterior basal-mid defect. However, no consensus was reached for the therapeutic decision concerning the LCX and the IMB: two observers advised to perform revascularization, while the two others recommended taking medication. During the integrated analysis, the four observers further agreed to treat the IMB with only medication. Also, though all the observers linked the perfusion defect in the antero/infero-lateral basal wall to the lesions in the LCX, only one observer advised to perform revascularization of the LCX. Figure 6.8 presents some visualizations of the SMARTVis system. Here, the integrated analysis of using the SMARTVis system resulted in an increase of the inter-observer therapeutic decision agreement.

6.4 Discussion

6.4.1 Additional diagnostic value of cardiac CTA and SPECT-MPI fused analysis

The results of our case-study, performed with four experts at two medical centers in seventeen patients, demonstrated that in several cases, the integrated analysis of cardiac CTA and SPECT-MPI has a clinical benefit, in the sense that both the inter-observer agreement increased and the therapy planning decisions were in better agreement with the reference standard.

Specifically, we found the tool to be of additional value in the diagnosis of patients who have perfusion defect(s) in fewer coronary territories than suspected vessel disease on CTA, i.e. who have a perfusion defect in one coronary territory and suspected double-/triple-vessel disease on CTA (diagnosis of patients 08, 10 and 13 improved; diagnosis of patients 02 and 07 remained identical), a perfusion defect in two coronary territories and suspected double-/triple-vessel disease on CTA (diagnostic of patients 01, 04, 11 and 14 improved). In such cases, the relation between the coronary territories with a perfusion defect and its supplying coronary arteries is uncertain, thus making the use of the patient-specific SMARTVis system helpful.

The case study further revealed that the image fusion as implemented in the SMARTVis system does not have additional diagnostic value for patients with 1) no coronary stenoses (diagnosis of patients 03, 09 and 15 remained identical), 2) suspected single-vessel disease on both CTA and SPECT-MPI (diagnosis of patient 16 remained identical), and 3) triple-vessel disease (diagnosis of patient 12 remained identical; diagnosis of patient 17 got worse). In fact, if a patient has no significant stenoses reported, but the SPECT-MPI study reveals the presence of perfusion defect(s), the observers consider that the perfusion defect(s) is/are not cause by obstruction in the epicardial coronary arteries, but may be the result of micro-vascular disease or of artifact. In case of suspected

single-vessel disease, it is clear which coronary is causing the perfusion defect, and, thus, integrating information in a patient-specific way leads to the same diagnosis as during side-by-side analysis. Also, patients with suspected triple-vessel disease do not benefit from such a combined approach.

To summarize, integrated analysis of cardiac CTA and SPECT-MPI using the SMARTVis system results in an additional diagnostic value primarily for patients with angiographic CAD that exceeds myocardial hypoperfusion on SPECT-MPI.

6.4.2 Comparison to previous studies

Our work differs from previously published ones (Nakaura et al., 2005; Gaemperli et al., 2007b,a, 2009; Slomka et al., 2009; Kaufmann, 2009; Santana et al., 2009; Sato et al., 2010) primarily by the way the information from CTA and SPECT-MPI is fused, and how the evaluation has been carried out. Previously, CTA images were registered (i.e. aligned) with SPECT-MPI images to provide fused 3D SPECT/CT images. We introduce a comprehensive visualization system to fuse multi-modal imaging data, and provide fused representations in both 2D and 3D for the convenience of the observer. Such an integration of cardiac CTA and SPECT-MPI anatomical and functional information into a single coordinated visual analysis tool is novel, maximizing the diagnostic complementarities of CTA and SPECT-MPI imaging modalities.

The results of the presented work are consistent with the conclusions presented in previously published work on fusion of cardiac CTA and SPECT-MPI for assessment of CAD, where fused CTA/SPECT-MI interpretation appears to provide added diagnostic information on the hemodynamically relevance of coronary artery lesions.

Fusion of cardiac anatomical and functional information for the assessment of CAD has been introduced by Nakaura et al. (2005). Based on four cases, the study suggested that fused interpretation improves the relationship of relevant coronary arteries and abnormal perfusion territory. Also, Sato et al. (2010) demonstrated that, based on a population of 130 patients, side-by-side combined interpretation of CTA and SPECT-MPI provides added diagnostic value, as compared to stand-alone CTA interpretation. Recently, in Gaemperli et al. (2007b,a, 2009), the authors further investigated the incremental diagnostic value of fused CTA/SPECT-MPI interpretation. In Gaemperli et al. (2007b), thirty-eight patients who underwent both CTA and SPECT-MPI (twenty-five additionally underwent ICA) and presented with at least one perfusion defect on SPECT-MPI were included in an evaluation study similar to ours (i.e. side-by-side vs. fused). The authors demonstrated that fused analysis provides added diagnostic information on pathophysiologic lesion severity not obtained with side-by-side analysis. The evaluations were performed by a consensus of two observers. In our work, four independent observers were involved in the evaluation, which allowed us to also investigate the added diagnostic value of fused analysis to reduce inter-observer variability in revascularization strategy and target vessel selection decisions. Also, Gaemperli et al. (2009) demonstrated that fusion of CTA and SPECT-MPI allows accurate detection of flow-limiting coronary stenoses (i.e. significant stenoses inducing ischemia) and that it is thus a potential gatekeeper for ICA and coronary revascularization. In our work, we provide additional insights concerning which patients are more likely to benefit from integrated analysis of fused CTA/SPECT-MPI.

6.4.3 Limitations and strengths of the study design

One limitation of our study is the modest population size. However, results were consistent among observers and datasets. A strength of our study was the use of four independent observers in the evaluation study.

Whether integrated analysis of fused CTA/SPECT-MPI using the SMARTVis system is more time-efficient than side-by-side interpretation remains to be investigated. The interpretation using the SMARTVis system took from 3 minutes to 15 minutes, depending on the complexity of the case and on the observer. In the current study, the observers only had a training session of a few minutes using one excluded patient to get familiar with the SMARTVis system. A reliable investigation of the time-efficiency would require a substantial longer time of use in clinical practice.

Over all, the observers were enthusiastic about the presented integrated visualization tool and some were eager to use the SMARTVis system in clinical practice.

Further investigation also remains to be done to determine which patients should undergo such examination (increased imaging costs and radiation dose versus patient's benefits). We do not recommend all patients to undergo both CTA and SPECT-MPI examination, but underline that if both tests are performed, integrated analysis is to be preferred.

6.5 Conclusion

Integrated analysis of fused cardiac CTA and SPECT-MPI using the SMARTVis system primarily results in additional diagnostic value for patients presenting coronary artery disease in more vessels than the number of reported perfusion defects. The SMARTVis comprehensive visualization system can be effectively used to assess disease status in multi-vessel CAD patients, offering valuable new options for the diagnosis and management of these patients.

chapter 7

Summary and Discussion

7.1 Summary

In this thesis, we described the development and evaluation of techniques for quantify cardiovascular anatomy and relating it to functional information using multi-modal imaging data, for the assessment of coronary artery disease. Cardiac and coronary artery tree models were created from CTA, and integrated together with functional quantification of the myocardium, derived from either MRI or SPECT-MPI, into a patient-specific comprehensive visualization system, called Synchronized Multimodal heART Visualization (SMARTVis).

7.1.1 Cardiovascular anatomy quantification in CTA

In the first chapters, we presented techniques to create the cardiac and coronary artery tree models from CTA images.

In clinical practice, the extraction of ventricular and atrial functional information, such as stroke volume and ejection fraction, requires accurate delineation of cardiac chambers. In **Chapter 2**, we described a fully automatic multi-atlas based method for segmenting the whole heart and cardiac chambers from CTA data. We investigated the method's accuracy and robustness on multicenter and multivendor CTA data. The 3D quantitative evaluation performed on 8 images resulted in a mean surface-to-surface error of 0.94 ± 1.12 mm and an average Dice coefficient of 0.93; the 2D quantitative evaluation performed on 60 multi-vendor datasets resulted in a mean surface-to-surface error of 1.26 ± 1.25 mm and an average Dice coefficient of 0.91. Additional semi-quantitative evaluation of 1380 CTA images demonstrated the robustness of the presented method: 49% of the images were very accurately segmented (below 1 mm error) and 29% were accurately segmented (error between 1 and 3 mm).

Extraction of coronary arteries from CTA data is a crucial step for accurate visualization, quantification, and pathology detection and quantification. In **Chapter 3**, we presented an automatic method to detect and quantify coronary artery stenoses from CTA data. Quantitative evaluation on 30 datasets showed, for the detection, a sensitivity of 29% and a PPV of 24% as compared to QCA, and a sensitivity of 21% and a PPV of 23% when compared to manual assessment on CTA. The stenosis degree was estimated with an absolute average difference of 31% when compared to QCA, and a weighted kappa value of 0.29 when compared to CTA. A Dice of 68% and 65% was reported for lumen segmentation of healthy and diseased vessel segments respectively. The results indicate that discrimination between significant and non-significant lesions remains a challenge and that a trade-off between the ability to detect significant lesions and the ability of ruling out disease needs to be made.

Recently, several other methods for coronary artery stenosis detection and quantification have been proposed in literature. However, the methods that are available are often not objectively evaluated or the results are difficult to compare, as experiments are usually often performed on data selected by the researchers, which can come from different institutions, scanners and populations. Moreover, researchers often use different evaluation measures, which make published methods difficult to compare. This has resulted in a growing interest in *evaluation frameworks* in medical image analysis, to compare different algorithms for a particular task on the same (clinically representative) data, using

the same evaluation protocol. In **Chapter 4**, we introduced a standardized evaluation framework, to reliably evaluate and compare the performance of algorithms devised to detect and quantify the coronary artery stenoses, and to segment coronary artery lumen in CTA data. This framework consists of a publicly available database with forty-eight CTA images, a reference standard derived from both CTA manual annotations and QCA analysis, and well-defined evaluation measures. The algorithms from 11 research groups were quantitatively evaluated and compared. Currently, the framework has over 50 subscriptions and its use is required for publishing results in high quality medical imaging journals.

7.1.2 Fused visualization of cardiac anatomical and functional information

In the last chapters, we presented a patient-specific comprehensive visualization system, called Synchronized Multimodal heART Visualization (SMARTVis), to integrate cardiac and coronary artery tree models extracted from CTA with perfusion information of the myocardium, derived from either perfusion MRI or SPECT-MPI.

In **Chapter 5**, we introduced the SMARTVis patient-specific visualization system, for relating coronary stenoses derived from CTA with perfusion deficits derived from MRI. The additional value of the comprehensive visualizations in assessing CAD was demonstrated through a first clinical evaluation, by performing a comparative diagnostic study and a case-study research evaluation involving two experts and four patients having suspected double-vessel disease. When using the SMARTVis system, a more reliable estimation of the relation between perfusion deficits and stenoses led to a more accurate diagnosis, as well as a better inter-observer diagnosis agreement.

In **Chapter 6**, we extended the SMARTVis system to integrate perfusion information from SPECT-MPI. We investigated the additional diagnostic value of fused CTA/SPECT-MPI analysis compared with side-by-side analysis, in patients with suspected CAD. A clinical evaluation was performed, involving four experts from two medical centers and 17 patients suspected of having single-, double- or triple-vessel disease. It was shown that the SMARTVis comprehensive visualization system can be effectively used to assess disease status in multi-vessel CAD patients, and is thus a valuable tool for the diagnosis and management of these patients.

In conclusion, the integrated visualization proposed in the SMARTVis system enables a *one-stop-shop* visual exploration of cardiac anatomical and functional data, to maximally exploit the complementary information of multiple imaging modalities. It has been confirmed that such comprehensive visualizations allow to effectively relate perfusion defects and coronary lesions, and that fused integrated analysis leads to a more accurate diagnosis.

7.2 Discussion

In this discussion, we summarize the main contributions of the thesis. We will first discuss the methodological contributions of each chapter, and place these into perspective of recent literature and developments in the field. Finally, we discuss future directions of research.

7.2.1 Cardiovascular anatomy quantification in CTA

Cardiac chambers delineation is a prerequisite for quantifying heart failure (e.g. volume quantification) and for integrated visualization of cardiac anatomical and functional information, and extraction of coronary arteries data is a crucial step for accurate visualization, quantification, and tracking of pathologies. In this thesis, a fully automatic multi-atlas based method for whole heart and cardiac chamber segmentation on CTA data have been proposed in **Chapter 2**, and an automatic method to detect and quantify coronary artery stenoses from CTA data has been presented in **Chapter 3**. Recently, the number of publications presenting and/or evaluating coronary artery stenosis detection and quantification techniques in cardiac CTA datasets is growing, thus increasing the need for a standardized evaluation framework. Therefore, we introduced a standardized evaluation framework in **Chapter 4** of this thesis, allowing the effective comparison of coronary artery stenosis detection and quantification methods, and coronary lumen segmentation algorithms, on CTA images. The approach we proposed in **Chapter 3** has been evaluated using this framework.

In **Chapter 2**, we did not explicitly evaluate whether our segmentation method allows accurate extraction of functional information from dynamic CTA data. However, Abadi et al. (2009) showed that, if a robust cardiac segmentation method is provided, chamber and myocardial volumes derived from the segmentation results give reliable functional measurements. Results of evaluation demonstrated that a robust and accurate automatic cardiac segmentation could be achieved with our approach, and thus we deduced that derivation of functional parameters should be possible using the presented segmentation method.

The evaluation study has provided very useful insight into the current state-of-the-art in coronary segmentation segmentation and stenosis detection/quantification. The most appropriate method for stenosis detection and quantification depends on the goal one wants to achieve. Especially, a trade-off needs to be made between having a good sensitivity and an acceptable detection rate. Also, though the coronary artery lumen wall can be automatically segmented with a precision similar to the expert's one, (semi-)automatic detection and quantification of coronary artery stenosis is still not a solved problem; performance of the quantification methods is in general much worse than the observers.

The concept of a comparative study for algorithms that address a particular image analysis task is well known; an overview of the existing medical image analysis evaluation framework is provided at *http://www.grand-challenge.org/*. The quality of an evaluation framework critically relies on the datasets that are made available for training and testing, and the quality of the reference standard. Currently, the framework presented

in **Chapter 4** is lacking datasets from one of the main CT scanner vendors (GE Healthcare); thus, the variety of CTA datasets provided could still be improved. Our evaluation framework provides images acquired with latest technologies (dual-source, 64 and 320 slice CT scanners), but these datasets may become outdated in a few years if a new generation of CT scanners becomes available. Thus, in the coming years, new datasets may be added to the initial ones, to cope with advances in CT scanner technologies and still provide clinically representative data.

A clear limitation of challenge remains that the evaluated algorithms are generally not available. In the future, the concept of a challenge would benefit from a framework where the evaluated algorithms become publicly available, such that it becomes possible to run the evaluated algorithms on other datasets, without having the burden of re-implenting the algorithm.Furthermore, having observed that each method has different strengths and weaknesses, it is interesting to consider their combination. The added-value of combining several algorithms as been investigated in two challenges (Niemeijer et al., 2011), where it was been shown that a combination of algorithms can outperform, on average, the best single algorithm. However, public availability of algorithms is the underlying necessary condition to combine existing algorithms.

At the moment, whereas CTA correlates well with QCA for measuring stenosis severity (Meijboom, W.B. and Meijs, M.F L. et al., 2008), the hemodynamic significance of a coronary artery stenosis can not be determined by CTA alone, but requires either a perfusion test (MRI or SPECT-MPI) or an invasive FFR measurement. In the coming years, CTA stand-alone may however allow the detection of flow-limiting lesions in patients with significant stenosis. Non-invasive FFR using CTA (CT-FFR) is a relevant research topic, and several research groups and companies are investigating new techniques to predict the hemodynamic significance of coronary lesions detected on CTA (Koo et al., 2011). As a future perspective, it would therefore be interesting to create an evaluation framework to investigate the diagnostic performance of CTA in determining the hemodynamic significance of coronary artery lesions using FFR measurements performed during CCA as a reference standard.

7.2.2 Fused visualization of cardiac anatomical and functional information

The ultimate goal of the work in this thesis is to combine the information extracted from CTA with functional information extracted from either perfusion MRI or SPECT-MPI, for the assessment of coronary artery disease. Relating a coronary stenosis to a perfusion defect is challenging due to the high anatomical variability of the coronary arteries between patients (Pereztol-Valdés et al., 2005).

In **Chapters 5 and 6**, the potential improvement of decision-making in the management of patients has been investigated and the results demonstrated that integrated visualization of data derived from complementary imaging techniques may offer valuable advantages in diagnosis, staging and treatment of CAD. Specifically, we found the SMARTVis tool to be of additional value in the diagnosis of patients who have perfusion defect(s) in fewer coronary territories than suspected vessel disease on CTA. However,

although our results were consistent and the expert feedback was positive, a larger study should be conducted in order to draw stronger conclusions.

Whether integrated analysis using the SMARTVis system is more time-efficient than side-by-side interpretation remains to be investigated. A reliable investigation of the time-efficiency would require a substantial longer time of use in clinical practice. Over all, the observers were enthusiastic about the presented integrated visualization tool and some were eager to use the SMARTVis system in clinical practice.

Introduction into clinical practice of the developed image processing and visualization techniques would still require substantial work. The system consists of multiple processing steps, and most of these steps are performed using individual research oriented software packages. The deployment of our cardiac segmentation and stenosis detection and quantification tools for daily clinical use would require, next to regulatory approvals, a further automation of the various processing steps, the integration of all individual research oriented software packages, and the creation of a graphical user-interface, to allow the user to visualize and manually correct automatically obtained segmentations and quantifications. Concerning the SMARTVis system, as a generic data representation was used in the implementation, the anatomical and functional information can be computed using any software used in daily clinical practice, provided that a conversion to our representation is possible.

Non-invasive angiography and functional testing provide complementary information which are important for the management of patient with suspected CAD. Hybrid cardiac imaging systems, and software allowing fusion of images obtained separately, are promising non-invasive techniques. It is expected that such systems will gain in popularity in the future, to reduce the number of patients unnecessarily referred for invasive coronary angiography examination. A clinical algorithm to determine which patients should undergo such examination has been proposed by Flotats et al. (2011) and highlighted that patients with intermediate risk for CAD would be more likely to benefit from hybrid cardiac imaging. Last, increased imaging costs and radiation dose associated with cardiac hybrid imaging should also be taken into consideration.

7.3 Conclusion

In conclusion, in this thesis, we developed and evaluated techniques to quantify cardiovascular disease on CTA imaging data, and proposed a novel comprehensive visualization system to assess coronary artery disease by integrating anatomical and functional information extracted from multi-modal imaging techniques.

The evaluation demonstrated that:

(i) accurate delineation of cardiac chambers from CTA images can be achieved using a multi-atlas based segmentation approach, enabling assessment of ventricular and atrial function

(ii) coronary artery lumen wall can be automatically segmented with a precision similar to the expert's one, but that (semi-)automatic detection and quantification of coronary artery stenosis is still not a solved problem

(iii) the SMARTVis system allows a more reliable estimation of the relation between perfusion deficits and stenoses, leading to a more accurate diagnosis, as well as a better inter-observer diagnosis agreement.

Bibliography

Abadi, S., Roguin, A., Engel, A., Lessick, J., 2009. Feasibility of automatic assessment of four-chamber cardiac function with MDCT: initial clinical application and validation. European Journal of Radiolo 74 (1), 175–181.

Achenbach, S., Schuhbaeck, A., Marwan, M., Bathina, R., Ovrehus, K., Anders, K., Hoffmann, U., Abbara, S., Aulbach, P., Ropers, D., Pflederer, T., Becker, C., Berman, D., Hausleiter, J., 2012. Multicenter evaluation of dual source CT coronary angiography in patients with intermediaite likelihood of coronary artery stenoses (MEDIC): Accuracy for the detection of individuals with significant coronary artery stenoses. Journal of American College of Cardiology 59 (1337), 61338–2.

Aljabar, P., Heckemann, R., Hammers, A., Hajnal, J., Rueckert, D., 2009. Multi-atlas based segmentation of brain images: atlas selection and its effect on accuracy. NeuroImage 46, 726–738.

Arnoldi, E., Gebregziabher, M., Schoepf, U., Goldenberg, R., Ramos-Duran, L., Zwerner, P., Nikolaou, K., Reiser, M., Costello, P., Thilo, C., 2010. Automated computer-aided stenosis detection at coronary CT angiography: initial experience. European Radiology 20 (5), 1160–1167.

Artaechevarria, X., Munoz-Barrutia, A., Ortiz-de Solorzano, C., 2009. Combination strategies in multi-atlas image segmentation: application to brain MR data. IEEE Transactions on Image Processing 28 (8), 1266 – 1277.

Austen, W., Edwards, J., Frye, R. L., Gensini, G., Gott, V., Griffith, L., McGoon, D., Murphy, M., Roe, B., Apr 1975. A reporting system on patients evaluated for coronary artery disease. Report of the Ad Hoc Committee for Grading of Coronary Artery Disease, Council on Cardiovascular Surgery, American Heart Association. Circulation 51 (4 Suppl), 5–40.

Baltaxe Milwer, M., Flórez-Valencia, L., Hernández-Hoyos, M., Magnin, I., Orkisz, M., aug. 2007. Fast-marching contours for the segmentation of vessel lumen in CTA cross-sections. In: Annual International Conference of the IEEE Engineering in Medicine and Biology Society. pp. 791 –794.

Bax, J., Beanlands, R., Klocke, F., Knuuti, J., Lammertsma, A., Schaefers, M., Schelbert, H., Von Schulthess, G., Shaw, L., Yang, G., et al., 2007. Diagnostic and clinical perspectives of fusion imaging in cardiology: is the total greater than the sum of its parts? Heart 93 (1), 16–22.

Beliveau, P., Setser, R., Cheriet, F., White, R., O'Donnell, T., 2007. Computation of coronary perfusion territories from CT angiography. In: Proceedings of Computers in Cardiology. Vol. 34. pp. 753–756.

Boogers, M., Broersen, A., van Velzen, J., de Graaf, F., El-Naggar, H., Kitslaar, P., Dijkstra, J., Delgado, V., Boersma, E., de Roos, A., Schuijf, J., Schalij, M., Reiber, J., Bax, J., Jukema, J., 2012. Automated quantification of coronary plaque with computed tomography: comparison with intravascular ultrasound using a dedicated registration algorithm for fusion-based quantification. European Heart Journal 33 (8), 1007–1016.

Boogers, M. J., Schuijf, J. D., Kitslaar, P. H., van Werkhoven, J. M., de Graaf, F. R., Boersma, E., van Velzen, J. E., Dijkstra, J., Adame, I. M., Kroft, L. J., de Roos, A., Schreur, J. H. M., Heijenbrok, M. W., Jukema, J. W., Reiber, J. H. C., Bax, J. J., Jul 2010. Automated quantification of stenosis severity on 64-slice CT: a comparison with quantitative coronary angiography. Journal of American College of 3 (7), 699–709.

Boxt, L., 2005. CT anatomy of the heart. International Journal of Cardiovascular Imaging 21, 13–27.

Broersen, A., Kitslaar, P., Frenay, M., Dijkstra, J., 2012. FrenchCoast: Fast, Robust Extraction for the Nice Challenge on COronary Artery Segmentation of the Tree. In: Proceedings of MICCAI Workshop "3D Cardiovascular Imaging: a MICCAI segmentation Challenge".

Brown, L., 1992. A survey of image registration techniques. ACM Computing Surveys 24 (4), 325–376.

Budoff, M. J., Achenbach, S., Blumenthal, R. S., Carr, J. J., Goldin, J. G., Greenland, P., Guerci, A. D., Lima, J. A. C., Rader, D. J., Rubin, G. D., Shaw, L. J., Wiegers, S. E., on Cardiovascular Imaging, A. H. A. C., Intervention, on Cardiovascular Radiology, A. H. A. C., Intervention, American Heart Association Committee on Cardiac Imaging, C. o. C. C., Oct 2006. Assessment of coronary artery disease by cardiac computed tomography: a scientific statement from the American Heart Association Committee on Cardiovascular Imaging and Intervention, Council on Cardiovascular Radiology and Intervention, and Committee on Cardiac Imaging, Council on Clinical Cardiology. Circulation 114 (16), 1761–1791.

Cerqueira, M., Weissman, N., Dilsizian, V., Jacobs, A., Kaul, S., Laskey, W., Pennell, D., Rumberger, J., Ryan, T., Verani, M., et al., 2002. Standardized myocardial segmentation and nomenclature for tomographic imaging of the heart a statement for healthcare professionals from the cardiac imaging committee of the Council on Clinical Cardiology of the American Heart Association. Circulation 105 (4), 539–542.

Cetin, S., Demir, A., Yezzi, A., Degertekin, M., Unal, G., 2013. Vessel tractography using an intensity based tensor model with branch detection. IEEE Transactions on Medical Imaging 32 (2), 348–363.

Cetin, S., Unal, G., 2012. Automatic detection of coronary artery stenosis in cta based on vessel intensity and geometric features. In: Proceedings of MICCAI Workshop "3D Cardiovascular Imaging: a MICCAI segmentation Challenge".

Cohen, J., 1968. Weighted kappa: nominal scale agreement with provision for scaled disagreement or partial credit. Psychological Bulletin 70 (4), 213–220.

Comaniciu, D., Meer, P., 2002. Mean Shift: a robust approach towards feature space analysis. IEEE Transactions on Pattern Analysis and Machine Intelligence 24 (5), 603–619.

Debruyne, M., Hubert, M., Suykens, J., 2008. Model selection in kernel based regression using the influence function. Journal of Machine Learning Research 9, 2377–2400.

den Dekker, M., de Smet, K., de Bock, G., Tio, R., Oudkerk, M., Vliegenthart, R., Dec 2012. Diagnostic performance of coronary CT angiography for stenosis detection according to calcium score: systematic review and meta-analysis. European Radiology 22 (12), 2688–2698.

Duval, M., Ouzeau, E., Precioso, F., Matuszewski, B., 2012. Coronary artery stenoses detection with random forest. In: Proceedings of MICCAI Workshop "3D Cardiovascular Imaging: a MICCAI segmentation Challenge".

Ecabert, O., Peters, J., Schramm, H., Lorenz, C., von Berg, J., Walker, M. J., Vembar, M., Olszewski, M. E., Subramanyan, K., Lavi, G., Weese, J., 2008. Automatic model-based segmentation of the heart in CT images. IEEE Transactions on Medical Imaging 27, 1189–1201.

Eslami, A., Aboee, A., Hodaei, Z., Moghaddam, M. J., Carlier, S., Katouzian, A., Navab, N., 2012. Quantification of coronary arterial stenosis by inflating tubes in CTA images. In: Proceedings of MICCAI Workshop "3D Cardiovascular Imaging: a MICCAI segmentation Challenge".

Faber, T., Santana, C., Garcia, E., Candell-Riera, J., Folks, R., Peifer, J., Hopper, A., Aguade, S., Angel, J., Klein, J., 2004. Three-dimensional fusion of coronary arteries with myocardial perfusion distributions: clinical validation. Journal of Nuclear Medicine 45 (5), 745–753.

Falk, E., Shah, P. K., Fuster, V., Aug 1995. Coronary plaque disruption. Circulation 92 (3), 657–671.

Fayad, Z., Fuster, V., 2001. Clinical imaging of the high-risk or vulnerable atherosclerotic plaque. Circulation 89 (4), 305–316.

Ficaro, E., Lee, B., Kritzman, J., Corbett, J., 2007. Corridor4DM: the Michigan method for quantitative nuclear cardiology. Journal of Nuclear Cardiology 14 (4), 455–465.

Flórez Valencia, L., Orkisz, M., Corredor Jerez, R. A., Torres González, J. S., Correa Agudelo, E. M., Mouton, C., Hernández Hoyos, M., 2012. Coronary artery segmentation and stenosis quantification in ct images with use of a right generalized cylinder model. In: Proceedings of MICCAI Workshop "3D Cardiovascular Imaging: a MICCAI segmentation Challenge".

Flotats, A., Knuuti, J., Gutberlet, M., Marcassa, C., Bengel, F., Kaufmann, P., Rees, M., Hesse, B., 2011. Hybrid cardiac imaging: SPECT/CT and PET/CT. A joint position statement by the European Association of Nuclear Medicine (EANM), the European Society of Cardiac Radiology (ESCR) and the European Council of Nuclear Cardiology (ECNC). European Journal of Nuclear Medicine and Molecular Imaging 38 (1), 201–212.

Folks, R. D., 2002. Interpretation and reporting of myocardial perfusion SPECT: a summary for technologists. Journal of Nuclear Medicine Technology 30 (4), 153–163.

Frangi, A., Niessen, W., Vincken, K., Viergever, M., 1998. Multiscale vessel enhancement filtering. In: Proc. of the 1st international conference on Medical Image Computing and Computer-Assisted Intervention (MICCAI). Vol. 1496. pp. 130–137.

Frangi, A. F., Niessen, W. J., Viergever, M. A., 2001. Three-dimensional modeling for functional analysis of cardiac images: a review. IEEE Transactions on Medical Imaging 20, 2–5.

Funka-Lea, G., Boykov, Y., Florin, C., Jolly, M. P., Moreau-Gobard, R., Ramaraj, R., Rinck, D., 2006. Automatic heart isolation for CT coronary visualization using graph-cuts. In: Proc. of the 3rd IEEE International Symposium on Biomedical Imaging : Nano to Macro (ISBI). pp. 614–617.

Gaemperli, O., Husmann, L., Schepis, T., Koepfli, P., Valenta, I., Jenni, W., Alkadhi, H., Lüscher, T., Kaufmann, P., 2009. Coronary CT angiography and myocardial perfusion imaging to detect flow-limiting stenoses: a potential gatekeeper for coronary revascularization? European Heart Journal 30, 2921–2929.

Gaemperli, O., Kaufmann, P., 2008. Hybrid cardiac imaging: more than the sum of its parts? Journal of Nuclear Cardiology 15 (1), 123–126.

Gaemperli, O., Saraste, A., Knuuti, J., 2012. Cardiac hybrid imaging. European Heart Journal of Cardiovascular Imaging 13 (1), 51–60.

Gaemperli, O., Schepis, T., Kalff, V., Namdar, M., Valenta, I., Stefani, L., Desbiolles, L., Leschka, S., Husmann, L., Alkadhi, H., Kaufmann, P., 2007a. Validation of a new cardiac image fusion software for three-dimensional integration of myocardial perfusion SPECT and stand-alone 64-slice CT angiography. European Journal of Nuclear Medicine and Molecular Imaging 34, 1097–1106.

Gaemperli, O., Schepis, T., Valenta, I., Husmann, L., Scheffel, H., Duerst, V., Eberli, F., Luscher, T., Alkadhi, H., Kaufmann, P., 2007b. Cardiac image fusion from stand-alone SPECT and CT: clinical experience. Journal of Nuclear Medicine 48 (5), 696–703.

Goldenberg, R., Eilot, D., Begelman, G., Walach, E., Ben-Ishai, E., Peled, N., 2012. Computer-aided simple triage (CAST) for coronary CT angiography (CCTA). International Journal of Computed Assisted Radiology and Surgery 7 (6), 819–827.

Goldenberg, R., Peled, N., 2011. Computer-aided simple triage. International Journal of Computer Assisted Radiology and Surgery 6 (5), 705–711.

Gülsün, M. A., Tek, H., 2008. Robust vessel tree modeling. In: Proc. of the 11th international conference on Medical Image Computing and Computer-Assisted Intervention (MICCAI'08). MICCAI '08. Springer-Verlag, Berlin, Heidelberg, pp. 602–611.

Gupta, V., Hendriks, E., Milles, J., van der Geest, R., Jerosch-Herold, M., Reiber, J., Lelieveldt, B., 2010. Fully automatic registration and segmentation of first-pass myocardial perfusion MR image sequences. Academic Radiology 17 (11), 1375–85.

Haase, J., Escaned, J., Montauban van Swijndregt, E., Ozaki, Y., Gronenschild, E., Slager, C., P.W., S., 1993. Experimental validation of geometric and densitometric coronary measurements on the new generation cardiovascular angiography analysis system (caasii). Catheterization and Cardiovascular Diagnosis 30, 104–114.

Halpern, E., Halpern, D., 2011. Diagnosis of coronary stenosis with CT angiography comparison of automated computer diagnosis with expert readings. Academic Radiology 18 (3), 324–333.

Hameeteman, K., Zuluaga, M. A., Freiman, M., Joskowicz, L., Cuisenaire, O., Flórez Valencia, L., Gülsün, M. A., Krissian, K., Mille, J., Wong, W. C. K., Orkisz, M., Tek, H., Hernández Hoyos, M., Benmansour, F., Chung, A. C. S., Rozie, S., van Gils, M., van den Borne, L., Sosna, J., Berman, P., Cohen, N., Douek, P. C., Sánchez, I., Aissat, M., Schaap, M., Metz, C. T., Krestin, G. P., van der Lugt, A., Niessen, W. J., van Walsum, T., Aug 2011. Evaluation framework for carotid bifurcation lumen segmentation and stenosis grading. Medical Image Analysis 15 (4), 477–488.

Hill, D., Batchelor, P. G., Holden, M., Hawkes, D. J., 2001. Medical image registration. Physics in Medicine and Biology 46 (3), R1–R45.

Isğum, I., Staring, M., Rutten, A., Prokop, M., Viergever, M., van Ginneken, B., 2009. Multi-atlas-based segmentation with local decision fusion. application to cardiac and aortic segmentation in CT scans. IEEE Transactions on Medical Imaging 28 (7), 1000–1010.

Kaufmann, P. A., 2009. Cardiac hybrid imaging: state-of-the-art. Annals of Nuclear Medicine 23, 325–331.

Kelm, B. M., Mittal, S., Zheng, Y., Tsymbal, A., Bernhardt, D., Vega-Higuera, F., Zhou, S. K., Meer, P., Comaniciu, D., 2011. Detection, grading and classification of coronary stenoses in computed tomography angiography. In: Proc. of the 14th international conference on Medical Image Computing and Computer-Assisted Intervention (MICCAI'11). Vol. 14. pp. 25–32.

Khan, M. F., Wesarg, S., Gurung, J., Dogan, S., Maataoui, A., Brehmer, B., Herzog, C., Ackermann, H., Assmus, B., Vogl, T. J., Aug 2006. Facilitating coronary artery evaluation in MDCT using a 3D automatic vessel segmentation tool. European Radiology 16 (8), 1789–1795.

Kirişli, H., Gupta, V., Kirschbaum, S., Neefjes, L., van Geuns, R., Mollet, N., Lelieveldt, B., Reiber, J., van Walsum, T., Niessen, W., 2011. A patient-specific visualization tool for comprehensive analysis of coronary CTA and perfusion MRI data. In: Proc. of SPIE Medical Imaging.

Kirişli, H., Gupta, V., Kirschbaum, S., Rossi, A., Metz, C., Schaap, M., van Geuns, R., Mollet, N., Lelieveldt, B., Reiber, J., van Walsum, T., Niessen, W., 2012. Comprehensive visualization of multimodal cardiac imaging data for assessment of coronary artery disease: first clinical results of the SMARTVis tool. International Journal of Computer Assisted Radiology and Surgery 7 (4), 557–571.

Kirişli, H., Schaap, M., Klein, S., Neefjes, L., Weustink, A., van Walsum, T., Niessen, W., 2010a. Fully automatic cardiac segmentation from 3D CTA data: a multiatlas based approach. In: Proc. of SPIE Medical Imaging. Vol. 7623. pp. 762305–9.

Kirişli, H., Schaap, M., Klein, S., Papadopoulou, S., Bonardi, M., Chen, C., Weustink, A., Mollet, N., Vonken, E. P. A., van der Geest, R., van Walsum, T., Niessen, W., 2010b. Evaluation of a multi-atlas based method for segmentation of cardiac CTA data: a large-scale, multi-center and multi-vendor study. Medical Physics 37 (12), 6279–6292.

Kirschbaum, S., Springeling, T., Rossi, A., Duckers, E., Gutiérrez-Chico, J., Regar, E., de Feyter, P., van Geuns, R., 2011. Comparison of adenosine magnetic resonance perfusion imaging with invasive coronary flow reserve and fractional flow reserve in patients with suspected coronary artery disease. International Journal of Cardiology 147, 184–186.

Kirschbaum, S., van Geuns, R., 2009. Cardiac magnetic resonance imaging to detect and evaluate ischemic heart disease. Hellenic Journal of Cardiology 50, 119–126.

Klein, S., Pluim, J. P. W., Staring, M., Viergever, M. A., 2009. Adaptive stochastic gradient descent optimisation for image registration. International Journal of Computer Vision 81, 227–239.

Klein, S., Staring, M., Murphy, K., Viergever, M. A., Pluim, J. P. W., 2010. elastix: a toolbox for intensity-based medical image registration. IEEE Transactions on Medical Imaging 29 (1), 196–205, software available from http://elastix.isi.uu.nl/.

Klein, S., Staring, M., Pluim, J. P. W., December 2007. Evaluation of optimization methods for nonrigid medical image registration using mutual information and b-splines. IEEE Transactions on Medical Imaging 16 (12), 2879–2890.

Klein, S., van der Heide, U., Lips, I., van Vulpen, M., Staring, M., Pluim, J. P. W., April 2008. Automatic segmentation of the prostate in 3D MR images by atlas matching using localized mutual information. Medical Physics 35 (4), 1407–1417.

Koo, B.-K., Erglis, A., Doh, J.-H., Daniels, D. V., Jegere, S., Kim, H.-S., Dunning, A., DeFrance, T., Lansky, A., Leipsic, J., Min, J. K., Nov 2011. Diagnosis of ischemia-causing coronary stenoses by noninvasive fractional flow reserve computed from coronary computed tomographic angiograms. results from the prospective multicenter DISCOVER-FLOW (diagnosis of ischemia-causing stenoses obtained via noninvasive fractional flow reserve) study. Journal of the American College of Cardiology 58 (19), 1989–1997.

Kühnel, C., Hennemuth, A., Oeltze, S., Boskamp, T., Peitgen, H., 2008a. Enhanced cardio vascular image analysis by combined representation of results from dynamic MRI and anatomic CTA. In: Proc. of SPIE Medical Imaging. Vol. 6918.

Kühnel, C., Hennemuth, A., Peitgen, H., Mahnken, A., 2008b. New analysis tools for the comprehensive assessment of the coronary arteries and myocardial viability in CT data sets. In: Proc. of Computers in Cardiology. Vol. 35. pp. 733–736.

Kybic, J., Unser, M., November 2003. Fast parametric elastic image registration. IEEE Transactions on Image Processing 12 (11), 1427–1442.

Lesage, D., Angelini, E. D., Bloch, I., Funka-Lea, G., Dec 2009. A review of 3D vessel lumen segmentation techniques: models, features and extraction schemes. Medical Image Analysis 13 (6), 819–845.

Lester, H., Arridge, S., 1999. A survey of hierarchical non-linear medical image registration. Pattern Recognition 32 (1), 129–149.

Levine, G. N., Bates, E. R., Blankenship, J. C., Bailey, S. R., Bittl, J. A., Cercek, B., et al., 2011. 2011 ACCF/AHA/SCAI Guideline for Percutaneous Coronary Intervention:Executive Summary: A Report of the American College of Cardiology Foundation/American Heart Association Task Force on Practice Guidelines and the Society for Cardiovascular Angiography and Interventions. Journal of the American College of Cardiology 58, 2550–2583.

Lor, K., Chen, C., 2012. Probabilistic model based evaluation of coronary artery stenosis on CTA. In: Proceedings of MICCAI Workshop "3D Cardiovascular Imaging: a MICCAI segmentation Challenge".

Lorenz, C., von Berg, J., 2006. A comprehensive shape model of the heart. Medical Image Analysis 10, 657–670.

Maintz, J., Viergever, M., 1998. A survey of medical image registration. Medical Image Analysis 2 (1), 1–36.

Meijboom, W.B. and Meijs, M.F L., Schuijf, J. D., Cramer, M. J., Mollet, N. R., van Mieghem, C. A. G., Nieman, K., van Werkhoven, J. M., Pundziute, G., Weustink, A. C., de Vos, A. M., Pugliese, F., Rensing, B., Jukema, J. W., Bax, J. J., Prokop, M., Doevendans, P. A., Hunink, M. G. M., Krestin, G. P., de Feyter, P. J., Dec 2008. Diagnostic accuracy of 64-slice computed tomography coronary angiography: a prospective, multicenter, multivendor study. Journal of the American College of Cardiology 52 (25), 2135–2144.

Melki, I., Talbot, H., Cousty, J., Pruvot, C., Knoplioch, J., Launay, L., Najman, L., 2012. Automatic coronary arteries stenoses detection in 3D CTA. In: Proceedings of MICCAI Workshop "3D Cardiovascular Imaging: a MICCAI segmentation Challenge".

Metz, C., Schaap, M., Weustink, A., Mollet, N., van Walsum, T., Niessen, W., 2009. Coronary centerline extraction from CT coronary angiography images using a minimum cost path approach. Medical Physics 36 (12), 5568–5579.

Milles, J., der Geest, R., Jerosch-Herold, M., Reiber, J., Lelieveldt, B., 2008. Fully automated motion correction in first-pass myocardial perfusion MR image sequences. IEEE Transactions on Medical Imaging 27 (11), 1611–1621.

Mittal, S., Zheng, Y., Georgescu, B., Vega-Higuera, F., Zhou, S., Meer, P., Comaniciu, D., 2010. Fast automatic detection of calcified coronary lesions in 3D cardiac CT images. In: Proc. of MICCAI workshop on Machine Learning in Medical Imaging (MLMI). Vol. 6357. pp. 1–9.

Mohr, B., Masood, S., Plakas, C., 2012. Accurate stenosis detection and quantification in coronary CTA. In: Proceedings of MICCAI Workshop "3D Cardiovascular Imaging: a MICCAI segmentation Challenge".

Nakaura, T., Utsunomiya, D., Shiraishi, S., Tomiguchi, S., Honda, T., Ogawa, H., Awai, K., Yamashita, Y., 2005. Three-dimensional cardiac image fusion using new CT angiography and SPECT methods. American Journal of Roentgenology 185, 1554–1557.

Nieman, K., Galema, T. W., Neefjes, L. A., Weustink, A. C., Musters, P., Moelker, A. D., Mollet, N. R., de Visser, R., Boersma, E., de Feijter, P. J., Dec 2009. Comparison of the value of coronary calcium detection to computed tomographic angiography and exercise testing in patients with chest pain. American Journal of Cardiology 104 (11), 1499–1504.

Niemeijer, M., Loog, M., Abràmoff, M. D., Viergever, M. A., Prokop, M., van Ginneken, B., 2011. On combining computer-aided detection systems. IEEE Transactions on Medical Imaging 30 (2), 215–223.

Öksüz, d., Ünay, D., Kadipaşaoğlu, K., 2012. A hybrid method for coronary artery stenosis detection and quantification. In: Proceedings of MICCAI Workshop "3D Cardiovascular Imaging: a MICCAI segmentation Challenge".

Penney, G. P., Weese, J., Little, J. A. e. a., 1998. A comparison of similarity measures for use in 2D/3D medical image registration. IEEE Transactions on Medical Imaging 17 (4), 586–595.

Pereztol-Valdés, O., Candell-Riera, J., Santana-Boado, C., Angel, J., Aguadé-Bruix, S., Castell-Conesa, J., Garcia, E., Soler-Soler, J., 2005. Correspondence between left ventricular 17 myocardial segments and coronary arteries. European Heart Journal 26 (24), 637–2643.

Peters, J., Ecabert, O., Meyer, C., Kneser, R., Weese, J., 2010. Optimizing boundary detection via simulated search with applications to multi-modal heart segmentation. Medical Image Analysis 14, 70–84.

Pluim, J. P. W., Maintz, J. B. A., Viergever, M. A., 2003. Mutual-information-based registration of medical images: A survey. IEEE Transactions on Medical Imaging 22 (8), 986–1004.

Pryor, D. B., Shaw, L., McCants, C. B., Lee, K. L., Mark, D. B., Harrell, F. E., Muhlbaier, L. H., Califf, R. M., 1993. Value of the history and physical in identifying patients at increased risk for coronary artery disease. Annals of Internal Medicine 118 (2), 81–90.

Pugliese, F., Hunink, M., Gruszczynska, K., Alberghina, F., Malagó, R., van Pelt, N., Mollet, N., Cademartiri, F., Weustink, A., Meijboom, W., et al., 2009. Learning curve for coronary CT angiography: what constitutes sufficient training? Radiology 251 (2), 359–368.

Raff, G. L., Abidov, A., Achenbach, S., Berman, D. S., Boxt, L. M., Budoff, M. J., Cheng, V., DeFrance, T., Hellinger, J. C., Karlsberg, R. P., 2009. SCCT guidelines for the interpretation and reporting of coronary computed tomographic angiography. Journal of Cardiovascular Computed Tomography 3 (2), 122–136.

Reiber, J. H., Serruys, P. W., Kooijman, C. J., Wijns, W., Slager, C. J., Gerbrands, J. J., Schuurbiers, J. C., den Boer, A., Hugenholtz, P. G., Feb 1985. Assessment of short-, medium-, and long-term variations in arterial dimensions from computer-assisted quantitation of coronary cineangiograms. Circulation 71 (2), 280–288.

Roger, V., Go, A., Lloyd-Jones, D., Benjamin, E., Berry, J., Borden, W., et al., 2012. Heart disease and stroke statistics 2012 update: a report from the American Heart Association. Circulation 125 (1), 2–220.

Rohlfing, T., Brandt, R., Menzel, R., Maurer, CR., J., 2004. Evaluation of atlas selection strategies for atlas-based image segmentation with application to confocal microscopy images of bee brains. NeuroImage 21, 1428–1442.

Sabuncu, M. R., Yeo, B. T. T., Van Leemput, K., Fischl, B., Golland, P., 2010. A generative model for image segmentation based on label fusion. IEEE Transactions on Medical Imaging 29, 1714–1729.

Santana, C., Garcia, E., Faber, T., Sirineni, G., Esteves, F., Sanyal et al., R., 2009. Diagnostic performance of fusion of myocardial perfusion and computed tomography coronary angiography. J Nuclear Cardiol 16, 201–211.

Sato, A., Nozato, T., Hikita, H., Miyazaki, S., Takahashi, Y., Kuwahara, T., Takahashi, A., Hiroe, M., Aonuma, K., 2010. Incremental value of combining 64-slice computed tomography angiography with stress nuclear myocardial perfusion imaging to improve noninvasive detection of coronary artery disease. Journal of Nuclear Cardiology 17 (1), 19–26.

Saur, S. C., Alkadhi, H., Desbiolles, L., Székely, G., Cattin, P. C., 2008. Automatic detection of calcified coronary plaques in computed tomography data sets. In: Proc. of the 11th international conference on Medical Image Computing and Computer-Assisted Intervention (MICCAI'08). Vol. 11. pp. 170–177.

Schaap, M., Metz, C. T., van Walsum, T., van der Giessen, A. G., Weustink, A. C., Mollet, N. R., Bauer, C., Bogunović, H., Castro, C., Deng, X., Dikici, E., O'Donnell, T., Frenay, M., Friman, O., Hernández Hoyos, M., Kitslaar, P. H., Krissian, K., Kühnel, C., Luengo-Oroz, M. A., Orkisz, M., Smedby, Ö., Styner, M., Szymczak, A., Tek, H., Wang, C., Warfield, S. K., Zambal, S., Zhang, Y., Krestin, G. P., Niessen, W. J., Oct 2009a. Standardized evaluation methodology and reference database for evaluating coronary artery centerline extraction algorithms. Medical Image Analysis 13 (5), 701–714.

Schaap, M., Neefjes, L., Metz, C., van der Giessen, A., Weustink, A., Mollet, N., Wentzel, J., van Walsum, T., Niessen, W., July 2009b. Coronary lumen segmentation using graph cuts and robust kernel regression. In: Jerry L. Prince, Dzung L. Pham, K. J. M. (Ed.), Proc. of Information Processing in Medical Imaging (IPMI). pp. 528–539.

Schaap, M., van Walsum, T., Neefjes, L., Metz, C., Capuano, E., de Bruijne, M., Niessen, W., 2011. Robust shape regression for supervised vessel segmentation and its application to coronary segmentation in CTA. IEEE Transactions on Medical Imaging 30 (11), 1974–986.

Schlosser, T., Mohrs, O., Magedanz, A., Nowak, B., Voigtländer, T., Barkhausen, J., Schmermund, A., April 2007. Noninvasive coronary angiography using 64-detector-row computed tomography in patients with a low to moderate pretest probability of significant coronary artery disease. Acta Radiologica 48 (3), 300–307.

Scholte, A., Roos, C., van Werkhoven, J., 2010. Function and anatomy: SPECT-MPI and MSCT coronary angiography. EuroIntervention 6 (G), 94–100.

Sdika, M., 2010. Combining atlas based segmentation and intensity classification with nearest neighbor transform and accuracy weighted vote. Medical Image Analysis 14, 219–226.

Shahzad, R., van Walsum, T., Kirişli, H., Tang, H., Metz, C., Schaap, M., van Vliet, L., Niessen, W., 2012a. Automatic detection, quantification and lumen segmentation of the coronary arteries using two-point centerline extraction scheme. In: Proceedings of MICCAI Workshop "3D Cardiovascular Imaging: a MICCAI segmentation Challenge".

Shahzad, R., van Walsum, T., Schaap, M., Rossi, A., Klein, S., Weustink, A., de Feyter, P., van Vliet, L. J., Niessen, W., 2012b. Vessel specific coronary artery calcium scoring: an automatic system. Academic Radiology, in press.

Slomka, P., Cheng, V., Dey, D., Woo, J., Ramesh, A., van Kriekinge, S., Suzuki, Y., Elad, Y., Karlsberg, R., Berman, D., Germano, G., 2009. Quantitative analysis of myocardial perfusion SPECT anatomically guided by coregistered 64-slice coronary CT angiography. Journal of Nuclear Medicine 50 (10), 1621–1630.

Studholme, C., Hill, D. L. G., Hawkes, D. J., 1996. Automated 3D registration of MR and CT images of the head. Medical Image Analysis 1 (2), 163–175.

Tang, H., van Walsum, T., van Onkelen, R., Hameeteman, R., Klein, S., Schaap, M., Tori, F. L., van den Bouwhuijsen, Q. J. A., Witteman, J., van der Lugt, A., van Vliet, L., Niessen, W. J., 2012. Semi-automatic carotid lumen segmentation for quantification of lumen geometry in multispectral MRI. Medical Image Analysis 16 (6), 1202–1215.

Termeer, M., Bescós, J., Breeuwer, M., Vilanova, A., Gerritsen, F., Gröller, M., 2007. CoViCAD: Comprehensive Visualization of Coronary Artery Disease. IEEE Transactions on Visualization and Computer Graphics 13 (6), 1632–1641.

Termeer, M., Bescós, J., Breeuwer, M., Vilanova, A., Gerritsen, F., Gröller, M., Nagel, E., October 2008. Visualization of myocardial perfusion derived from coronary anatomy. IEEE Transactions on Visualization and Computer Graphics 14 (6), 1595–1602.

Teßmann, M., Vega-Higuera, F., Fritz, D., Scheuering, M., Greiner, G., 2009. Multi-scale feature extraction for learning-based classification of coronary artery stenosis. In: Proc. of SPIE Medical Imaging.

Thévenaz, P. an Bierlaire, M., Unser, M., 2008. Halton sampling for image registration based on mutual information. Sampling Theory Signal Image Processing 7 (2), 1410–171.

Thévenaz, P., Ruttimann, U. E., Unser, M., 1998. A pyramid approach to subpixel registration based on intensity. IEEE Transactions on Image Processing 7 (1), 27–41.

Thévenaz, P., Unser, M., December 2000. Optimization of mutual information for multiresolution image registration. IEEE Transactions on Medical Imaging 9 (12), 2083–2099.

Turk, G., O'Brien, J., 1999. Shape transformation using variational implicit functions. In: Proc. of the 26th annual conference on Computer Graphics and Interactive Technique. pp. 335 –342.

Türkvatan, A., Biyikoğlu, S., Büyükbayraktar, F., Olçer, T., Cumhur, T., Duru, E., May 2008. Clinical value of 16-slice multidetector computed tomography in symptomatic patients with suspected coronary artery disease. Acta Radiologica 49 (4), 400–408.

van Rikxoort, E., Isgum, I., Arzhaeva, Y., Staring, M., Klein, S., Viergever, M. A., Pluim, J. P. W., van Ginneken, B., 2010. Adaptive local multi-atlas segmentation: application to the heart and the caudate nucleus. Medical Image Analysis 14 (1), 39–49.

van Walsum, T., Schaap, M., Metz, C., van der Giessen, A., Niessen, W., 2008. Averaging centerlines: mean shift on paths. In: Proc. of the 11th international conference on Medical Image Computing and Computer-Assisted Intervention (MICCAI'08). Vol. 11. Springer, pp. 900–907.

van Werkhoven, J., Schuijf, J., Gaemperli, O., Jukema, J., Boersma, E., Wijns, W., Stolzmann, P., Alkadhi, H., Valenta, I., Stokkel, M., Kroft, L., de Roos, A., Pundziute, G., Scholte, A., van der Wall, E., Kaufmann, P., Bax, J., 2009. Computed tomography and gated single-photon emission computed tomography in patients with suspected coronary artery disease. Journal of American College of Cardiology 53, 623–632.

Wang, C., Moreno, R., Smedby, Ö., 2012. Vessel segmentation using implicit model-guided level sets. In: Proceedings of MICCAI Workshop "3D Cardiovascular Imaging: a MICCAI segmentation Challenge".

Wesarg, S., Khan, M. F., Firle, E. A., Sep 2006. Localizing calcifications in cardiac CT data sets using a new vessel segmentation approach. Journal of Digital Imaging 19 (3), 249–257.

Weustink, A., de Feyter, P., 2011. The role of multi-slice computed tomography in stable angina management - a current perspective. Netherlands Heart Journal 19, 336–343.

Wolz, R., Aljabar, P., Hajnal, J., Hammers, A., Rueckert, D., the Alzheimer's Disease Neuroimaging Initiative, 2010. LEAP: Learning embeddings for atlas propagation. NeuroImage 49 (2), 1316–1325.

Xu, Y., Liang, G., Hu, G., Yang, Y., Geng, J., Saha, P. K., Jan 2012. Quantification of coronary arterial stenoses in CTA using fuzzy distance transform. Computerized Medical Imaging and Graphics 36 (1), 11–24.

Yang, G., Broersen, A., Petr, R., Kitslaar, P., de Graaf, M., Bax, J. J., Reiber, J. H. C., Dijkstra, J., 2011. Automatic coronary artery tree labeling in coronary computed tomographic angiography datasets. Computing in Cardiology 38, 109–112.

Yang, G., Kitslaar, P., Frenay, M., Broersen, A., Boogers, M. J., Bax, J. J., Reiber, J. H. C., Dijkstra, J., Apr 2012. Automatic centerline extraction of coronary arteries in coronary computed tomographic angiography. International Journal of Cardiovascular Imaging 28 (4), 921–933.

Yin, R. K., 2009. Case Study Research: Design and Methods, 4th Edition. SAGE Publications.

Zambal, S., Hladuvka, J., Kanitsar, A., Bühler, K., 2008. Shape and appearance models for automatic coronary artery tracking. In: Proceedings of MICCAI Workshop 3D Segmentation in the Clinic: A Grand Challenge II.

Zheng, Y., Barbu, A., Georgescu, B., Scheuering, M., Comaniciu, D., 2008. Four-chamber heart modeling and automatic segmentation for 3D cardiac CT volumes using marginal space learning and steerable features. IEEE Transactions on Medical Imaging 27, 1668–1681.

Zhou, C., Chan, H.-P., Chughtai, A., Patel, S., Hadjiiski, L. M., Sahiner, B., Wei, J., Kazerooni, E. A., 2010. Automated segmentation and tracking of coronary arteries in cardiac CT scans: comparison of performance with a clinically used commercial software. In: Proc. of SPIE Medical Imaging. Vol. 7624.

Zuluaga, M. A., Magnin, I. E., Hernández Hoyos, M., Delgado Leyton, E. J. F., Lozano, F., Orkisz, M., Mar 2011. Automatic detection of abnormal vascular cross-sections based on density level detection and support vector machines. International Journal of Computed Assisted Radiology and Surgery 6 (2), 163–174.

Samenvatting

Het hart- en vaatstelsel

Het hart pompt bloed door het lichaam. Het bestaat uit twee boezems en twee kamers, en vier hartkleppen. De hartweefsel bestaat uit drie lagen. De binnenste laag heet het endocardium, deze staat in contact met het bloed. De buitenste laag, de laag om het hart, heet het epicardium. Tussen deze twee lagen bevindt zich het myocardium: de hartspier die zorgt voor het samentrekken van het hart. Figuur 1.1 laat de anatomie van het hart zien.

De hartcyclus bestaat uit twee fasen: systole en diastole. Tijdens systole wordt het bloed uit de hartkamers naar het lichaam gepompt, en tijdens diastole worden de hartkamers weer gevuld met bloed. Dat laatste gebeurt weer in twee stappen: eerst een passieve vulling, waarbij de kleppen naar de kamers opengaan, en dan een actieve, waarbij de boezems samentrekken, en bloed de kamers in pompen.

De slagaders die de hartspier van zuurstofrijk bloed voorzien heten de kransslagaders. De kransslagaders zijn aftakkingen van de aorta, de meeste mensen hebben er twee: de rechter en de linker kransslagader. De linker kransslagader bestaat uit een gemeenschappelijk deel (linker hoofdstam), die vervolgens splitst in twee takken. Figuur 1.2 laat een overzicht zien van de kransslagaders. Het volledige stelsel van kransslagaders wordt gewoonlijk in 17 segmenten onderverdeeld, zoals afgebeeld in Figuur 1.4.

Ziekten van het hart

Hart falen doet zich voor als het hart niet in staat is voldoende bloed door het lichaam te pompen. Ter compensatie kan de frequentie van de hartslag verhoogd worden, of kunnen de hartkamers groter worden, om zo voldoende bloed te kunnen pompen. Op de lange duur kunnen zulke compensaties schadelijk zijn voor de gezondheid, en bijv. leiden tot een te hoge frequentie van de normale hartslag of een te groot hart.

De hoeveelheid bloed die naar de hartspier stroomt, wordt minder als een kransslagader vernauwd of compleet afgesloten wordt de de vorming van plak. De hoeveelheid zuurstof en voeding voor het deel van de hartspier dat gevoed wordt door deze kransslagader wordt dan ook minder. Dit gebrek aan zuurstof en voeding heet ischemie, en de vernauwing heet een stenose. De gevolgen van verminderde toevoer van zuurstof en voeding aan de hartspier kunnen een tijdelijk effect hebben. Als deze vermindering echter lang duurt, kunnen delen van de hartspier onherstelbaar beschadigd raken; dit is een hartaanval. Om dit te voorkomen is het van groot belang vernauwingen in kransslagaders vroegtijdig op te kunnen sporen.

Diagnose van kransslagaderziekte: beeldvormende technieken

Allerlei beeldvormende technieken kunnen gebruikt worden voor de diagnose van kransslagaderziekte. De keuze voor welke, en hoeveel, technieken hangt af van de voorgeschiedenis van de patient en de huidige symptomen.

Conventionele kransslagader angiografie is een procedure om de kransslagaders af te beelden, en is momenteel de gouden standaard beeldvormende techniek voor de diagnose van zieke kransslagaders. Hierbij wordt een contrast middel in de kransslagaders

ingebracht, waarna met behulp van Röntgen stralen de met contrast gevulde slagaders, en mogelijke vernauwingen, worden afgebeeld. Figuur 1.5 laat twee voorbeelden van kransslagader angiogrammen zien. Daarnaast kan een draad met een zeer kleine drukmeter aan de tip in de kransslagader worden ingebracht. Hiermee kan bepaald worden of een vernauwing in het bloedvat daadwerkelijk beperkend is voor de bloeddoorstroming.

Computer tomografie angiografie (CTA) is een andere beeldvormende techniek die gebruikt kan worden om te bepalen of de vorming van plak tot vernauwingen van kransslagaders heeft geleid. Bij een CTA onderzoek wordt ook gebruik gemaakt van Röntgenstralen. De verzwakking van deze straling vanuit verschillende oriëntaties rond het lichaam wordt gemeten, en daarna worden computer technieken gebruikt om hieruit een driedimensionale afbeelding van het hart en de kransslagaders te berekenen. Figuur 1.6 laat een CT scanner zien, en ook verschillende manieren om een CTA plaatje te presenteren. Magnetische resonantie (MR) kan gebruikt worden om de bloeddoorstroming van de hartspier af te beelden. Afwijkingen in de hartspier die het gevolg kunnen zijn van kransslagaderziekte, zoals te weinig bloeddoorstroming, of littekenweefsel na een hartaanval, kunnen hiermee in beeld gebracht worden. Bij MR wordt gebruikt gemaakt van een sterk magnetisch veld, radiogolven en computer technieken om een afbeelding te maken. Een voorbeeld MR scanner, een spoel om het hart af te kunnen beelden, en een aantal plaatjes van het hart uit een serie MR afbeeldingen, is te zien in Figuur 1.7.

Nucleaire geneeskunde omvat de beeldvorming die gebruikt maakt van radioactieve materialen. Single-photon emissie computer tomografie (SPECT) kan gebruikt worden voor de diagnose van de aanwezigheid en de ernst van kransslagaderziekte. Het radioactieve materiaal dat ingebracht wordt, hoopt zich op in de hartspier en zendt gammastralen uit. Na detectievan deze stralen worden computer technieken gebruikt om een driedimensionaal beeld van de activiteit van de hartspier te vormen. Figuur 1.8 laat een SPECT/CT scanner zien, en voorbeeld SPECT plaatjes.

Als zowel CTA als SPECT voor de diagnose van kransslagaderziekte gebruikt worden, moet de expert de beelden met anatomische informatie (CTA) en functionele informatie (SPECT) mentaal combineren om een uiteindelijke diagnose te stellen. Elk stukje hartspier waarvan het SPECT een verminderde activiteit laat zien, moet gerelateerd worden aan een vernauwing in een kransslagader. Op deze manier wordt duidelijk welke vernauwingen problemen aan de hartspier veroorzaken. Het gecombineerd gebruik van zowel CTA en SPECT is dus alleen van toegevoegde waarde als het verband tussen vernauwingen in de kransslagader en verminderde activiteit in een deel van de hartspier duidelijk gelegd kan woren. De mogelijkheden die deze gecombineerde aanpak biedt voor de diagnose is de belangrijkste reden om beide afbeeldingsvormen te gebruiken voor de diagnose en de behandeling van kransslagaderziekte.

Dit proefschrift

Het „Hart in drie dimensies" project was een samenwerking tussen vier onderzoeksgroepen op het gebied van de biomedische beeldverwerking aan drie universiteiten (Biomedical Imaging Group Rotterdam, Erasmus MC, Rotterdam; Division of Image Processing, LUMC, Leiden; Quantitative Imaging Group, Imaging Science and Technology, Faculty of Applied Sciences, Delft University of Technology, Delft; Vision lab, Delft University of Technology, Delft), en een consortium van vier bedrijven (Medis Medical Imaging Systems BV, Leiden, the Netherlands; Cardialysis BV, Rotterdam, the Netherlands; BioClinica, Leiden, the Netherlands; Oldelft Ultrasound, Delft, the Netherlands), in Nederland. Drie promovendi waren bij het project betrokken: Hortense Kirişli, Vikas Gupta en Rahil Shahzad.

Het werk beschreven in dit proefschrift heeft als doel het ontwikkelen en evalueren van technieken voor het bepalen van kransslagaderziekte op basis van CTA beelden, en voor de gecombineerde afbeelding van kransslagaders (uit CTA) en activiteit van de hartspier (uit MRI of SPECT). Voor dit laatste is een patient-specifiek visualisatiesysteem ontwikkeld. De strategie bestaat uit drie stappen:

(i) Een automatische manier om de boezems en kamers van het hart automatisch te bepalen in CTA afbeeldingen.

(ii) Een half-automatische manier om vernauwingen van kransslagaders op te sporen in CTA afbeeldingen, en de mate van vernauwing te bepalen. Hiervoor is ook systeem voor een gestandaardiseerde manier voor de evaluatie van dit soort algoritmen ontwikkeld. Dit systeem is gebruikt om algoritmen van elf verschillende onderzoeksgroepen met elkaar (en met de gouden standaard) te vergelijken.

(iii) Een systeem voor gecombineerde en geïntegreerde afbeelding van kransslagaders uit CTA met de activiteit van de hartspier (uit MRI of SPECT): het SMARTVis systeem, waarmee het verband tussen vernauwingen in kransslagaders en verminderde activiteit van delen van de hartspier eenvoudig in beeld gebracht kan worden. Beide varianten van het systeem, één voor MRI afbeeldingen, en één voor SPECT afbeeldingen, zijn in het ziekenhuis getest en vergeleken met de standaard manier van afbeelden en beoordelen, waarbij de beeldinformatie niet geïntegreerd maar los naast elkaar wordt gepresenteerd.

Résumé
pour les non-initiés

Le système cardiovasculaire

Le *cœur* est un organe musculaire qui distribue le sang dans le corps humain. Il est constitué de deux *oreillettes*, deux *ventricules* et quatres *valves*. Les oreillettes reçoivent le sang de la circulation sanguine ; les ventricules l'éjectent. Le sang désoxygéné pénètre dans l'oreillette droite via la veine cave superieure, puis est pompé dans le ventricule droit via la valve triscupide, avant d'être éjecté au travers de la valve pulmonaire dans les poumons, via les artères pulmonaires. Le sang est alors oxygéné dans les poumons. Le sang oxygéné revient des poumons dans l'oreillette gauche via les veines pulmonaires, puis est pompé dans le ventricule gauche au travers de la valve mitrale, avant d'être éjecté au travers de la valve aortique, et distribué à l'ensemble du corps via le systeme vasculaire.

Le muscle cardiaque est constitué de 3 couches : l'*endocarde* (couche la plus interne), le *péricarde* (couche la plus externe), et le *myocarde*, tissu musculaire compris entre l'endocarde et le pericarde, responsable de la contraction du cœur. Une vue detaillée du cœur est présentée sur la **Figure 1.1**.

Le cycle cardiaque est divisé en deux phases : *systole* et *diastole*. Lors de la *systole*, le sang oxygéné est éjecté du ventricule gauche vers l'aorte via la valve aortique, et le sang désoxygéné est éjecté du ventricule droit vers l'artère pulmonaire via la valve pulmonaire. Les deux autres valves, mitrale et tricupide, sont alors fermées, afin d'éviter tout reflux sanguin dans les oreillettes. Lors de la diastole, les ventricules se remplissent de sang. Du sang oxygéné remplit le ventricule gauche et du sang désoxygéné remplit le droit. La diastole est divisée en deux phases : le remplissage *passif*, induit par l'ouverture des valves auriculo-ventriculaires, et le remplissage *actif*, resultant de la contraction des oreillettes. Les valves aortiques et pulmonaires sont alors fermées.

Les artères approvisionnant le myocarde en sang oxygéné sont appelées *artères coronaires*. Les *artères coronaires* naissent de l'aorte. **Figure 1.2** présente une vue d'ensemble de l'anatomie cardiovasculaire. L'artère coronaire droite (RCA) approvisionne le ventricule droit et la partie inferieure du ventricule gauche. L'artère coronaire gauche comporte une branche commune (LM), puis est divisée en deux branches (LAD, LCX). La branche LAD, et ses branches diagonales, approvissionnent la region antérieure du ventricule gauche ; la branche LCX, et ses branches marginales, approvisionnent la region latérale du ventricule gauche. En général, les artères coronaires peuvent être divisées en 17 segments, comme indiqué sur la **Figure 1.4**.

Les pathologies cardiaques

L'*insuffisance cardiaque* survient lorsque les capacités du cœur à pomper le sang et à le distribuer au reste du corps sont alterées. Cette pathologie peut être due à un dysfonctionnement systolique, c'est-à-dire à une reduction de la quantité de sang ejectée part les ventricules, ou à un disfonctionnement diastolique, c'est-à-dire à des difficultées de remplissage des ventricules. Pour compenser, le rythme cardiaque du patient peut augmenter, ou les ventricles peuvent s'hypertrophier ou se dilater, afin d'ameliorer le remplissage et/ou l'éjection. Dans le temps, de tels mécanismes compensatoires peuvent être nuisibles (tachycardie, dilatation des ventricules trop importante,...)

L'oxygène et les nutriments nécessaires au fonctionnement normal du cœur sont acheminés au myocarde par le sang, via les artères coronaires. Si une ou plusieurs artères coronaires se bouchent (partiellement ou complètement), la quantité de sang acheminée au myocarde est reduite, et, par conséquent, moins d'oxygène et de nutriments sont delivrés à certaines régions du cœur. Les cellules du myocarde irriguées par cette (ou ces) artère(s) ne sont alors plus oxygénées. Le déséquilibre entre les besoins du cœur en oxygène et l'apport issu de la circulation sanguine coronarienne est appelé *ischémie myocardique*, et le rétrécissement des artères coronaires est appelé *sténose* (**Figure 1.3**). Les dommages causés au myocarde par les sténoses coronariennes peuvent être reversibles ou irreversibles, suivant la durée du défaut d'oxygénation. Au-delà de 6h sans oxygénation, le myocarde devient nécrosé et nous parlons alors d'*infarctus du myocarde*. En langage courant, cette pathologie est appelée *crise cardiaque* ou simplement *infarctus*. Il est donc crutial de détecter le plus tôt possible les stenoses coronariennes, afin de les traiter et de prevenir l'infarctus du myocarde.

Imagerie médicale et diagnostic de la cardiopathie coronarienne

De nombreuses techniques d'imagerie médicale existent afin de diagnostiquer la cardiopathie coronarienne. Le choix concernant quel(s) examen(s) d'imagerie médicale, et combien d'entre eux, doivent être éffectués dépend des symptômes et de l'historique médical du patient.

La **coronarographie** est l'examen de référence en cas de suspicion de cardiopathie coronarienne. C'est un examen médical invasif, permettant de visualiser les artères coronaires, qui utilise la technique de radiographie aux rayons X et l'injection d'un produit de contraste iodé. Une petite incision est pratiquée dans la partie haute de la cuisse afin d' accéder à l'artère fémorale et de permettre l'introduction d'un cathéter dans l'aorte, permettant l'injection d'un produit de contraste dans les artères coronaires. **Figure 1.5.** présente un example d'image obtenu grâce à la coronarographie, appelé *angiogramme*. Etant donné plusieurs de ces angiogrammes, les 17 segments des artères coronaires (**Figure 1.4**) sont inspectés et classifiés comme étant normal ou présantant des sténoses (visuallement plus de 20% de rétrécissement de l'artère coronaire). Les sténoses de ces derniers segments sont alors quantifiés grâce à un logiciel informatique (Reiber et al., 1985). Si le rétrécissement est supérieur à 50%, la sténose coronaire est alors *significative*, et peut induire une ischémie myocardique et justifier un traitement. En complément, une sonde miniature peut être introduite dans l'artère coronaire présentant une sténose, afin de déterminer si le rétrecissement compromet la circulation sanguine dans l'artère. La pression est alors calculée avant et après la stenoses ; si la différence est supérieure a 20%, la sténose effectivement compromet le flux sanguin dans l'artère coronaire.

La **tomodensitométrie** (TDM), dite aussi scanographie, est une technique d'imagerie médicale non-invasive qui consiste à mesurer l'absorption des rayons X par les tissus puis, par traitement informatique, à numériser et enfin reconstruire des images 2D ou 3D des structures anatomiques. La **tomodensitométrie cardiaque** permet de determiner s'il y a formation de sténose(s) dans les artères coronaires. Durant cet examen, un agent de contraste iodé est injecté par voie intraveineuse au patient, afin de faire ressortir le contraste des vaisseaux sanguins sur les images ; les artères coronaires apparaissent

alors hyperdenses, c'est-à-dire plus blanches. Aussi, des bêta-bloquant peuvent être délivrés au patient, afin de reduire son rythme cardiaque et améliorer la qualité de l'image. **Figure 1.6.** présente un exemple de scanner (a), d'image 2D du coeur obtenue grâce à la tomodensitométrie (b), et d'images 2D transversales permettant d'inspecter les artères coronaires et de detecter/quantifier les sténoses (c,d).

L'**imagerie par résonance magnétique** (IRM) du cœur est une technique d'imagerie médicale non-invasive permettant de créer des images détaillées cœur. La création d'images nécessite un champ magnétique puissant (produit par un aimant supraconducteur), afin de générer une magnétisation des tissus par alignement des moments magnétiques de spin. A la différence des autres examens d'imagerie médicale, l'IRM n'utilise pas la technique de radiographie aux rayons X. Une antenne, placée autour de la cage thoracique du patient, produit des signaux détectés pas le scanner. Ces signaux sont alors transformés, grâce à des outils informatiques, en une serie d'images. Durant l'examen, une solution saline peut être administrée au patient par voie intraveineuse, afin de faire ressortir le contraste des cavites du cœur sur les images. L'IRM cardiaque est utilisée afin de déterminer les dommages causés au myocarde par la cardiopathie coronarienne. L'examen se divise en deux : une acquisition au repos, et une soumise au stress. La perfusion myocardique de stress est alors comparée à celle de repos. **Figure 1.7.** présente un exemple de scanner IRM (a), d'antenne thoracique (b), et de sequence de perfusion myocardique de stress obtenue par IRM (c).

La **tomoscintigraphie par émission monophotonique** (TEMP) est une technique d'imagerie médicale non-invasive basée sur la scintigraphie. L'examen nécessite l'injection préalable d'un produit radioactif émetteur de rayonnements gamma. L'image est alors realisée à l'aide d'un ensemble de gamma caméras qui tournent autour du patient. De même que l'examen IRM cardiaque, l'examen TEMP cardiaque est utilisé afin de déterminer les dommages causés au myocarde par la cardiopathie coronarienne, et se divise aussi en deux phases : une acquisition au repos, et une soumise au stress. **Figure 1.8.** présente un exemple de scanner TEMP (a), d'images TEMP (b), et d'images utilisées durant l'interpretation (c).

Afin de diagnostiquer la cardiopathie coronarienne non-invasivement, la tomodensitométrie, permettant de detecter les sténoses, ainsi que l'IRM ou la TEMP cardiaque, permettant de déterminer les dommages causés au myocarde, sont généralement employées. S'agissant de techniques d'imagerie médicale complémentaires, mais indépendantes, l'expert doit alors mentalement intègrer les informations anatomiques et fonctionnelles du cœur. Chaque région du myocarde présentant une déficience doit être correlée à une sténose, de manière à déterminer quelle(s) sténose(s) effectivement compromettent le flux sanguin, et doivent être traitées. Mais, corréler une sténose coronaire à une region du myocarde souffrant d'ischemie constitue un défi, car la position des artères coronaires est propre à chaque individu. Par conséquent, l'interprétation conjointe des données anatomiques et fonctionnelles via un modèle cardiaque spécifique à chaque individu pourrait améliorer le diagnostic des patients souffrant de cardiopathie coronarienne.

Cette thèse

Le project « Heart In 3D » a été mené grâce à la collaboration entre quatre centres de recherche en imagerie biomédicale, implantés dans trois universités néerlandaises (Biomedical Imaging Group Rotterdam, Erasmus MC, Rotterdam ; Division of Image Processing, LUMC, Leiden ; Quantitative Imaging Group, Imaging Science and Technology, Faculty of Applied Sciences, Delft University of Technology, Delft ; Vision lab, Delft University of Technology, Delft). Trois thésards ont travaillé sur ce project (Hortense A. Kirişli, Vikas Gupta et Rahil Shahzad).

Le but du project « Heart In 3D » était de développer des algorithmes mathématiques et des logiciels afin de connecter différents diagnostics cardiaques, c'est-à-dire les informations concernant les artères coronaires et le myocarde, obtenus via differentes techniques d'imagerie médicale. De nouveaux algorithms et outils de quantification devaient être developpés afin de supporter le diagnostic des maladies cardiovasculaires.

Le but du travail présenté dans cette thèse est de développer et d'évaluer de nouvelles techniques pour quantifier, sur image scanographique, les maladies cardiovasculaires, ainsi que d intègrer ces informations anatomiques avec celles fonctionnelles, extraites des images de perfusion myocardique grâce à l'imagerie IRM ou TEMP, afin de mieux diagnostiquer la cardiopathie coronarienne. Corréler une sténose coronaire avec une région du myocarde souffrant d'ischemie constitue un défi, car la position des artères coronaires est propre à chaque individu. Nous nous attacherons donc particulièrement à étudier l'impact de l'interprétation conjointe des données anatomiques et fonctionnelles sur le diagnostic de la cardiopathie coronarienne, en utilisant un modèle cardiaque spécifique à chaque patient.

Le travail présenté dans ce manuscrit de thèse se compose des points suivants :

(i) **Segmentation 3D des cavités cardiaques sur images tomodensitométriques** Dans le **Chapitre 2**, un algorithme entièrement automatisé de délinéation des cavités cardiaques est présenté et évalué quantitativement et qualitativement en utilisant, respectivement, 60 et 1420 images tomodensitométriques du cœur, acquises en utilisant des scanners de differentes marques (Siemens, Philips, Toshiba et GE) dans divers centres médicaux dans le monde.

(ii) **Détection et quantification des sténoses coronariennes sur images tomodensitométriques** Dans le **Chapitre 3**, un algorithme automatisé de détection et quantification des sténoses coronariennes sur images tomodensitométriques est présenté et évalué, par comparaison des perfomances de notre algorithme avec celles obtenues par annotation manuelle des sténoses sur images tomodensitométriques par un consensus de 3 experts, et celles obtenues par measures automatiques sur images coronarographiques. Dans le **Chapitre 4**, nous introduisons une plateforme standardisée afin d'évaluer de manière fiable et de comparer les performances des algorithmes dediés à la détection et quantification des sténoses coronariennes, ainsi qu'à la segmentation de la lumière des artères coronaires, sur images tomodensitométriques. Les algorithmes de 11 centres de recherche ont été quantitativement évalués et comparés.

(iii) **Intègration des informations anatomiques et fonctionnelles provenant de diverses techniques d'imagerie médicale** Dans le **Chapitre 5**, un logiciel dédié à l'analyze intègrée des données anatomiques et fonctinnelles du cœur est présenté. Le système, appelé SMARTVis, permet la mise en relation des sténoses coronaires et des zones myocardiques souffrant d'ischémie, via l'utilisation d'un modèle cardiaque spécifique à chaque patient intègrant les informations dérivées des images TDM et IRM. Les résultats d'une première evaluation clinique, durant laquelle deux experts ont analysé quatre cas de patients présentant des sténoses dans deux des principales artères coronaires, sont rapportés. Dans le **Chapitre 6**, le logiciel SMARTVis a été étendu afin d'être compatible avec les diagnostics dérivés des images TEMP. La valeur ajoutée de l'analyse integrée par rapport à l'analyse indépendante des informations anatomiques et fonctionnelles a été étudiée. Les resultats d'une seconde evaluation clinique, realisée par 4 experts provenant de 2 differents centres médicaux et impliquant 17 patients suspectés d'avoir une cardiopathie coronarienne, sont reportés. Ces études cliniques ont permis de conclure que l'analyse intègrée des données cardiaques anatomiques et fonctionnelles peut effectivement être utilisée afin de diagnostiquer la cardiopathie coronarienne, et qu'elle offre de nouvelles options pour la gestion des patients.

Publications

Journal Papers

- **H.A. Kirişli**, M. Schaap, S. Klein, S.L. Papadopoulou, M. Bonardi, C.H. Chen, A.C. Weustink, N.R.A. Mollet, E.P.A. Vonken, R.J. van der Geest, T. van Walsum and W.J. Niessen, Evaluation of a multi-atlas based method for segmentation of cardiac CTA data: a large-scale, multicenter and multi-vendor study, *Medical Physics*, 37(12):6279–6292, 2010.
- **H.A. Kirişli**, V. Gupta, S. Kirschbaum, A. Rossi, C.T. Metz, M. Schaap, R.J. van Geuns, N.R.A. Mollet, B.P.F. Lelieveldt, J.H.C. Reiber, T. van Walsum and W.J. Niessen, Comprehensive visualization of multimodal cardiac imaging data for assessment of coronary artery disease: first clinical results of the SMARTVis tool, *International Journal of Computer Assisted Radiology and Surgery*, 7(4):557–571, 2012.
- V. Gupta, **H.A. Kirişli**, E.A. Hendriks, R.J. van der Geest, W.J. Niessen, J.H.C. Reiber and B.P.F. Lelieveldt, Cardiac MR perfusion image processing techniques: A Survey, *Medical Image Analysis*, 16(4):767–785, 2012.
- C.T. Metz, N. Baka, **H.A. Kirişli**, M. Schaap, S. Klein, L. Neefjes, N.R.A. Mollet, B.P.F. Lelieveldt, M. de Bruijne, W.J. Niessen and T. van Walsum, Regression-based cardiac motion prediction from single-phase CTA, *IEEE Transactions on Medical Imaging*, 31(6):1311–1325, 2012.
- **H.A. Kirişli**, M. Schaap, C. Metz, A.S. Dharampal, W.B. Meijboom, S.L. Papadopoulou, A. Dedic, K. Nieman, M.A. de Graaf, M.F.L. Meijs, M.J. Cramer, A. Broersen, S. Cetin, A. Eslami, L. Flórez-Valencia, K.L. Lor, B. Matuszewski, I. Melki, B. Mohr, I. Öksüz, R. Shahzad, C. Wang, P.H. Kitslaar, G. Unal, A. Katouzian, M. Orkisz, C.M. Chen, F. Precioso, L. Najman, S. Masood, D. Ünay, L. van Vliet, R. Moreno, R. Goldenberg, E. Vuçini, G.P. Krestin, W.J. Niessen, T. van Walsum, Standardized evaluation framework for evaluating coronary artery stenoses detection, stenoses quantification and lumen segmentation algorithms in Computed Tomography Angiography, *Submitted*
- **H.A. Kirişli***, V. Gupta*, R. Shahzad*, I. Al Younis, A. Dharampal, R.-J.M. van Geuns, A. Scholte, M.A. de Graaf, R.M.S. Joemai, K. Nieman, L. van Vliet, T. van Walsum, B.P.F. Lelieveldt and W.J. Niessen *(* shared first authorship)*, Additional diagnostic value of integrated analysis of cardiac CTA and SPECT-MPI using the SMARTVis system in patients with suspected coronary artery disease, *Submitted*
- R. Shahzad*, **H.A. Kirişli***, C. Metz, H. Tang, W.J. Niessen, L. van Vliet and T. van Walsum *(* both authors contributed equally to this research)*, Automatic detection and quantification of coronary artery stenoses using contrast enhanced CT scans, *Submitted*

Conference Papers

- **H.A. Kirişli**, M. Schaap, S. Klein, L. Neefjes, A.C. Weustink, T. van Walsum and W.J. Niessen, Fully automatic cardiac segmentation from 3D CTA data: a multiatlas based approach, *Proc. SPIE Medical Imaging 2010: Image Processing*, Vol. 7623, 2010.
- C.T. Metz, N. Baka, **H.A. Kirişli**, M. Schaap, T. van Walsum, S. Klein, L. Neefjes, N.R.A. Mollet, B.P.F. Lelieveldt, M. de Bruijne and W.J. Niessen, Conditional Shape Models for Cardiac Motion Estimation, *13th International Conference on Medical Image Computing and Computer Assisted Intervention - MICCAI*, 13(Part I):452–459, 2010.

- **H.A. Kirişli**, V. Gupta, S. Kirschbaum, L. Neefjes, R.J. van Geuns, N.R.A. Mollet, B.P.F. Lelieveldt, J.H.C. Reiber, T. van Walsum and W.J. Niessen, A patient-specific visualization tool for comprehensive analysis of coronary CTA and perfusion MRI data, *Proc. SPIE Medical Imaging 2011: Visualization, Image-Guided Procedures, and Modeling*, Vol.7964, 2011.
- V. Gupta, M. Van de Giessen, **H.A. Kirişli**, S. Kirschbaum, W.J. Niessen and B.P.F. Lelieveldt, Robust motion correction in the frequency domain of cardiac MR stress perfusion sequences, *15th International Conference on Medical Image Computing and Computer Assisted Intervention - MICCAI*, 15(Part I):667–674, 2012.
- R. Shahzad, T. van Walsum, **H.A. Kirişli**, H. Tang, C.T. Metz, M. Schaap, L.J. van Vliet and W.J. Niessen, Automatic detection, quantification and lumen segmentation of the coronary arteries using a two point centerline extraction scheme, *15th International Conference on Medical Image Computing and Computer Assisted Intervention - MICCAI - Workshop proceedings - 3D Cardiovascular Imaging: A MICCAI segmentation challenge*, 2012.

Conference Abstracts

- **H.A. Kirişli**, V. Gupta, S. Kirschbaum, L. Neefjes, R.J. van Geuns, N.R.A. Mollet, B.P.F. Lelieveldt, J.H.C. Reiber, T. van Walsum and W.J. Niessen, Integrated visualization and analysis of coronary arteries and myocardial perfusion, *NVPHBV Fall 2009 - BioMedical Image Analysis*, 2009.
- **H.A. Kirişli**, V. Gupta, S. Kirschbaum, L. Neefjes, R.J. van Geuns, N.R.A. Mollet, B.P.F. Lelieveldt, J.H.C. Reiber, T. van Walsum and W.J. Niessen, Integrated visualization and analysis of coronary arteries and myocardial perfusion, *International Journal of Computer Assisted Radiology and Surgery (CARS)*, 2010.
- **H.A. Kirişli**, V. Gupta, S. Kirschbaum, L. Neefjes, R.J. van Geuns, N.R.A. Mollet, B.P.F. Lelieveldt, J.H.C. Reiber, T. van Walsum and W.J. Niessen, A patient-specific visualization tool for comprehensive analysis of coronary CTA and perfusion MRI data, *3rd Dutch Conference on Bio-Medical Engineering (BME)*, 2011.
- **H.A. Kirişli**, V. Gupta, R. Shahzad, S. Kirschbaum, A. Rossi, R.J. van Geuns, N.R.A. Mollet, B.P.F. Lelieveldt, J.H.C. Reiber, T. van Walsum and W.J. Niessen, SMARTVis: a computer-aided diagnosis system for comprehensive visualization and analysis of multi-modal cardiac imaging data for the assessment of coronary artery disease, *European Congress of Radiology (ECR)*, 2012.
- R. Shahzad, D Bos, C.T. Metz, **H.A. Kirişli**, A. van der Lugt, L. J. van Vliet, W.J. Niessen and T. van Walsum, Automatic method for quantification of pericardial fat on non-enhanced cardiac CT, *European Congress of Radiology (ECR)*, 2013.

Workshop Proceedings

- **H.A. Kirişli**, M. Schaap, T. van Walsum, A. Dharampal, K. Nieman, G.P. Krestin and W.J. Niessen, Editorial - 3D Cardiovascular Imaging: a MICCAI segmentation challenge - Coronary Artery Stenoses Detection and Quantification Evaluation Framework, *15th International Conference on Medical Image Computing and Computer Assisted Intervention - MICCAI - Workshop proceedings - 3D Cardiovascular Imaging: A MICCAI segmentation challenge*, 2012.

PhD portfolio

PhD period: 2008 – 2013
Departments: Radiology & Medical Informatics
Research schools: ASCI, COEUR.

In-depth courses

21st International School for Computer Science Researchers
on 'Molecular and Medical Image Analysis and BioInformatics', Lipari, Sicilia 2009
Knowledge-Driven Image Segmentation (ASCI) 2009
Biomedical English Writing and Communication (Erasmus MC) 2010
Advanced Pattern Recognition (ASCI) 2010
Cardiovascular Imaging and Diagnostics (COEUR) 2010
C++ course (BIGR) 2010
Heart Failure (COEUR) 2011
Dutch courses (Erasmus MC)
Level A2 (Beginner) ..... 2011 - 2012
Level B1 (Intermediaire) 2012
Cardiovascular Clinical Epidemiology (COEUR) 2012

International Conferences (attendance/presentation)

Visual Computing for Bio-Medicine (VCBM),
Delft, the Netherlands (attendance) 2008
Functional Imaging & Modelling of the Heart (FIMH),
Nice, France (attendance) 2009
SPIE Medical Imaging 2010,
San Diego, CA, USA (oral presentation) 2010
Computer Assisted Radiology Surgery (CARS),
Geneva, Switzerland (poster presentation) 2010
IEEE International Symposium on Biomedical Imaging (ISBI),
Rotterdam, the Netherlands (attendance) 2010
SPIE Medical Imaging 2011,
Orlando, FL, USA (oral presentation) 2011
European Congress of Radiology (ECR),
Vienna, Austria (workshop attendance) 2012
Medical Image Computing and Computer-Assisted Intervention (MICCAI),
Nice, France (workshop organization) 2012

Seminars and Workshops

Netherlands Forum for Biomedical Imaging (NFBI),
Delft, the Netherlands 2009
New clinical aspects of heart failure (COEUR),
Rotterdam, the Netherlands 2009
Netherlands Forum for Biomedical Imaging (NFBI),
Leiden, the Netherlands 2010
Biomarkers for Risk Prediction (COEUR),
Rotterdam, the Netherlands 2010
Visualization and Virtual Reality in Medicine,
Geneva, Switzerland 2010
PhD Career Day 2010
Personal Branding
It's All about YOU: Creating Project Ownership
Rotterdam, the Netherlands 2010
Detection of early atherosclerosis (COEUR),
Rotterdam, the Netherlands 2011
MIC-GPU: High-Performance Computing for Medical Imaging on GPU,
Orlando, FL, USA 2011
Early Career Professional Development in Medical Imaging,
Orlando, FL, USA 2011
Erasmus MC PhD day 2011
Defend your thesis
How to print your thesis,
Rotterdam, the Netherlands 2011
Postdoc Network Erasmus MC meeting
Workshop: Leadership, a real challenge?!
Rotterdam, the Netherlands 2011
EPAR PhD Career day
Career choice
Know your qualities
Rotterdam, the Netherlands 2012
Postdoc Network Erasmus MC meeting,
Networking: social skills and attitude
Rotterdam, the Netherlands 2012

Other presentations

Nederlandse Vereniging voor Patroonherkenning en Beeldverwerking (NVPHBV),
Leiden, the Netherlands 2009
Dutch BME conference,
Egmond aan Zee, the Netherlands 2011
Research seminars ..... 2008 - 2012

Biomedical Imaging Group Rotterdam (4x)
Department of Medical Informatics (2x)
Department of Radiology (1x)
Medical Informatics PhD days 2009

Other

Teaching Assistant Introduction to Image Processing for Medical Students,
Rotterdam, the Netherlands ..... 2009 - 2011
Supervising practical and excursions, BIGR Trip 2010
Lecture to TU Delft MSc students,
Rotterdam, the Netherlands 2011
Rotterdam, the Netherlands 2013
Member of the Erasmus MC team of the Van Noordwijk Stipendium
Battle of the Universities,
Leiden, the Netherlands 2011
Demonstrations at the 'Heart In 3D' booth at ECR,
Vienna, Austria 2012
Organization of international workshop 2012
'3D Cardiovascular Imaging: a MICCAI segmentation challenge'
Nice, France
Reviewing for
Vis Week Conference 2011
Medical Physics ..... 2011 - 2012
IEEE Transactions on Medical Imaging 2012
IEEE Transactions on Information Technology in Biomedicine 2012
MICCAI Conference 2013

Acknowledgments

From October 2008 to March 2013, I have been working as a PhD student at the Erasmus Medical Center in Rotterdam. In this section, I would like to take the opportunity to thank my supervisors and colleagues, for generously sharing their experiences with me, as well as my friends and family, for their unconditional support, love and patience.

To my promoters, co-promoter and PhD committee members

Mijn diepste dank gaat in de eerste plaats aan mijn eerste promotor, Prof.dr. W.J. Niessen. Dear Wiro, it has been such a great pleasure to work at the BIGR (Biomedical Imaging Group Rotterdam), I am very glad that you offered me the possibility to be one of your PhD students. Not only are you a great *boss*, you are also joyful and gentle; thank you for supporting me during the few hard moments through my PhD. And not to forget, I have always been impressed by your dancing skills, from disco to hip-hop, you got the move :)!

Mijn tweede promotor. Dear Prof.dr.ir. J.H.C. Reiber, I would like to thank you once again for giving a lecture during our MICCAI'12 workshop, and sharing with us your deep insight into the latest developments in cardiac CTA and MRI. It contributed to make our workshop a success!

Mijn co-promotor, Dr.ir. T. van Walsum. Dear Theo, what a great supervisor you are, I truly enjoyed working with you, and especially during the last two years. I wish you all the best with the IGI group. Also, it was fun going roller skating with you, together with Rahil and Nóra, during the Wednesday Night Skate Rotterdam; hope to see you there sometimes this summer too!

Prof.dr.ir. B.P.F. Lelieveldt, dear Boudewijn, thank you for welcoming me at the LKEB! Though I visited the group very irregularly (you may count them on the fingers of one hand), I appreciated the feedback on the visualization papers, and your support for clinical collaboration with LUMC.

The inner committee members, Prof. W.J. Niessen, Prof. J.H.C. Reiber, Dr. K. Nieman, Prof. B. van Ginneken, Prof. P.J. de Feyter, and Dr. J.G. Bosch; the plenary committee members, Prof. G. Unal, Prof. M.G.M. Hunink, and Prof. L.J. van Vliet; Dr. T. van Walsum; thank you for your time and efforts to read my thesis, as well as willingness to attend my defense. Also, I would like to thank Desiree and Petra for their support with all administrative tasks, the printing of my PhD thesis, and the organization of my defense.

To my dearest colleagues

Thank you to the many health care professionals from Erasmus MC, LUMC and UMCU who took the time to meet with me or exchange emails; I would not have become so knowledgeable about cardiovascular diseases and its management without you. More particularly, I would like to thank Elina for the hours she spent on visually inspecting cardiac segmentations (Chapter 2), Sharon for sharing her MRI database with me, as well as Alexia, Anoeshka, Robert-Jan, Dr. A. Scholte (LUMC) and Dr. I. al Younis (LUMC) for their involvement in the clinical evaluations of the SMARTVis system (Chapters 5 and 6). Last, I am eternally grateful to Koen, Anoeshka, Elina, Bob, Admir, Matthijs (UMCU) and Michiel (LUMC) for their contribution in collecting and annotating datasets for the coronary artery stenoses evaluation framework (Chapter 4).

The evaluation framework is the work of my PhD I am the most proud of; *when there is teamwork and collaboration, wonderful things can be achieved*. Therefore, I would like to thank Michiel, Coert and Theo for always being available to brainstorm with me, as well as assist me with the website and programming. Thank you for trusting me to complete successfully the evaluation framework! Caroline, it was a great pleasure to co-organize the "3D Cardiovascular Imaging: a MICCAI segmentation challenge" workshop with you. Also, I am grateful to all the challenge participants, who contributed to the success of the evaluation framework; I have been very pleased to meet all of you in Nice! More particularly, my appreciation goes to Pieter and Alexander (LUMC), Maciej (CREATIS), Rodrigo (CMIV) and Roman (Rcadia) for their thorough feedback on the evaluation framework and manuscript. Maciej, thank you for proof-reading the french summary of this PhD thesis! Prof. Gözde Unal, I am very pleased that you came from Turkey to be part of my committee. Last, I would like to thank Toshiba Medical Visualization Systems Europe (Edinburgh, UK) and Medis Medical Imaging BV (Leiden, the Netherlands) for supporting financially the workshop.

Rahil and Vikas, my *"Heart In 3D" buddies* and professional photographers! Both our lives and PhD were full of pitfalls, twists and turns, but somehow, we made it! Thank you for your great support and teamwork. I enjoyed conferences we visited together, and especially FIHM'09 and MICCAI'12 (our first and last) in Nice, amazing Côte d'Azur!

Michiel, thank you for sharing your knowledge with me and guiding me into my research the first years of my PhD. Stefan, thank you for patiently explaining me the deepest secrets of Elastix. Reinhard, Coert and Michiel, thank you for the Mevislab assistance! Coert, many thanks for sharing with me the Latex sources of your thesis, and especially the code for the turning heart :) Coert, Reinhard en Renske, veel succes bij Quantib! Coert and Nóra, it was a great pleasure to work with you on the cardiac motion prediction. Nóra, thank you for the *paranymph* experience, it was an honor to be standing next to you on November 16^{th} 2012! Nóra and Azadeh, thank you for the nice time in San Diego and San Fransisco, I deeply enjoyed the girly shopping, the sightseeing, the Iranian's night, and the real American burger experience! Arna, thank you for experiencing with me the Manta roller coaster at the Sea World in Orlando, I enjoyed every second of spinning, gliding, water skimming and flying! The Lipari summer school will remain on of the most unforgettable time of my PhD; thank you Nóra, Esben, Christophe, Nicolas, Akin, Chris, Michael, Çağatay for all the fun we had over there, next to the nice lectures! TT and Rahil, office roomies for 4 years, thank you for making the working atmosphere so friendly and relax. I will truly miss you! Gerardo, enjoy the best office for few weeks! Miroslav and Valerio, you are great musicians! To my *generation* of PhD students, Marius, Reinhard, Rahil, TT, Arna, Esben, Diego, Hakim, I wish you all the best in finalizing your PhD! Petit clin d'oeil aux *Frenchies*, Émilie, Pierre, Jean-Marie, Guillaume, qui ont choisi comme moi en 2008 de venir faire de la recherche au sein de BIGR; bon courage à tous! Gabrielle, encore merci pour les *after-work drinks* et *chat*, c'était cool de t'avoir parmis nous en 2011! And of course, a big wave to all my other BIGR colleagues, without whom these acknowledgments would not be complete – too many to list, but I am truly indebted to you all! Wishing you a lot of fun in the new building! As ever, many thanks to all the members of the Medical Informatics and Radiology departments. I deeply enjoyed all the drinks, birthday cakes, research talks and outings with you!

To my dearest friends

When I started my PhD, I first dedicated 100% of myself to my research, neglecting my social life. After some months (to not say years), I realized that happiness does not only result from work achievements, but that fulfilled social and personal life equally contribute to it. I therefore started to live life to the fullest, finally achieving the right balance between professional and personal life. I am therefore grateful to the persons that made my time in the Netherlands more enjoyable, and particularly to the following ones.

Rahil, my first paranymph. It probably took me as much time to get used to your Indian accent that it took you to understand my *Frenglish*, but at the end, we got to understand each other pretty well :) You have been a great colleague, always willing to turn the heating on and off on demand, to serve (free!) Nespresso coffee, and to listen to my complains as a psychiatrist; but you are an even more awesome friend! Never bored of keeping me company during girly movies (I believe I still own you some action movies company ;)) while sharing pop-corn, and always in for some sweetness (croissants, chocolate cakes, ice creams,...). I enjoyed the many weekends we have spent together in Rotterdam, our Turkish and Indian cooking workshops and diners. Thank you so much for joining me in Paris at Christmas 2012 (now we know, there is no fireworks at the Eiffel Tower for New Year!!!) and for all the other smaller trips we have done together at conferences, in Vienna and Nice. All my support for the last months of your PhD, looking forward to visit India with you sometimes, and you will always be more than welcome in Chamonix for a frightening first ski session :D!

Émilie, Myrtille :), my second paranymph, now almost a year you joined the BIGR. What is gripping is your persistence; you have your own (strong) opinion on things, and are always willing to share (and discuss!) it with others. I like it! Thank you so much for introducing me to *Causette* (parce qu'on nous prend encore trop souvent pour des quiches); I finally enjoy reading a women's magazine, which is, by the way, not only intended to women, so guys, don't hesitate to go through one of them, you may be surprised! Thanks a lot for the salted butter caramel imported directly from your hometown in Brittany and the chocolates, I would love to remain your private MeVisLab support for the next three years! To many more girly days at the spa, sushi nights, beers, wine and cocktails (mojitos!), dance classes (aïe, aïe, aïe!), and NOW&WOW parties!

My ever-fabulous and supportive friend, Elifcan, canım benim! Almost 8 years that we know each other! We first met in Toulouse in 2005, where we both had unforgettable time. After what, I moved to the Netherlands and you decided to go on with your studies in Canada. Though kilometers separated us, we were always there to cheer each other up, and share the most exciting secrets of our life :) I had great time with you and your family the past three summers in Turkey; Sehriban & Hüseyin, Dilara, beni ağırladığınız için çok teşekkür ederim. From the historical heart to the ultra-chic shopping malls, the beautiful bridges on the Bosphorus, and the chilling time smoking narguile, drinking *çay* and eating *gözleme*, I love Istanbul! Can't wait to come visit you once again, and I am waiting for you here in the Netherlands too!

Hélène et Julien, premiers à oser venir me rendre visite dans le *Grand-Nord*, en juillet 2011. C'est avec grand plaisir que je vous ai accueilli et fait, avec Rahil, la visite guidée! Un grand merci pour la crémaillère à Paris, dommage pour celle de Lyon, mais ce n'est que partie remise! J'attends avec impatience de venir en weekend dans votre (future!) maison de campagne, pour boire l'apéro autour d'un barbecue et jouer à la pétanque.

Jérôme et Ronan, vous avez survécu aux 40 km de vélo pour aller visiter Kinderdijk, ainsi qu'au bien mérité *kapsalon*! Tout mon respect à Ronan qui a réussi à se jeter à l'eau à la plage de Rockanje; Jérôme, la mer du Nord t'attend toujours! Maintenant que ma thèse est finie, j'espère avoir l'opportunité de vous rendre visite à Toulouse, histoire de faire un plongeons dans votre piscine, de me relaxer sur votre matellas gonflable tout en sirotant un cocktail, et d'avoir un aperçu des Maldives en admirant votre aquarium.

Miryam et Vanessa, mes *poulettes* de Toulouse, que j'ai un peu perdu de vue pendant ces quatres dernières années. Miryam, je suis très heureuse que tu puisses venir assister à ma soutenance. Ce weekend ne sera certainement pas suffisant pour rattraper ces dernières années, mais nous aurons certainement l'occasion d'aller se dorer au soleil, ou de se faire un *girly city-trip* ensemble très prochainement. Vanessa, Londres n'est pas loin, et pourtant, je n'y suis toujours pas allée... c'est sur ma *short todo* liste, alors je te dis à très vite :)!

Stéphanie et Annie, un grand merci pour m'avoir acceuilli pendant 4 ans dans votre maison à Overschie. C'était cool de partager la maison avec toi Steph, et de papoter en français. Le quartier me manque!

One of my passions being dancing, I would like to thank my salsa teachers, dance partners and friends, and more particularly, Andrea, Humberto, Meng-Hoa and Abigail, Lars, Amanda, Samantha, John and Nancy, Andre and Jose, Katarina and Arnold, with who I learned my first dancing steps in 2010. Marleen, sweet little Cupid, without who I would not have met Piem. Many thanks to Taiti and Cristel from *TC Dance Company*, who contributed to improve my technique during the past year, and let me experience the swing of happiness through dancing! Jolene, Judith, Bart and Miguel, Nóra, Azadeh and Noemí, I deeply enjoyed the many salsa parties we have been together, as well as the several coffees, chat and dinners. Noemí, I enjoyed very much visiting you in Madrid, looking forward to the next time in Barcelona, and I am thrilled that you and Hector will come in June!

Also, I would like to thank Algina & Arjan, Chan Mi & Kevin, Kirsten & Renard, Loraine & Arnold, Yoki, Martijn, Koert, Jorinde & Ronald, Nadine & Nick, Zoya & Pedram, Faryda, for all the drinks, diners, (cocktail and birthday) parties, barbecues, game nights... you all contributed to make me enjoy more the Netherlands!

Je voudrais aussi remercier mes ami(e)s de Chamonix, sans qui mes weekends express et vacances à la montagne n'auraient pas été les mêmes. Jérèm', j'espère pouvoir me faire une sortie snowboard avec toi l'hiver prochain, alors récupère bien! Claire, c'était cool de te voir et d'aller s'embourber dans la boue au festival Paléo ensemble! Stéphanie et Damien, vous êtes les bienvenus aux Pays-Bas avec Céleste, *anytime*!

Last, I would like to thank my fitness teachers and friends from David Lloyd. Tamara and Namita, hartelijk bedankt voor de bodyPump en bodyBalance groepslessen! Het heeft bijgedragen om mijn leven spanningen te verminderen. Esco, Inge, Theo, many thanks for the Tuesday evening coffee and chat. Without to forget, thank you Ihor for initiating me to squash, and for our, though very irregular, always enjoyable matches! And after the effort, the reward; Riri, I love your *Twinkle* (cup)cakes!

To my family

I would like to express my gratitude to my family members, for their unconditional support: to my mum, Martine, to my dad and step-mother, Kayhan and Nilgün, to my sister, cutest niece and her daddy, Amélie, Laura and Nicolas, to my Turkish family, Kenan and Nurgül, Barkan and Berkut, Ayşen, Fatma, and to my god mothers, Janette & Amor and Nadine. *Un grand merci à tous, çok teşekkür ederim!*

Last, I would like to thank Piem, my life and dance partner, who was there for me to enjoy the best moments, cheered me up during the worse, and without who the last year of my PhD would not have been so pleasant. I believe I made it hard for you sometimes, you can blame my determination :). I deeply enjoyed all our trips, from the closest for a weekend at De Beukenhof in Oegstgeest, to the furthest for a week road-trip in Andalusia; looking forward to many more! Thank you for your patience, faith and ... endurance!

Hortense Ayla Kirişli,
April 5th 2013

About the author

Hortense Kirişli was born on August 17, 1986 in Bonneville (France) and grew up in Chamonix-Mont-Blanc.

From 2003 to 2005, she made preparatory classes for entrance exams into French National Engineering Schools, at the lycée Berthollet in Annecy, France, during which she acquired a large range of theoretical knowledge in Mathematics and Physics.

From 2005 to 2008, she followed a training in electronics, with a specialization in signal and image processing, at the École Nationale Supérieure d'Electrotechnique, d'Electronique, d'Informatique, d'Hydraulique et des Télécomunications (ENSEEIHT), Toulouse, France. In 2008, she first took part of a student project at the Centre National d'Études Spatiales (*http://www.cnes.fr/*), during which an automatic tool was developed for measuring beach surfaces on high resolution satellite images. After what, she worked on her Master's thesis, which was entitled "Optimization of the Astronomical Geo-location Methods for the Marine Mammal Tracking". The project was carried out at Collecte Localisation Satellites (*http://www.cls.fr/*), Toulouse, France.

In September 2008, she received her Engineering degree in Electronics. After her graduation, she started working on her PhD project at the Biomedical Imaging Group Rotterdam (BIGR), Erasmus MC, the Netherlands, on CTA Quantification and Multi-modal Visualization for Assessing Coronary Artery Disease. She was involved in the cardiovascular image processing theme group, focusing on cardiac segmentation and quantification from CTA images. She also organized a cardiovascular "Grand Challenge" on coronary artery stenoses detection / quantification and lumen segmentation (*http://coronary.bigr.nl/stenoses/*). The results of this work are described in this thesis.

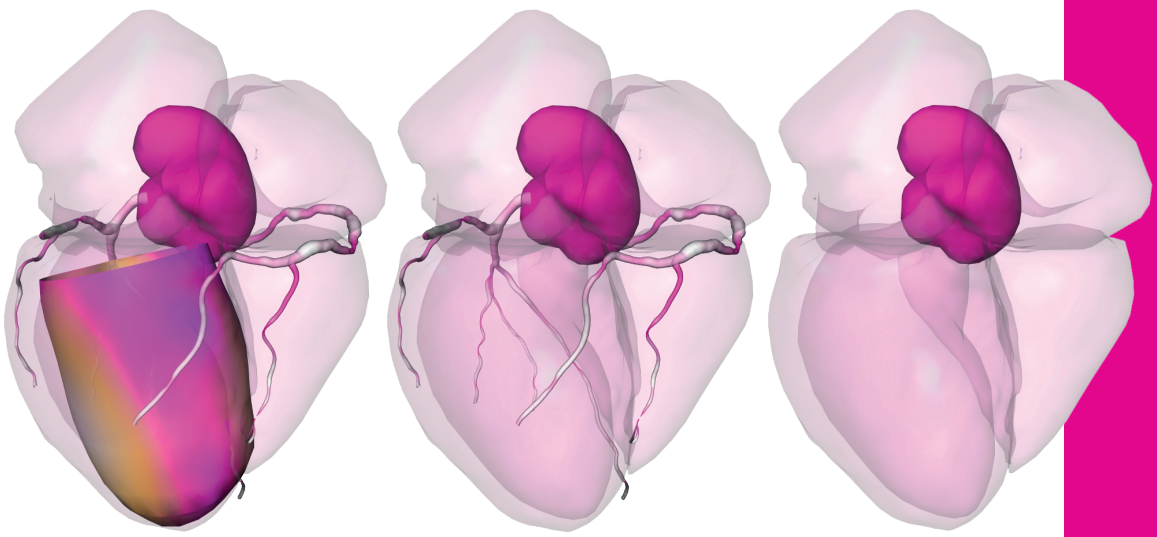

ISBN 978-90-6464-661-4

CTA Quantification and Multi-modal Visualization
for Assessing Coronary Artery Disease